Response of Grooved Composites to Transversely Distributed and Localized Spherical Contact Loadings

by

Holly K Jeffrey

B.S. Aerospace Engineering
Massachusetts Institute of Technology, 2008

Submitted to the Department of Aeronautics and Astronautics
in partial fulfillment of the requirements for the degree of

Master of Science in Aeronautics and Astronautics

at the

MASSACHUSETTS INSTITUTE OF TECHNOLOGY

February 2011

Author .....
Department of Aeronautics and Astronautics
January 7, 2011

Certified by .....
Professor Paul A. Lagacé
Professor of Aeronautics and Astronautics and Engineering Systems
Thesis Supervisor

Accepted by .....
Professor Eytan Modiano
Professor of Aeronautics and Astronautics
Chair, Committee on Graduate Students

Response of Grooved Composites to Transversely Distributed and Localized Spherical Contact Loadings

by

Holly K Jeffrey

Submitted to the Department of Aeronautics and Astronauticson January 7, 2011,
in partial fulfillment of the requirements for the degree of
Master of Science in Aeronautics and Astronautics

Abstract

The response of a grooved composite specimen to two contact loading situations is studied; load applied via a transversely oriented cylindrical indenter and via a localized spherical ball-ended indenter. The philosophy of the Building Block Approach is used to develop these tests in the current study in that the cylindrical indenter creates a "two-dimensional loading" (transversely distributed) case, and the spherical indenter adds complexity to the system and creates a "three-dimensional loading" (localized spherical) case. The final failure and initial permanent deformation, in the form of crushing, is investigated, along with the effect of laminate configurations and ply angles. The is done by using the two indenters, six different laminates, and two types of tests to study the grooved composite specimens, 1 inch wide by 2 inches long, of 78 to 80 plies. This work uses a specimen configuration and testing technique developed in previous work. A computed microtomography technique is used to examine select specimens to ascertain the extent of the internal damage. Specimens subjected to the "two-dimensional loading" case exhibit four Behavior Types of the load-stroke response. Several aspects of the response are used to characterize the Behavior Types, including initial linear regions, knee loads, reverse knee loads, second linear regions, and changes in slopes. The responses of the two loading cases indicate that the details of the laminate play a significant role in the load-stroke response for the "two-dimensional loading" case, whereas the details of the loading play a more significant role for the "three-dimensional loading" where only one type of load-stroke behavior is generally displayed. In the "three-dimensional loading" case, significant crushing occurs which is not seen in the "two-dimensional loading" case. This is visible due to the localized loading for the "three-dimensional loading" case, and impacts the overall load-stroke response. The 90° plies, in addition to the "mesh" created by the ply angles in the laminate, and the "ply angle mismatch" within a laminate, affect the ability of the laminate to resist indentation and the load-stroke response. Recommendations for further work are presented.

Thesis Supervisor: Paul A. Lagacé
Title: Professor of Aeronautics and Astronautics and Engineering Systems, Massachusetts Institute of Technology

Acknowledgments

I owe thanks to many people for their input, which came in many forms, on this thesis.

First and foremost, to my adviser Professor Paul Lagace. Without his help and guidance, this project, and especially the actual writing, may have never been completed. He has been an excellent mentor throughout this experience.

To all the people who have helped with this research: John Kane for always having creative solutions to testing problems and helping me to learn to run the testing machines, Jeff Chambers for all kinds of help, from running microCT scans to interpreting edits, Chris and Yusuke for their preceding work, especially as I learned much from the work Yusuke did previously. An a special thanks to my UROPs, Kim and Jonathan, who spent many hours creating indenters, laminates, and samples for me to use. All the members of TELAMS were wonderful to work with and bounce ideas off, and I thank you all for being wonderful.

In addition to my labmates in TELAMS, who I consider to be great friends, I also want to thank all the other friends who kept me sane throughout the entire process. This includes friends in Aero-Astro, those at MIT, those all around Boston, and everyone at home.

Of course, many thanks to my family, and especially my parents. There were times that they were more confident in me than I was. I really cannot express how much I appreciate everything you've done for me.

Foreword

This work was preformed in the Technology Laboratory for Advanced Materials and Structures (TELAMS) of the Department of Aeronautics and Astronautics at teh Massachusetts Institute of Technology. This work was sponsored by The Boeing Company under teh General Terms Agreement between MIT and Boeing as Boeing Award Number MIT-BA-GTA-1.

Table of Contents

List of Figures

List of Tables

Nomenclature

x - direction aligned with specimen length

y - direction aligned with specmen width and groove

z - direction perpendicular to plane of fibers

θ - fiber direction, degrees from x

h - specimen height

Chapter 1

Introduction

Composite materials, especially carbon fiber reinforced polymers (CFRPs), have come into greater use in the last several years [1]. They are desirable for use, especially in systems where weight savings of are significant consideration, due to beneficial material properties, such as high specific stiffness and strength, fatigue and corrosion resistance, and their ability to be customized for use in different applications. While there are many potential benefits in using composite materials, their use in industry has been slow to take place and their applications have been limited. This is largely the result of the complex nature of their response to loading, and particularly that their failure behavior is not well explained or captured by current theories [2]. Carbon fiber composites are generally loaded in the plane of the fibers as this is the direction that is reinforced. Furthermore, the behavior due to loading perpendicular to the fibers is less understood. As a result of the lack of understanding, the use of composite materials has been limited to relatively simple shapes and load applications in the plane of the fibers.

Despite the lack of understanding and predictability of the failure of composites, their used has recently seen significant increases in the aerospace industry. They have been used in military planes for some time, but only in the last decade have they been applied to commercial jets as a significant portion of the structure. The Boeing 787 is the first such commercial application in which over 50% of the weight of the structure is carbon fiber composite [3]. Airbus has designed a competitor to the 787,

the A350, which is also primarily made of composite materials, a significant increase from the Airbus A380 which is approximately 25% composite by weight and their most recent new large commercial jet released [3]. This exemplifies the siginificant increase in use that composite materials are seeing in the aerospace industry. To continue this expansion of use, the response of more complicated structures to more types of loadings needs to be better understood.

One particular loading type of aerospace structures that needs to be understood is its ability to withstand impact. With certain additional conditions met, quasi-static indentation testing can be a good alternative to impact testing [4–6]. These tests are used for investigation of loading transverse to the plane of the fibers in fiber composite materials. In general, out-of-plane loadings are generated by contact loading. The material will have better ability to sustain loadings due to these contact stresses if the shapes of the indenter and the specimen are complementary, thus maximizing the area over which the load is transfered to the specimen.

An example of an application of a transversely loaded composite structure is the design of a telescopic wing spar by Sarh et al [7, 8]. This component, which is made of grooved composite segments and is connected by ball bearings, would generate concentrated contact loadings in the composite. This configuration is a key component in the Advanced Flying Automobile (AFA) design. The spar would allow the vehicle to change from an "aircraft" mode where the wing with the spar is extended, to an "automobile" mode where the wing with the spar is collapsed and stored. The dual modes are aimed to overcome common problems with a flying car, such as how to prevent too much drag or cross-sectional area while in driving mode. In flight, the loads on the wings need to be transferred from the tips of the wings to the fuselage, and the load would mostly be carried by the telescopic spar. In the spar, which is made of several grooved segments, the only way to transfer a load is through the ball bearings in the grooves. A weight savings of 50% of the spar weight would be achieved by changing 4 of 7 spar segments from steel to composite.

While the AFA is one possible application for a telescopic spar, additional applications could include Unmanned Aerial Vehicles (UAVs) and commercial jets. Long

range UAVs such as the Global Hawk have large aspect ratios, with wingspans of up to 40 meters, and as a result require large spaces for storage [9]. The ability to collapse and store the wings would improve space requirements for storage. Similarly, the commercial jet industry could benefit from the ability to collapse a wing. Commercial jets with a telescopic wing of carbon fiber composite would allow for larger wingspans without a need for reconfiguration of gate space. There also would be relatively less increase in weight due to the use of the lighter material.

For the use of a grooved composite spar to be realized in any application, the response of the composite with a groove and the contact loading needs to be understood. To do this, the behavior that results from the contact loading of the interface from the steel ball bearing and the composite groove needs to be investigated, and analysis alone is not sufficient for composite structures due to the complex nature of their response for damage and failure considerations. The building block approach, as described in Composite Materials Handbook 17, which involves starting at basic material property levels and increasing complexity of a specimen and loading, is used to develop the understanding of a composite structure and will be used as part of this work [10].

The primary objective of the work reported here is to consider several different parameters of a composite specimen subject to contact loading, and bound the possible responses. In Chapter 2, the work that has been reported in the literature to study grooved composites is examined. One note is that the amount of such work is relatively small. After this consideration, the greater detail of the objectives of this work to achieve better understanding of the response of a grooved composite, along with the overall approach, are discussed in Chapter 3. The different experimental procedures used in this work, from manufacturing through to testing, are described in Chapter 4. The results of the tests of the samples are presented in Chapter 5, while the analysis of these results and proposed explanations and interpretations are presented in Chapter 6. Final conclusions and recommendations for possible future work are given in Chapter 7.

Chapter 2

Previous Work

It is important to consider the previous work that has been done on grooved composites, as well as on composites subject to contact loads, particularly quasi-static loads. Research where the test method and specimen geometry were developed has been examined. This helps to establish knowledge that can be used in the current work.

2.1 Transverse Loading of Composites

Transverse loading of composites, both static and dynamic, has received significant attention primarily because of its application to the impact response of composite structures. This particularly includes emphasis on the resulting damage. Composite structures have been shown to be sensitive to out-of-plane impact loads, and these impacts can occur during any phase of the life of a composite structure, from manufacturing to operation [11]. Abrate compiled two reviews of the work done in the area of impact loads [11, 12]. As a result of the work done in such studies, the ASTM standard D7136/D7136M-07 was developed. This standard is for measuring laminate damage due to impact [13]. More recent impact damage studies have included work to determine the delamination thresholds due to impact [14, 15], and work with more complex loadings such as initial stresses [16]. Further testing has focused on glass fiber composites rather than carbon fiber composites, such as in the work conducted

by Rilo and Ferreira and by Yang and Cantwell [15, 17], or on sandwich structures (e.g. [18]).

Quasi-static testing has been used to examine the response of laminated composites to impact loads. Many studies have been done to determine under what conditions quasi-static loading emulates impact response [4–6]. These have found that the maximum contact force can be used to characterize the damage response of the laminate. Quasi-static indentation work on laminates has led to the development of ASTM standard D6264/D6264M-07 for measuring the damage of a laminate subject to a quasi-static indentation force [19]. This test standard is designed to allow observation of the damage response of a composite structure. However little experimental work in the area of quasi-static indentation of composites has been done outside of use to evaluation of the impact response. Additional experimental studies which load carbon fiber composites transverse to the fibers lead to significant bending [20], which primarily leads to a global structural response, rather than an isolated response as a result of the introduction of a transverse load. For example, in one study [20], circular carbon fiber plates with simply-supported boundary conditions were examined. It was found that the displacement at the load application point of the specimen was greater than the thickness. This results in bending leading to delaminations, rather than damage and failure as a direct result of the load application, and so is not directly related to the current work.

Analytical models for the response of two elastic bodies contacting each other were originally developed by Hertz [21]. The Hertzian contact solution is used to determine the contact area, stress distribution and relative approach of the bodies and is the basis for much of the analytical work on the subject of indentation of laminates. This has been adapted for application to composites, and researchers found these results were in good agreement with experimental data [22–25]. Finite element modeling has become more popular in recent years with the availability of commercial software, and for modeling the behavior of composites and the quasi-static indentation case [26–30]. This allows for greater exploration and understanding of what occurs in the composite. The modeling work that directly pertains to grooved composites is

discussed in the following section.

2.2 Grooved Composites

There is relatively little work that has been done examining composites with grooves. The work that has been done in this area has primarily been specific to a certain application rather than considering general issues. For example, Montay et al. examined residual stresses in a composite with the compliance method [31]. In this work, a flat groove was incrementally drilled into a composite to determine the gradient of residual stresses within a laminate by an adaptation of the compliance method. Furthermore, a thin, cross-ply laminate was considered in this work. Overall, the groove was used only to determine residual stresses, and the response of the composite with the groove when loaded was not considered. Hoppel et al. developed a buttress groove made of composites for transmitting shear load [32, 33]. The buttress groove is a device that looks like a squared end of a sawtooth. This includes a pressure flank that is oriented mostly perpendicular to the length of the structure to transmit shear loads. A load was applied to the vertical edge of the protruding groove and different laminates were studied to optimize the ability of the structure of transmit the load from the pressure flank to the base laminate. However, this structure is designed to transmit load only in one direction, and is reinforced for this purpose. Both these investigations were of designs with specific applications.

An analytical investigation of a grooved composite subject to a transverse load was conducted by Bastien [29, 30]. This work looked at isotropic and composite materials with a groove and modeled the application of a contact load using finite element analysis. The effects of boundary conditions and geometric parameters on the response of the specimen were examined. This work looked at two-dimensional and three-dimensional models, and assumed the specimen is loaded uniformly along the groove for the three-dimensional model. It was found that the two-dimensional models generally were able to simulate the response of the three-dimensional structure. A key finding of this work was that there were three parts to the response: one, a

global response due to the overall configuration, which is affected by the boundary conditions of the structure; two, a local response due to removal of material to create the groove; and, three, a local response due to the contact loading at the groove. In addition, this work showed that the overall response of the laminate was very similar to that of an isotropic structure, except local to the groove where the effect of different ply angles on the local stiffness is significant.

A recent study was completed by Kobayashi where a grooved composite test specimen and experimental method for testing these specimens when subject to an out-of-plane contact load were developed [34]. This work included a preliminary study, based on the short beam specimen of ASTM Standard D2344/D2344M-00 [35]. The specimen configuration in the standard is designed to cause a delamination due to shear. The preliminary work found that the response of the grooved specimen was not affected by loading of the groove for a specimen and using the test technique based on the short beam shear standard [34]. This led to the use of rigid backface boundary conditions for testing, as well as a more compact specimen. In this configuration, the effects of the groove were directly manifested in the failure. This study also led to refinement of the layup and manufacturing techniques, and determination of necessary materials for the uniform contact loading study. The uniform loading was verified by measuring strains at either end of the groove. Finally, the experimental procedures were verified on a second laminate.

With the exception of work directly preceding the current study [34], very little has been done to observe the general response of a grooved composite, and even less has been done to study a composite loaded perpendicular to the in-plane fibers in the groove. The analytical study by Bastien [29, 30] influenced the work of Kobayashi [34], which are key to the current work. The experimental procedures developed by Kobayashi are employed in the current work. The uniform loading of the specimen along the groove is used on multiple laminates, and modified to study a non-uniform loading in the groove.

Chapter 3

Objectives and Approach

The primary focus of this work is to better understand the response of grooved composite configurations building towards understanding the behavior of a grooved composite spar. Previous work established the specimen geometry and basic test method [34]. Additional test parameters are to be investigated in the current work. In the test configuration established in the previous work, a cylinder is used to provide a uniformly distributed load along the groove of the specimen. This leads to a stress and strain state which is unchanging relative to the direction of the groove, but varies in the two orthogonal directions. The development of the test method for this "two-dimensional loading" included verification of the method for multiple laminate configurations. This parameter of laminate configuration is further varied in the current work. In addition, a three-dimensional concentrated loading, where the loading causes variation in the stress and strain state in all directions, is also examined. Several different laminates are tested, and the effect of different ply angles and laminate configuration on the behavior is studied. In the original work, the specimens were loaded until final failure occurred. As well as testing the composites until final failure, the load at which permanent deformation first occurs is investigated in the current work.

3.1 Use of Building Block Approach

Analysis of composite materials in structures is generally not sufficient for capturing the full response of these structures, particularly with regard to damage and failure, due to the complex response that composite configurations cause. Composite structures are often subject to multiple modes of damage leading to failure, and are sensitive to in-plane and out-of-plane loads and how these they are applied. In addition, there is currently no analytical method that sufficiently captures and predicts the behavior of a composite structure with respect to damage and failure [10]. The building block approach, as described in Composite Materials Handbook 17, is used to develop the understanding of the behavior of a composite structure. The objective of the building block approach is to develop an understanding of the structural response in the overall design, particularly as to how damage will occur and the structure will ultimately fail. The methodology starts at basic material property levels and progresses through the complexity of a specimen and loading. A graphic representation of the overall building block approach, including the levels involved, is shown in Figure 3.1. The current work is a part of the overall building block approach in the consideration of the design of a composite telescopic wing spar. The work employs low-level specimens with a variety of configurations and adds complexity through the type of loading considered.

Building the understanding of the structural response at the component level requires starting at the lowest level of the pyramid with simple test specimens and adding complexities and features to move up levels of the pyramid. Behaviors seen at the higher levels of the pyramid need to be exhibited at the lower levels in order to employ, at the higher levels, the understanding established at the lower levels. This leads to the necessity of "loops" within the building block approach to fully explain the behavior of the specimen being studied at any level. The building block approach allows for experimental identification of different damage and failure modes at different levels for complex composite structures. At higher levels of the building block approach, structural complexity is added to the loading or configuration of the

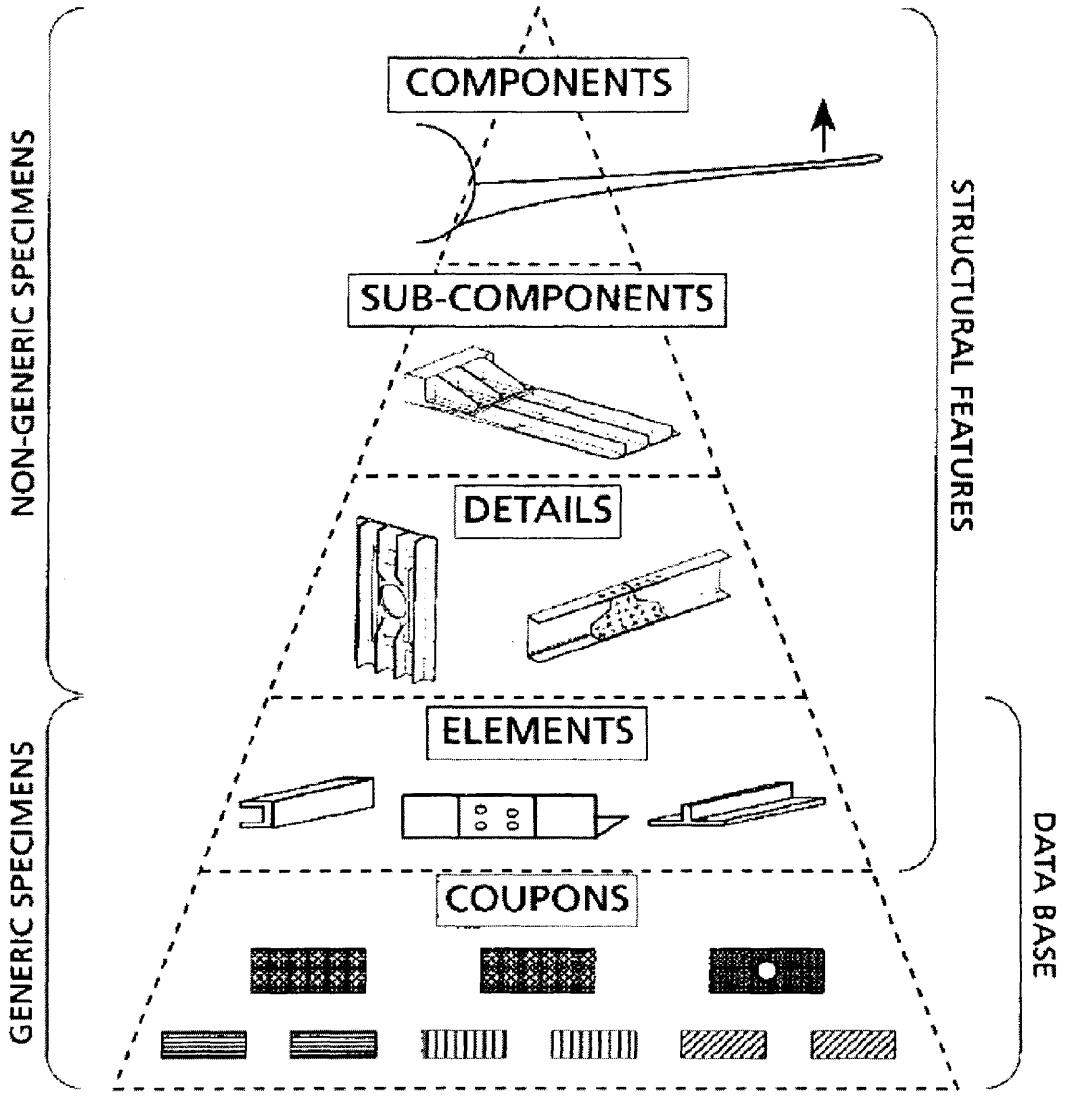

Figure 3.1 Pyramid representation of Building Block Approach [10].

specimen to determine the effect of the added complexity. Material behaviors, such as basic damage modes, need to be displayed at lower levels. If a "new" behavior is first shown at a higher level, such as the element level, it is necessary to return to lower level studies, and then characterize this behavior in order to better document and characterize that behavior for use at higher levels. For example, going between element-level test specimens and detail-level specimens multiple times would create one of these loops of study. Full-scale component-level specimens can eventually be tested for final validation. At this level of testing, all behavior must have previously been seen and documented.

In the context of this work, the building block approach is employed when investigating two of the three objectives. This is further described in the following sections. Part of the building block approach is to add complexity to a system to better understand the response of the structure. In this work, there are two loading configurations used, one of which has a more complex response than the other. In addition, to more fully characterize the behavior at low levels, different laminate configurations are studied.

3.2 Objectives

The primary objective of the current work is to investigate and determine the effects of added complexity from a uniform loading condition to a non-uniform loading applied to a grooved composite specimen. This uses the test method and loading configuration previously developed, and adapts the method for the concentrated loading case. The second objective of this work is to investigate both initiation of damage and final failure of the specimens. For this, specimens are tested in two ways. One is to final failure. The other is until first permanent deformation, or"crushing", is measurable. The final objective is to examine the effect of different ply angles and laminate configurations. For this, six laminates are tested with ply angles ranging from 0° to 90°. Experimental methods are presented in Chapter 4.

3.2.1 Effects of Added Complexity

In this work, there are two loading configurations that are examined: "two-dimensional loading" and "three-dimensional loading". The "two-dimensional loading" is the loading configuration that was used in the initial development of the general test method. This loading was developed to generate a basic two-dimensional response in the specimen with no variation in the width direction. The specimen is a rectangular block with a cylindrical groove in the top face. For the "two-dimensional loading" case, a cylinder is used to apply a load along the length of the groove. This test configuration and associated method were developed to ensure that the loading along the length of the groove would be uniform [34]. This is considered to generate a two-dimensional response as the stress-strain state of the specimen is constant along the length of the groove (i.e. width, or y-direction, of the specimen). A schematic of this "two-dimensional loading" case with the cylinder indenter is shown in Figure 3.2.

The "three-dimensional loading" configuration is used to investigate the response of the specimen when subject to a single concentrated load in the center of the groove, such as would be generated by a ball bearing. This case is considered to be a "three-dimensional loading" as the response generated changes relative to the location along the groove, in the y-direction, as well as in the other two directions, the x- and z-directions, that were affected in the "two-dimensional loading" case. The "three-dimensional loading" indenter used is representative of a single ball bearing in a groove. The idealized case and actual indenter used for the "three-dimensional loading" case are shown in Figure 3.3. This "three-dimensional loading" generates a more complex response than that of the "two-dimensional loading" case, as further described.

For the "two-dimensional loading" case, a cylinder with approximately the same radius as that of the groove is used to apply the distributed load to the specimen. A ball-ended indenter with the same radius as the groove is used to apply a concentrated load at the center of the specimen groove for the "three-dimensional loading" case. A modified indenter was used to avoid problems with the specimen and the load

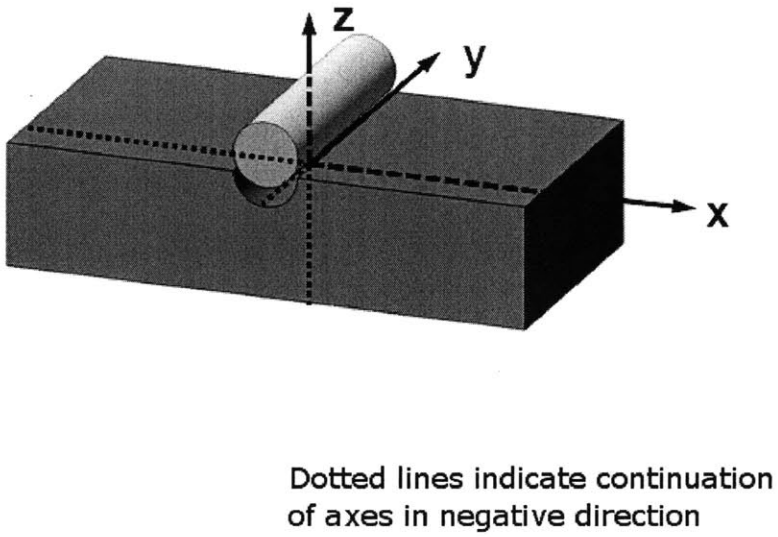

Figure 3.2 Illustration of distributed "two-dimensional loading" configuration.

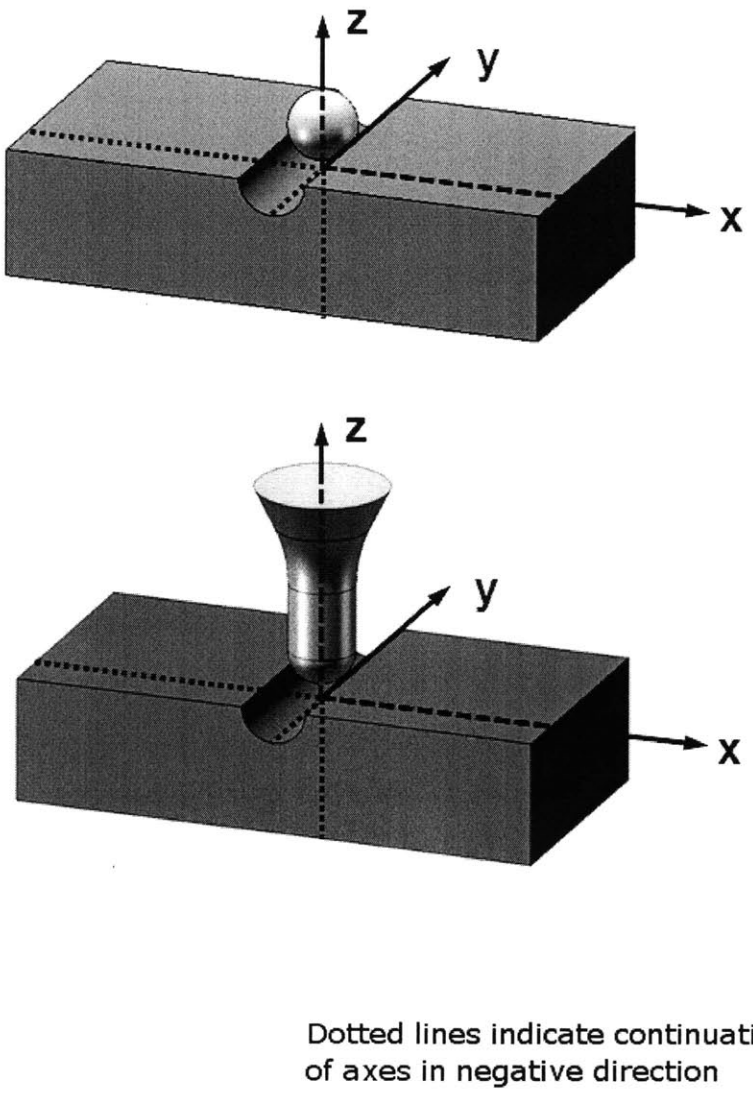

Figure 3.3 Illustration of (*top*) idealized test case, and (*bottom*) actual "three-dimensional loading" applicator.

applicator contacting each other than through a single ball in the groove. This is further described in Section 4.1.

In the "two-dimensional loading" case, the response is uniform through the specimen along the groove. Previous work to validate the test method showed that the strain state of the specimen was the same at either end of the groove. With the "three-dimensional loading" case, response will not be uniform along the groove direction of the specimen due to the changing nature of the approximate point load. These two loading configurations bound the response of the grooved composite subject to a transverse load with the ball-ended indenter used to approximate a single ball bearing.

3.2.2 Damage Initiation and Failure

The behavior up to final failure of the specimen needs to be studied in order to be able to fully characterize the behavior of the transversely loaded composite configuration. This is necessary for later efforts to work to predict such behavior and verify those efforts. To accomplish this, a specimen is loaded with one of the load applicators until it reaches final failure. During this loading, load and indenter displacement data is taken and subsequently used to characterize the specimen.

In addition, the load at which permanent deformation, or "crushing", first occurs also needs to be studied. This load may be related to the limit load of the composite, as the first permanent deformation is a form of damage and failure. Once ball bearings in the structure of the telescopic spar have created a permanent deformation of the groove, further consideration must be able to determine whether the configuration will perform as designed. This potentially results in the load for the first permanent deformation having an impact on the design limit load of the structure. For each of the loading conditions, with the cylinder and with the ball-ended indenter, and for each of the laminates considered, tests are completed to final failure and to find the first permanent deformation. The specifics of the configurations of these tests are described in Section 4.4. The data collected from these tests, time, load and indenter displacement, are used to characterize the behavior of different test specimens as per

their different configurations.

3.2.3 Effects of Ply Angles and Laminate Configuration

In previous work, the test method had been validated for alternate laminates. This work builds on that and examines how several different laminates, with a range of ply angles, behave when subjected to transverse loading in the groove. There are six laminates tested: two with 90° plies and four without. The different laminates examined are listed in Table 3.1. The $[\pm 45/0/90]_{10S}$ laminate is also referred to as quasi-isotropic, and the $[90/0]_{20S}$ laminate is also referred to as cross-ply. The other laminates are $[\pm\theta/0]_{13S}$, and are considered in order to investigate the effects that the ply angle has on the response of the laminate. The number of repeating sets of different ply angles (10, 13 or 20) was chosen so that the different laminate configurations would be approximately the same thickness as set in the original work on the specimen configuration. Previous work found that the thickness below the groove is a key parameter, and the thickness of 78 to 80 plies allows the effect of the loading in the groove to be isolated from boundary condition effects [29, 30, 34].

For each laminate, four types of tests are conducted: crushing and failure tests with "two-dimensional loading", and crushing and failure tests with "three-dimensional loading". Initially three specimens of each laminate, load application, and test type are tested. The one exception in this regard is failure tests of the quasi-isotropic laminate subject to "two-dimensional loading" as these tests were conducted in development and validation work [34]. That data is used in the current work for comparison. The current tests allow for the different investigations that were discussed. The overall test matrix, showing the initial plan of the number of samples of each type to be performed, is shown in Table 3.2.

Table 3.1 Laminates used to examine effects of ply angles and laminate arrangement

Laminates
$[\pm 45/0/90]_{10S}$
$[90/0]_{20S}$
$[\pm 15/0]_{13S}$
$[\pm 30/0]_{13S}$
$[\pm 45/0]_{13S}$
$[\pm 60/0]_{13S}$

Table 3.2 Initial test matrix

	"2-D Loading"		"3-D Loading"	
Laminate	Failure	Crushing	Failure	Crushing
$[\pm 45/0/90]_{10S}$	9*	3	3	3
$[90/0]_{20S}$	3	3	3	3
$[\pm 15/0]_{13S}$	3	3	3	3
$[\pm 30/0]_{13S}$	3	3	3	3
$[\pm 45/0]_{13S}$	3	3	3	3
$[\pm 60/0]_{13S}$	3	3	3	3

*9 samples from previous work [34].

Chapter 4

Experimental Procedures

To ensure the validity of comparing specimens between multiple loading configurations and different layups, uniform procedures were used to manufacture and test the specimens. All specimens were made using Toray Composites P707AG-15 preimpregnated (prepreg) material. The unidirectional prepreg is supplied in rolls that are 24 inches in width. The material is made by Toray Composites from Toray T700GC-12K-31E carbon fibers impregnated with #2510 matrix system. The material, as provided by Toray, Inc, has a fiber volume fraction of approximately 65% and a nominal ply thickness defined to be 0.006 inches. The manufacturing and testing procedures were created and validated in previous work for the "two-dimensional loading" tests [34] and modified in this work for the "three-dimensional loading" tests. Groove measurement techniques were developed and used to validate the machining process and the consistency of the groove depth. After testing, computed microtomography techniques were used to examine the entire volume of selected specimens and to determine the damage that occurred during testing.

4.1 Details of Specimen and Load Applicators

The basic design of the specimen and associated manufacturing techniques used in this work were developed in previous work [34]. These details are used in this work and enhanced as needed. In these latter cases, further description is provided

herein. The overall specimen is shown in Figure 4.1. Axes identifying the directions of x, y, and z are used to refer to the specimen and are shown in that figure. The x-direction is the 0° fiber direction, the y-direction is 90° from this and along the groove, along the plane of the ply. The z-direction is in the thickness/height direction of the specimen, perpendicular to all fibers. All specimens are 2 inches in length in the 0° fiber (x-) direction and 1 inch in width (y-) direction. The height of the specimens varies slightly due to the different number of plies in the different laminate configurations used. There were either 78 or 80 plies in the laminates, which lead to a height of approximately 1/2 inch. The specimens have a semicircular groove perpendicular to the length. This groove is 1/8 inches in depth.

Two load applicators are used in the testing of the specimens. These load applicators are shown in Figure 4.2. One is a cylinder used to apply a distributed load along the length of the groove. This is defined in Section 3.2.1 as the "two-dimensional loading" case as the loading is distributed uniformly along the y-direction and changes only in the xz-plane. This load applicator is a 1-inch long cylinder with a radius of 0.25 inches. The applicator is made of M2/M7 steel with a Rockwell hardness of C62 to C64. Previous work found that softer steel alloys led to deformation of the indenter in addition to deformation and failure of the composite [34], therefore this material was again used for the load applicator.

The second load applicator was developed to create the "three-dimensional loading" case as described in Section 3.2.1. Initial testing made it apparent that there was a need for a load applicator that allowed for significant applicator displacement into the specimen. The design of the "three-dimensional loading" applicator needs to prevent contact between the indenter and specimen during testing such that no piece of the indenter outside of the 0.25 inch diameter of the indenter head makes contact with the specimen. This load applicator is a ball-ended indenter, made of maraging steel, with a 0.5-inch long cylinder with the same radius. The material is initially soft so that it can be easily machined. The indenter is machined from a rod of 0.5-inch diameter using a lathe. Once it has been machined to the proper shape, it is then heat treated at 900°F for 6 hours. After heat treatment, the material has

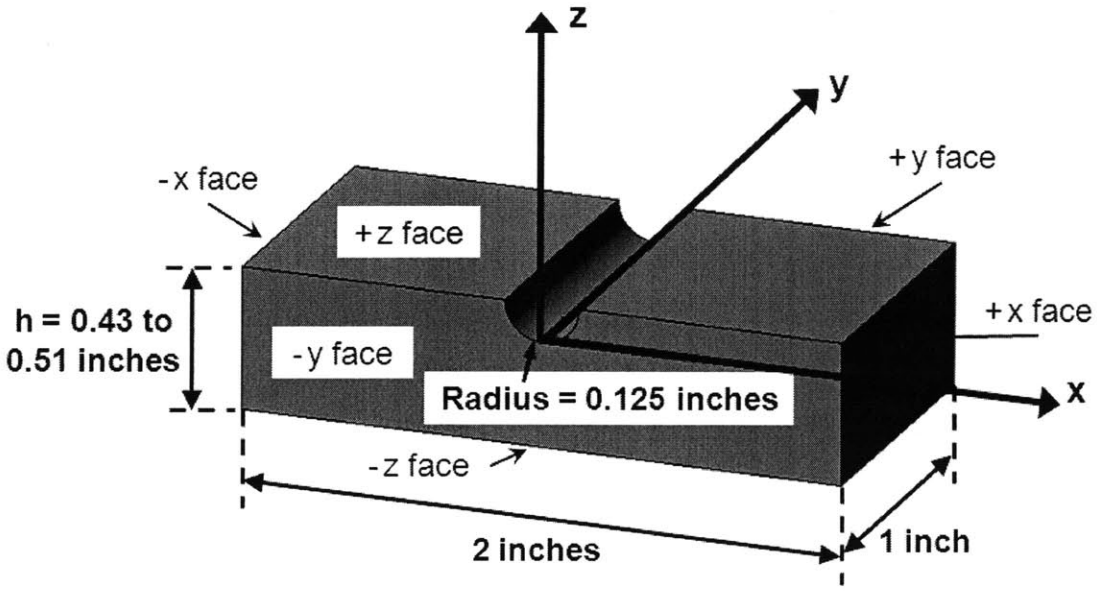

Figure 4.1 Schematic of specimen with dimensions, axes and labels indicating faces.

a Rockwell hardness of C48. The resulting indenter has a hemispherical end with a radius of 0.125 inches, a 0.5-inch-long cylinder with this radius, and expands to the 0.5 inch diameter of the original rod over a distance of 0.25 inches. The larger top surface allows for easier installation by enabling this surface to be placed with tape against the machine head. With these two surfaces being parallel and the symmetry of the indenter, this ensures that the indenter will be parallel with the machine head axis of displacement. The height of the entire indenter is 0.75 inches.

4.2 Manufacture of Specimens

The first step in the manufacture of the specimens involved laminate layup. Each layer was cut from the unidirectional tape using a utility knife and an aluminum template coated with nonporous Teflon, a fabric coated in polytetrafluoroethylene that does not stick to prepreg. After removing the tape from a storage freezer, it was unrolled onto a cutting table with a glass surface. The cutting procedure for the 0° and 90° plies is the same with the template rotated for the 90° plies. A single rectangular template 6 inches by 7 inches in dimension was used. The 0° direction is considered to be parallel to the fibers and along the 7-inch direction. Any angles are measured positive counterclockwise from the fiber direction. In order to save material, each angled ply was cut in two sections, with the resulting seam being parallel to the fibers in all the angled plies. An example of such is shown for a +45° ply in Figure 4.3. This ensures high quality manufacturing.

Once all the plies for a plate of a particular laminate have been cut (78 to 80 plies, depending on the laminate), they are stacked in sublaminates of 18 to 21 plies. The number of plies in the sublaminate is based on the arrangement of plies in the laminate. For laminates with two or four angles, there are 20 plies in the sublaminates, with five or ten groups of each of the ply angles (+45°, -45°, 0° and 90°, or 90° and 0°). For laminates with three angles, either 18 or 21 plies are in the sublaminates, with six or seven groups within these containing all ply angles. To ensure proper alignment of the plies, they are stacked using an aluminum corner that was previously established

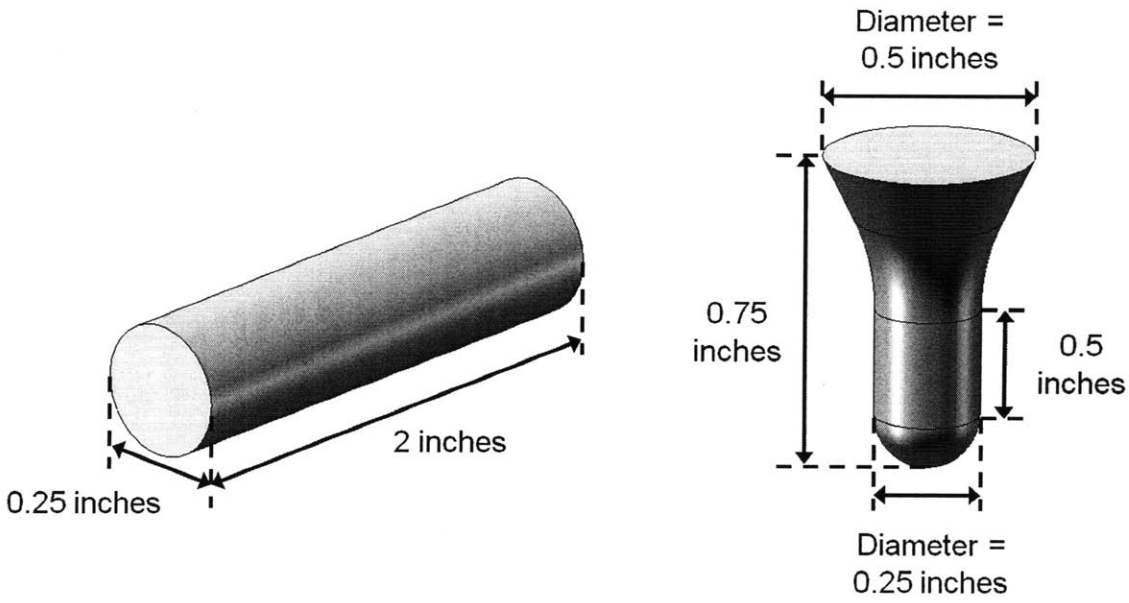

Figure 4.2 Schematic of load applicators for: (*left*) the "two-dimensional loading" case, and (*right*) "three-dimensional loading" case.

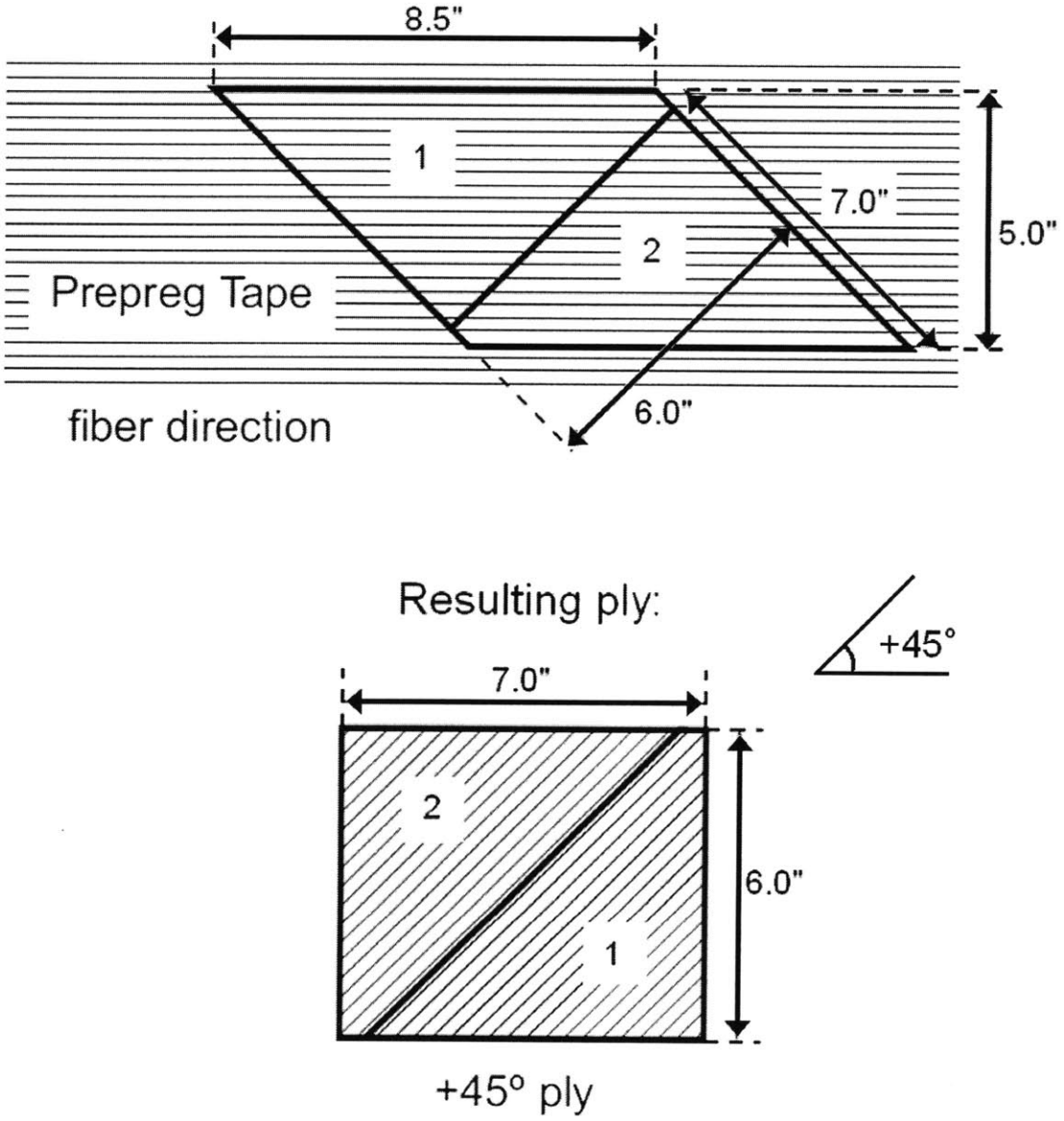

Figure 4.3 Schematic of (*upper*) ply cutting, and (*lower*) assembly for a 45° ply.

to be properly aligned. This corner is marked on the backing paper of each of the subgroups to ensure that they are matched properly when later stacked together for curing. For each laminate, there are four sublaminates that are stacked to create the full laminate.

To reduce the void fraction of the cured laminate, each sublaminate of approximately 20 plies is consolidated. A cork dam is first built around this sublaminate on an aluminum vacuum table coated with nonporous Teflon. The dam setup and sublaminate are sealed in vacuum bagging and a vacuum of at least 28 in Hg is applied for 15 minutes.

After the completion of this consolidation process for each of the four sublaminates, these sublaminates are stacked with the established proper corners of each sublaminate matched to form the complete laminate, using an aluminum corner to continue to ensure accurate stacking. Here, the aluminum corner is approximately the size of the laminate with a height of 1 inch. That aluminum corner assembly forms part of the dam that surrounds the laminate and wrapping materials during cure.

The laminate is then prepared for curing. The overall order of materials employed for cure is shown in Figure 4.4. The laminate is prepared in the following manner:

1. A nonporous Teflon sheet covers the 0.5-inch thick aluminum cure plate.

2. The previously employed aluminum corner is used as two sides of a dam, and a cork dam is built around the other two sides of the laminate, on the cure plate. The dam has inner dimensions about the size of the laminate. The cork dam is approximately 1/8 inch taller than the laminate. The laminate is then removed from this cure assembly.

3. A nonporous Teflon sheet that is large enough to be wrapped completely around the laminate is allowed to rest over the dams on the cure plate.

4. The laminate is covered with peel ply on the top and bottom. The top piece of this material is about the same size as the laminate, while the bottom piece is

about 3 inches longer than the laminate. This bottom piece is aligned on one 6-inch end of the laminate and wraps approximately 3 inches over the top of the laminate.

5. The wrapped laminate is placed onto the cure plate within the dams, on the nonporous teflon that was previously placed over the dams. This is placed so that the good corner of the laminate is aligned with the aluminum corner.

6. A piece of porous Teflon is placed on top of the peel ply.

7. An aluminum top plate of the same planar dimensions as the laminate is wrapped in nonporous Teflon. This plate has a height of 1/8 inch.

8. The wrapped top plate is placed on top of the laminate and porous Teflon, also aligned with the aluminum corner.

9. A piece of porous Teflon is placed on top of the cure plate.

10. The large piece of nonporous Teflon, which extends over the dams, is wrapped around the laminate, cure plate, and porous Teflon, and secured with flash tape.

11. The entire area of the wrapped laminate and dams is covered in fiberglass breather to ensure a good vacuum throughout the laminate.

12. The entire resulting setup is covered with vacuum bagging and sealed with vacuum tape.

With these steps complete, all materials for cure are now in place. The vacuum seal is checked before curing by applying a vacuum of 28 in Hg and turning off the vacuum pump for 5 minutes to ensure the vacuum level does not fall more than 5 in Hg in 5 minutes.

To cure the laminate, Toray recommends a vacuum of at least 22 in Hg and bringing the laminate to a temperature of 270±10°F for a period between two and two and a half hours. Due to the thick nature of the laminate, this was modified to ensure that the laminate first came to a temperature of 270°F throughout its

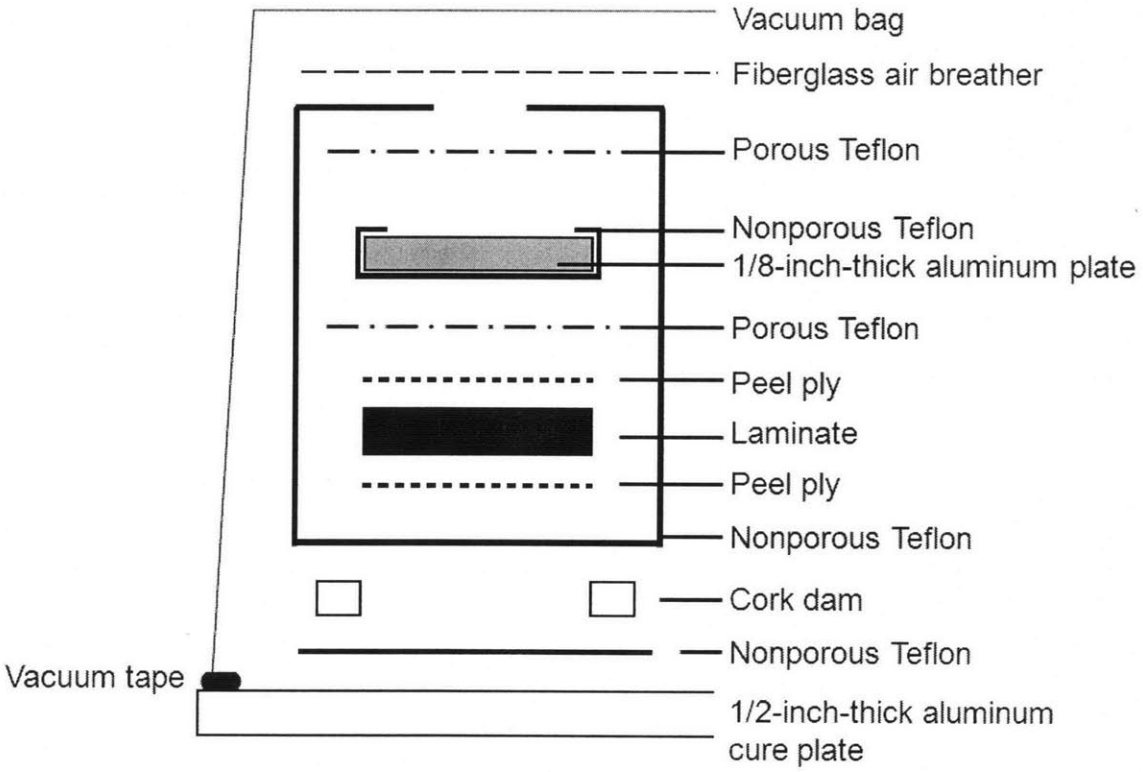

Figure 4.4 Schematic of materials used for laminate cure.

thickness. This was verified in the development of the experimental method [34]. In the modified cure cycle, the vacuum of 27 in Hg is first applied, and the temperature of the autoclave is brought to 180°F for 30 minutes and then brought to the cure temperature of 270°F for 150 minutes. After this time, the cure cycle is completed by turning off any heaters and releasing the vacuum.

Once the plate has been cured, it is machined in two steps using diamond-coated tools to create individual specimens. The specimens are first cut approximately to size using a circular blade mounted on a milling machine. The blade has a 10-inch diameter and a 220-grit diamond cutting edge. This is run at a rate of 110 rpm. The table moves at a rate of 1.1 feet per minute to feed the plate by the blade. In this step, the plate is cut into blocks slightly larger than 1 inch by 2 inches, approximately 1/8 inch oversize in each direction. The blocks are then refined and grooved using diamond-coated end mills and a three-axis mill in a second step.

To refine the specimens to size, a Crystallume 4-flute, 2200-grit diamond-coated, carbide square-end mill with a diameter of 3/8 inches is used. This end mill has a tolerance of ± 0.0005 inches. The $\pm x$ and $\pm y$ faces are machined with the flat-end mill to refine the specimen to 2 inches in length in the x-direction, along the 0° fibers, and 1 inch in width in the y-direction. Once the specimen is properly machined to form and size, the groove is machined into the top face with a Crystallume 4-flute, 2200-grit diamond-coated carbide ball-end mill with a diameter of 1/4 inch. This end mill has a tolerance of +0.0005 inches, -0.0010 inches. The groove is machined to be cylindrical with a depth of 1/8 inch, matching the radius of the end mill. The center of the groove is 1 inch from each of the x-faces as defined in Figure 4.1. The center of the end mill is positioned at this location. The end mill is then positioned so it will cut a cylindrical groove with a depth of 1/8 inch by forward the end mill 0.1250 inches from the +z face of the specimen. The end mill begins just touching the -y face and moves forward toward the +y face of the specimen, resulting in a groove one inch in length. Once the groove is machined, the specimen is ready for measurement and testing. The final resulting specimen is of the dimensions shown in Figure 4.1.

4.3 Measurement of Groove

To document the good manufacturing and machining of the groove, a laser measurement system was employed to measure the groove depth. This was done using the top of the specimen as the reference. The measurement system, shown in Figure 4.5, uses an x-y-positioning stage and sample holder with a laser displacement sensor to determine the groove depth.

The positioning stage has 6 inches of movement in the x-direction and 3 inches of movement in the y-direction. Both directions have a placement accuracy of 0.001" for alignment. A 1/4-inch-thick aluminum specimen holder is attached to the positioning stage both to ensure that the specimen does not move during measurement and that it can be returned to the same location when necessary. The positioning stage has grooves that allow the specimen holder to be bolted to these. The specimen holder is made of three pieces of aluminum. One is L-shaped and the specimen is placed flush against it. One is placed about 1/4 inch from the L-shaped piece and has a third piece, a swinging arm, bolted to it and attached to the L-shaped bracket with a spring. The swinging arm is used to hold the specimen against the L-shaped piece.

The laser displacement sensor is a Keyence LB-70(W) series laser with a measurement range of 60 to 140 mm from the target. The laser is set so that the target is about 100 mm from the positioning stage. There is a stability light that is green or yellow when the item being examined is in the acceptable range, and red when out of range. This is used to ensure the validity of the measurement. The laser is attached to a DC power supply set to approximately 15 V and allowed to stabilize for 30 minutes before use. The laser has an accuracy of 0.001 volts that is used as an output and converted to displacement at 5 mm/V or 0.197 inches/V. This gives a measurement accuracy of 0.0002 inches.

Before testing the specimens, 40 of the manufactured specimens were measured to check for the quality of machining of the groove. Measurement of these 40 selected specimens showed high quality machining. In these measurements, the specimen and laser were first aligned with the laser positioned over the deepest part of the groove.

In this measurement procedure for each specimen, the points around the groove and its top that were measured in the xz-plane are at various y-locations and are shown in Figure 4.6. The procedure begins by the measurement of the groove bottom at 20 points, every 0.05", along the y-direction. After a complete run at x equals 0", the specimen is adjusted 0.025" along the x-direction and measured again at 20 points along the width, y-direction, of the specimen. This was repeated for the 6 points in the x-direction to each side of the groove bottom.

The different points were measured to ensure that the deepest part of the groove was measured, to determine the groove depth, and to observe the shape of the groove. The locations at which the groove was measured are shown in Table 4.1. For each x-location, measurements were made at all the y-locations. Thus, 20 data points were collected when the laser was positioned at x equal to any particular value. This was repeated until data was collected for 13 points of the x-direction across the groove, at each of 20 y-locations along the groove. This resulted in a total of 210 data points for characterization of the machining of the groove. The depth of the groove was determined from this data. The multiple data points at each y-location were used to ensure the groove was circular and that the deepest points were determined. This data is used to determine the standard deviation of the groove depth measurement.

4.4 Test Procedures

There are four types of tests used in this work to characterize the behavior of the grooved composites. Many techniques employed are uniform across the types of tests. All testing was performed using a hydraulic MTS machine with a load cell with a maximum capacity of 200 kN. Rigid backface boundary conditions were used for all cases with the -z face of the specimen resting on a flat plate of steel with a thickness of 0.5 inches. The specimens are free to move and deform in the length and width directions. A stroke rate of 0.1 mm/min is used for all tests. The machine does this by moving the lower head up at this rate. This leads to failure in 10 to 15 minutes in accordance with ASTM D6264/D6264M, the testing standard for concentrated load

Table 4.1 Locations of groove depth measurements

x-locations [inches]	y-locations [inches]
-0.150	-0.500
-0.125	-0.450
-0.100	-0.400
-0.075	-0.350
-0.050	-0.300
-0.025	-0.250
0.000	-0.200
0.025	-0.150
0.050	-0.100
0.075	-0.050
0.100	0.000
0.125	0.050
0.150	0.100
	0.150
	0.200
	0.250
	0.300
	0.350
	0.400
	0.450
	0.500

quasi-static indentation of fiber-reinforced polymers. This was used as a basis in the development of the initial test [19, 34].

Prior to installation of the support plates on the machine heads, a planar outline of the specimen, 2 inches by 1 inch, is drawn in the center of the lower support plate. The center of the top support plate is marked as well. The support plates for testing are installed on the MTS machine heads by placing them on the lower machine head and adjusting the support plates, by eye, to the center of that machine head. The top support plate has double-sided tape on its top face so that it sticks to the top machine head throughout installation and testing. The machine heads are closed manually until there is a 10 kN load applied to ensure the top support plate will be secured to the top machine head. The machine heads are then opened to a separation of at least one foot, and the top support plate remains attached to the center of the top machine head due to the double-sided tape. With the machine heads open, the system then is calibrated for load using the MTS control tower to automatically calibrate the system.

The data acquisition system, consisting of a 16-bit National Instruments A/D board and Power Macintosh G3 computer, with the software LabView 5.0, is set up with respect to the control tower of the MTS machine used in the tests. This is configured to record time, load, and machine stroke data, and conversion constants from voltage to load or stroke are set to match the MTS control tower. During tests, data is recorded at a frequency of 1 Hz. The control tower is used to set the head close rate of the MTS machine at 0.1 mm/min and the maximum position of the lower machine head. The initial position is set manually with the specimen and indenter in place.

The installation procedures of the indenter and specimen vary between the "two-dimensional loading" with the cylinder indenter, and the "three-dimensional loading" with the ball-ended indenter. Schematics of the two test setups are shown in Figure 4.7 and Figure 4.8. In the case of the "two-dimensional loading", the cylinder indenter is placed in the groove by hand and aligned to be flush at one end using a flat surface. Due to the length of the cylinder, this assures it is flush with the specimen at the

opposite end. The specimen and indenter are then installed together in the center of the rigid backface support, using the specimen outline. The top plate contacts the top of the cylinder when the manual closing of the machine heads takes place. For the "three-dimensional loading", the specimen is first placed on the lower machine head and support plate. The ball-ended indenter is then installed at the marked center of the top support plate with double-sided tape, and the specimen is adjusted by hand until the indenter is approximately centered over the groove. Next, in an iterative process, the machine heads are closed manually and the specimen is further adjusted to be centered. This is stopped when there is a 0.5 mm gap between the groove and the indenter. At this small opening, a final adjustment is made using markings on the top of the specimen to center the indenter in the y-direction. For the x-direction, the radius of the indenter is centered in the radius of the groove.

After this installation of the indenter and specimen, the machine heads are closed manually, using the head position controls on the control tower, until a compressive load of 0.15 kN is achieved. At that point, the data acquisition is started, followed immediately by starting the testing machine.

For failure tests, the test continues until failure is reached. This is defined as a sudden load drop of at least 50% of the maximum load in the "two-dimensional loading" case or a persistent inability to carry additional load in the "three-dimensional loading" case. The persistent inability to carry additional load is defined as a stroke of 0.25 mm with no increase in load beyond the maximum load. For crush tests, the tests specimens are initially tested to a stroke of 0.3 mm. The specimen is then unloaded and the groove is measured with the laser measurement system to check for permanent deformation as compared to the original measurements. Such changes are indicative of crushing. This process is repeated, incrementally increasing the load, until crushing is detected. For the "three-dimensional loading" case, the load increment is 1 kN. For the "two-dimensional loading" case, the load increment is 5 kN. These increments were determined by initial testing, and are subsequently described.

Initial crush testing on the quasi-isotropic and $[\pm 45/0]_{13S}$ laminates determined the increments to be used. For the "three-dimensional loading" case, 1 kN was deter-

mined as the increment. The process began with the use of a smaller increment of 0.5 kN. This was chosen based on an ability to control the load to this level of accuracy. It was determined that this load increment did not cause any change of significance. Measurement showed that any crushing detected was minimal and that the change in groove depth was no more than one standard deviation of the groove depth. The initial testing also lead to numerous loading and unloading cycles. This could lead to repeated friction and contact loading, thus resulting in surface damage not representative of the crushing being investigated. The load increment was then doubled to 1 kN. Subsequent testing with this 1 kN load increment showed good results to determine initial crushing, and that established the increment to be 1 kN. A similar process was used for the "two-dimensional loading" case beginning with the defined 1 kN load increment from the "three-dimensional loading" case. This caused similar results and concerns as the lower load increment in the "three-dimensional loading" case. Based on the number of loading-unloading cycles in this case as compared to the "three-dimensional loading" case, the load increment was increased to 5 kN. Subsequent testing showed good results to determine initial crushing for this case, and this established the increment to be 5 kN for the "two-dimensional loading" case.

In addition to using the laser measurement system to ensure good machining of the groove, the system is used to check for permanent deformation of a specimen in the groove after loading. The measurement procedure to look for crushing is slightly different in the "two-dimensional loading" and "three-dimensional loading" cases. This is necessary since crushing will occur in a localized area in the "three-dimensional loading" case, at the point of contact of the indenter in the specimen. In the "two-dimensional loading" case, crushing is to happen along the entire length of the groove. For both cases, the groove depth is measured after loading. This is similar to the measurement prior to testing, with the deepest part of the groove measured and the top of the specimen used to establish the current depth at 20 points along the groove.

In the case of the "three-dimensional loading" via the ball-ended indenter, once the depth of any point in the loading area of the groove is larger than the original groove

depth plus one standard deviation of the groove depth, permanent deformation is said to have occurred. This is checked against the original data to ensure that the point at which permanent deformation occurred is not an outlier from the original machining and measurement. For the "two-dimensional loading" case via the cylinder, crushing is considered to occur when this is manifested along the entire length of the groove. The average groove depth of the tested sample is thus used to determine if crushing has occurred. Again, permanent deformation, or crush, is said to have occurred once the change in average groove depth exceeds the standard deviation on the groove measurement.

4.5 Computer Microtomography

After testing, several samples were examined using a nondestructive X-ray technique that allows the examination of the entire volume of a specimen. This is computed microtomography, which is a medical technique adapted to engineering applications. This process takes many X-ray readings of a sample and stores the data. This allows the volume of the specimen to be reconstructed from the acquired data. Once the volume has been reconstructed, "virtual cuts" of a specimen can be made to determine what has occurred in the specimen at locations that are not visible from the surface. A schematic of each of the "virtual cuts" as used is shown in Figure 4.9. This work was done at facilities at the Harvard Center for Nanoscale Systems using the X-Tek HMXST225 machine.

The system functions by exciting an electron source. The electrons are focused and hit a target that generates X-rays. The X-rays scatter and hit the specimen, and the intensity of the X-rays are captured by a charge-coupled device (CCD) detector, and used to compute the density of the specimen. This allows the volume to be reconstructed from the different densities [36].

To examine the full volume of the specimen, the sample is installed in the machine, and a tungsten or molybdenum target is used. The molybdenum target leads to "softer" X-rays than those generated by the tungsten target. It was determined,

through this testing, that molybdenum produced better results when scanning carbon fiber reinforced polymers, as the molybdenum target leads to clearer reconstructions of the volume and more details are visible. Once this was established, scans were done using the molybdenum target. Scanning parameters are set using the control program. The voltage and amperage of the X-ray source is set such that the best real time image is visible. This was normally between 45 and 70 kV and 120 and 210 μA. The volume to be scanned is adjustable, and can be approximately the size of the specimen. This is set slightly larger than the specimen to ensure that everything of interest is scanned, and uses two images at 90° to each other. Once this has been set, the system is calibrated by moving the sample out of the area between the X-ray source and target, and capturing black and white reference images. This is done by first turning off the X-rays and collecting 128 black images. The X-rays are then turned on, and 128 white images are captured. The data from these images is averaged for each pixel on a X-ray detector. The data is recorded by a CCD camera behind the X-ray detector. This data sets the maximum and minimum values for the gray scale for each pixel. Once this has been done, the sample is moved back into place and the scan is started.

Once data capture is complete, a software package is used to reconstruct the images into the volume. The first and last few acquired images are first compared to ensure that the entire volume has been captured. If there are no sudden jumps between the beginning and end images, the entire volume has been scanned. If not, the volume is rescanned. Then the volume that is to be reconstructed is selected as close to the specimen as possible. The images are also squared away by rotating the images and comparing these to a straight line. From these adjustments, the volume is reconstructed.

After reconstruction, another program is used to examine the volume by taking virtual cuts of the specimen to look for damage. An example of a cut of the reconstructed specimen is shown in Figure 4.10. By cutting away parts of the virtual specimen, the interior can be examined. In addition, single planes of the specimen at any inclination can be examined and damage progressions can become apparent.

This technique shows damage due to crushing that is not visible without destructive testing, as well as additional damage in failure tests that is not visible at the surface.

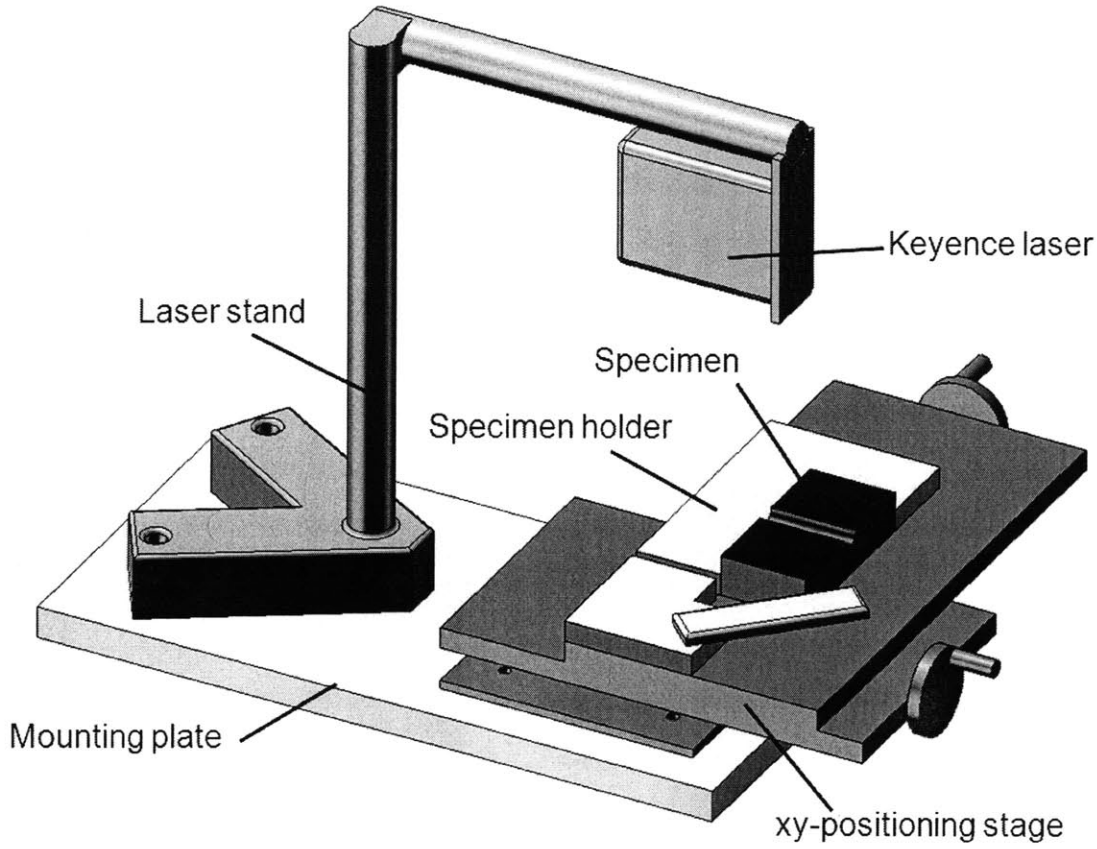

Figure 4.5 Schematic of groove measurement setup.

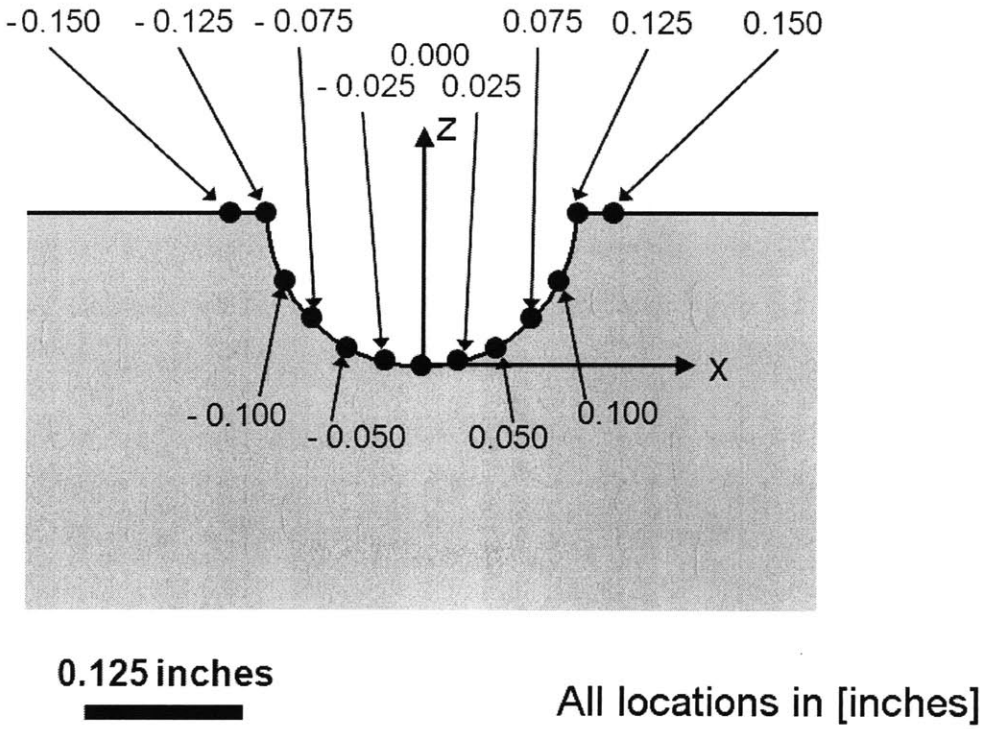

Figure 4.6 Schematic closeup of groove with x-locations of groove measurement. (Note: These locations were measured at the twenty points of y-location along the width of the specimen given in Table 4.1.)

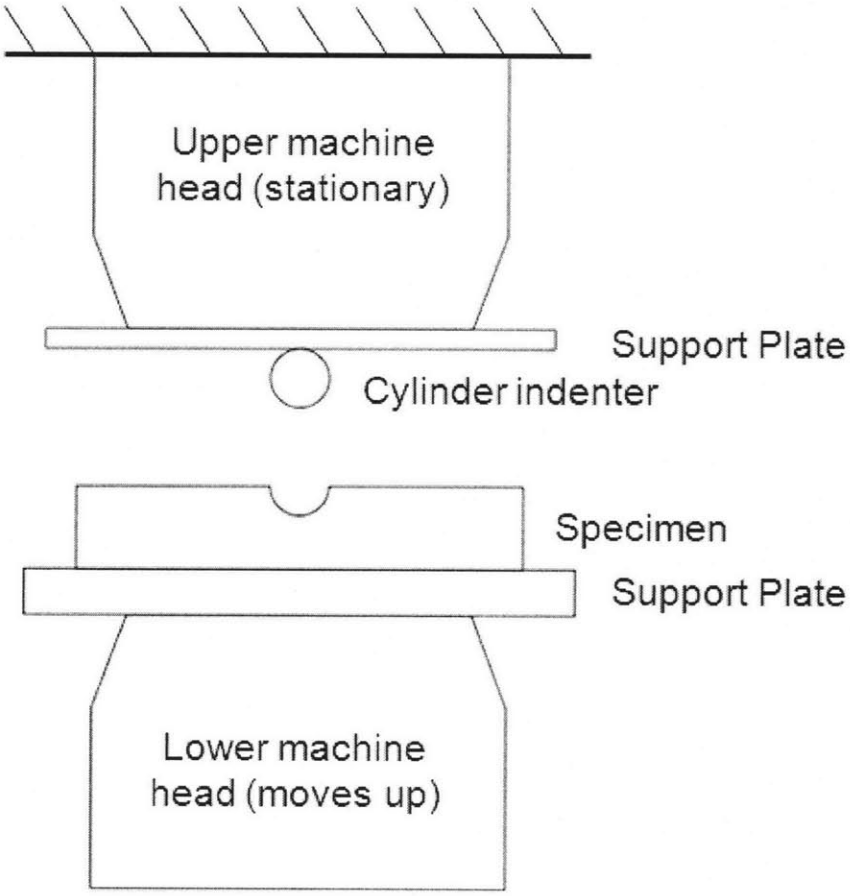

Figure 4.7 Schematic of the "two-dimensional loading" configuration with the cylinder indenter.

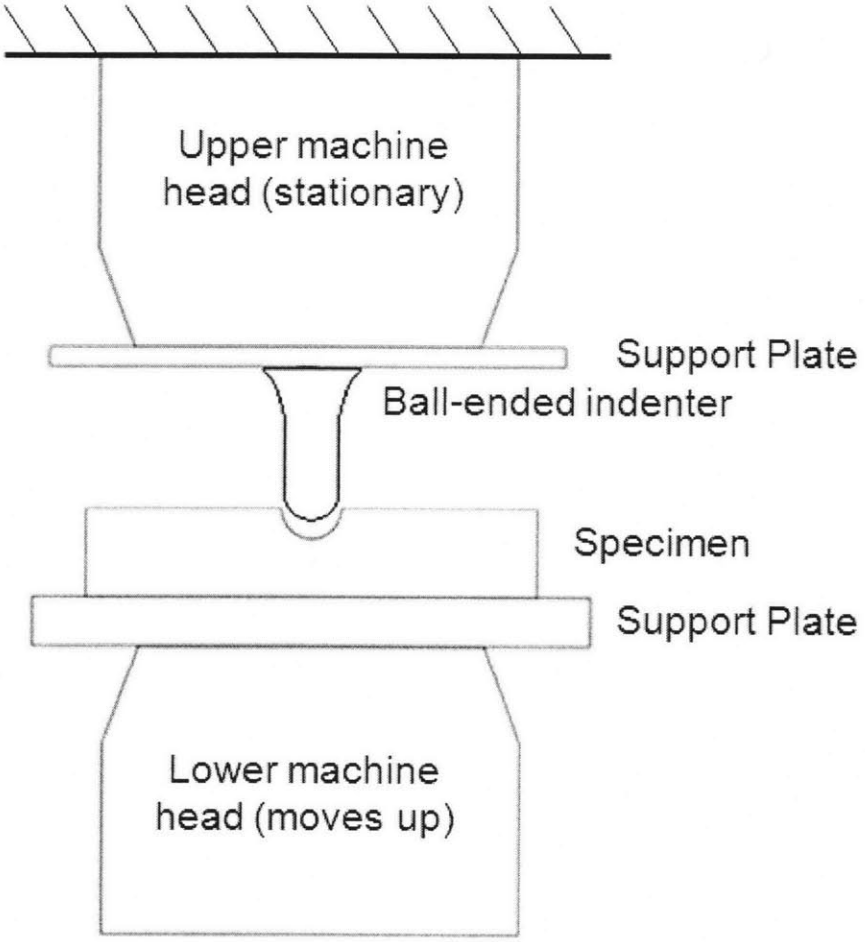

Figure 4.8 Schematic of the "three-dimensional loading" configuration with the ball-ended indenter.

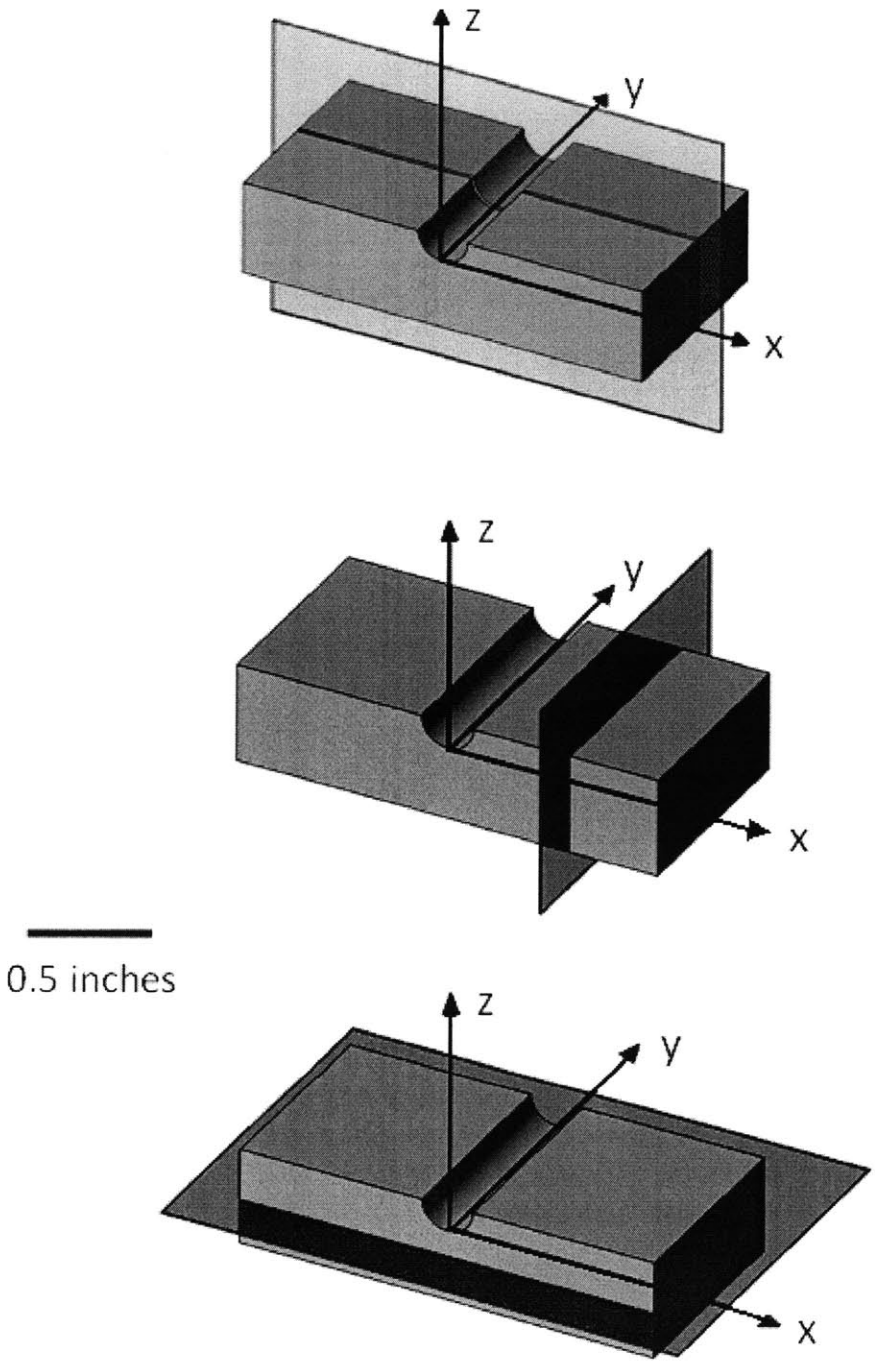

Figure 4.9 Schematic of "virtual cuts" of (*top*) xz-plane, (*middle*) yz-plane, and (*bottom*) xy-plane

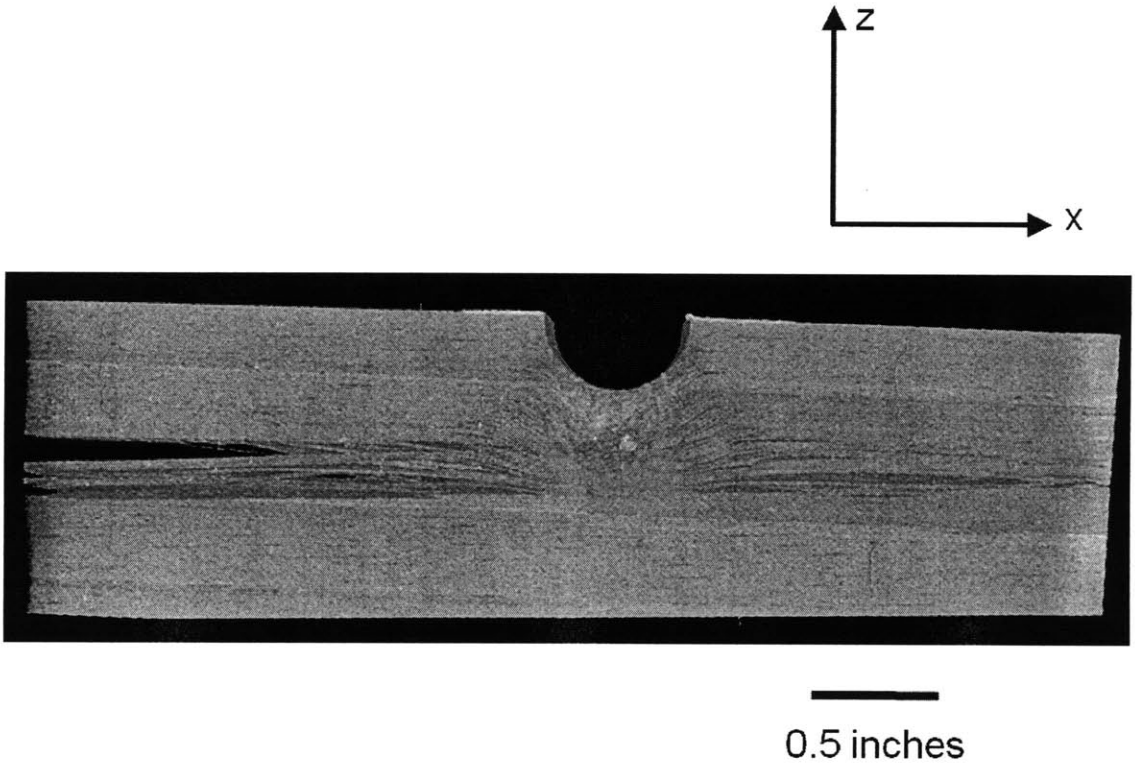

Figure 4.10 Virtual "cut" of a tested and reconstructed specimen, showing the xz-plane.

Chapter 5

Test Results

Overall, 81 specimens were manufactured and tested in this work using the techniques described in Chapter 4, with at least 12 samples per laminate. These were tested for each of the two loading conditions as described in Chapter 3, "two-dimensional" and "three-dimensional", and to either final failure or first crushing load. The test matrix showing all the tests conducted and used in this work is shown in Table 5.1. In addition, 9 specimens tested in previous work were considered in the overall assessment [34]. Of these overall specimens, 54 were tested to final failure and the remaining 36 were tested until crushing first occurred. Specimens and layups were compared based on the load and stroke data recorded during testing. Observations were made on the tested specimens from visual inspection and computed microtomography scanning.

5.1 "Two-Dimensional Loading" Specimens

All "two-dimensional" tests were conducted using the cylinder load applicator. As shown in Table 5.1, 46 tests were assessed with this loading. Of these, 9 specimens were tested to final failure in previous work [34], with 19 more tested to final failure in this work. 18 specimens were tested to determine the lower bound for crushing.

For each laminate, at least three specimens were tested to final failure with the "two-dimensional" cylinder indenter configuration. Data collected during testing, in

Table 5.1 Final test matrix

	"2-D Loading"		"3-D Loading"		
Laminate	Failure	Crushing	Failure	Crushing	**Total**
$[\pm 45/0/90]_{10S}$	9*	3	5	3	**20**
$[90/0]_{20S}$	5	3	5	3	**16**
$[\pm 15/0]_{13S}$	3	3	3	3	**12**
$[\pm 30/0]_{13S}$	3	3	5	3	**14**
$[\pm 45/0]_{13S}$	5	3	5	3	**16**
$[\pm 60/0]_{13S}$	3	3	3	3	**12**
Total	**28**	**18**	**26**	**18**	

*9 samples from previous work [34].

addition to time, were load in kilonewtons and stroke of the lower machine head. The testing machine is considered to be rigid, so stroke of the machine head translates directly to the stroke of the indenter into the carbon fiber layup of the specimen.

The load versus stroke curves shown in Figures 5.1 to 5.7 are representative of the response of the specimens for each laminate configuration. There are two representative load versus stroke responses for the quasi-isotropic specimens, as shown in Figures 5.1 and 5.2. The plots for all specimens are available in Appendix A.

The load-stroke responses show several common characterization items in the behavior in all tests of the "two-dimensional" loading cases. These common observed items include an initial region with a linear slope, a "knee load" immediately after which the slope of the response was less than that in the initial linear region, a "reverse knee load" after which the slope of the response increases, a second region with a linear slope, and a maximum load.

All the specimens tested with the "two-dimensional" load applicator configuration had the initial region of linear load versus stroke behavior. This initial linear region does not coincide with the beginning of the test, but is displayed between loads of approximately 20 kN to 40 kN. This region was used to characterize the slope of the linear region of the specimen, and the slope was found using linear regression. This behavior can be seen in all the representative responses.

For the "two-dimensional loading" configurations, five of the six laminates had a "knee load" at which the slope of the load versus stroke behavior decreased compared to the initial slope. The determination of the point at which the knee load occurs is based on the initial linear slope for each specimen. A line with a slope 1.5% smaller than the initial linear slope is used to determine the knee load. This line of lesser slope intersects the extended initial linear region line at a zero load, and the point at which it crosses the load versus stroke repsonse is the knee load. This amount, 1.5%, was determined through testing different distances. A difference of 1.0% was not significantly distinguishable from the initial slope. A difference of 2.0% crossed the load-stroke response at a load significantly past the location at which the response deviated from the initial linear reagion. The knee load occurred at loads between

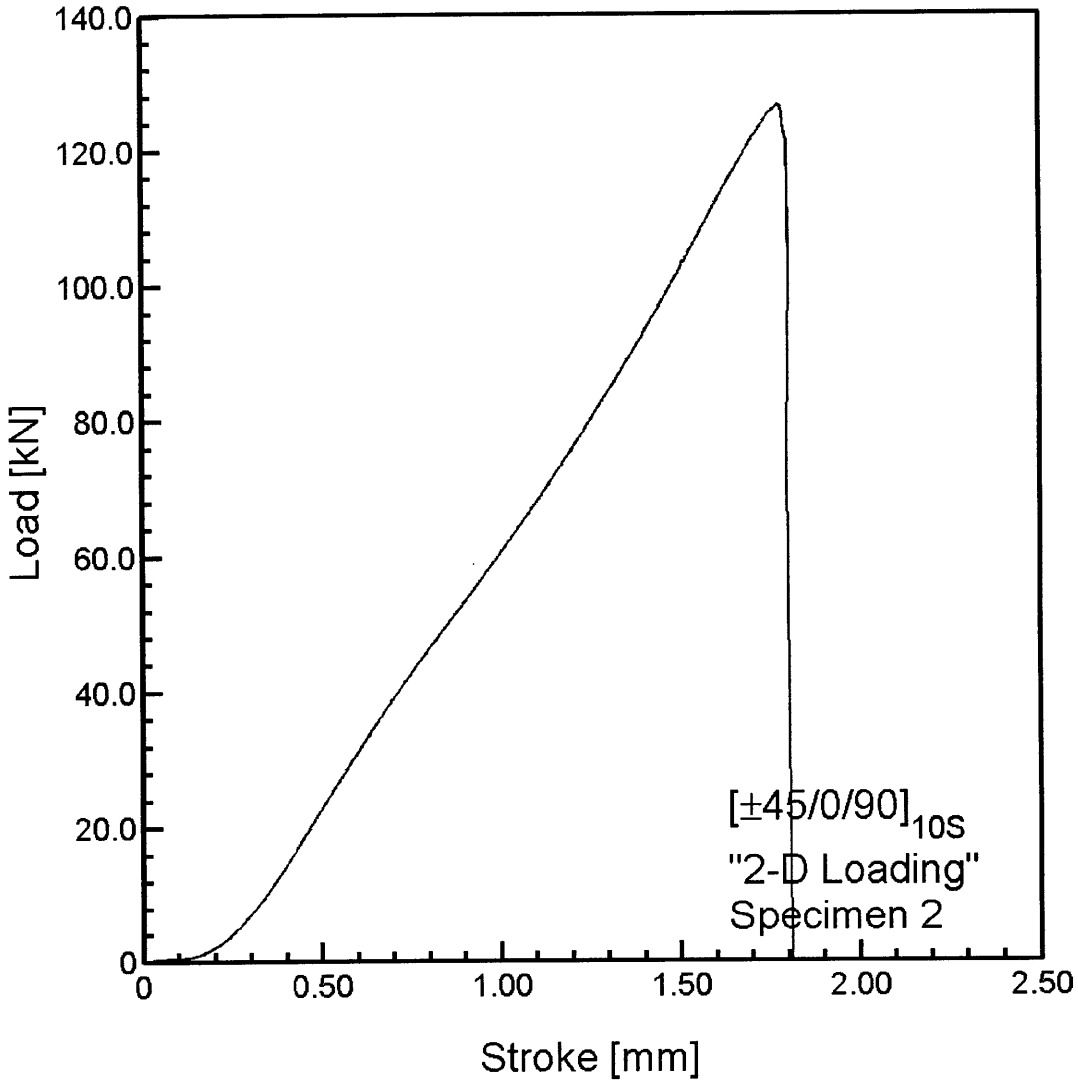

Figure 5.1 Load versus stroke for $[\pm 45/0/90]_{10S}$ Specimen 2 tested to failure with the "two-dimensional loading", from previous work [34].

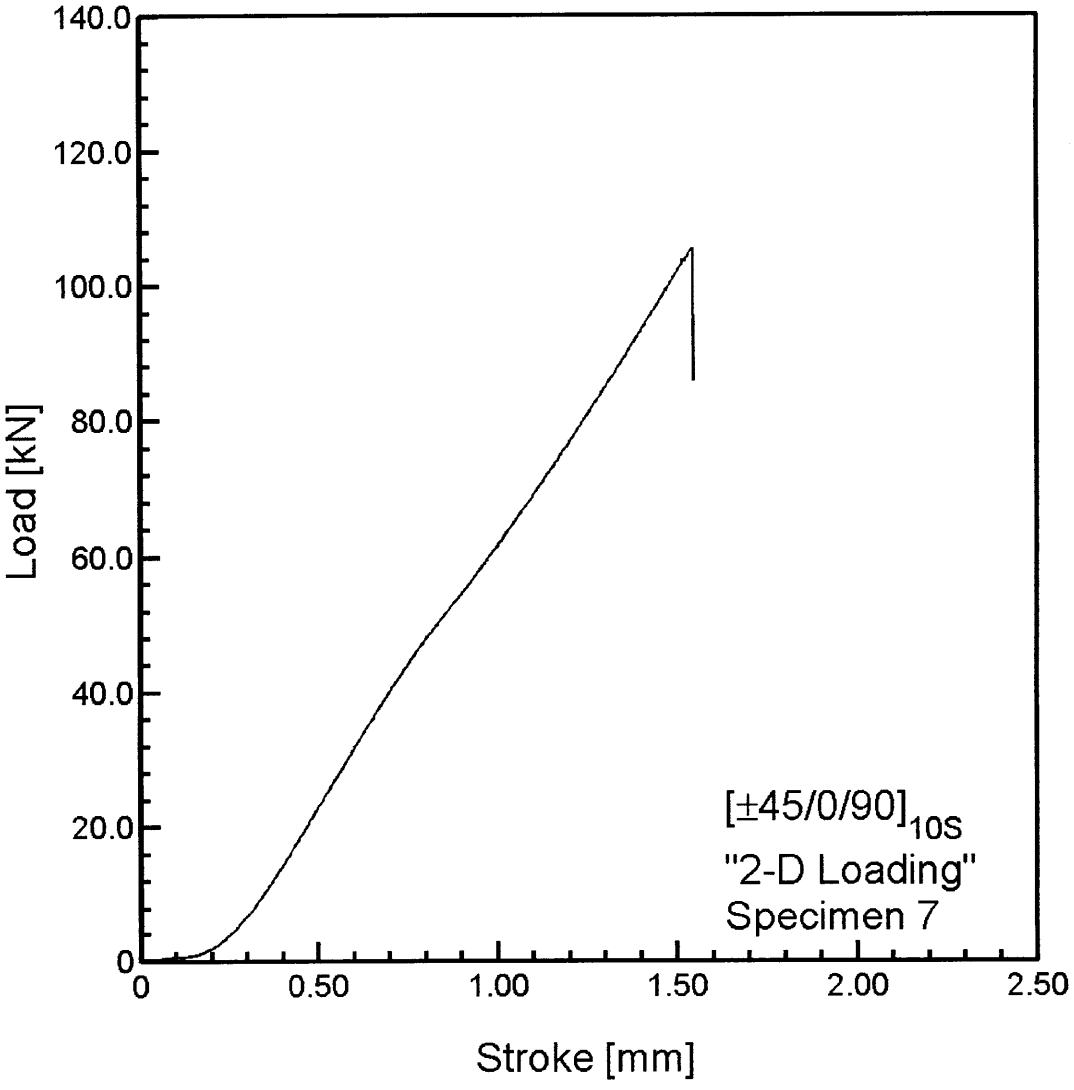

Figure 5.2 Load versus stroke for $[\pm 45/0/90]_{10S}$ Specimen 7 tested to failure with the "two-dimensional loading", from previous work [34].

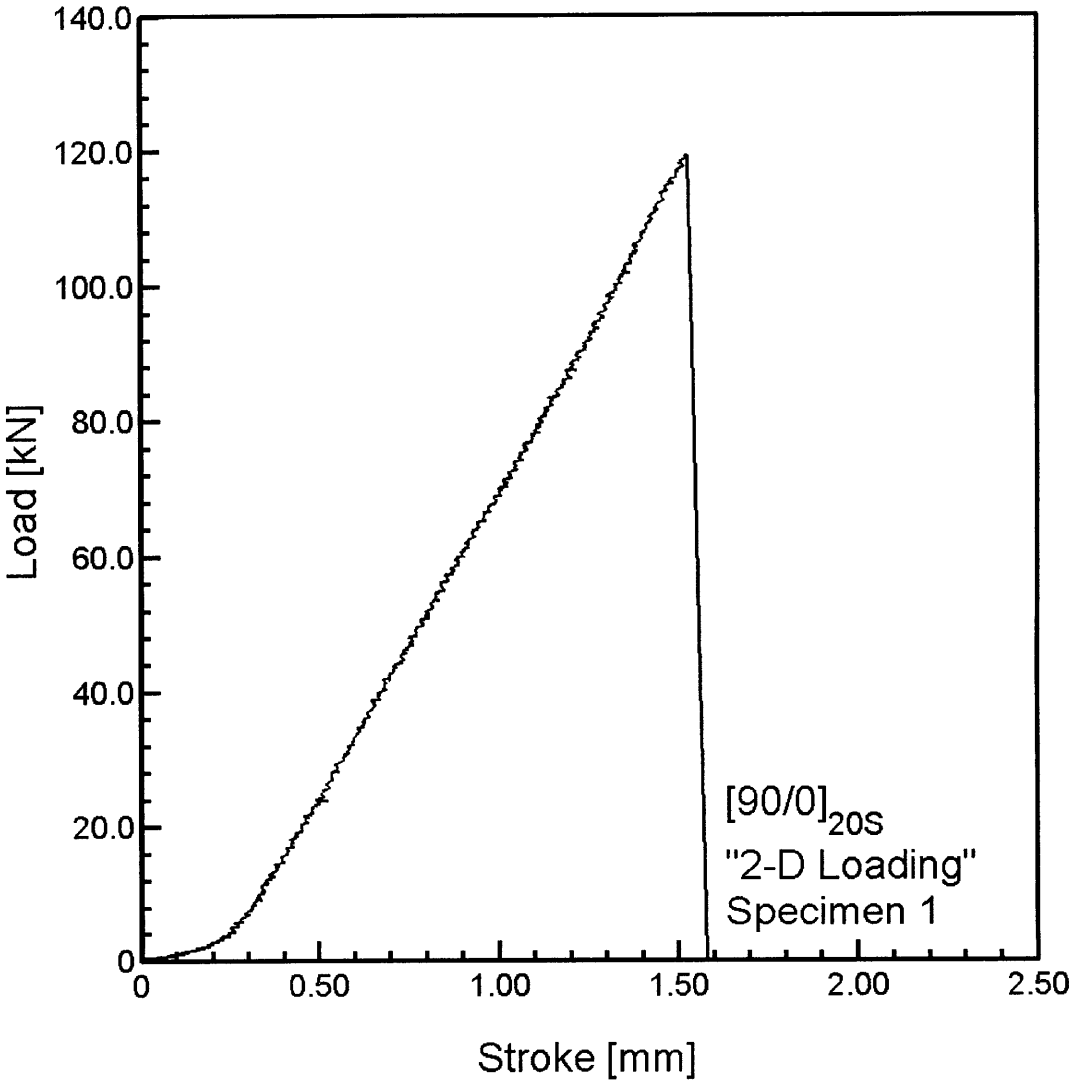

Figure 5.3 Load versus stroke for $[90/0]_{20S}$ Specimen 1 tested to failure with the "two-dimensional loading".

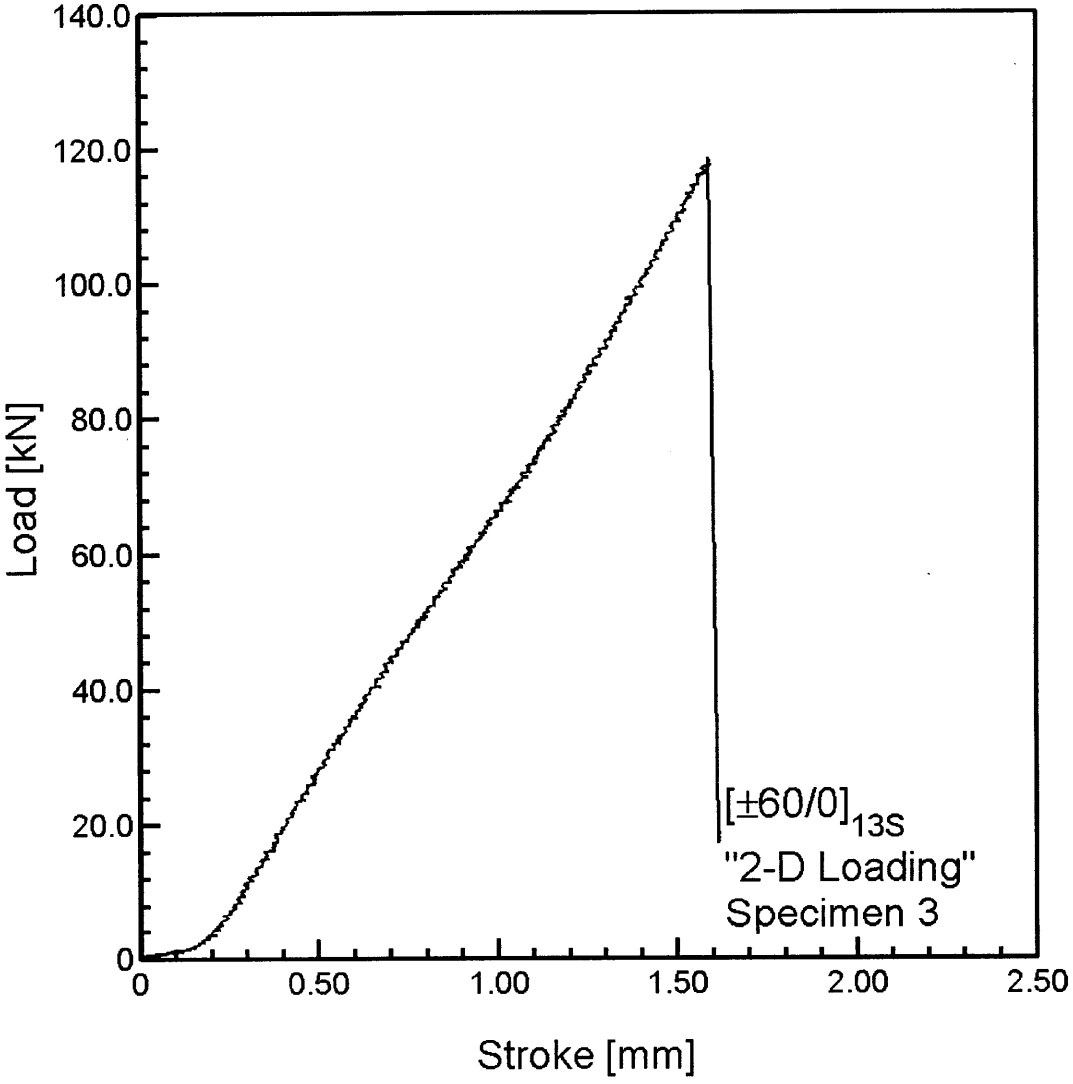

Figure 5.4 Load versus stroke for $[\pm 60/0]_{13S}$ Specimen 3 tested to failure with the "two-dimensional loading".

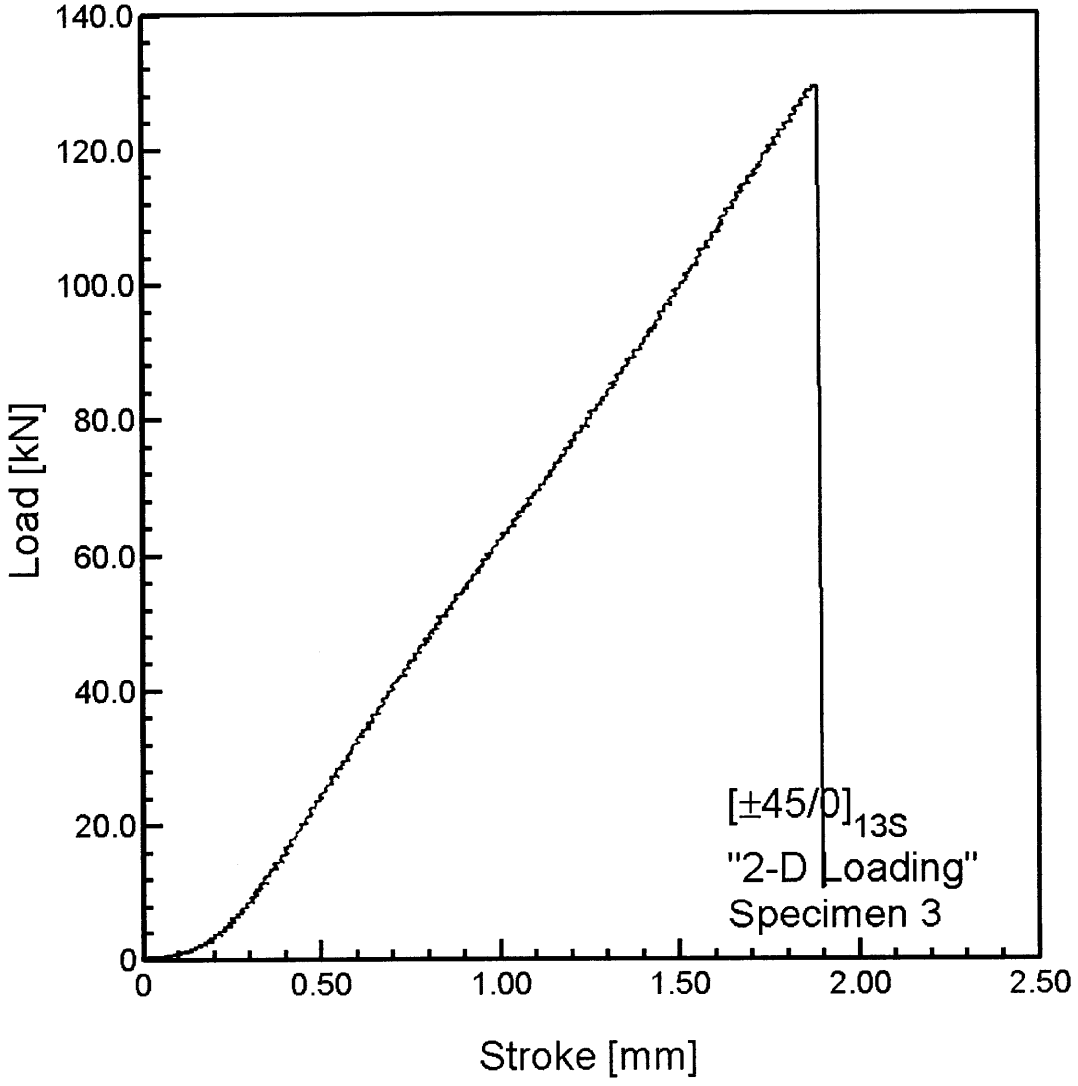

Figure 5.5 Load versus stroke for $[\pm 45/0]_{13S}$ Specimen 3 tested to failure with the "two-dimensional loading".

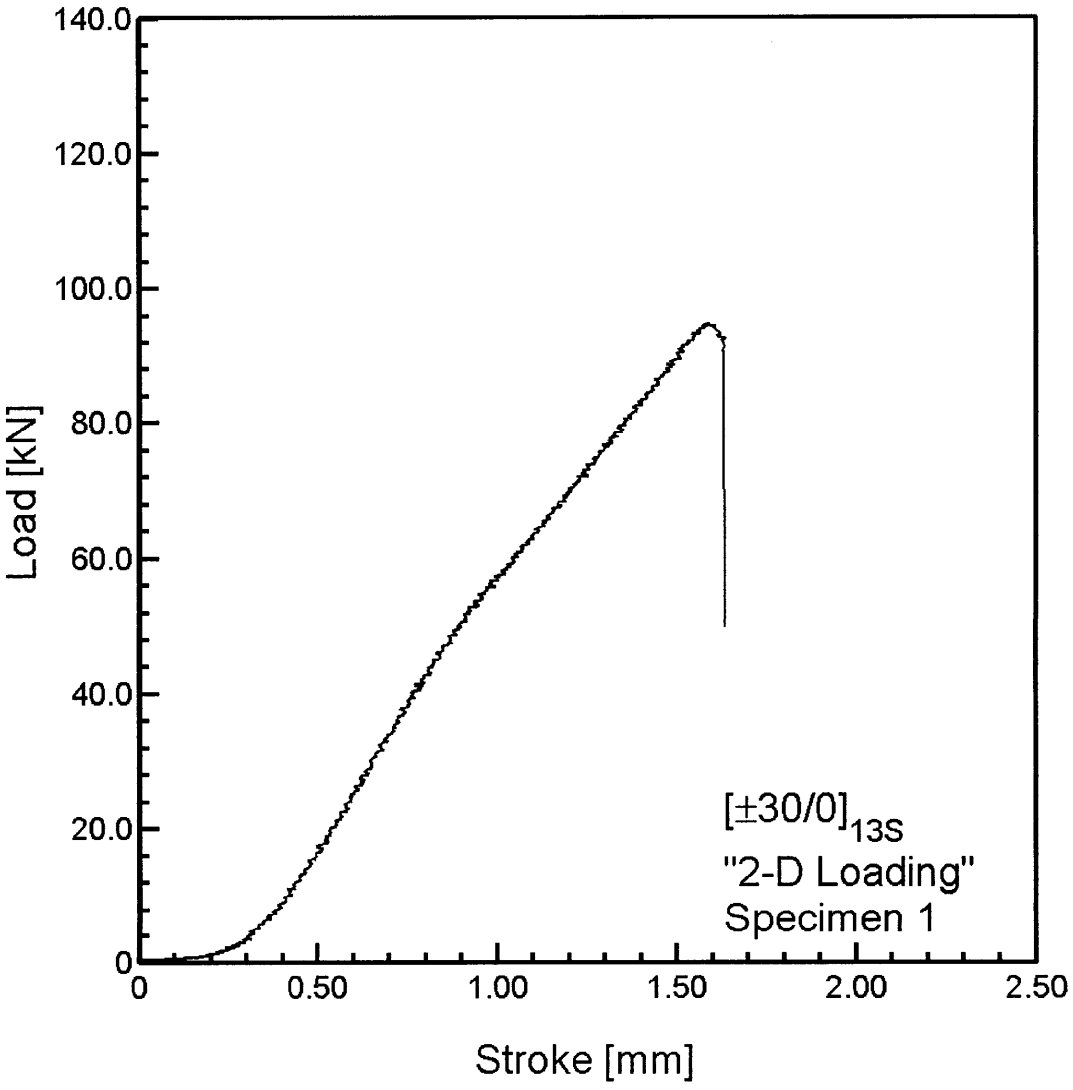

Figure 5.6 Load versus stroke for $[\pm 30/0]_{13S}$ Specimen 1 tested to failure with the "two-dimensional loading".

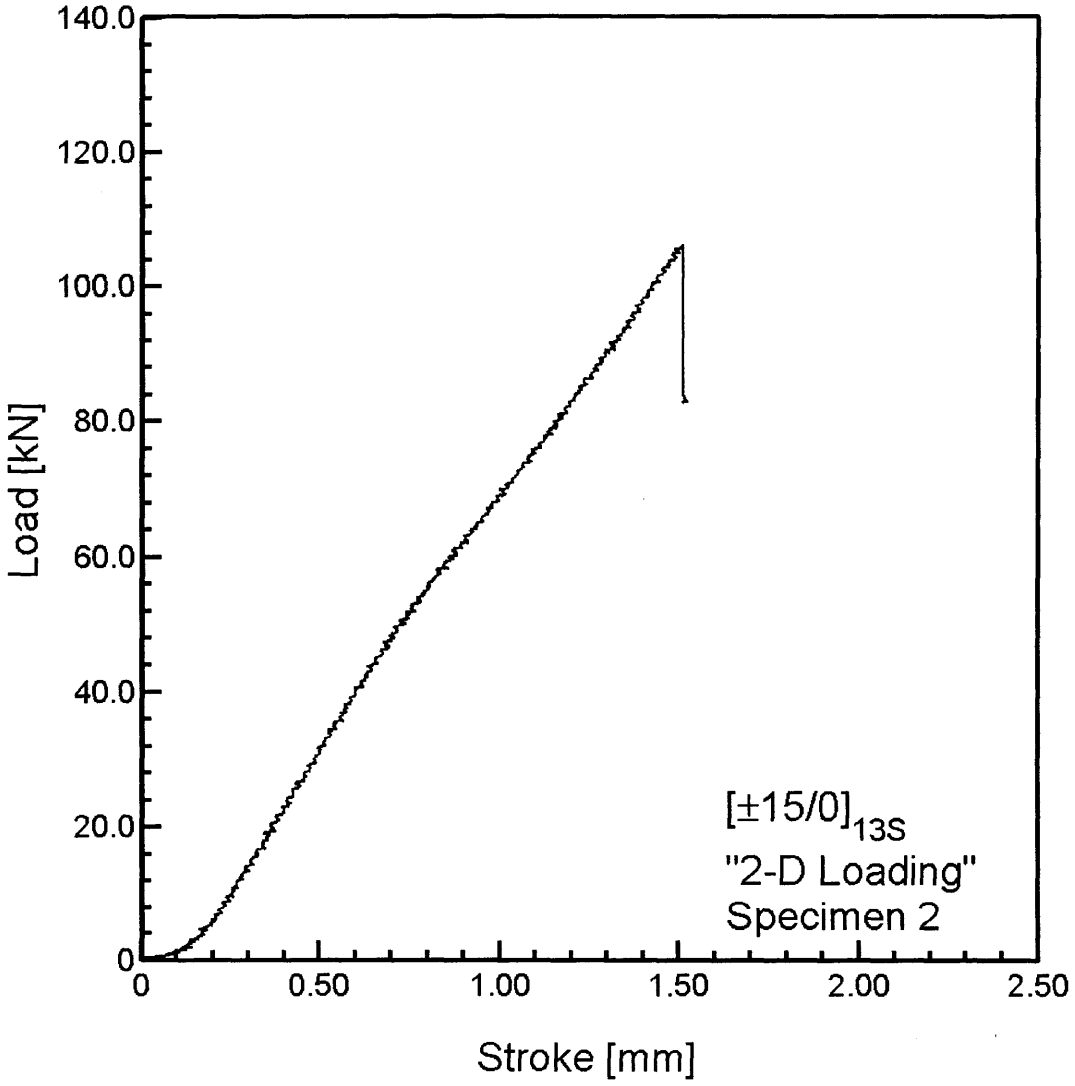

Figure 5.7 Load versus stroke for $[\pm 15/0]_{13S}$ Specimen 2 tested to failure with the "two-dimensional loading".

44.0 to 56.2 kN. The laminate that did not show this characteristic is the cross-ply laminate, $[90/0]_{20S}$. Specimen 4 of the $[\pm 45/0]_{13S}$ laminate did not exhibit a knee load, although the other specimens of the laminate did. For these specimens, the linear region continued significantly past the load at which a knee load occured in the load-stroke response of other specimens, until a reverse knee load occurred, which is discussed shortly. This behavior is shown in Figure 5.3.

All laminates exhibited a second region of linear behavior. The point at which the second linear region is reached is dependent on other aspects of the behavior of the laminate, specifically the knee load and reverse knee load. The slope for the second linear region is determined using linear regression. The region that is used is determined by eye, with the use of a straight-edge. The three laminates that had both a knee load and reverse knee load under "two-dimensional loading" are $[\pm 45/0/90]_{10S}$, $[\pm 60/0]_{13S}$, and $[\pm 45/0]_{13S}$, as well as Specimen 3 of the $[\pm 30/0]_{13S}$ laminate (see Figures 5.1, 5.2, 5.4, and 5.5). The slope of the second linear region for these cases is approximately the same as the initial region, or stiffer than that of the initial linear region. For the specimens that showed a second linear region that was approximately the same as the initial region, the second slope was within 3.0 kN/mm of the initial slope, which is less than a 4.0% change. Any specimens that show a greater slope in the second linear region have an increase of at least 8.0 kN/mm, which is a change of over 10.0% from the initial slope. All specimens of the $[\pm 15/0]_{13S}$ laminate, two specimens of the $[\pm 30/0]_{13S}$ laminate, and Specimen 1 of the $[\pm 45/0]_{13S}$ laminate exhibit only a knee load preceding the second linear region (see Figures 5.6 and 5.7), with the second linear region slope decreasing relative to the initial linear slope. For these specimens, the change in slope from the second linear region is at least 9%, and ranges up to 27%. All specimens of the cross-ply laminate exhibit only a reverse knee load, and reach this second linear region after this reverse knee load. For the $[\pm 45/0]_{13S}$ specimens, there was one case, Specimen 4 under the "two-dimensional loading" configuration, which exhibited a reverse knee load. The second linear region for these specimens show an increase in slope of at least 6.0 kN/mm, or at least 7.0% over the initial slope. The increase in slope is up

to 18% for these cases.

As noted in the previous paragraph, several of the laminates show a reverse knee load. For three laminates this is in addition to the initial knee load. In all cases where the reverse knee load behavior is exhibited, it leads to the second linear region. The reverse knee load is determined by eye, using a straight line drawn through the second linear region. This also is followed by an increased slope relative to the slope immediately preceding the reverse knee load. For the cross-ply laminate specimens and Specimen 4 of the $[\pm 45/0]_{13S}$ laminate, the reverse knee load is preceded immediately by the initial linear region. For these specimens with only a reverse knee load, this occurs between 79.8 kN and 101.1 kN. For the specimens of the quasi-isotropic and $[\pm 60/0]_{13S}$ laminates, as well as three specimens of the $[\pm 45/0]_{13S}$ laminate and $[\pm 30/0]_{13S}$ Specimen 3, a knee load follows the initial linear region as previously noted. The decreased slope in the response after the knee load immediately precedes the reverse knee load, although the response in this region is not necessarily linear. The reverse knee loads for these specimens occur between 61.0 kN and 76.6 kN. The reverse knee load is exhibited in the responses shown in Figures 5.1 to 5.5.

The second linear region can have three possible characteristics relative to the initial linear region. This linear region can have a greater slope than the initial slope, the two slopes can be approximately equal, or the slope can decrease relative to the initial slope. For specimens that exhibit a reverse knee load behavior, the second linear region has a slope that is either approximately the same as or greater than the initial linear region. For specimens that had only a knee load, the slope of the second linear region is less than that of the initial linear region.

The maximum load, in many cases, is followed immediately by a sudden drop in load, associated immediately with both a delamination of the specimen and final failure. In some cases, this load drop indicates a nearly complete inability to carry load, as is shown in Figures 5.3, 5.4, and 5.5. In other cases, the sudden load drop is not indicative of a complete loss of load-carrying capability, but is a partial loss of this capability. This is shown in Figures 5.1 and 5.7. In some cases, after the maximum load is reached, a relatively small degradation of the load-carrying capability occurs

before a sudden load drop. This behavior is shown in Figure 5.6. In all cases, when a sudden drop in load did occur, it was associated with final failure which was observed as a delamination causing the specimen to break into multiple pieces.

For each laminate, at least three specimens were tested. Averages of the values from the specimens for each laminate are used to characterize and compare the laminates subject to loading via the "two-dimensional loading" configuration. The results for each specimen and the resulting averages for each laminate are given in the following tables: maximum load in Table 5.2, initial linear slope in Table 5.3, second linear region in Table 5.4, knee load in Table 5.5, and reverse knee load in Table 5.6.

These behavior characteristics, the knee load, reverse knee load, and slope of the second linear region relative to the initial linear region, lead to the classification of four "Behavior Types" of the load versus stroke response. These Behavior Types are:

Behavior Type A: There is an initial linear region of behavior preceding a knee load. This is followed by a region with a decrease in slope and then a reverse knee load. The second linear region, which follows the reverse knee load, has a slope that is approximately equal to the slope of the initial linear region.

Behavior Type B: There is an initial linear region of behavior preceding a knee load. This is followed by a region with a decrease in slope and then a reverse knee load (similar to Behavior Type A). The second linear region, which follows the reverse knee load, has a slope that is greater (at least 8.0 kN/mm) than that of the slope of the initial linear region.

Behavior Type C: There is an initial linear region preceding a knee load. The knee load leads to a second linear region. This linear region has a slope that is less (at least 7.9 kN/mm) than that of the initial linear region. There is no reverse knee load.

Behavior Type D: There is an initial linear region preceding a reverse knee load. (This initial linear region continues to a load significantly beyond the knee load of other Behavior Types.) The reverse knee load is followed by a second linear

region with a slope that is greater (at least 6.0 kN/mm) than that of the slope of the initial linear region. There is no knee load.

A summary of the Behavior Type for each specimen under the "two-dimensional loading" configuration is given in Table 5.7. Two of the laminates exhibit only one Behavior Type. All specimens of the cross-ply laminate show Behavior Type D. All specimens of the $[\pm 15/0]_{13S}$ laminate show Behavior Type C. The quasi-isotropic laminate and the $[\pm 60/0]_{13S}$ laminate exhibit both Behavior Types A and B, which are similar except for the value of the second linear slope relative to the initial linear slope. The $[\pm 30/0]_{13S}$ laminate exhibits both Behavior Types C and B. Only one of the laminates exhibits more than two of the different Behavior Types with the $[\pm 45/0]_{13S}$ laminate exhibiting all four of the different Behavior Types.

The specimens were visually, by unaided eye, examined after failure. The specimens subject to "two-dimensional loading" failed in two manners, described in previous work as Mode A and Mode B [34]. Mode A involves a major delamination that initiates near the bottom of the groove. An example of such a case is shown in Figure 5.8. Mode B involves a line of damage through-the-thickness of the specimen, leading to a delamination. This delamination occurs as far through-the-thickness as the midplane of the specimen. An example of this case is shown in Figure 5.9. All the "two-dimensional loading" specimens exhibited one of these failure modes, and the figures are generally representative of the two failure modes. The quasi-isotropic laminate exhibited both Mode A and Mode B failures. Other laminates only exhibited either Mode A or Mode B. The $[\pm 60/0]_{20S}$, $[\pm 30/0]_{20S}$, and $[\pm 15/0]_{20S}$ laminates failed in Mode A. The cross-ply and $[\pm 45/0]_{20S}$ laminates failed in Mode B. Photographs of all the specimens after testing are in Appendix B.

For each laminate, three specimens were tested with the "two-dimensional" loading to determine the lower bound for crushing. This was done via the process described in Section 4.4, with the 5 kN load increment between examinations for crushing. In this case, within a laminate, each of the three specimens showed the same load for measurable crushing within this 5 kN increment. The loads at which crushing occurred for each laminate are shown in Table 5.8. Photographs of the specimens

Table 5.2 Maximum loads[a] for the specimens under "two-dimensional loading"

	Laminate					
Specimen	$[\pm 45/0/90]_{10S}$[b]	$[90/0]_{20S}$	$[\pm 60/0]_{13S}$	$[\pm 45/0]_{13S}$	$[\pm 30/0]_{13S}$	$[\pm 15/0]_{13S}$
1	95.5	119.4	90.4	140.3	94.8	121.7
2	126.2	110.0	101.2	131.6	103.1	106.2
3	125.7	124.1	118.6	129.3	111.5	118.6
4	104.9	117.7		127.8		
5	127.1	113.8		133.6		
6	104.9					
7	105.3					
8	125.1					
9	130.3					
Average	**116.1**	**117.0**	**103.4**	**132.5**	**103.1**	**115.5**

[a] All values in [kN].

[b] These 9 results are from tests conducted in previous work [34].

Table 5.3 Initial linear slopes[a] for the specimens under "two-dimensional loading"

	Laminate					
Specimen	$[\pm 45/0/90]_{10S}$[b]	$[90/0]_{20S}$	$[\pm 60/0]_{13S}$	$[\pm 45/0]_{13S}$	$[\pm 30/0]_{13S}$	$[\pm 15/0]_{13S}$
1	81.6	90.7	85.0	93.4	88.3	77.7
2	81.5	83.1	79.8	76.8	86.8	84.8
3	77.9	95.1	82.7	80.1	79.6	89.4
4	82.9	97.0		69.5		
5	79.0	95.1		79.6		
6	82.3					
7	86.5					
8	80.3					
9	79.5					
Average	**81.3**	**92.2**	**82.5**	**79.9**	**84.9**	**84.0**

[a] All values in [kN/mm].

[b] These 9 results are from tests conducted in previous work [34].

Table 5.4 Second linear slopes[a] for the specimens under "two-dimensional loading"

	Laminate					
Specimen	$[\pm 45/0/90]_{10S}$[b]	$[90/0]_{20S}$	$[\pm 60/0]_{13S}$	$[\pm 45/0]_{13S}$	$[\pm 30/0]_{13S}$	$[\pm 15/0]_{13S}$
1	80.4	101.0	84.6	78.2	64.7	68.7
2	93.9	89.1	81.4	82.9	69.8	69.6
3	96.2	107.0	91.0	82.3	82.6	81.5
4	83.7	105.4		92.0		
5	95.6	106.7		95.8		
6	85.0					
7	84.4					
8	94.3					
9	95.0					
Average	**89.8**	**101.8**	**85.7**	**86.2**	**72.4**	**73.3**

[a] All values in [kN/mm].

[b] These 9 results are from tests conducted in previous work [34].

Table 5.5 Knee loads[a] for the specimens under "two-dimensional loading"

	Laminate					
Specimen	$[\pm 45/0/90]_{10S}$[b]	$[90/0]_{20S}$	$[\pm 60/0]_{13S}$	$[\pm 45/0]_{13S}$	$[\pm 30/0]_{13S}$	$[\pm 15/0]_{13S}$
1	44.0	DNE[c]	53.8	54.4	50.1	50.3
2	44.0	DNE	51.0	45.3	55.8	52.4
3	48.0	DNE	53.2	56.2	54.5	52.0
4	45.0	DNE		DNE		
5	41.0	DNE		51.8		
6	44.0					
7	44.0					
8	41.0					
9	45.0					
Average	**44.0**	**-**	**52.7**	**51.9**	**53.5**	**51.6**

[a] All values in [kN].

[b] These 9 results are from tests conducted in previous work [34].

[c] DNE signifies the knee load "Does Not Exist" for this specimen.

Table 5.6 Reverse knee loads[a] for the specimens under "two-dimensional loading"

	Laminate					
Specimen	$[\pm 45/0/90]_{10S}$[b]	$[90/0]_{20S}$	$[\pm 60/0]_{13S}$	$[\pm 45/0]_{13S}$	$[\pm 30/0]_{13S}$	$[\pm 15/0]_{13S}$
1	63.6	96.0	61.1	DNE[c]	DNE	DNE
2	76.6	88.4	61.0	75.1	DNE	DNE
3	74.7	101.1	68.6	70.3	66.0	DNE
4	65.8	99.6		79.8		
5	75.5	98.3		76.0		
6	66.5					
7	67.2					
8	76.3					
9	74.6					
Average	**71.2**	**96.7**	**63.6**	**76.3**	**-**	**DNE**

[a] All values in [kN].

[b] These 9 results are from tests conducted in previous work [34].

[c] DNE signifies the reverse knee load "Does Not Exist" for this specimen.

Table 5.7 Behavior Types for the load-stroke response for the specimens under "two-dimensional loading"

	Laminate					
Specimen	$[\pm 45/0/90]_{10S}$ [a]	$[90/0]_{20S}$	$[\pm 60/0]_{13S}$	$[\pm 45/0]_{13S}$	$[\pm 30/0]_{13S}$	$[\pm 15/0]_{13S}$
1	A	D	A	C	C	C
2	B	D	A	B	C	C
3	B	D	B	A	A	C
4	A	D		D		
5	B	D		B		
6	A					
7	A					
8	B					
9	B					

[a] These 9 results are from tests conducted in previous work [34].

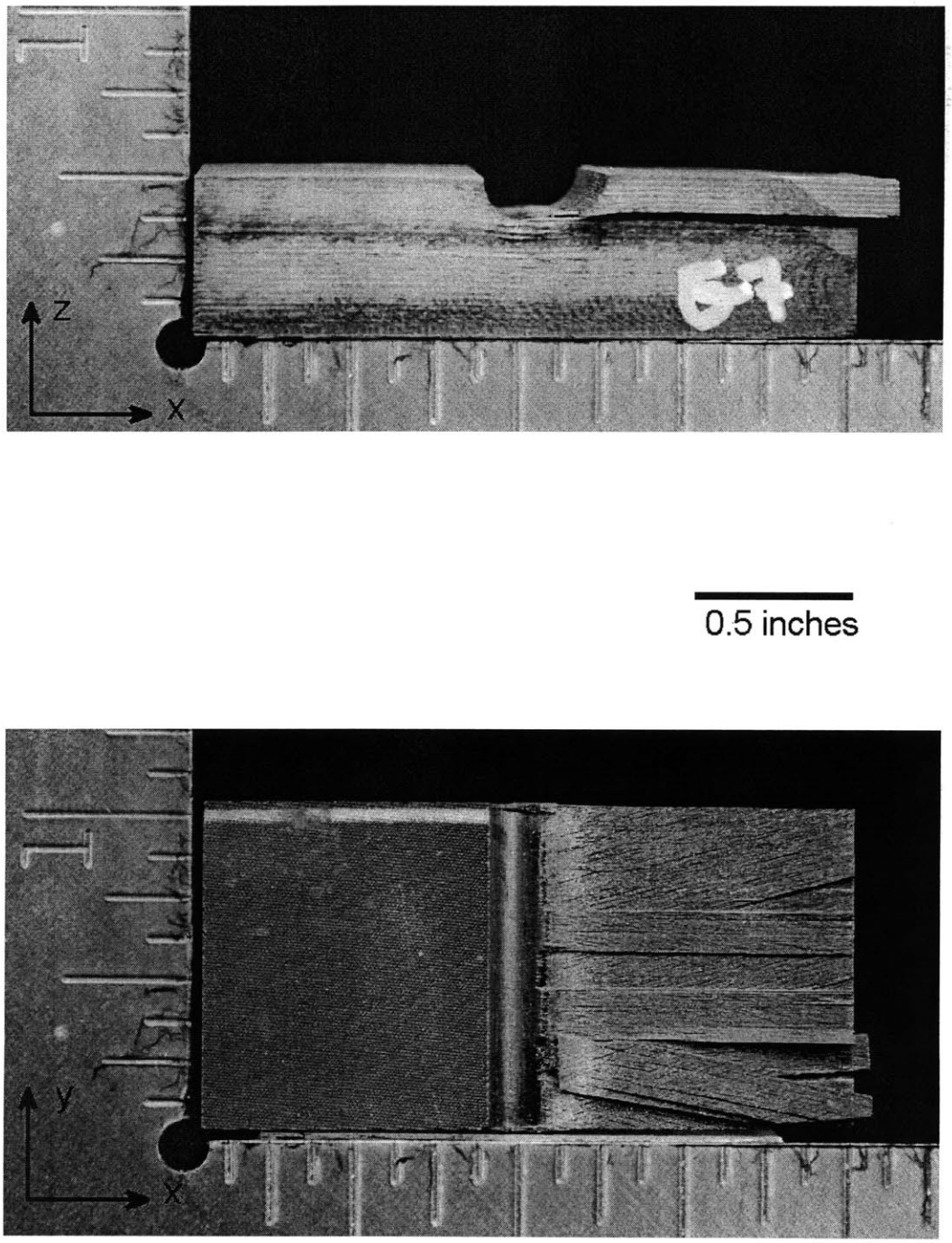

Figure 5.8 Photographs of failure via Mode A with delamination at the bottom of the groove of $[\pm 15/0]_{13S}$ Specimen 1, tested to failure in "two-dimensional loading", shown via (*top*) side view, and (*bottom*) top view with delamination surfaces exposed.

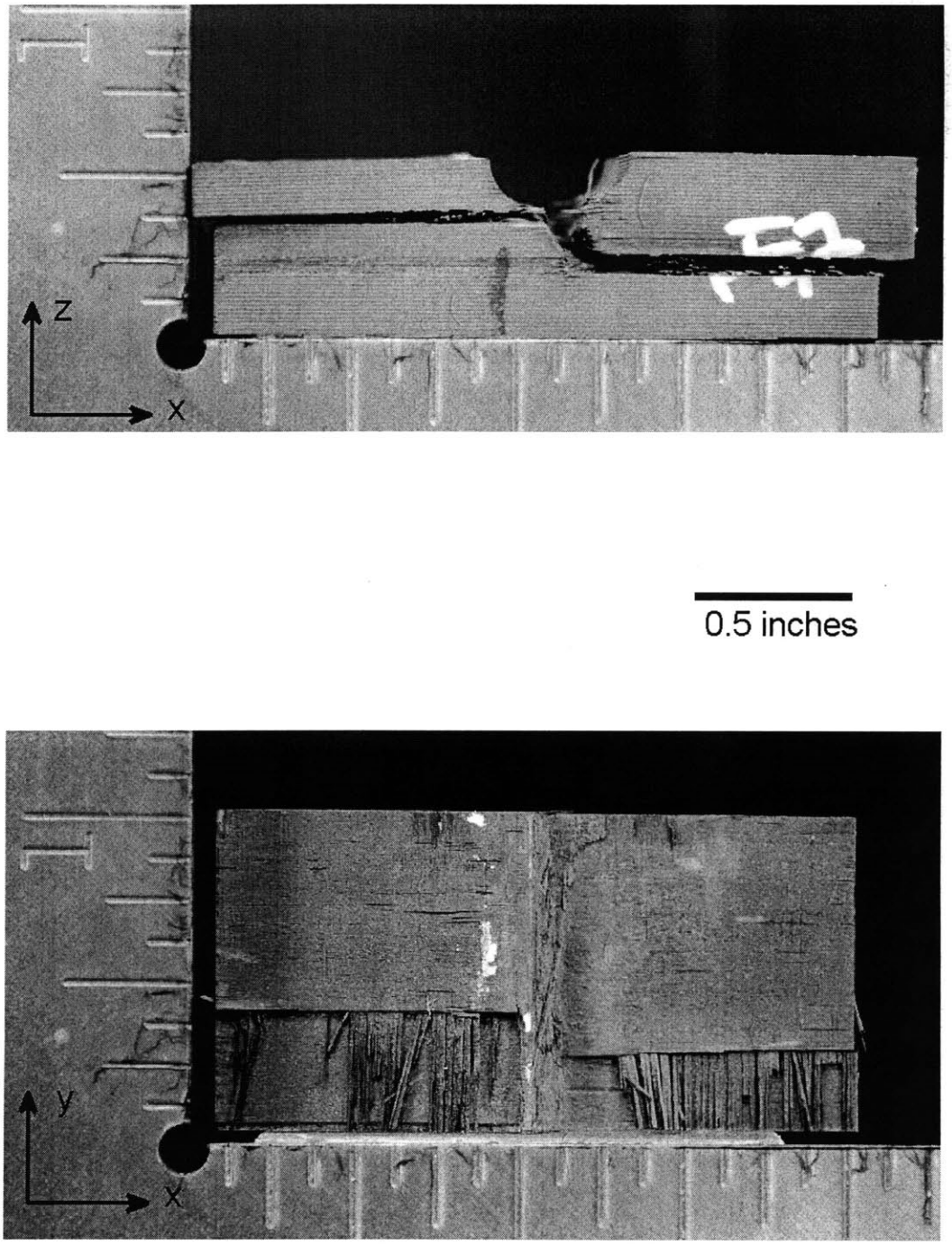

Figure 5.9 Photographs of failure via Mode B with through-the-thickness line of damage leading to delamination failure at the bottom of the groove of $[90/0]_{20S}$ Specimen 1, tested to failure in "two-dimensional loading", shown via (*top*) side view, and (*bottom*) top view with delamination surfaces exposed.

after testing for crushing are available in Appendix D.

5.2 "Three-Dimensional Loading" Specimens

The ball-ended indenter was used for the "three-dimensional loading" test configuration. A total of 44 tests were completed, with 26 specimens tested to failure and 18 specimens tested until crushing first occurred. The breakdown of the tests is shown in Table 5.1.

For the "three-dimensional loading" tests to final failure, at least three specimens were tested for each laminate. These tests were completed using the methods described in Section 4.4, and the same data was collected as for the specimens loaded in the "two-dimensional loading" configuration. Representative load versus stroke responses are shown in Figures 5.10 to 5.15. The load versus stroke responses for all specimens are available in Appendix A.

The specimens tested in the "three-dimensional loading" configuration showed several common characterization items. As in the "two-dimensional loading" configuration, the specimens loaded in the "three-dimensional loading" configuration showed an initial region with a linear slope, and this was followed by a knee load in all cases. The laminates tested with the "three-dimensional loading" configuration reached a second region with a linear slope. Most specimens showed a slow degradation of the load-carrying capability after a maximum load was reached, rather than a sudden load drop as with the case of the "two-dimensional loading".

For the "three-dimensional loading" specimens, all specimens displayed linear behavior at loads from 10 kN to 15 kN, whereas this occurred at higher loads of 20 kN to 40 kN in the "two-dimensional loading" configuration. This different region was used to calculate the initial linear slope for the "three-dimensional loading" case. This initial linear region can be seen in Figures 5.10 to 5.15.

As in the case of the "two-dimensional loading" configuration, a second linear region of behavior occurs in all the "three-dimensional loading" specimens. For all specimens subject to this loading, the slope of the second linear region is less than

Table 5.8 Crushing load for the laminates under "two-dimensional loading"

Laminate	Crushing Load [kN]
$[\pm 45/0/90]_{10s}$	45.0
$[90/0]_{20s}$	50.0
$[\pm 15/0]_{13s}$	45.0
$[\pm 30/0]_{13s}$	60.0
$[\pm 45/0]_{13s}$	45.0
$[\pm 60/0]_{13s}$	50.0

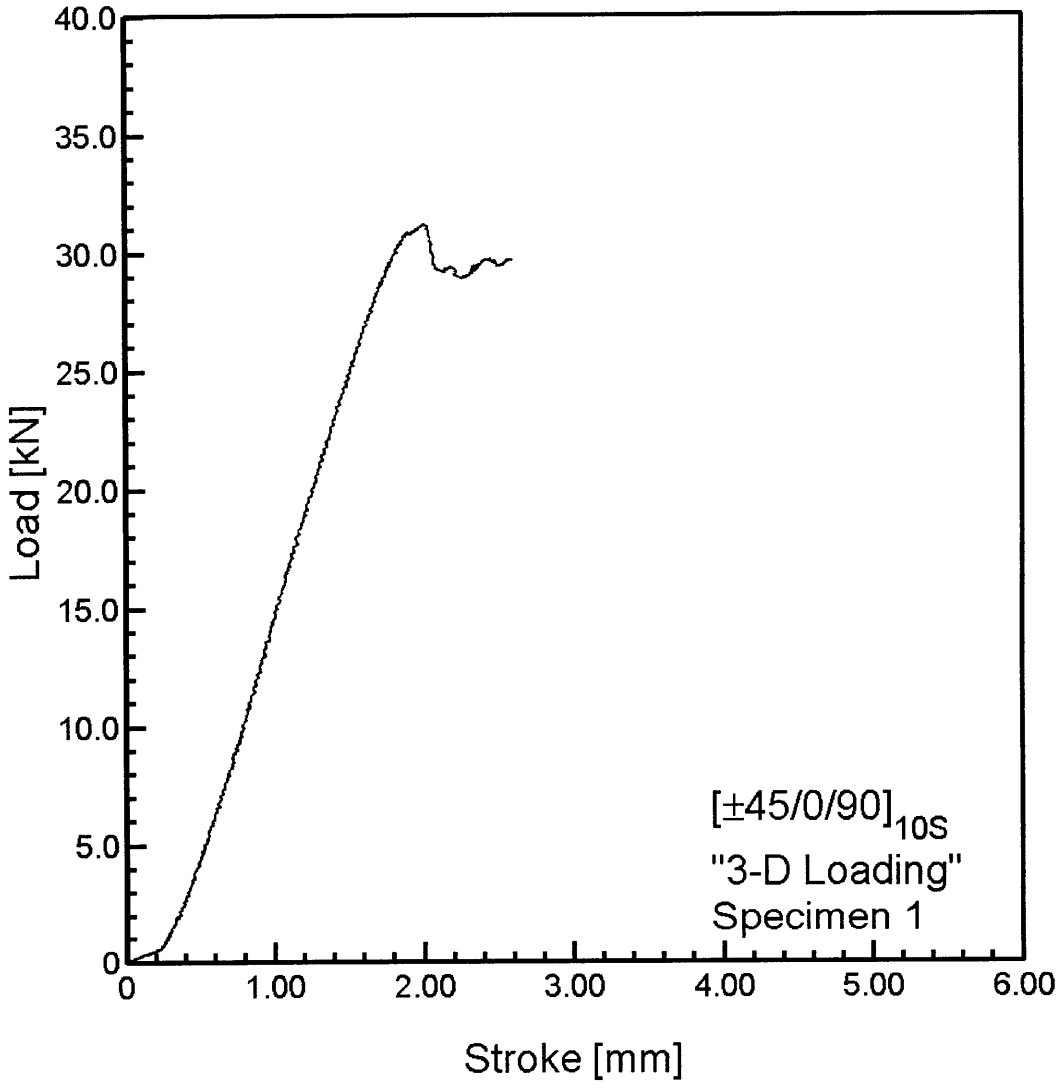

Figure 5.10 Load versus stroke for $[\pm 45/0/90]_{10S}$ Specimen 1 tested to failure with the "three-dimensional loading".

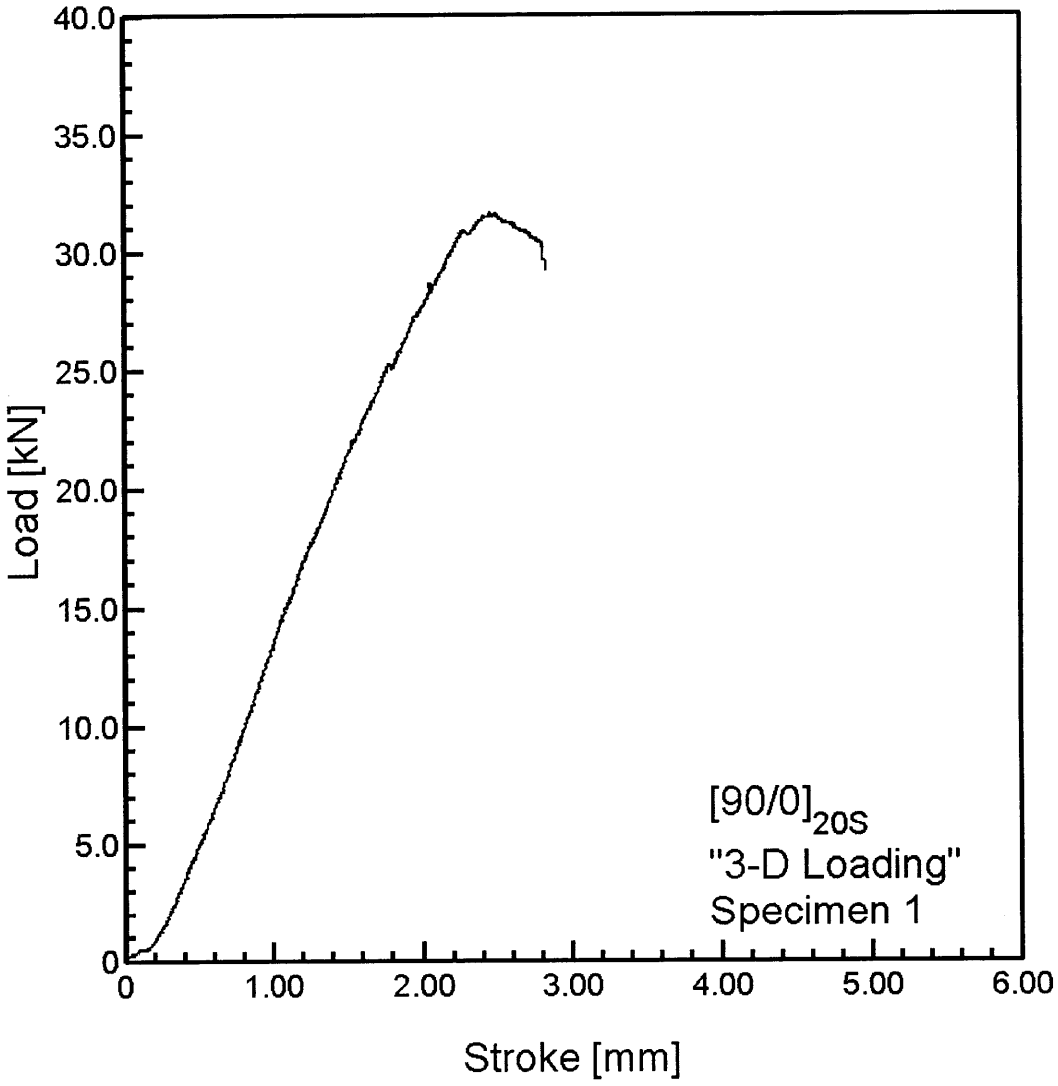

Figure 5.11 Load versus stroke for $[90/0]_{20S}$ Specimen 1 tested to failure with the "three-dimensional loading".

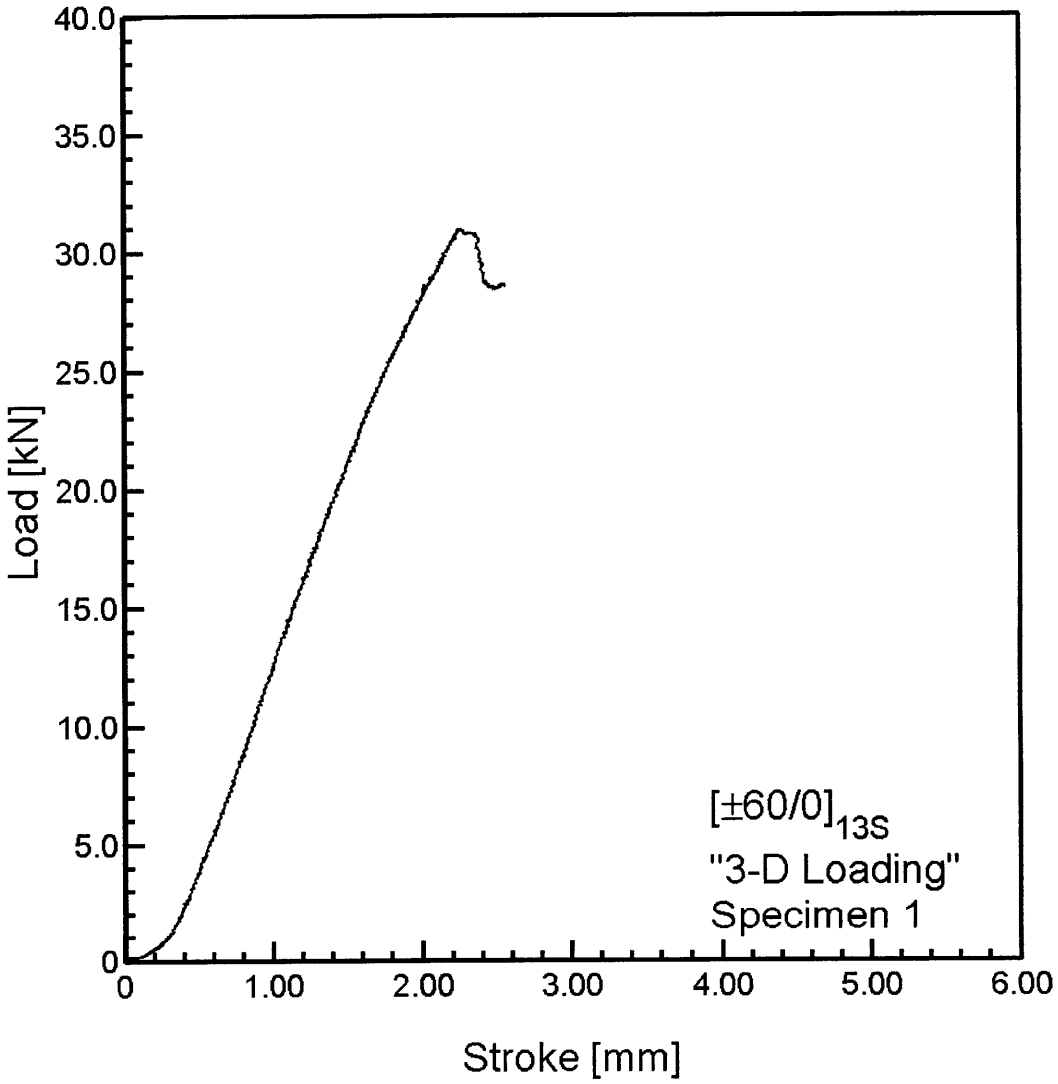

Figure 5.12 Load versus stroke for $[\pm 60/0]_{13S}$ Specimen 1 tested to failure with the "three-dimensional loading".

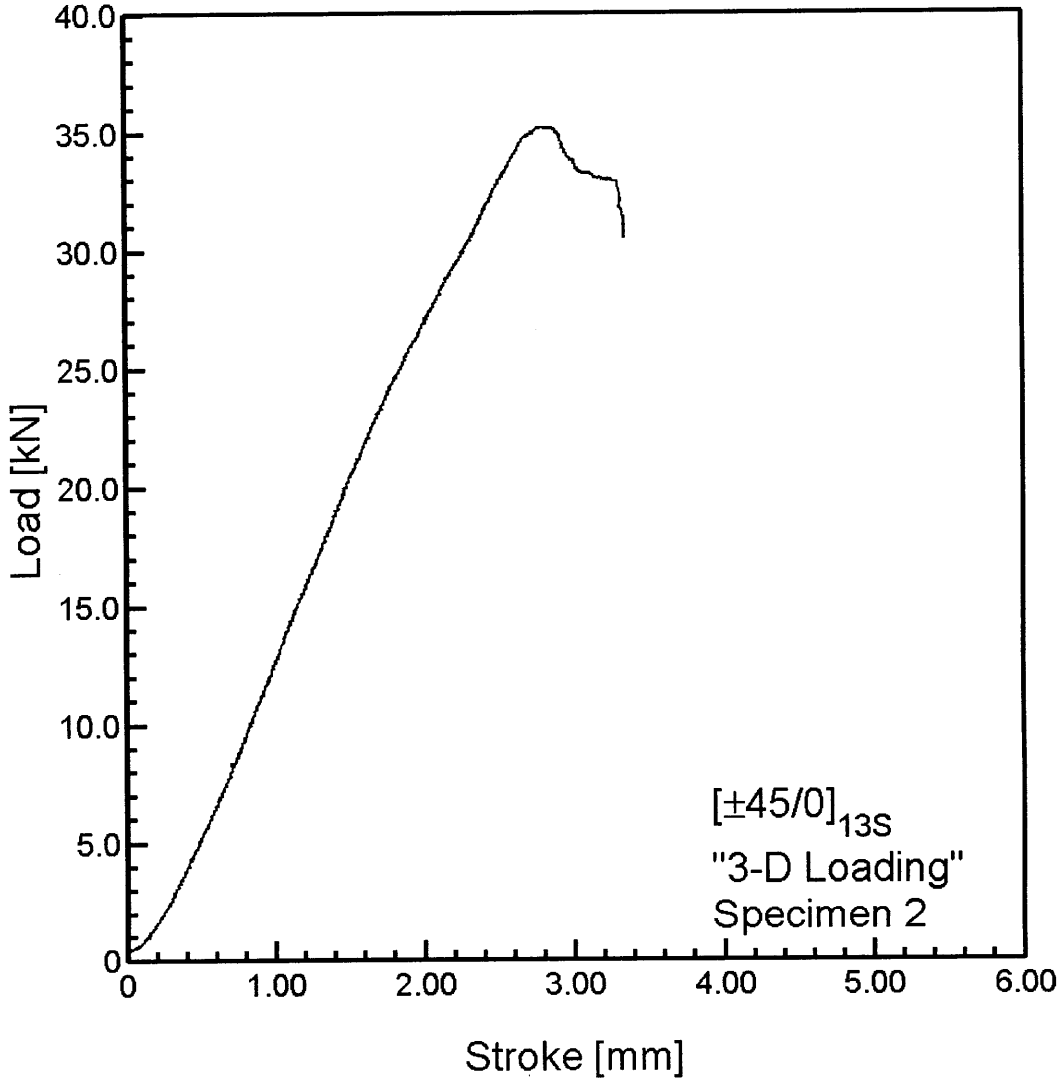

Figure 5.13 Load versus stroke for $[\pm 45/0]_{13S}$ Specimen 2 tested to failure with the "three-dimensional loading".

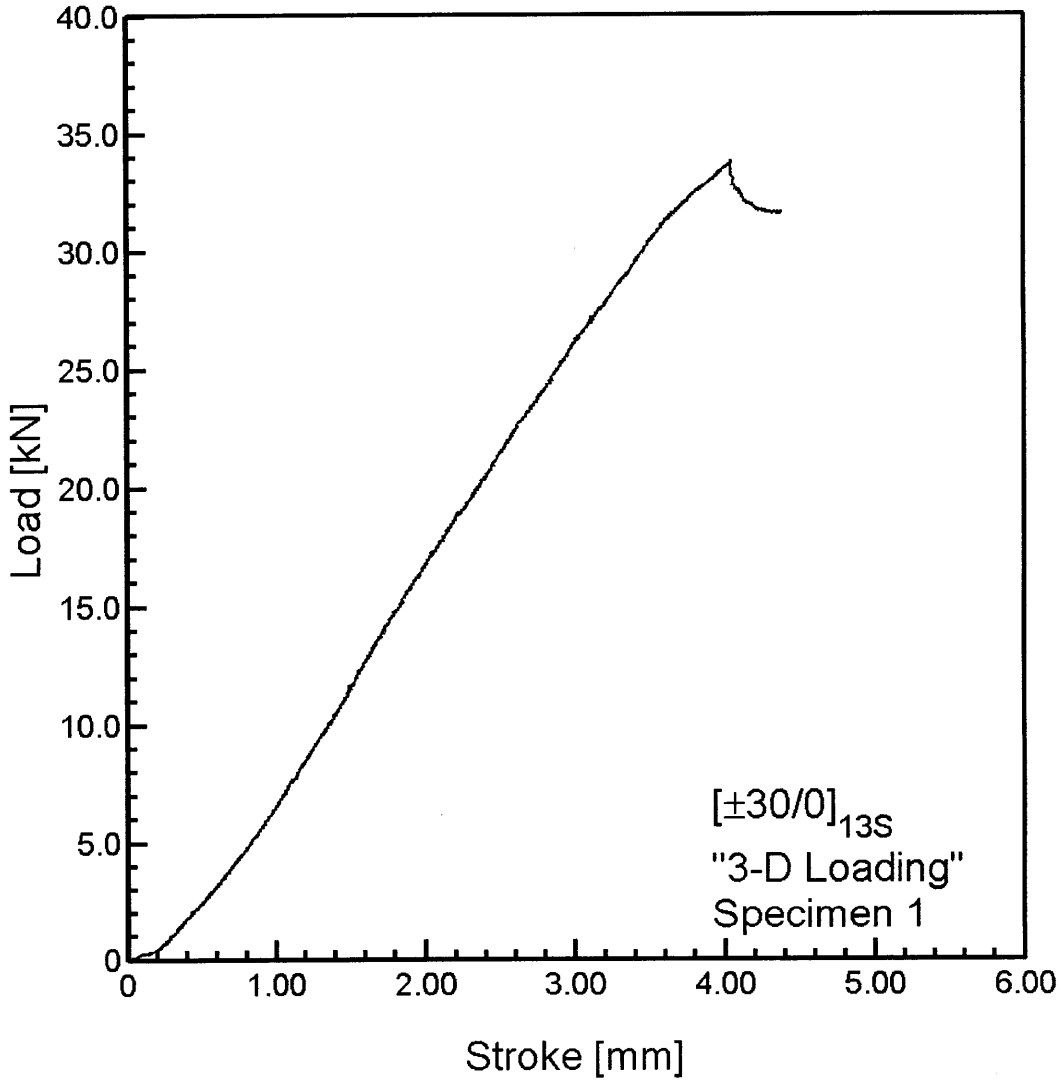

Figure 5.14 Load versus stroke for $[\pm 30/0]_{13S}$ Specimen 1 tested to failure with the "three-dimensional loading".

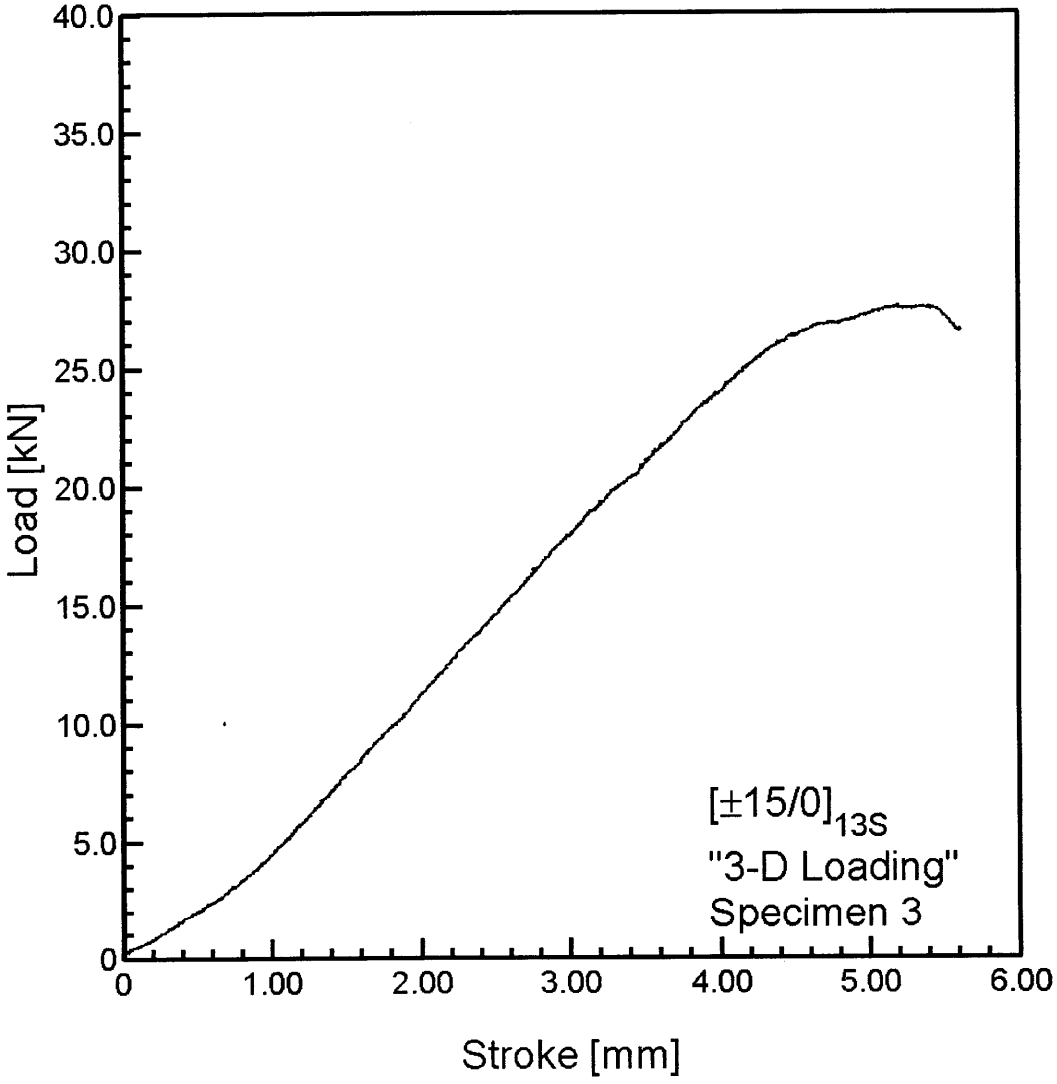

Figure 5.15 Load versus stroke for $[\pm 15/0]_{13S}$ Specimen 3 tested to failure with the "three-dimensional loading".

that of the initial linear region in contrast to the varied behavior shown for the "two-dimensional loading". The slope of the second linear region was determined using linear regression, and the region over which this was applied was determined by eye with a straight-edge. This second linear region can be seen in the responses in Figures 5.10 to 5.15. For the "three-dimensional loading" specimens, the slope of the second linear region was at least 6.8%, and as much as 36.7%, less than than the slope of the initial linear region.

A knee load is shown in all the "three-dimensional loading" specimens. The knee load is in a transition region from the initial linear region to the second linear region. Since the existence of a knee load also occurred in the case of the "two-dimensional loading", the same method was used to calculate the value of the knee load as that used for the "two-dimensional loading" case. Thus, a line with a 1.5% smaller slope than the initial linear slope is drawn from the point of zero load for the extended linear region and the point at which it crosses the initital linear region is the knee load. This value of 1.5% was determined via the same process that was used in the "two-dimensional loading" case. For the cross-ply laminate, there is a knee load in the "three-dimensional loading" that did not occur for the "two-dimensional loading". The existence of the knee loads are observed in Figures 5.10 to 5.15. With the "three-dimensional loading", all laminates exhibit a knee load in the load-stroke response, but there is no reverse knee load as is seen in some of the "two-dimensional loading" laminates and specimens.

In the "two-dimensional loading" case, a sudden load drop indicated final failure of a specimen. In the "three-dimensional loading" case, this did occur in three specific cases: $[\pm 45/0/90]_{10S}$ Specimen 5, $[90/0]_{20S}$ Specimen 5, and $[\pm 30/0]_{13S}$ Specimen 4. However, the "three-dimensional loading" specimens generally reached a maximum load, and this was followed by a degradation of the load-carrying capability, and then a persistent inability to carry additional load. This behavior is shown in all the representative load versus stroke curves. The maximum load the specimen is able to carry is of interest in all cases.

The averages of the results from the specimens tested for each laminate are used

to characterize and compare the laminates tested in the "three-dimensional loading" configuration. The results for each specimen and the resulting averages for each laminate are given in the following tables: maximum load in Table 5.9, initial linear slope in Table 5.10, knee load in Table 5.11, and second linear slope in Table 5.12.

Once the specimens failed and the tests were completed, the specimens were examined visually by unaided eye. All specimens showed a delamination below the bottom of the groove as part of the damage. The distance below the groove at which the delamination occurred depends on the laminate of the specimen. However, the specimens did not break into multiple pieces as happened in the case of "two-dimensional loading". The distance below the groove, in the z-direction, measured at the center of the xz-surface, at which the main delamination occurs is shown in Table 5.13. Crushing near the indenter has a significant impact on the failure behavior of the "three-dimensional loading" specimens. In the "three-dimensional loading" cases, the indenter pushed a significant distance into the material. This distance is as much as 5.75 mm before degradation of load-carrying capability. This led to a delamination significantly below the groove, as shown in Figure 5.16. In these specimens, the delamination did not run uniformly between two plies, but instead jumped between several plies. This also can be seen in Figure 5.16. At the outer xz-surface, this jump of the delamination is often visible. This initiation point of the jump is in the interior of the specimen, closer to the indenter contact point, and not visible from the outer surface. While the specific location of the delamination varies, the general behavior shown in Figure 5.16 is representative of most "three-dimensional loading" specimens. However, three specimens of the cross-ply laminates, Specimens 1, 4, and 5, did not show any jump between plies of the delamination. Representative photographs of this behavior are shown in Figure 5.17. Photographs of all "three-dimensional loading" specimens after testing are in Appendix C.

For each laminate, three specimens were tested with the "three-dimensional loading" to find the lower bound for crushing. This was done using the process described in Section 4.4, with the 1 kN load increment between examinations for crushing. Within the laminates, each of the three specimens showed the same load for mea-

Table 5.9 Maximum loads[a] for the specimens under "three-dimensional loading"

	Laminate					
Specimen	$[\pm 45/0/90]_{10S}$	$[90/0]_{20S}$	$[\pm 60/0]_{13S}$	$[\pm 45/0]_{13S}$	$[\pm 30/0]_{13S}$	$[\pm 15/0]_{13S}$
1	31.2	31.7	31.0	37.8	33.9	30.5
2	34.2	34.9	33.6	35.2	35.8	29.7
3	31.6	32.6	33.6	35.6	36.5	27.6
4	33.5	31.8		34.2	40.6	
5	36.7	33.9		35.7	35.1	
Average	**33.4**	**33.0**	**32.7**	**35.7**	**35.4**	**29.3**

[a] All values in [kN].

Table 5.10 Initial linear slopes[a] for the specimens under "three-dimensional loading"

	Laminate					
Specimen	$[\pm 45/0/90]_{10S}$	$[90/0]_{20S}$	$[\pm 60/0]_{13S}$	$[\pm 45/0]_{13S}$	$[\pm 30/0]_{13S}$	$[\pm 15/0]_{13S}$
1	22.0	17.8	17.8	16.5	10.8	8.3
2	22.4	22.7	19.0	15.7	11.7	7.9
3	20.7	19.6	17.4	16.0	12.6	6.9
4	22.4	19.3		15.5	14.8	
5	21.9	20.1		17.0	10.97	
Average	**21.7**	**19.9**	**18.0**	**16.1**	**11.7**	**7.7**

[a] All values in [kN/mm].

Table 5.11 Knee loads[a] for the specimens under "three-dimensional loading"

	Laminate					
Specimen	$[\pm 45/0/90]_{10S}$	$[90/0]_{20S}$	$[\pm 60/0]_{13S}$	$[\pm 45/0]_{13S}$	$[\pm 30/0]_{13S}$	$[\pm 15/0]_{13S}$
1	20.1	17.9	21.4	21.5	19.2	20.8
2	23.8	20.0	20.5	20.7	21.3	19.7
3	19.0	18.7	21.1	18.2	20.0	19.8
4	20.1	17.3		21.3	21.5	
5	28.5	17.7		23.5	20.8	
Average	**22.3**	**18.3**	**21.0**	**21.0**	**20.1**	**20.1**

[a] All values in [kN].

Table 5.12 Second linear slopes[a] for the specimens under "three-dimensional loading"

	Laminate					
Specimen	$[\pm 45/0/90]_{10S}$	$[90/0]_{20S}$	$[\pm 60/0]_{13S}$	$[\pm 45/0]_{13S}$	$[\pm 30/0]_{13S}$	$[\pm 15/0]_{13S}$
1	18.2	12.3	12.2	13.1	8.6	6.7
2	20.5	16.9	13.9	11.8	10.0	6.0
3	18.2	12.4	12.3	12.5	11.3	5.9
4	18.8	13.2		13.2	13.8	
5	19.6	14.6		14.4	9.3	
Average	**19.1**	**13.9**	**12.8**	**13.0**	**10.6**	**6.2**

[a] All values in [kN/mm].

Table 5.13 Distance[a] below groove of major delamination for the specimens under "three-dimensional loading"

	Laminate					
Specimen	$[\pm 45/0/90]_{10S}$	$[90/0]_{20S}$	$[\pm 60/0]_{13S}$	$[\pm 45/0]_{13S}$	$[\pm 30/0]_{13S}$	$[\pm 15/0]_{13S}$
1	0.09	0.11	0.09	0.11	0.12	0.13
2	0.10	0.10	0.11	0.12	0.13	0.15
3	0.10	0.11	0.12	0.12	0.11	0.14
4	0.08	0.10		0.11	0.13	
5	0.10	0.10		0.12	0.11	
Average	**0.08 in**	**0.10 in**	**0.11 in**	**0.12 in**	**0.12 in**	**0.14 in**

[a] All values in [in].

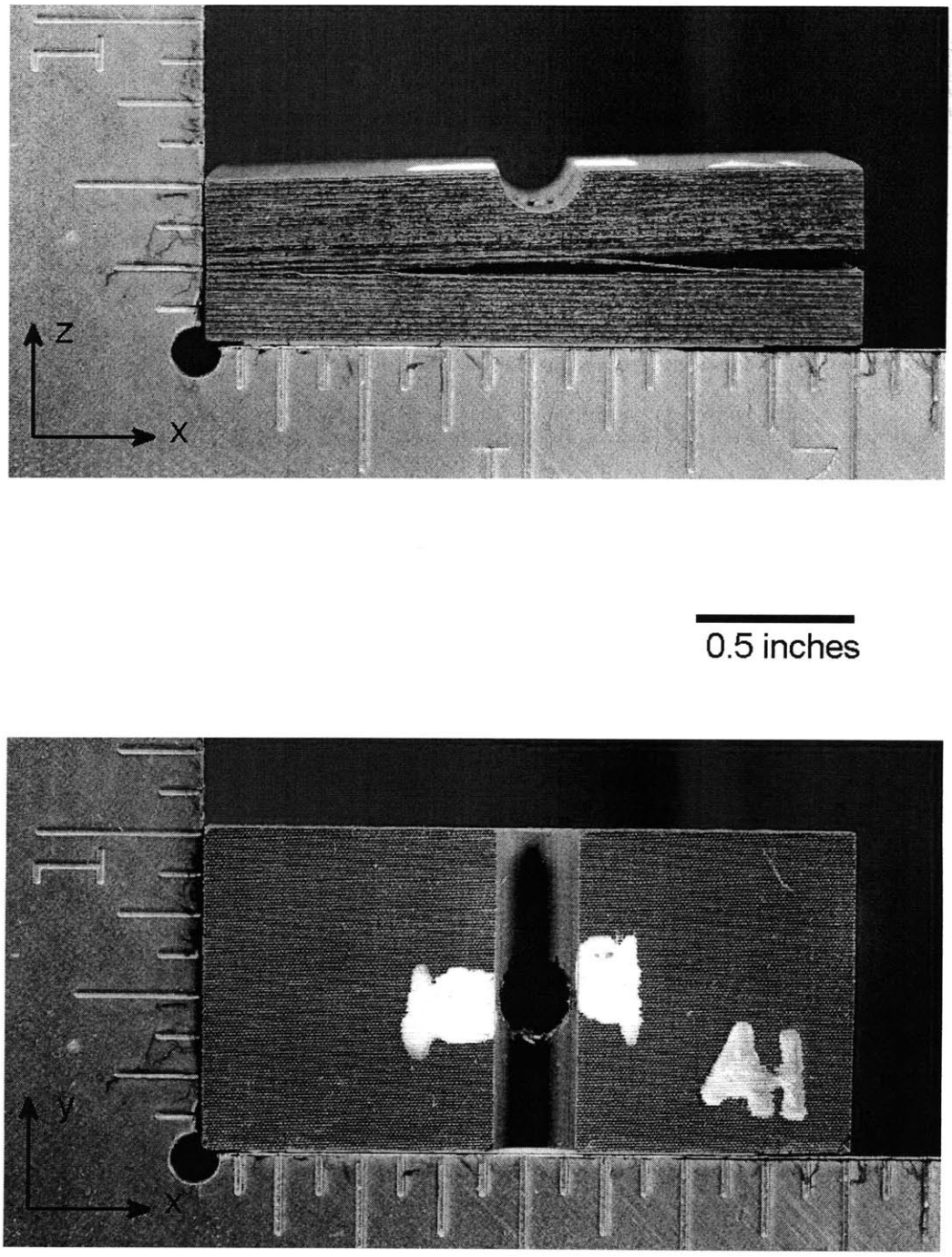

Figure 5.16 Photographs of nonuniform delamination failure below the groove of $[\pm 45/0]_{13S}$ Specimen 1, tested to failure in "three-dimensional loading" shown via (*top*) side view, and (*bottom*) top view with crater from indenter visible.

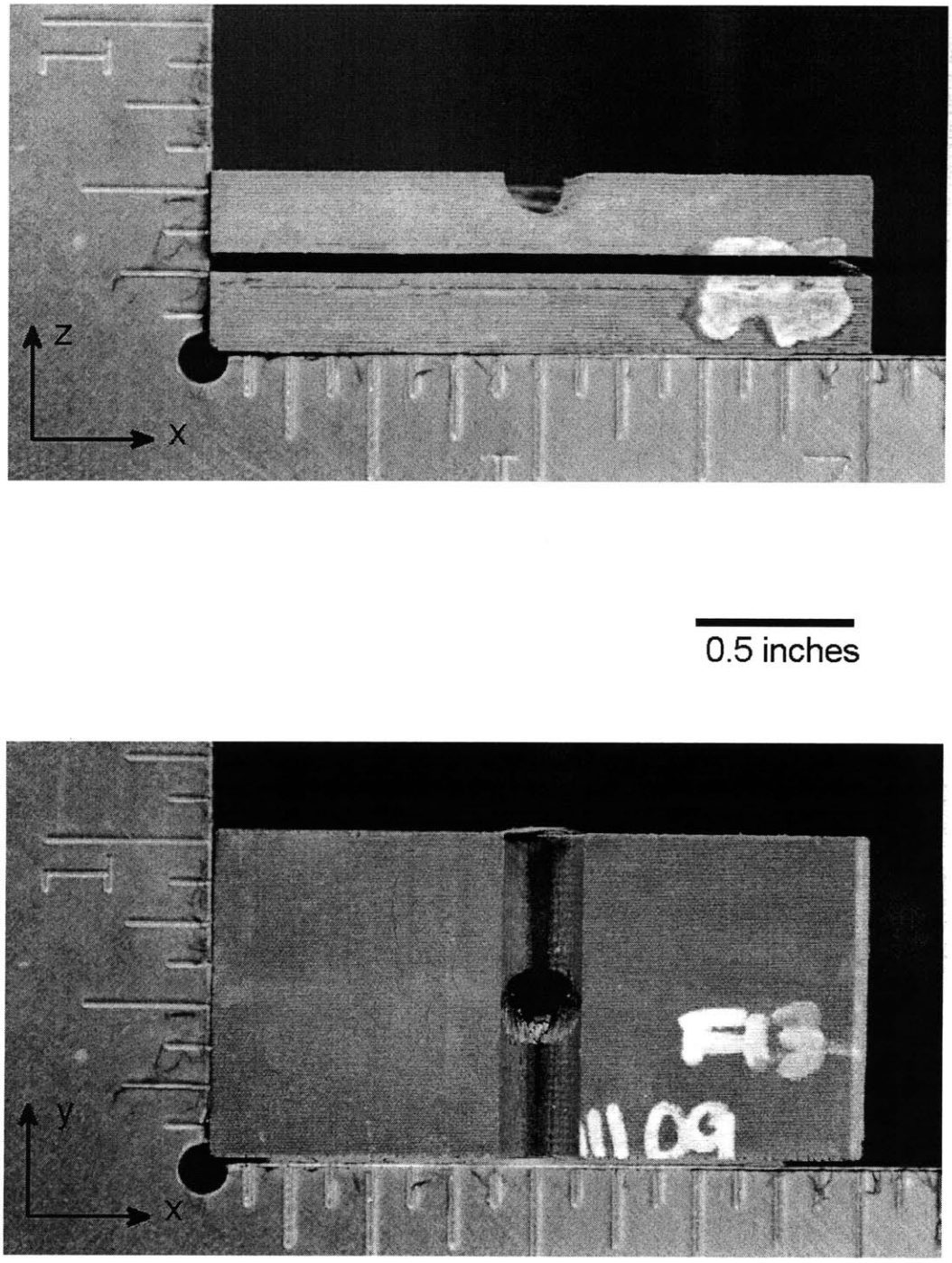

Figure 5.17 Photographs of uniform delamination failure below the groove of $[90/0]_{20S}$ Specimen 4, tested to failure in "three-dimensional loading" shown via (*top*) side view, and (*bottom*) top view with crater from indenter visible.

surable crushing within that 1 kN increment. The loads at which crushing occurred for each laminate are shown in Table 5.14. Photographs of the "three-dimensional loading" specimens after crushing are in Appendix E.

5.3 Characterization of Internal Damage

Once testing to failure or testing for crushing was completed, select specimens were examined using the nondestructive testing method of computed microtomography, as described in Section 4.5. Two specimens that were tested to failure in the "three-dimensional loading" were examined. However, no specimens tested to failure via the "two-dimensional loading" were examined since they are in multiple sections after failure. The reconstruction of the failed "three-dimensional loading" specimens, which are described shortly, was used to validate the scanning technique as a means of visualizing the internal damage, and it was deemed that more would be learned from the crushing specimens. The virtual reconstructions of these specimens, as described in Section 4.5, allows for characterization of internal damage that could not be surmised from the outer visual examination of the specimen. In the case of testing to crushing, one specimen was scanned for each laminate and case of load applicator for a total of 12 reconstructions of crushing specimens. The crushing load was the same for each specimen within a laminate and load type.

Two specimens were scanned after being tested to failure in the "three-dimensional loading" configuration: $[\pm 30/0]_{13s}$ Specimen 2 and $[\pm 15/0]_{13S}$ Specimen 3. However, only "virtual cuts" of $[\pm 15/0]_{13S}$ Specimen 3 are presented herein as the scans for $[\pm 30/0]_{13S}$ Specimen 2 are not of high enough quality to sufficiently indicate needed details. The $[\pm 15/0]_{13S}$ Specimen 3 was scanned and reconstructed as it showed a transverse crack on the external surface, which was not seen in other specimens. The external damage of Specimen 3 of the $[\pm 15/0]_{13S}$ laminate is shown in Figure 5.18. There is a delamination and a crater from the indenter, and, in addition, there is transverse cracking which is visible on the yz-face of the specimen, on the +x side. However, this is not shown as the cracking is not visible in the photograph. "Virtual

Table 5.14 Crushing load for the laminates under "three-dimensional loading"

Laminate	Crushing Load [kN]
$[\pm 45/0/90]_{10S}$	14.0
$[90/0]_{20S}$	7.0
$[\pm 15/0]_{13S}$	4.5
$[\pm 30/0]_{13S}$	11.0
$[\pm 45/0]_{13S}$	10.0
$[\pm 60/0]_{13S}$	8.0

cuts" of the reconstruction of the same specimen are shown in Figures 5.19, 5.20, 5.21, and 5.22.

The major delamination that is visible at the outer surface of $[\pm 15/0]_{13S}$ Specimen 3, as seen in the side surface photograph of Figure 5.18, can be seen in each of the four "virtual cuts" taken along the yz-plane as presented. This is indicated in Figure 5.19, at a location of 0.45 inches from the center of the groove along the x-direction, as the delamination that spans approximately 0.75 inches of the 1-inch width of the specimen. This occurs approximately 0.28 inches up from the bottom of the specimen (z = - 0.19 inches). The bottom of the specimen is used as a reference location from which to measure, as the bottom of the groove, at z equal to 0, is not usually visible. In this "virtual cut" of a yz-plane shown in Figure 5.19, the delamination does not occur uniformly between the same two plies. At a location of y approximately equal to - 0.25 inches (approximately 0.25 inches from the xz-surface), and at approximately the same z-location of 0.28 inches from the bottom surface of the specimen, the plies between which the delamination occurs changes. However, despite the change of ply interface, from additional observation with "virtual cuts" of the specimen, it is apparent that this is a continuation of the same major delamination previously discussed. While this jumps between ply interfaces, the additional observation shows that the delaminations are connected. These are connected by transverse damage, primarily in the matrix, as fingers of fibers can be seen externally by eye. These are shown in the top photograph in Figure 5.18.

The major delamination is again visible at the "virtual cut" that is approximately 0.15 inches from the center of the groove, shown in Figure 5.20. However, at this location in the laminate, the delamination occurs for a length of only approximately 0.3 inches into the width of the specimen, still at a z-location approximately 0.28 inches from the bottom of the specimen. At this location, the load applicator has caused damage leading to material displacement. The delamination at that z-location, approximately 0.28 inches above the bottom of the specimen, does not occur over the same distance or at the same associated ply as in the "virtual cut" of Figure 5.20 that is farther from the groove and load application. At the "virtual cut" of Figure 5.20,

there is an additional delamination that runs from the right edge of the specimen, at y = - 0.50 inches, inwards to a point approximately 0.25 inches towards the center of the specimen, at y = - 0.25 inches, at a z-location approximately 0.3 inches from the bottom of the specimen. This delamination is not visible from the outer surface of the specimen.

Continuing through the specimen along its length (the x-direction), a "virtual cut" that is 0.06 inches from the center of the groove is shown in Figure 5.21. The major delamination, at the z-location 0.28 inches from the bottom of the specimen and visible in the previous "virtual cuts", is visible at this "virtual cut" for approximately 0.25 inches into the width of the specimen. The other delamination shown from the right edge of the specimen, at approximately y from 0.20 to 0.25 inches in the previous "virtual cut", is again visible here, at the same y-location of 0.20 to 0.25 inches, and z-location of approximately 0.3 inches from the bottom of the specimen. Finally, progressing to a "virtual cut" at the center of the groove (x = 0 inches) as shown in Figure 5.22, the major delamination that is visible at the outer surface, and the second delamination, which is not visible from the outside, are still visible at the same z-locations as in the previous cuts. The major delamination is visible approximately 0.25 inches into the specimen from the left edge of the figure (y = -0.50 to -0.25 inches). The second delamination is visible for approximately 0.25 inches on the right edge (y = 0.25 to 0.50 inches) of the figure but is not as "uniform" in its appearance at this "virtual cut". This delamination begins at the right edge of the specimen and continues for approximately 0.15 inches at a z-location 0.3 inches from the bottom of the groove. At this point, 0.15 inches from the right edge, there are three small delaminations that occur for another 0.125 inches (y = 0.125 to 0.25 inches) at a z-location of 0.28 inches from the bottom of the groove.

The three "virtual cuts" shown in Figures 5.20, 5.21, and 5.22, show evidence of displaced material and related minor delaminations between many of the plies. At the "virtual cut" that is at x = 0.15 inches, shown in Figure 5.20, this region of damage is somewhat kite-shaped and spans approximately half the width at its widest point in the center of the specimen. This damage occurs over a height of approximately

0.3 inches, and reaches up to nearly 0.05 inches from the top of the specimen. In this kite-shaped region, the plies are no longer straight, but bent towards the bottom of the specimen. There also is damage in this region that appears as separations between many of the plies. This behavior is shown in Figures 5.21 and 5.22 as well, although in both of these "virtual cuts", the displaced plies and minor delaminations do not occur uniformly through the center of the width of the specimen, but instead on either side of a region with additional damage.

This region of additional damage in the two "virtual cuts" taken in the groove, shown in Figures 5.21 and 5.22, are evidence of crushing near the load application point of the "three-dimensional loading" configuration. In Figure 5.21, there is a region with a higher density than most of the specimen in the center of the width, at a height starting approximately 0.1 inches from the bottom of the specimen. This region has a height of approximately 0.1 inches and a width of approximately 0.2 inches, and is indicated by the superposed ellipse in the figure. The higher density of this region is indicated by the lighter color of the region. This is a basic output of the X-Tek computed microtomography system which detects densities through the use of X-rays. A similar region is visible and highlighted in Figure 5.22. In this case, the region is larger with a height of approximately 0.2 inches and a width of approximately 0.3 inches.

These same two "virtual cuts" also show evidence of significant ply damage in the region of indenter contact. The ply damage can be seen in Figure 5.21 at the center of the width of the specimen. This damage occurs over an area with a width of approximately 0.2 inches and a height of approximately 0.25 inches, from the top of the "virtual cut" in this figure. Here, the plies do not curve uniformly or show uniform minor delaminations, but show non-uniform ply damage. This "virtual cut" is near the inside edge of the groove, and the edge indenter contact region. Ply damage immediately around the area where the indenter contacted the specimen is also visible in Figure 5.22. The ply damage in this area indicates much damage to the plies and fibers has occurred, but there is no uniform nature to the damage.

The "virtual cut" at the center of the groove, shown in Figure 5.22, shows ad-

ditional damage to the specimen at the tip of contact. This is the crater that is left after removal of the "three-dimensional loading" applicator and is visible in the photograph of top surface in Figure 5.18. Prior to testing, the bottom of the groove was flat. The "three-dimensional loading" indenter pushed into the specimen during testing, leaving the crater that is visible in the surface photograph of Figure 5.18 and the "virtual cut" of Figure 5.22. In Figure 5.22, there is a superimposed half-circle indicating the relative size and shape of the indenter. The indenter is a cylinder with a hemi-spherical end. However, the edges of the material in this cut are not uniform, indicating that material rebounded into the area where the indenter had been upon the removal of the indenter.

As previously indicated, six specimens that were tested to the crushing bound for the "two-dimensional loading" configuration, and six laminates that were tested using the "three-dimensional loading" configuration were scanned via the computed microtomography method. In the case of the "two-dimensional loading", there was a measurable deformation at the loads given in Table 5.8. However, in the microtomography reconstructions of the volume, no clear effect of the crushing is visible. A typical "virtual cut" of a specimen subject to "two-dimensional loading" and loaded to crushing is shown in Figure 5.23, with the cut at the bottom of the groove. In contrast, the localized load application of the "three-dimensional loading" led to clear identification of the damage caused when crushing occurs. This effect can be seen in "virtual cuts" of a specimen subjected to the "three-dimensional loading" crushing test shown in Figures 5.24, 5.25, and 5.26.

The "virtual cut" at the bottom of the groove, z = 0 inches, of $[\pm 60/0]_{13S}$ Specimen 4 is shown in Figure 5.24. In this specimen, the bottom of the machined groove is at a 0° ply, and a dark elongated oval region is visible at this "virtual cut". This is at the point of indenter contact. The material that was at this location was pushed into the plies below due to crushing. Below the bottom of the groove, at z = - 0.006 inches, crushing causes one ply to be pushed into the ply below. This can be seen in Figure 5.25 where fibers from a 0° ply are visible in the plane that was only a +60° ply prior to testing. The area where this occurs is highlighted with an ellipse around the

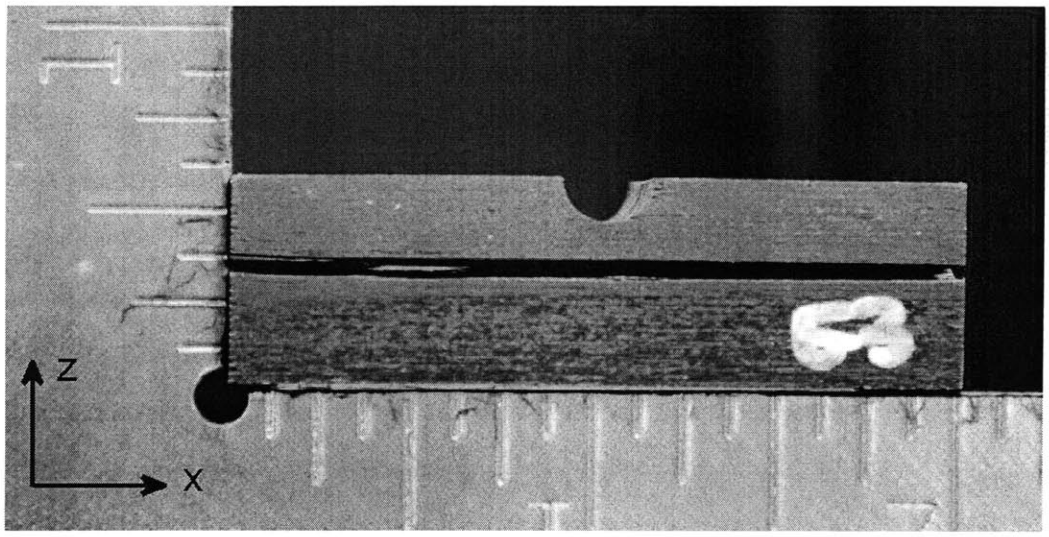

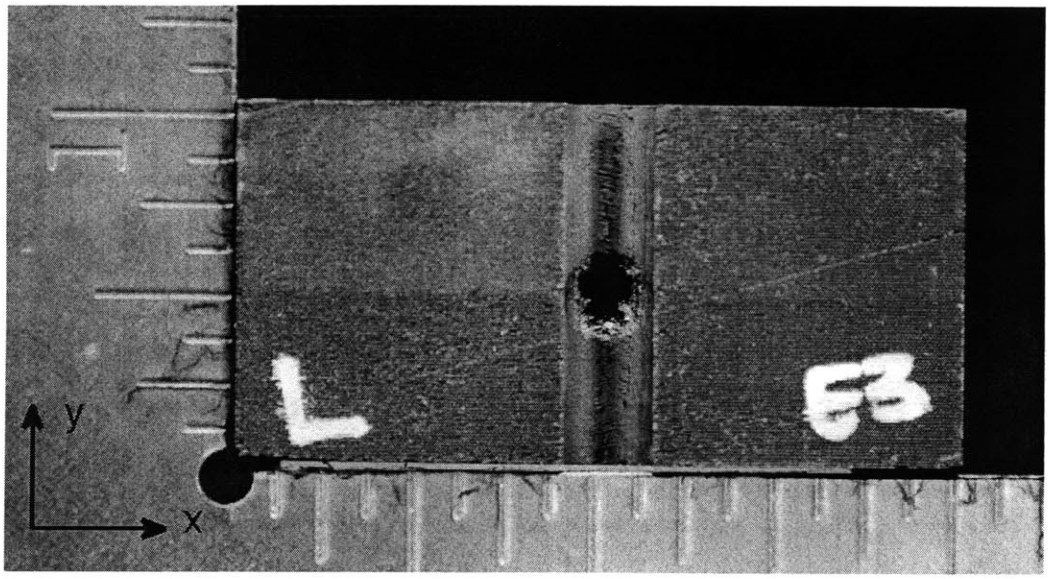

Figure 5.18 Photographs of $[\pm 15/0]_{13S}$ Specimen 3, tested to failure in "three-dimensional loading" via (*top*) side view, and (*bottom*) top view with crater from indenter visible.

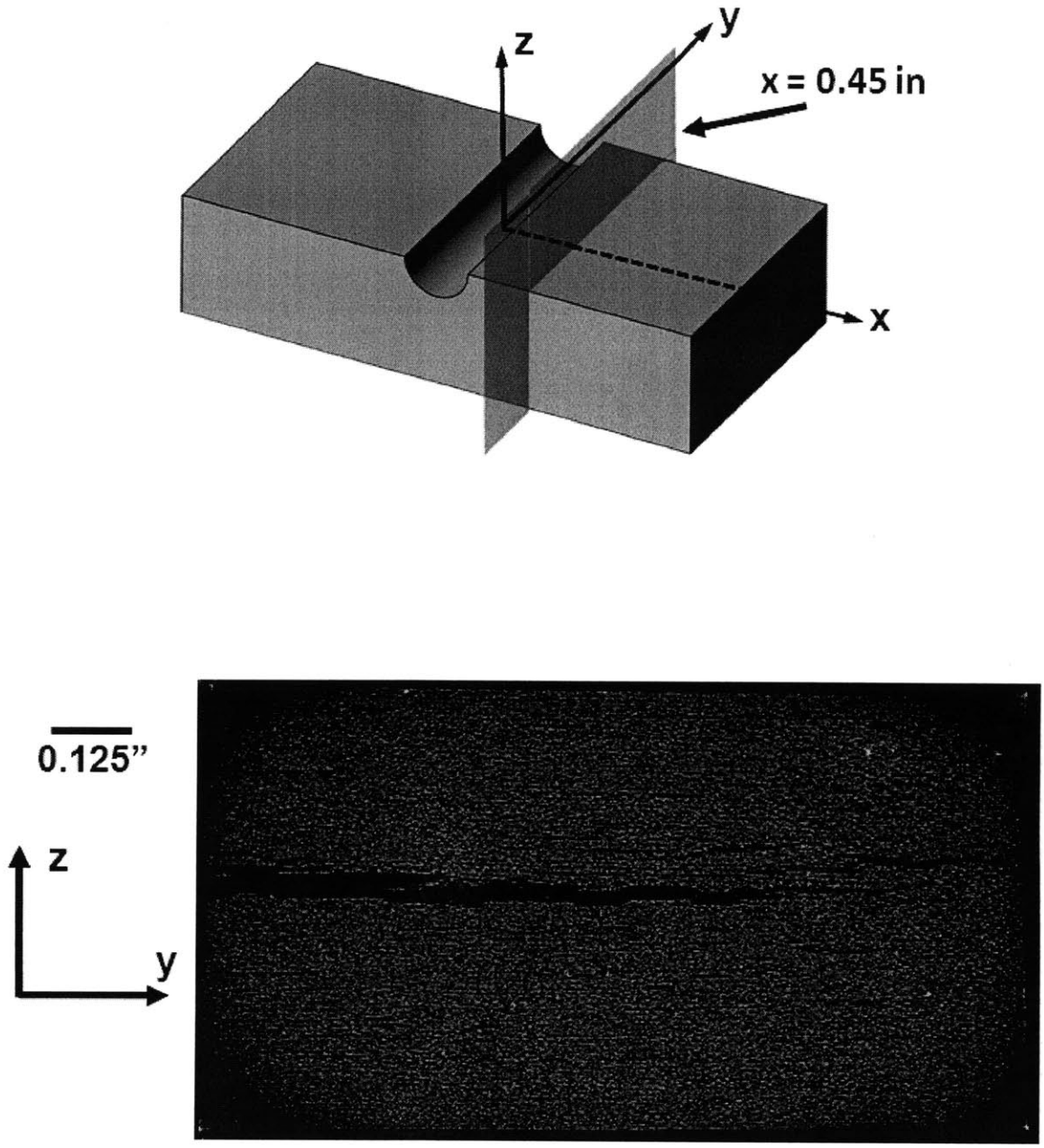

Figure 5.19 "Virtual cut" via computed microtomography of $[\pm 15/0]_{13S}$ Specimen 3 tested to failure in "three-dimensional loading" with (*top*) location of the "virtual cut", 0.45 inches from center of groove, and (*bottom*) actual image.

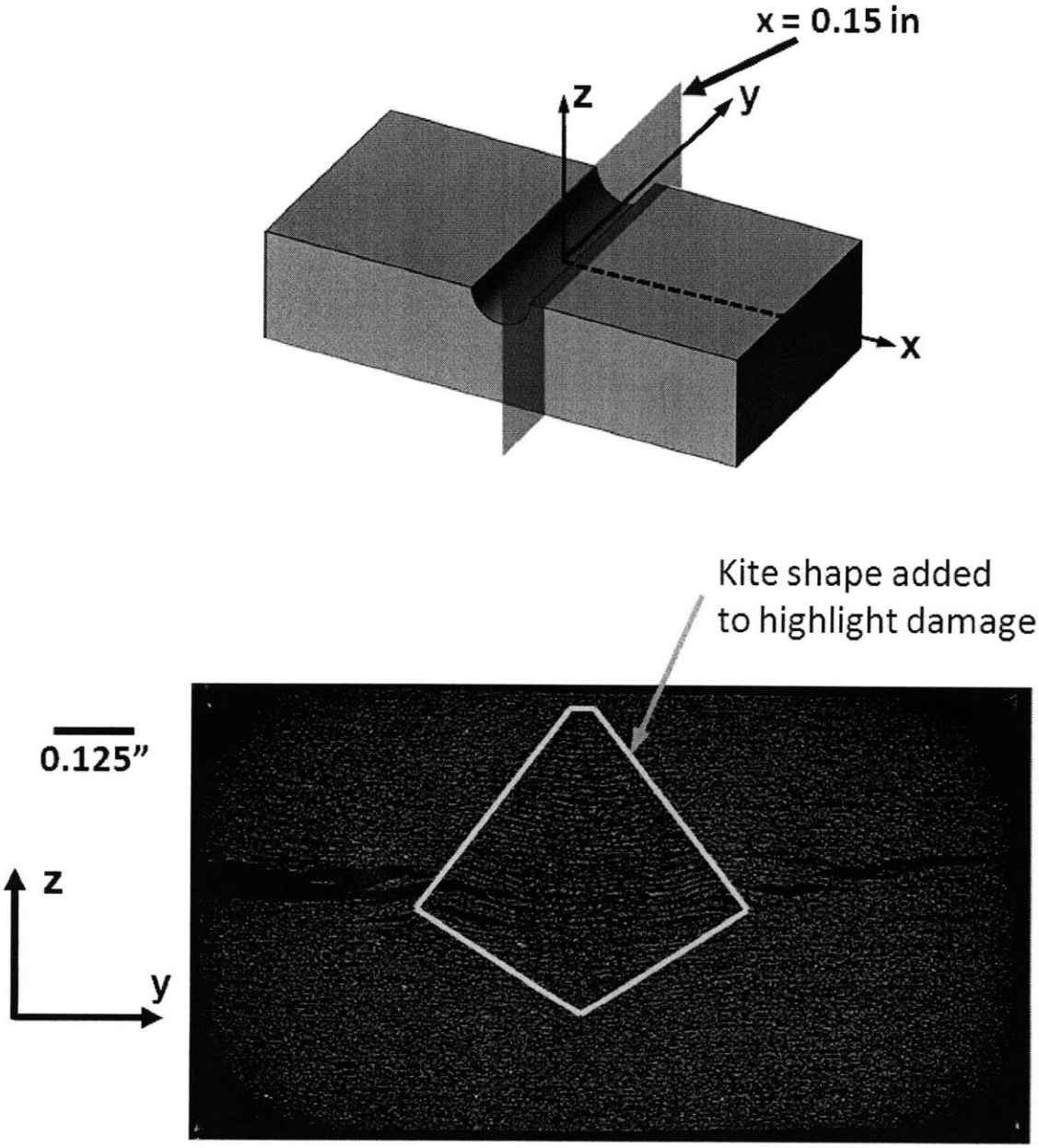

Figure 5.20 "Virtual cut" via computed microtomography of $[\pm 15/0]_{13S}$ Specimen 3 tested to failure in "three-dimensional loading" with (*top*) location of the "virtual cut", 0.15 inches from center of groove, and (*bottom*) actual image with kite-shape superimposed to indicate a region of damage.

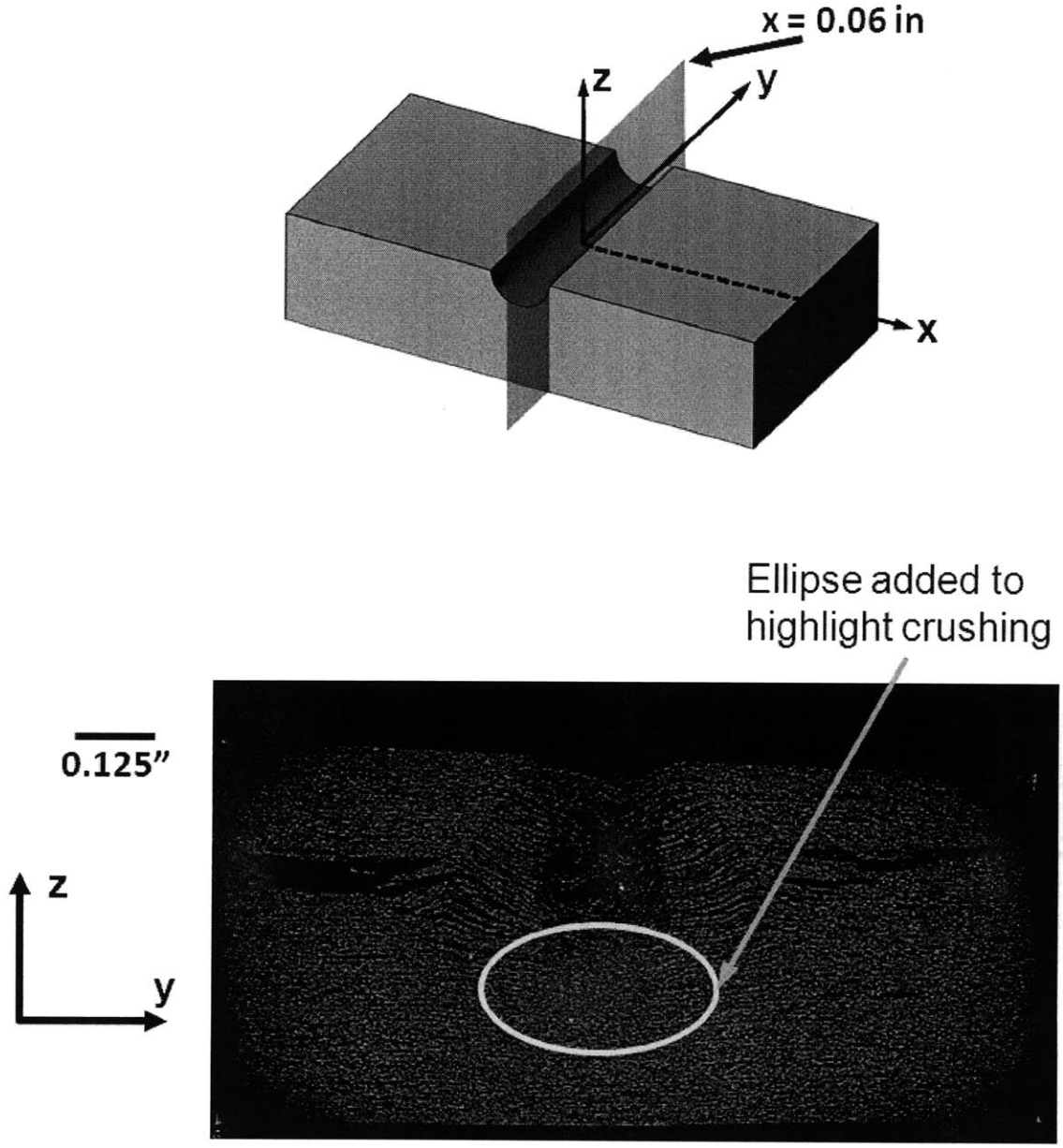

Figure 5.21 "Virtual cut" via computed microtomography of $[\pm 15/0]_{13S}$ Specimen 3 tested to failure in "three-dimensional loading" with (*top*) location of the "virtual cut", 0.006 inches from center of groove, and (*bottom*) actual image with ellipse superimposed to indicate region of crushing.

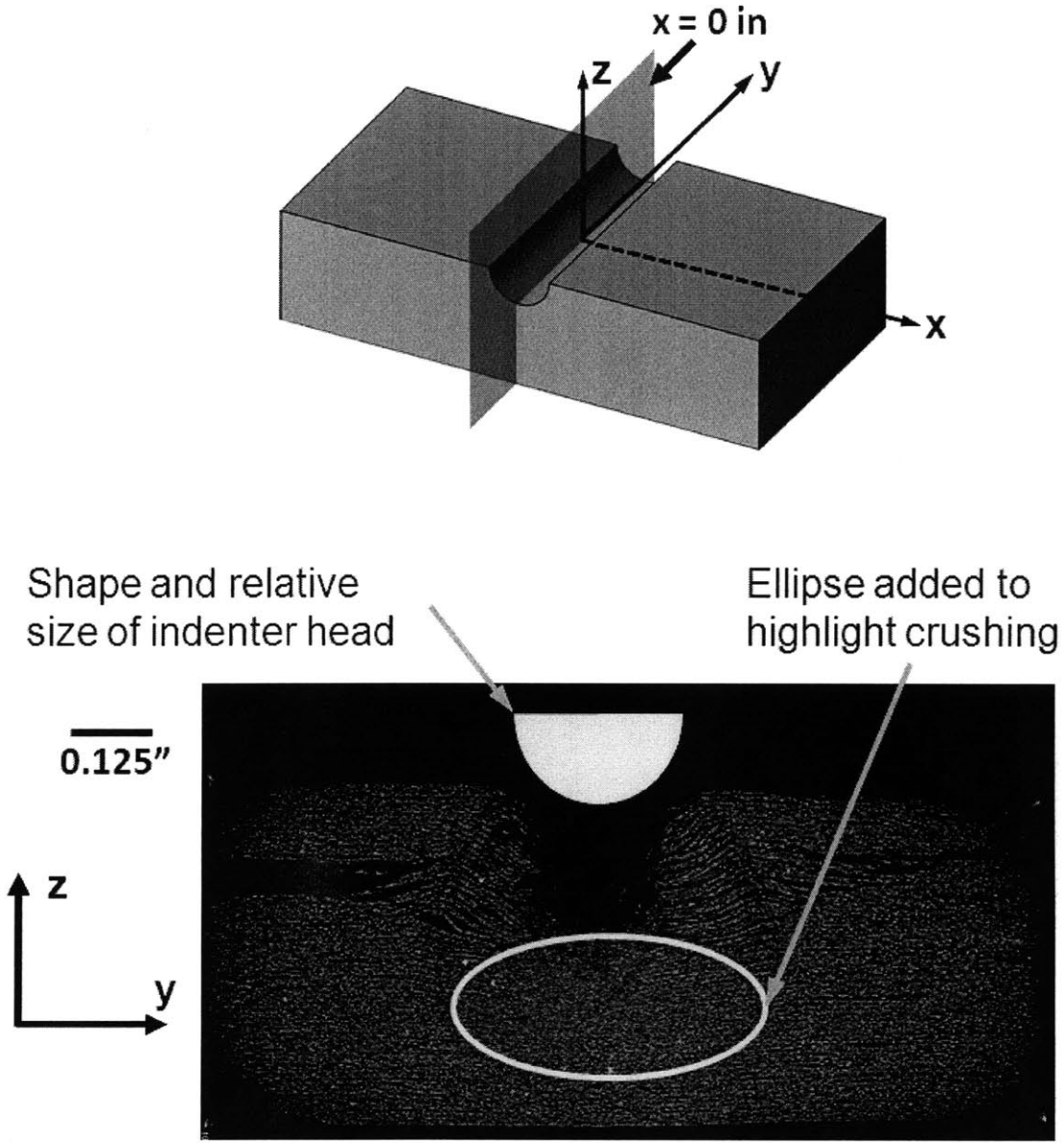

Figure 5.22 "Virtual cut" via computed microtomography of $[\pm 15/0]_{13S}$ Specimen 3 tested to failure in "three-dimensional loading" with (*top*) location of the "virtual cut", at center of groove, and (*bottom*) actual image with ellipse superimposed to indicate region of crushing.

specific region. The original location of evidence of damage in the form of crushing is visible well below the contact point in these virtual reconstructions. In the case of this particular specimen, damage was visible up to 12 plies below the bottom of the groove. This is at a $-60°$ ply, at a z-location of - 0.07 inches, as shown in Figure 5.26 by the lighter area in the center of the "virtual cut". The higher density of this region is indicated by the lighter color of the region, and this area is indicated by the ellipse superimposed on the figure.

Representative cuts for the other laminates are shown in Figures 5.27 to 5.30 and show similar characteristics. Note that a "virtual cut" of $[\pm 45/0]_{13s}$ Specimen 4 is excluded due to poor quality. For example, a dark elongated oval at the bottom of the groove, z = 0 inches, which is similar to the damage seen in Figure 5.24 can be seen in the "virtual cuts" of $[\pm 45/0/90]_{10S}$ Specimen 6 and $[90/0]_{13S}$ Specimen 6, shown in Figures 5.27 and 5.28. Evidence of displaced plies below the bottom of the groove and point of indenter contact can be seen in the "virtual cuts" of $[\pm 30/0]_{13s}$ Specimen 6 and $[\pm 15/0]_{13s}$ Specimen 4, shown in Figures 5.29 and 5.30. These are similar in nature to that shown in Figure 5.25, with fibers of different angles than the base ply at that location evident in a region near the center of those scans.

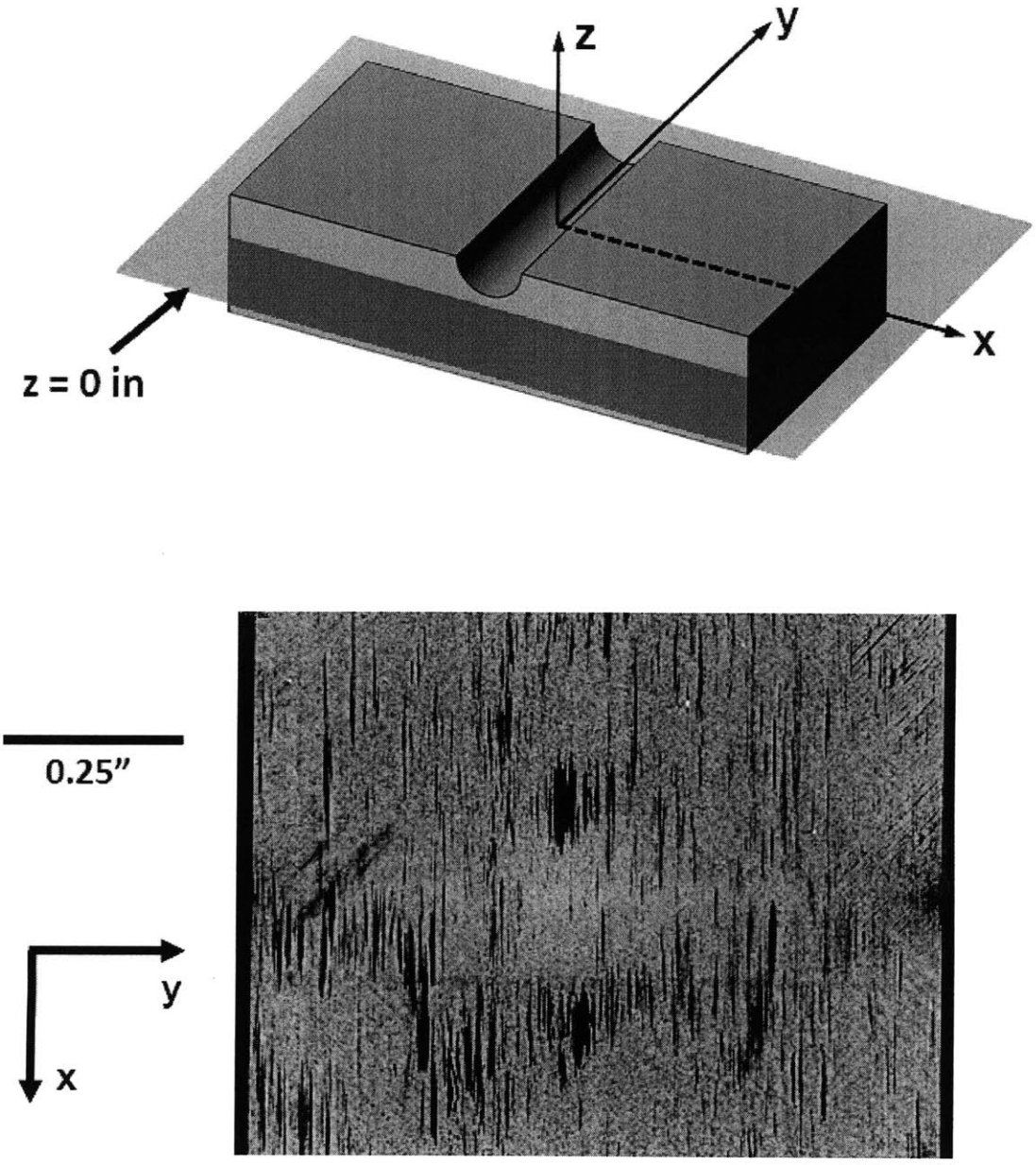

Figure 5.23 "Virtual cut" via computed microtomography of $[\pm 45/0]_{13S}$ Specimen 4 tested to crushing in "two-dimensional loading" with (*top*) location of the "virtual cut", at bottom of groove, and (*bottom*) actual image.

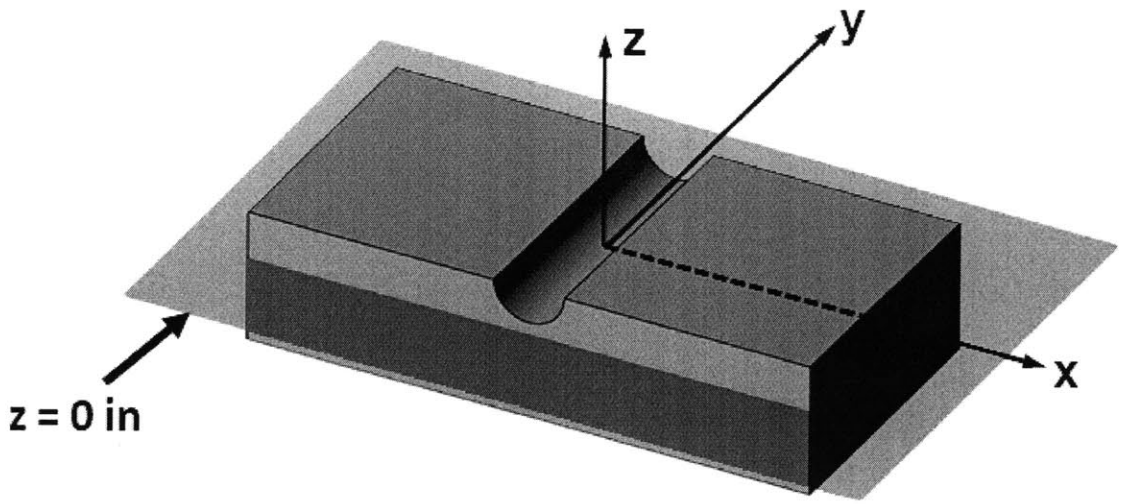

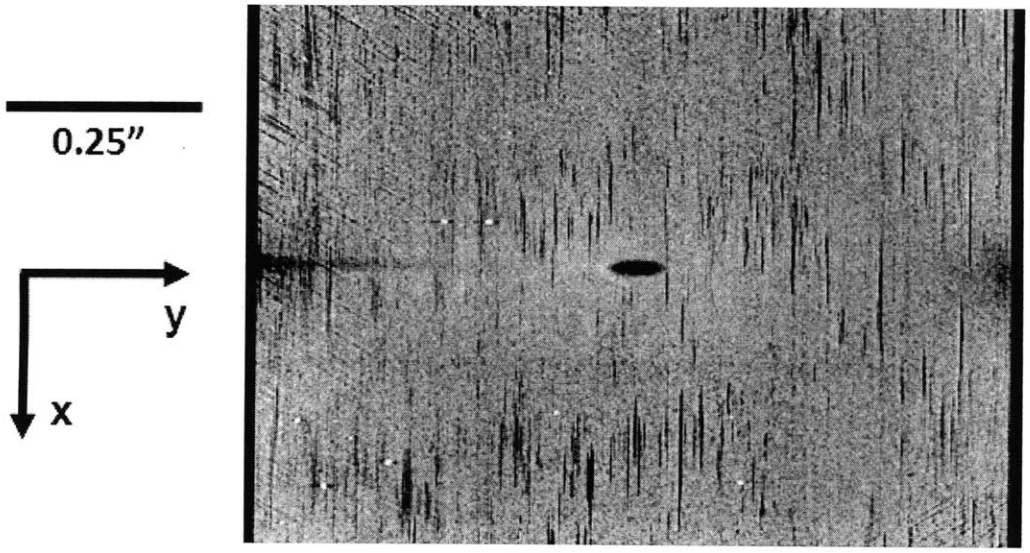

Figure 5.24 "Virtual cut" via computed microtomography of $[\pm 60/0]_{13S}$ Specimen 4 tested to failure in "three-dimensional loading" with (*top*) location of the "virtual cut", at bottom of groove, and (*bottom*) actual image.

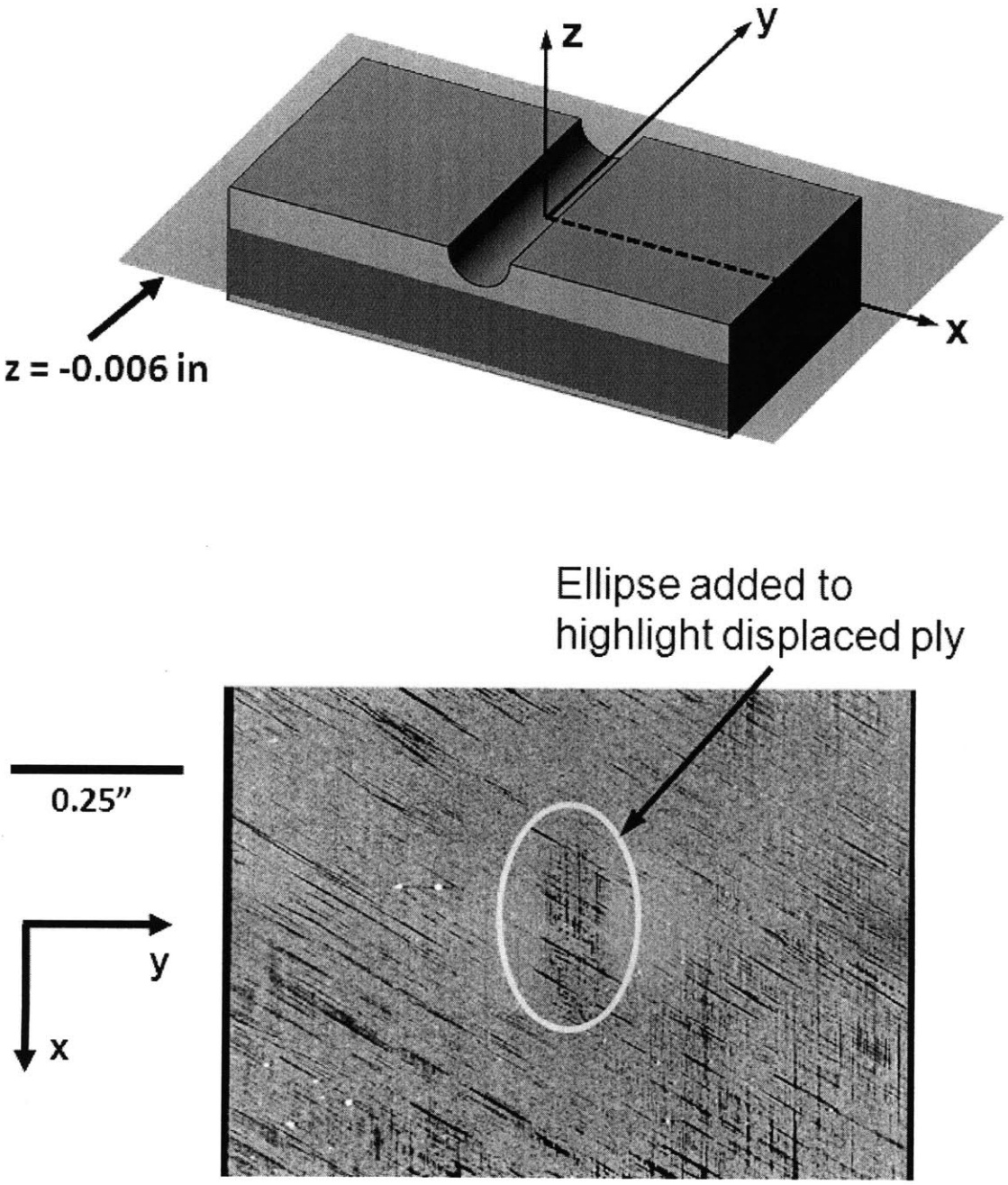

Figure 5.25 "Virtual cut" via computed microtomography of $[\pm 60/0]_{13S}$ Specimen 4 tested to failure in "three-dimensional loading" with (*top*) location of the "virtual cut", 0.006 inches below bottom of groove, and (*bottom*) actual image with ellipse superimposed to indicate region of displaced ply.

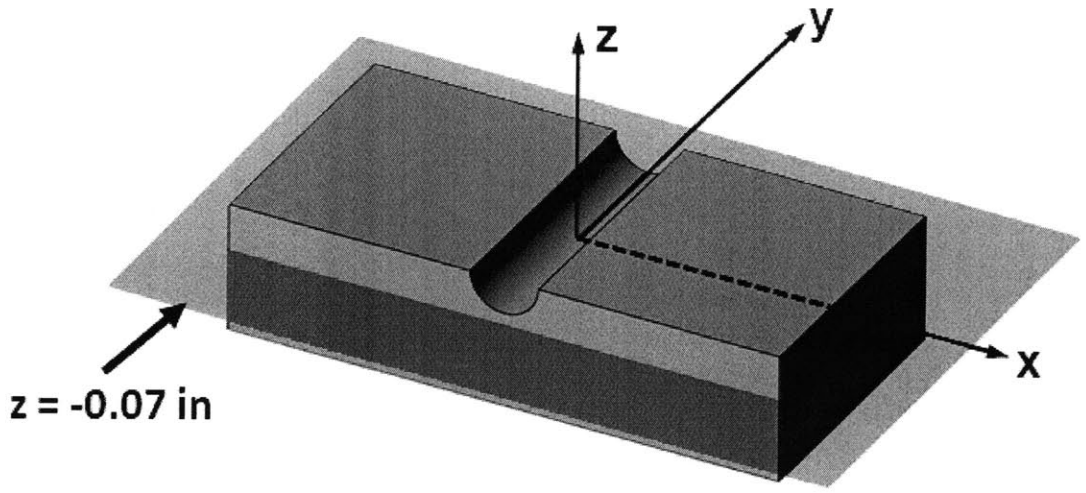

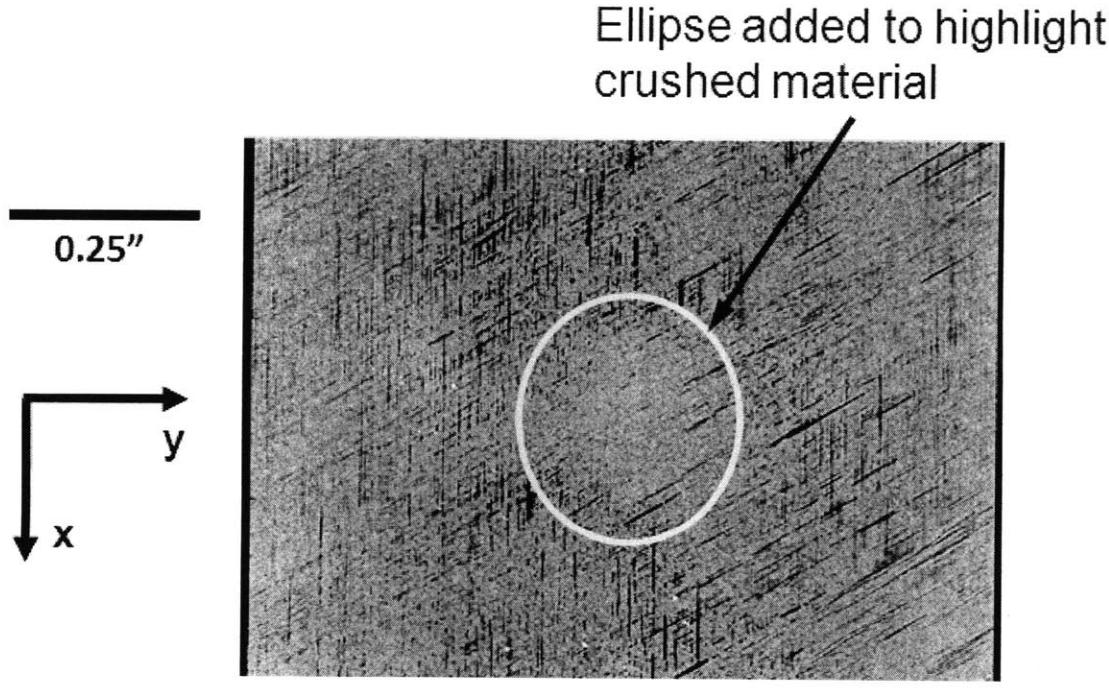

Figure 5.26 "Virtual cut" via computed microtomography of $[\pm 60/0]_{13S}$ Specimen 4 tested to failure in "three-dimensional loading" with (*top*) location of the "virtual cut", 0.07 inches below bottom of groove, and (*bottom*) actual image with ellipse superimposed to indicate region of crushed material.

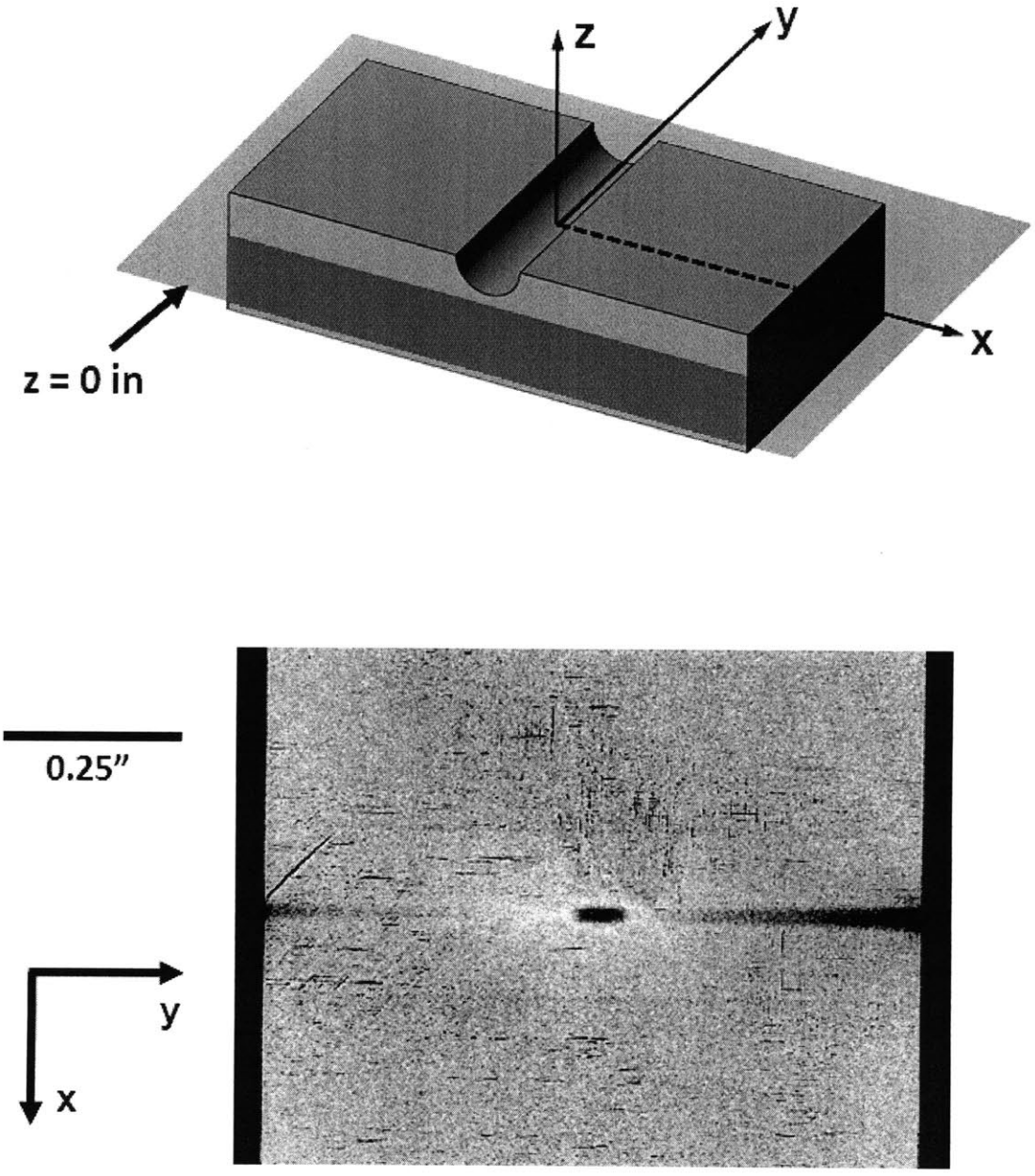

Figure 5.27 "Virtual cut" via computed microtomography of $[\pm 45/0/90]_{10S}$ Specimen 6 tested to failure in "three-dimensional loading" with (*top*) location of the "virtual cut", at bottom of groove, and (*bottom*) actual image.

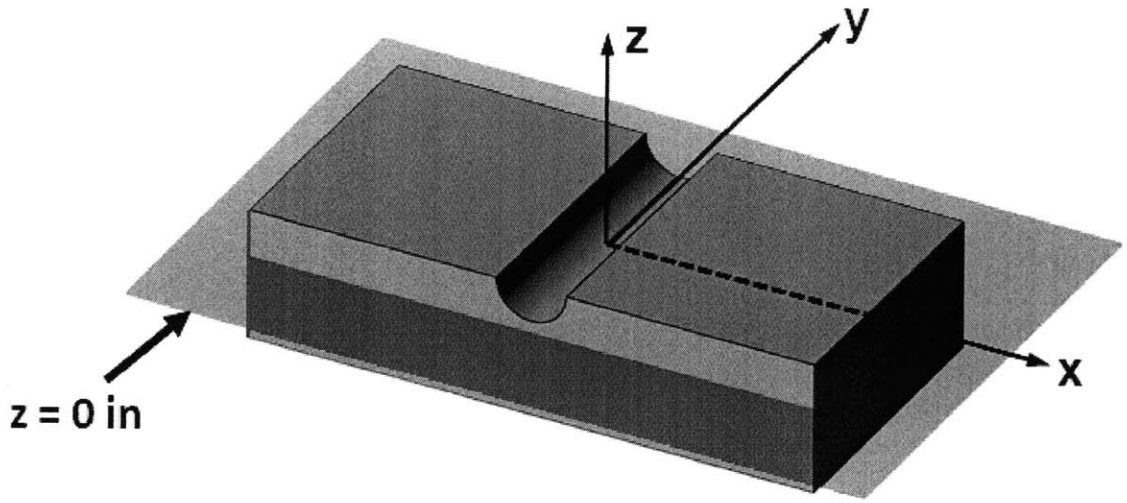

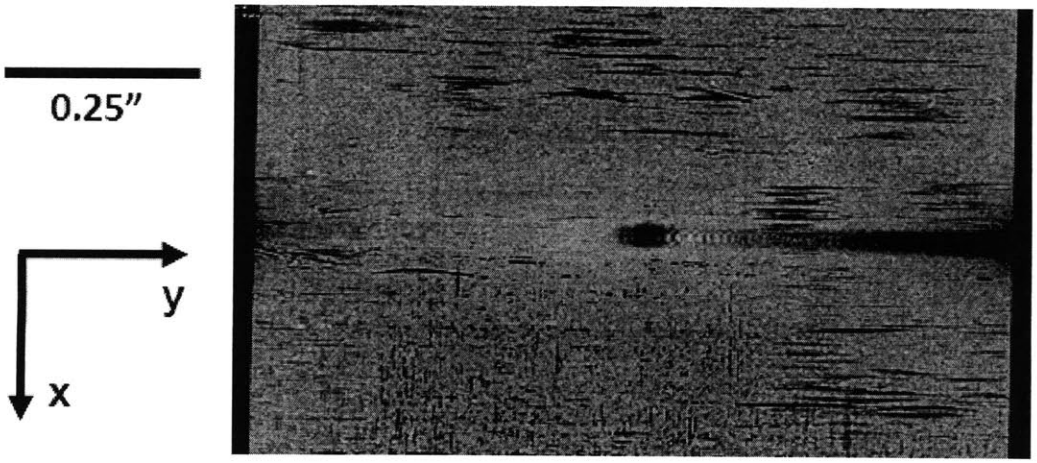

Figure 5.28 "Virtual cut" via computed microtomography of $[90/0]_{20S}$ Specimen 6 tested to failure in "three-dimensional loading" with (*top*) location of the "virtual cut", at bottom of groove, and (*bottom*) actual image.

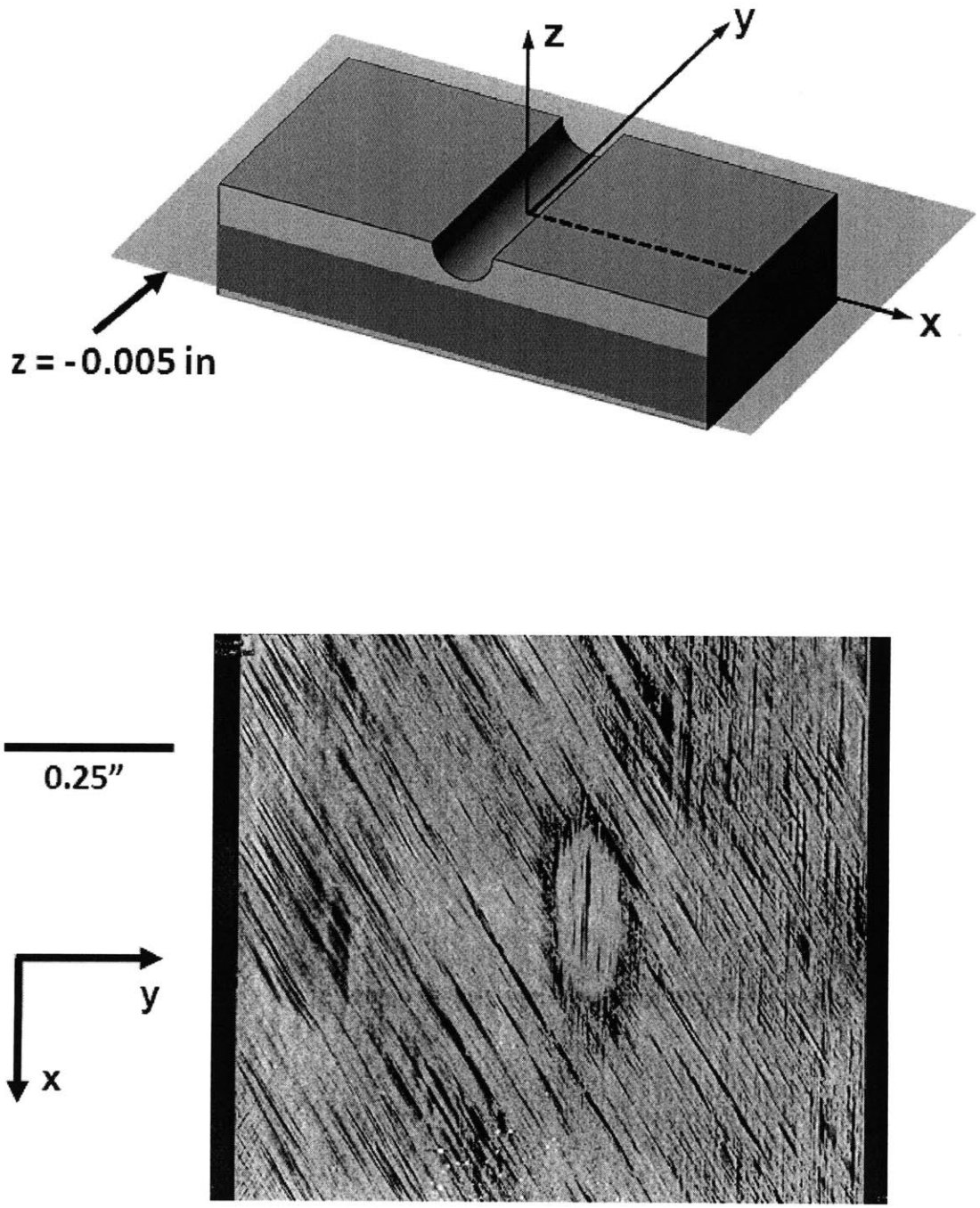

Figure 5.29 “Virtual cut” via computed microtomography of $[\pm 30/0]_{13S}$ Specimen 6 tested to failure in “three-dimensional loading” with (*top*) location of the “virtual cut”, 0.005 inches below the bottom of the groove, and (*bottom*) actual image.

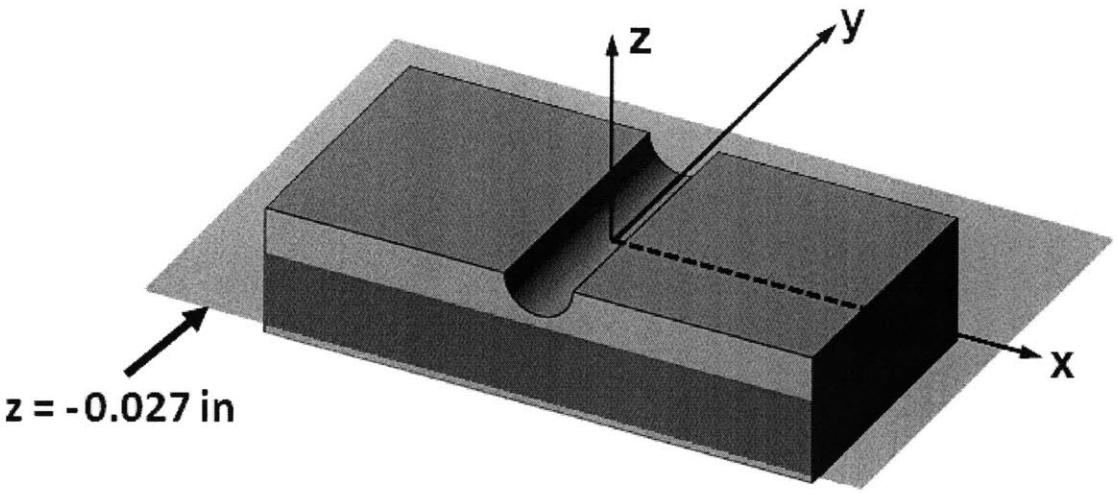

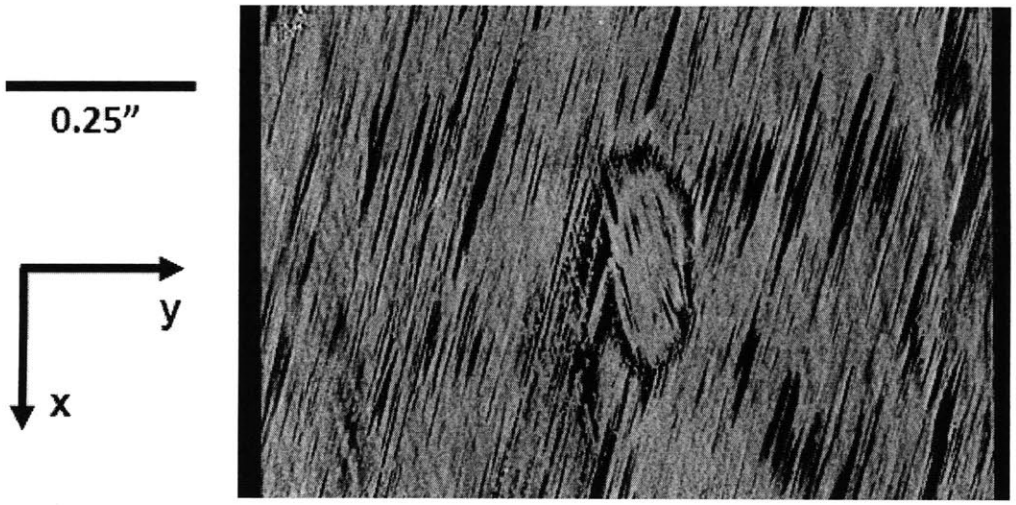

Figure 5.30 "Virtual cut" via computed microtomography of $[\pm 15/0]_{13S}$ Specimen 4 tested to failure in "three-dimensional loading" with (*top*) location of the "virtual cut", 0.027 inches below the bottom of the groove, and (*bottom*) actual image.

Chapter 6

Discussion

There are three main objectives of this work. One is to determine the effects of added complexity in the overall configuration of specimen and indenter as part of the Building Block Approach. This is done by using a "three-dimensional loading" as well as a "two-dimensional loading". The second is to investigate the initial permanent damage and failure behavior. This is done through finding the crushing load, as well as finding the load-stroke response of testing to final failure. Finally, a range of ply angles and different laminate configurations are used to determine the affects of these variables on initial damage and failure behavior. The testing results presented in Chapter 5 are discussed in this chapter in the context of these primary objectives, with the second objective of initial damage and failure behavior discussed in the context of the first objective dealing with the loading conditions. In addition, there is some discussion of the difference between the "two-dimensional loading" and "three-dimensional loading" within the context of the effect of ply angles on the laminate behavior.

6.1 "Two-Dimensional" versus "Three-Dimensional Loading"

The are several key differences observed between the two loading conditions in all parts of the testing. This ranges from the initial crushing behavior to the post-mortem observations. The crushing of the specimens is discussed first as this occurs before the final failure and other behaviors used to compare the loadings in terms of indentation and load. The contrasts of the two loading cases are particularly apparent in the computed microtomography of the crushing specimens. The general pattern of the internal damage can be surmised from the external damage in some cases. However, the exact damage cannot be seen. The microtomography reconstruction allows for determination of the exact nature of the internal damage after testing. In the case of the specimens tested to final failure, the reconstruction allows for better assessment of delaminations, matrix cracking, and fiber fracture, which are the modes of composite damage involved with the failure. In addition, significant compaction of the material in the specimen occurs in the region below the "three-dimensional" indenter for that loading case. This form of damage is highlighted in Figures 5.21 and 5.22.

In the case of the permanent deformation caused by the "three-dimensional loading", most of the damage is not visible from the exterior, but the microtomography reconstruction allows for determination of true extent of the damage caused at the crushing load. In the "virtual cuts" of $[\pm 60/0]_{13S}$ Specimen 4, there is evidence of displaced material from the bottom of the groove, as well as crushing shown by multiple plies in one xy-plane of a specimen. This damage is seen in Figures 5.24 to 5.26. The "virtual cuts" show that the damage can be seen well below the surface. This damage is also within a region without any traditional forms of damage in a composite, namely matrix cracking, fiber fracture, or delamination.

The displacement as a result of crushing with the "two-dimensional loading" was measured with a laser measurement system, as described in Section 4.5. However, when the selected "two-dimensional loading" cases were reconstructed using computed microtomography, damage was not visible in the specimens. This is likely a result of

the location of any potential visible effects of the crushing. In the "three-dimensional loading" case, the evidence of crushing is visible in the area immediately at and below the point of contact of the ball-ended indenter. For the "two-dimensional loading" case, the evidence of crushing should also be visible adjacent and immediately below the point of contact of the indenter. However, the contact is spread along the entire length of the groove. As a result of the distributed contact, the crushing, while measurable, could not be seen with the reconstructions as it is not focused at a specific point of contact as for the ball-ended indenter of the "three-dimensional loading" case.

After ultimate failure, the specimens of each loading case show similarities within a loading case. However, there are significant differences when compared across loading cases. Those specimens of the "two-dimensional loading" case exhibit a failure which initiates approximately at the bottom of the groove, and ultimately leads to at least one delamination over half the specimen, from the groove along an x-direction, until the specimen is in multiple pieces. In contrast, the "three-dimensional loading" specimens show a major delamination, as can be seen in photographs of the specimens as in Figures 5.16 to 5.18. However, this damage does not originate at the original bottom of the groove, but approximately at the same z-location as the indenter reaches, at least in the reconstructed specimen, at the point of contact between the indenter and specimen. The delamination does not originate immediately at the point of contact, but after a region of damage in the xy-plane that is best characterized as crushing as the region is denser, and no other signs of damage are discernible. The location of the initiation of the delamination should be investigated in future work. In the area where the only damage is the delaminataion, i.e. away from the groove and point of contact, the delamination changes ply interfaces for many of the "three-dimensional loading" specimens. In addition, around the load application point of the "three-dimensional loading", the delamination is not continuous from the -x face to the +x face for the entire width of the specimen. In the region near the indenter contact at failure, there are sections of the plies that, after failure, occupy multiple z-locations, as can be seen in Figures 5.20 to 5.22. Along with the denser region of material indicated in the "virtual cuts", the angled plies in the region of

indenter contact, indicate that the crushing in the "three-dimensional loading" cases has a significant impact on the failure behavior.

It is noted that there was no testing that looked at the damage manifestation between initial crushing and final failure. Further work to examine and understand this damage manifestation should be conducted. This could be done by loading a specimen, in either loading case, to a prescribed level, based on findings from this work, and then examining the damage using the computed microtomography technique. To establish an understanding of the damage manifestation, the specimen could be re-loaded, to a higher load, and then reexamined.

From observation of the failed specimens and their overall load-stroke behavior, it is clear that the general behaviors between the different loading types are dissimilar. The "three-dimensional loading" specimens generally show consistent load-stroke shapes across all laminate configurations. This shape is an initial linear region, followed by a knee load and second linear region, which continues to the maximum load. In contrast, the "two-dimensional loading" specimens show several different Behavior Types, which are generally consistent within a laminate, but not for all "two-dimensional loading" specimens. The knee load and second linear region, that occur in all "three-dimensional loading" cases, only occur in some of the "two-dimensional loading" tests. The only behavior that occurs in all specimens for the "two-dimensional loading" is the initial linear region. However, it does not occur in the same load-stroke region for the various laminate configurations. This is indicative of a mechanism causing a change of the behavior between the loading cases.

The crushing that occurs in the "three-dimensional loading" specimens significantly impacts the behavior of these specimens. For the "two-dimensional loading" specimens, the crushing load occurs at approximately the same load as the knee load. This indicates that the accumulation of damage up to this point is related to the change in behavior which manifests itself in the load versus stroke behavior as the knee load. For example, as shown in Figure 5.15, the knee load occurs at 52.4 kN for Specimen 2 of the $[\pm 15/0]_{13S}$ laminate, and the crushing load for this laminate is 50.0 kN. By comparison, the specimens of the "three-dimensional loading" show the

knee load at approximately the same value of 20.6 kN, but each laminate has a significantly lower crushing load, where the largest crushing load is 14.0 kN. Furthermore, specimens which do not exhibit a knee load in the "two-dimensional loading" do still reach a point of meàsurable crushing. Thus, there is some additional damage that occurs that may lead to the existence of a knee load, although this damage mechanism has not yet been identified. This behavior is likely related to the ply angles in the laminate and is discussed in Section 6.2.

The behavior at the time of final failure varies across the loadings, where the "two-dimensional loading" specimens generally show a sudden load drop, and the "three-dimensional specimens" primarily show a degradation of the load-carrying capability. This behavior is shown in Figures 5.1 to 5.7 and 5.10 to 5.15. The "two-dimensional loading" specimens generally display a sudden loss of load-carrying capability, associated with a complete delamination of the laminate of at least half of the length of the specimen. The "three-dimensional loading" specimens, in general, show a slower degradation of the load-carrying capability. This may be due to the densification below the load application in this loading case, as well as the ability for minor damages to occur as the specimen is no longer able to carry additional load. The "three-dimensional loading" load-carrying degradation should be closer to representative of the behavior of the eventual application of this work. A study with multiple ball bearings in the groove should be conducted as part of the Building Block Approach by adding complexity to determine the effects of interacting contact points.

6.2 Effects of Ply Angles

Overall, the "three-dimensional loading" specimen responses showed a consistent general load-stroke response, from a linear region to a knee load to a second linear region. This indicates that the local loading, via ball-ended indenter, has a significant impact on the overall load-stroke response and failure of the laminate. For the "two-dimensional loading" specimens, there are several Behavior Types exhibited, and in this case there is a distributed loading from a cylinder along the length of the

groove. This indicates that for the case with the load distributed across a greater area, the details of the specimen, especially the laminate configuration, have a significant impact on the load-stroke response and failure.

Each of the laminates can be considered to have an overall "mesh" of angles that affects indentation resistance. The quasi-isotropic laminate has the largest number of plies at different angles and also has the angles between these plies with the smallest difference. For the $[\pm\theta/0]_{13S}$ laminates, the "mesh" decreases with values of the ply angles at $+\theta$ and $-\theta$. This definition of "mesh" is also related to the "ply angle mismatch", defined as the net angle between fiber directions in adjacent plies, with 90° as a maximum value. Laminate behavior is subsequently discussed in terms of these definitions of "mesh" and "ply angle mismatch".

In the "three-dimensional loading case", as the laminates go from quasi-isotropic and cross-ply and then from $[\pm 60/0]_{13S}$ to $[\pm 15/0]_{13S}$ with decreasing values of θ, there is a decrease in resistance to indentation. This is shown in Table 5.10 in that the initial linear slopes decrease in the same order. The slopes indicate that the 90° plies play a significant role in the ability of the laminate to resist indentation. It is not clear if it is that these plies are aligned with the groove or that they are perpendicular to the 0° fibers and therefore create a "mesh", which leads to this indentation resistance. Work should be done to examine different laminate configurations to determine which causes the change in indentation resistance.

The decrease in load from initial to second linear region is also related to ply angles and laminate configuration. Overall, the quasi-isotropic laminate has the greatest initial and second slope, and the least percentage decrease in slope from initial to second linear regions. By contrast, the cross-ply laminate and $[\pm 60/0]_{13S}$ have the greatest percentage loss of load-per-stroke capability. This indicates that the tighter "meshing" also contributes to prevention of degradation of load-per-stroke capability.

For the "two-dimensional loading" specimens, there were four Behavior Types exhibited, as described in Section 5.1. Within a laminate, the Behavior Type exhibited was consistent across the specimens. In addition, these different Behavior Types are related to other characteristic behaviors. Within the quasi-isotropic laminate speci-

mens, all the specimens which exhibit Behavior Type A reach a maximum load below 110 kN. All specimens which exhibit Behavior Type B reach a maximum load greater than 125 kN. For all of these quasi-isotropic specimens subject to "two-dimensional loading", the bottom of the groove is in precisely the same ply [34]. This indicates that there is some unidentified detail of the initial contact and crushing damage which has a significant impact on the overall behavior and maximum load before ultimate failure.

In previous work, Kobayashi defined two Failure Modes exhibited by specimens tested in "two-dimensional loading" [34]. The current work shows agreement between the Failure Modes defined by Kobayashi and the Behavior Types for quasi-isotropic specimens subject to "two-dimensional loading": specimens exhibiting Behavior Type A exhibited Failure Mode A, a delamination emanating from the bottom of the groove, and specimens exhibiting Behavior Type B exhibited Failure Mode B, which is transverse damage from the groove leading to delamination. Within these laminates, Behavior Type and Failure Mode are related to the magnitude of the maximum load, in that the maximum load for Behavior Type A is less than 110 kN and for Behavior Type B is greater than 125 kN.

Two laminates showed no variability in Behavior Type: the cross-ply laminate and the $[\pm 15/0]_{13S}$ laminate, which exhibited Behavior Types C and D, respectively. The cross-ply laminate has the greatest ply angle mismatch, while the $[\pm 15/0]_{13S}$ has the least. There is evidence that Behavior Type D lead to Failure Mode B, as the cross-ply specimens all showed this type of failure, although the maximum load for these specimens showed substantial variation, unlike the quasi-isotropic specimens. The $[\pm 15/0]_{13S}$ specimens all exhibited Failure Mode A. Based on the data in Table 5.2, there does not appear to be a direct correlation between Behavior Type and maximum load for the non-quasi-isotropic specimens.

In this work, the $[\pm 30/0]_{13S}$ specimens exhibited Behavior Types C and A, but in previous work, specimens of this laminate exhibited only Behavior Type C [34]. This would indicate that Behavior Type C is the typical behavior of this laminate, and that there was an additional, as-yet-unknown, variable at play in the recent work.

The $[\pm 45/0]_{13S}$ laminate is considered an intermediate, or "bridging", case in regard to "mesh" and "ply angle mismatch", due to its fiber orientation compared to that of the other laminates. It exhibits all four Behavior Types, while characteristics such as maximum load and slope of the initial linear region are generally uniform. Behavior Type D generally occurs in the laminates with greater "ply angle mismatch", while C occurs in those with less "ply angle mismatch" which are closer to unidirectional; the $[\pm 45/0]_{13S}$ laminate shows both Behavior Types. The correlation between behavior type and angle is due to the differing orientation of fibers to groove, with the cross-ply and $[\pm 60/0]_{13S}$ laminates having fibers relatively more parallel to the groove, and the $[\pm 15/0]_{13S}$ and $[\pm 30/0]_{13S}$ laminates having less of a "mesh", with the fibers being relatively more perpendicular to the groove.

The effect of the "mesh" and "ply angle mismatch" should be further investigated by testing additional laminates. In particular, laminates of a $[\pm\theta]_{20S}$ should be tested under both loading cases. A $[\pm 45]_{20S}$ laminate would have the same "mesh" and "ply angle mismatch" as the cross-ply case, but may have a different load-stroke response, which would indicate that there is an additional variable related to the angle of the fibers from the groove.

Chapter 7

Conclusions and Recommendations

The use of carbon fiber composite structures has been limited to relatively simple structures, and primarily in-plane loadings. This investigation examines the response of a composite specimen subjected to out-of-plane loading, and focuses on a structure with the added detail of a groove. The transverse loading is applied in this groove, in an effort to understand the response of a grooved composite specimen subjected to two different loading configurations. The effect of adding complexity was investigated by testing with "two-dimensional loading" and "three-dimensional loading" configurations. A study on the initial damage was conducted, as well as testing to final failure. The effect of different laminate configurations was also examined.

The conclusions that can be drawn from this study are:

1. The responses of the "two-dimensional loading" and "three-dimensional loading" specimens are generally dissimilar, from the initial crushing displacement to the final failure response. The specimen geometry after ultimate failure is also dissimilar.

2. Significant crushing occurs in the "three-dimensional loading" case, whereas there is not as much evidence of displaced material, indicative of crushing, in the "two-dimensional loading" case. This indicates that the crushing in the "three-dimensional loading" case is a primary contributor to the difference in the behavior between the two loading cases.

3. The crushing of the "three-dimensional loading" specimens is localized due to the contact of the ball-ended indenter. As a result, the damage is visible with the microtomography reconstruction and "virtual cuts". The distribution along the length of the groove of the "two-dimensional loading" case results in the crushing not being visible in the "virtual cuts", although the crushing is measurable with the laser system.

4. The load-stroke response of the specimens across laminates is generally consistent in the "three-dimensional loading" case, whereas there are four different load-stroke responses for the "two-dimensional loading" specimens, generally consistent within a laminate. This indicates that the specifics of the laminate have a larger influence on the response for the "two-dimensional loading" case, whereas the loading, and resultant crushing, has a more significant impact for the "three-dimensional loading" case.

5. In the "three-dimensional loading" configuration, the indentation resistance is related to the "mesh" created by the different ply angles in the laminate, and the 90° plies, along with the "ply angle mismatch". In addition, the laminate configuration with the tightest "mesh", that is the greatest "ply angle mismatch", is, overall, the most resistant to indentation.

6. The "ply angle mismatch" of a laminate generally leads to certain Behavior Types, where the laminates closer to unidirectional generally exhibit Behavior Type C, which includes a knee load, and those that are cross-ply show Behavior Type D, which includes a reverse knee load. The laminates between these configurations, such as the quasi-isotropic laminate, generally show Behavior Types A and B, which include both a knee load and reverse knee load, a summation of Behavior Types C and D.

7. The laminate which exhibited all Behavior Types, the $[\pm 45/0]_{13S}$, has fiber directions away from the 0° which "bridge" the other θ fiber directions, and as a result, the laminate bridges the Behavior Types. In addition, this has a

"mesh" which is in the middle of the range of tightest to loosest.

Based on the results of this investigation, recommendations for further research include:

1. Damage manifestation testing should be conducted to understand the response of the configuration between initial deformation and final failure. This could utilize techniques included in this work, by testing a specimen to a certain load and examining the damage using computed microtomography. Behaviors to examine include the location and initiation of the major delamination which occurs in the "three-dimensional loading" case.

2. Further testing of the laminate configurations tested here, and additional laminate configurations, should be conducted to determine how much variability there is in the behavior of a single laminate. This will affect the ability to predict behavior of a given configuration of laminate and load applicator.

3. The response of the additional laminate configuration of $[\pm\theta]_{20S}$ should be investigated in an effort to understand the effect of "ply angle mismatch" versus relative fiber direction to the orientation of the groove. For example, the cross-ply laminate and a $[\pm 45]_{20S}$ laminate have the same "ply angle mismatch" but may have very different load-stroke responses due to the different ply orientation relative to the groove.

4. The experimental work conducted to date has examined load application perpendicular to the xy-plane of the laminate within which the fibers run. The behavior with a load applied at an angle to the xy-plane should be investigated to understand how partial in-plane loading affects the response.

5. The work to-date has considered only two loads: the "two-dimensional loading" which is a uniformly distributed load, and the "three-dimensional loading" which is representative of a single ball bearing in the groove. Additional work should study the effect of multiple ball bearings in the groove and its effect on the response of the grooved composite.

6. Finite element analysis of the configurations should be employed to understand the different behaviors shown, and lead to an understanding of the damage manifestation.

References

[1] CompositesWorld.com. Aviation Outlook: Composite Aerostructures in General Aviation, June 2008. http://www.compositesworld.com/articles/aviation-outlook-composite-aerostructures-in-general-aviation.

[2] M. Hinton, A. Kaddour and P. Soden. A Comparison of the Predictive Capabilities of Current Failure Theories for Composite Laminates, Judged Against Experimental Evidence. *Composites Science and Technology*, 64:1725–1797, 2002.

[3] CompositesWorld.com. Boeing Sets Pace for Composite Usage in Large Civil Aircraft, 2005. http://www.compositesworld.com/hpc/issues/2005/May/865.

[4] P. Lagace, J. Williamson, P. Tsang, E. Wolf and S. Thomas. A Preliminary Proposition for a Test Method to Measure (Impact) Damage Resistance. *Journal of Reinforced Plastics and Composites*, 12:584–601, 1993.

[5] W. Jackson and Jr. C. Poe. The Use of Impact Force as a Scale Parameter for the Impact Response of Composite Laminates. *Journal of Composite Technology and Research*, 15(4):282–289, 1993.

[6] Y. Kwon and B. Sankar. Indentatio-Flexure and Low-Velocity Impact Damange in Graphite Epoxy Laminates. *Journal of Composites Technology and Research*, 15(2):101–111, 1993.

[7] B. Sarh. "Telescopic wing". U.S. Patent 4,824,053, April 1989.

[8] B. Sahr. Advanced Flying Automobile, 2008. http://www.afaco.com.

[9] United States Air Force. RQ-4 Global Hawk, November 2009. http://www.af.mil/information/factsheets/factsheet.asp?id=13225.

[10] Composite Materials Handbook 17 (CMH-17-3F). *Polmer Matrix Composites: Materials Usage, Design, and Analysis.* Volume 3F, Chapter 4, June 2002.

[11] S. Abrate. Impact on Laminated Composite Materials. *Applied Mechanics Review*, 44(4):155–190, 1991.

[12] S. Abrate. Impact on Laminated Composite Materials: Recent Advances. *Applied Mechanics Review*, 47(11):517–544, 1994.

[13] ASTM D7136/D7136M - 07. *Standard Test Method for Measuring the Damage Resistance of a Fiber-Reinforced Polymer-Matrix Composite to a Drop-Weight Impact Event.* American Society for Testing and Materials, 2007.

[14] G. Schoeppner and S. Abrate. Delamination Threshold Loads for Low Velocity Impact on Composite Laminates. *Composites: Part A*, 31:903–915, 2000.

[15] F. Yang and W. Cantwell. Impact Damage Initiation in Composite Materials. *Composites Science and Technology*, 70:336–342, 2010.

[16] S. Khalili, R. Mittal and N. Panah. Analysis of Fiber Reinforced Composite Plates Subjected to Transverse Impact in the Presence of Initial Stresses. *Composite Structures*, 77(2):263–268, 2007.

[17] N. Rilo and L. Ferreira. Experimental Study of Low-Velocity Impacts on Glass-Epoxy Laminated Composite Plates. *International Journal of Mechanics and Materials in Design*, 4:291–300, 2008.

[18] B. Lascoup, Z. Aboura, K. Khelili and M. Benzeggagh. Impact Response of Three-Dimensional Stitched Sandwich Composite. *Composite Structures*, 92(2):347–353, 2010.

[19] ASTM D6264/D6264M - 07. *Standard Test Method for Measuring the Damage Resistance of a Fiber-Reinforced Polymer-Matrix Composite to a Concentrated Quasi-Static Indentation Force.* American Society for Testing and Materials, 2007.

[20] G. Caprino, A. Langella and V. Lopresto. Elastic Behaviour of Circular Composite Plates Transversely Loaded at the Centre. *Composites: Part A*, 33:1191–1197, 2002.

[21] H. Hertz. Uber die Beruhrung fester Elastischer Korper. *Journal Reine Angle Mathematik*, 92:156–171, 1882.

[22] S. Yang and C. Sun. Indentation Law for Composite Laminates. *Composite Materials: Testing and Design*, STP 787:425–449, 1982.

[23] T. Tan and C. Sun. Use of Statical Indentation Laws in the Impact Analysis of Laminated Composite Plates. *Journal of Applied Mechanics*, 52:6–12, 1985.

[24] D. Cairns and P. Lagace. Thick Composite Plates Subjected to Lateral Loading. *Journal of Applied Mechanics*, 54:611–616, 1987.

[25] E. Wu and K. Shyu. Response of Composite Laminates to Contact Loads and Relationship to Low Velocity Impact. *Journal of Composite Materials*, 27:1443–1464, 1993.

[26] P. Mahajan. Contact Behavior of an Orthotropic Laminated Beam Indented by a Rigid Cylinder. *Composites Science and Technology*, 58:503–513, 1998.

[27] K. Varadi, Z. Neder, J. Flock, and K. Friedrich. Numerical and Experimental Contact Analysis of a Steel Ball Indented into a Fibre Reinforced Polymer Composite Material. *Journal of Materials Science*, 33:841–851, 1998.

[28] Y. Aoki, H. Suemasu, and T. Ishikawa. Damage Propagation in CFRP Laminates Subjected to Low Velocity Impact and Static Indentation. *Advanced Composite Materials*, 16(1):45–61, 2007.

[29] C. Bastien. "Response of a Grooved Plate Subjected to Out-of-Plane Contact Loading". S.M. Thesis, September 2008.

[30] C. Bastien and P. Lagace. Response of Grooved Laminated Plates to Out-of-Plane Contact Loading. In *Proceedings of the 50th AIAA/ASME/ASCE/AHS/ASC Structures, Structural Dynamics and Materials Conference*, Palm Springs, CA, 2009.

[31] G. Montay, O. Sciot, X. Gong, A. Cherouat, and J. Lu. Determination of the residual stresses in composite laminate using the compliance method. In *Proceedings of the 7th International Conference on Residual Stresses (ICRS-7)*, pages 533–538, Materials Science Forum, 2005.

[32] C. Hoppel, T. Bogetti, and J. J.W. Gillespie. Devices for transmitting high shear loads in composite structures. In *Proceedings of the American Society for Composites Eleventh Technical Conference*, pages 437–446, American Society for Composites, 1996.

[33] T. Bogetti and C. Hoppel. "Composite Structure for Transmitting High Shear Load". U.S. Patent 6,535,272, June 1997.

[34] Y. Kobyashi. "Establishment of an Experimental Method for a Grooved Composite Subjected to Out-of-Plane Contact Loading". S.M. Thesis, September 2009.

[35] ASTM D2344/D2344M - 0. *Standard Test Method for Short-Beam Strength of Polymer Matrix Composite Materials and Their Laminates.* American Society for Testing and Materials, 2000.

[36] F. Holler D. Skoog and S. Crouch. *Principles of Instrumental Analysis.* Brooks Cole, sixth edition, 2007.

Appendix A

Load-Stroke Response Data for Failure Specimens

The load versus indenter displacement plots for all specimens tested to failure (as discussed in Chapter 5) are presented in this appendix. Plots for the "two-dimensional loading" configuration are first presented, followed by plots for the "three-dimensional loading" configuration. The testing procedures are those discussed in Chapter 4. Data for all specimens presented here were tested until failure.

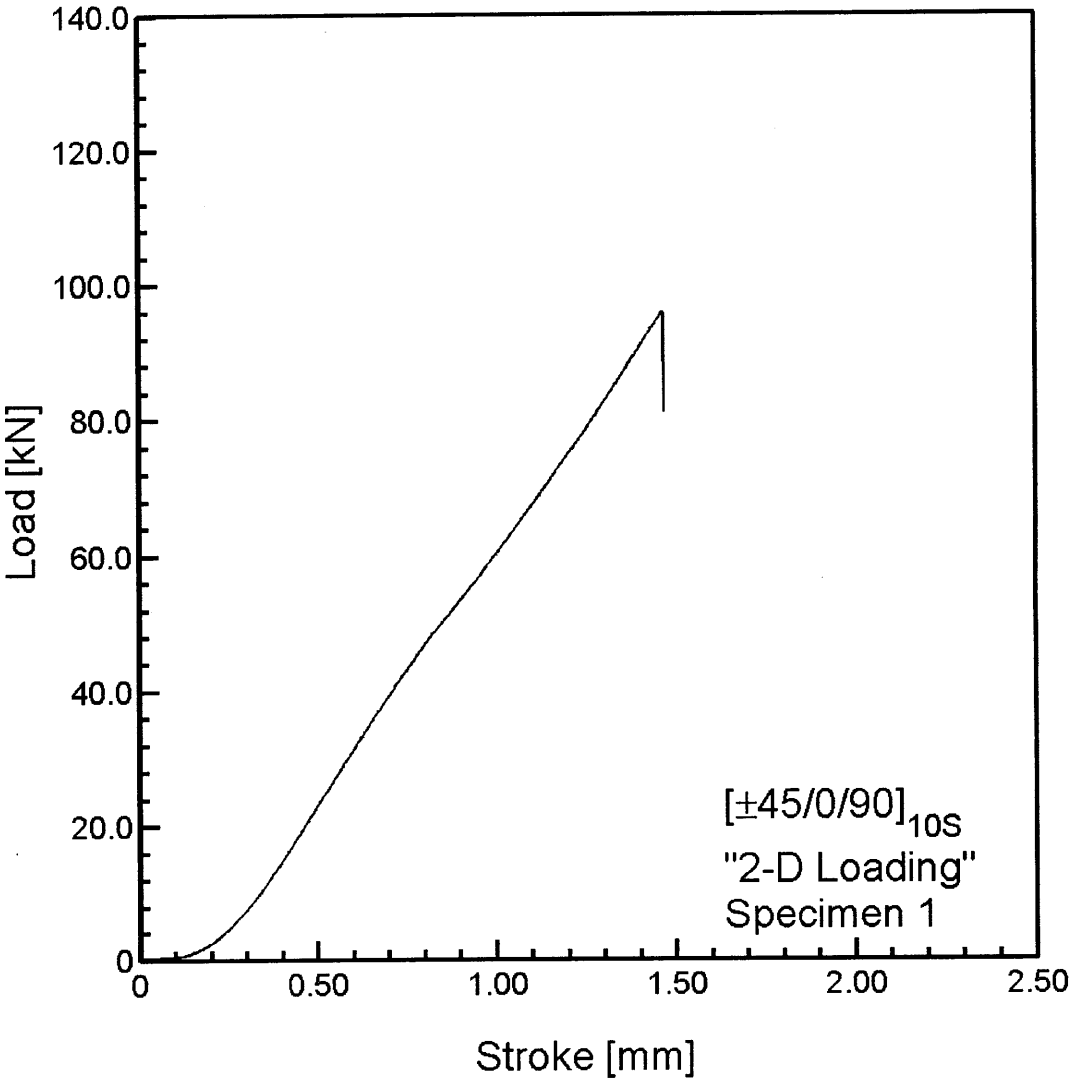

Figure A.1 Load versus stroke for $[\pm 45/0/90]_{10S}$ Specimen 1, from previous work [34], tested to failure in "two-dimensional loading".

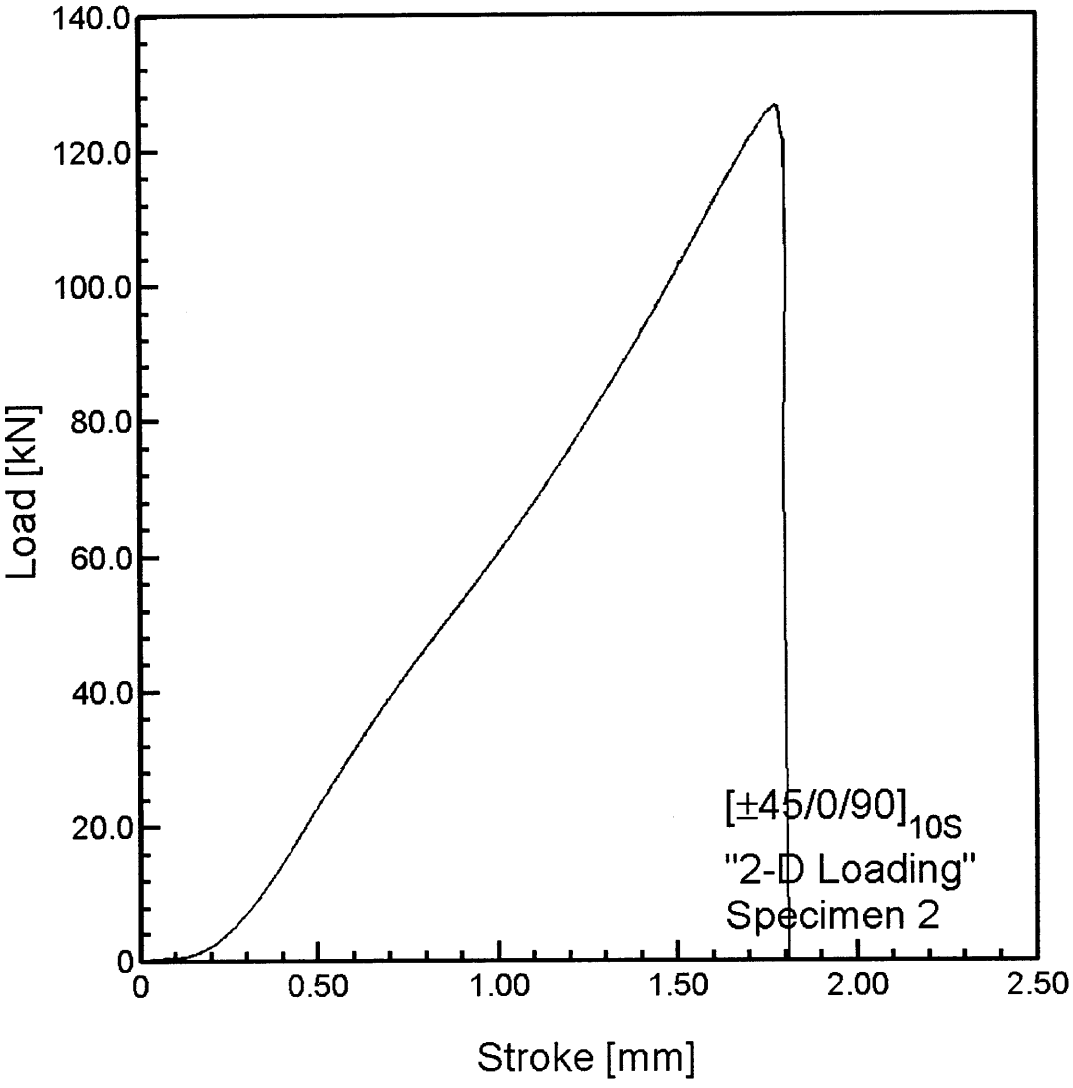

Figure A.2 Load versus stroke for $[\pm 45/0/90]_{10S}$ Specimen 2, from previous work [34], tested to failure in "two-dimensional loading".

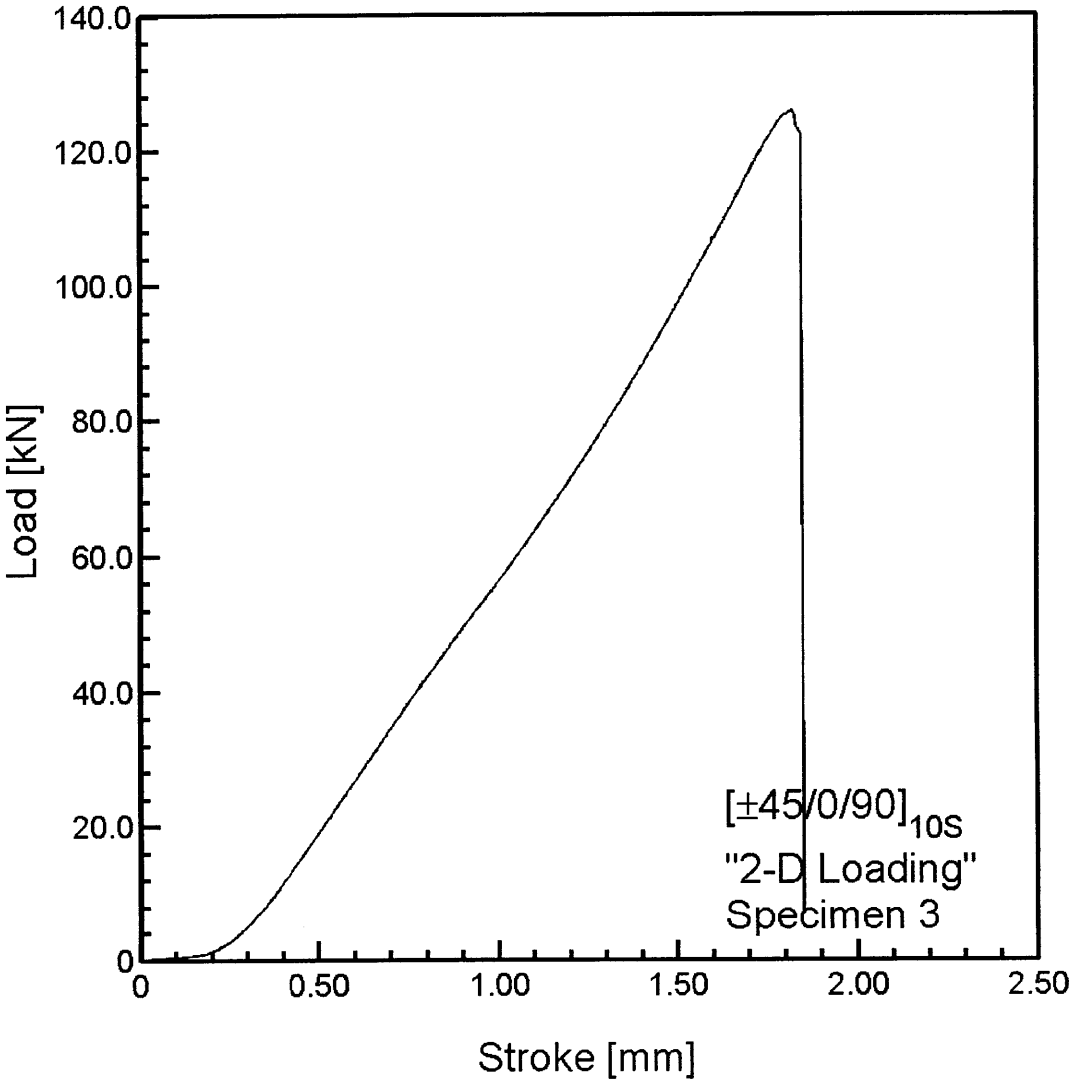

Figure A.3 Load versus stroke for $[\pm 45/0/90]_{10S}$ Specimen 3, from previous work [34], tested to failure in "two-dimensional loading".

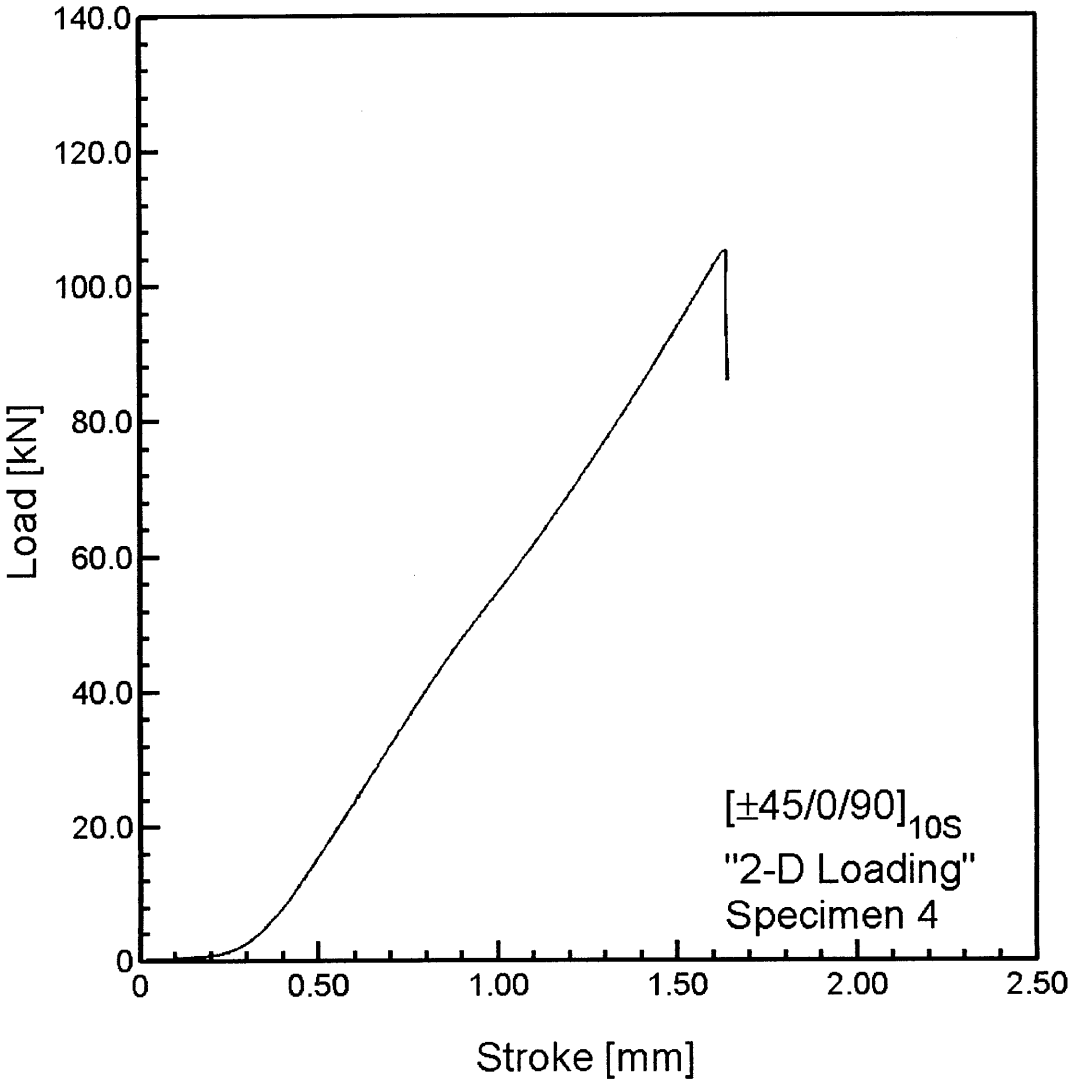

Figure A.4 Load versus stroke for $[\pm 45/0/90]_{10S}$ Specimen 4, from previous work [34], tested to failure in "two-dimensional loading".

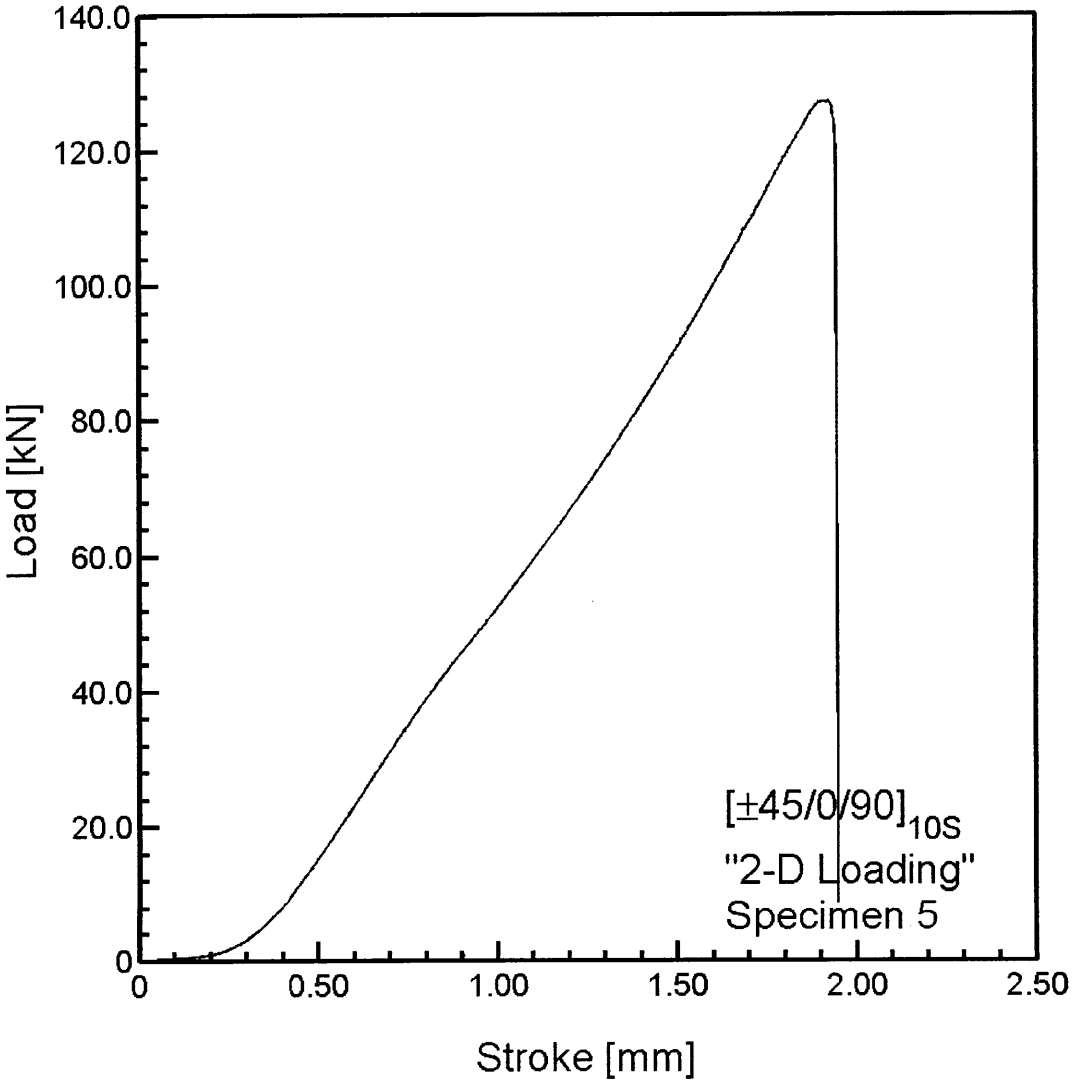

Figure A.5 Load versus stroke for $[\pm 45/0/90]_{10S}$ Specimen 5, from previous work [34], tested to failure in "two-dimensional loading".

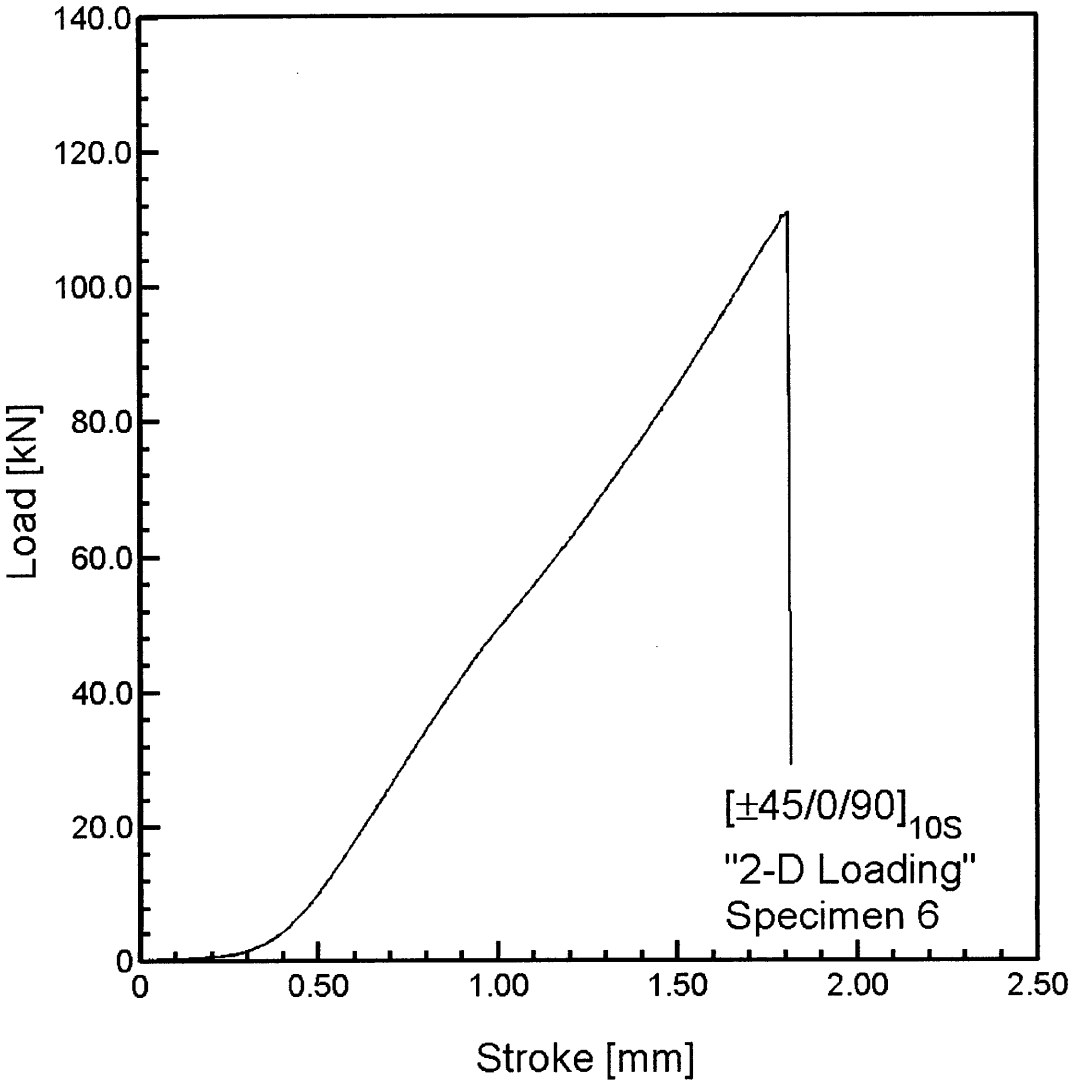

Figure A.6 Load versus stroke for $[\pm 45/0/90]_{10S}$ Specimen 6, from previous work [34], tested to failure in "two-dimensional loading".

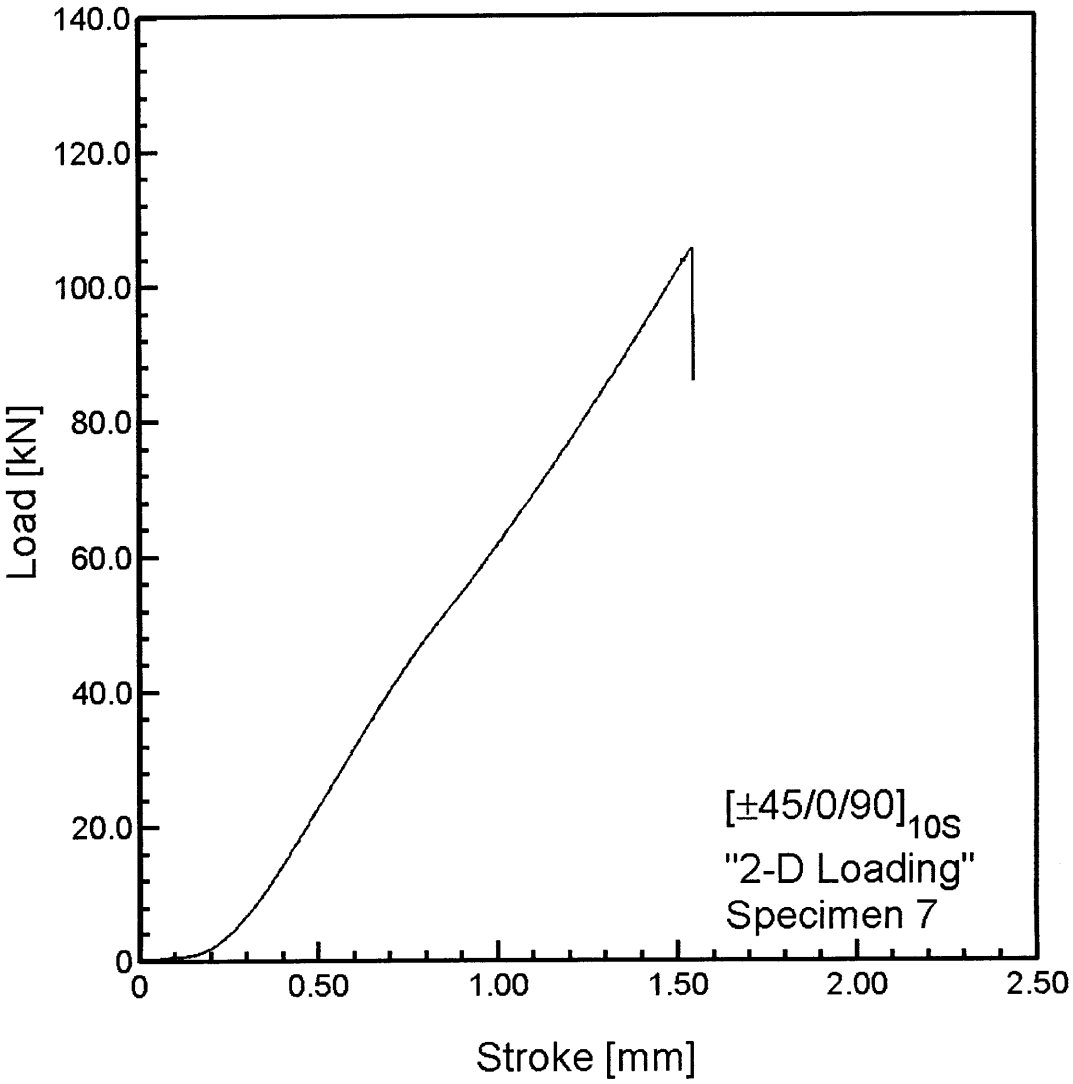

Figure A.7 Load versus stroke for $[\pm 45/0/90]_{10S}$ Specimen 7, from previous work [34], tested to failure in "two-dimensional loading".

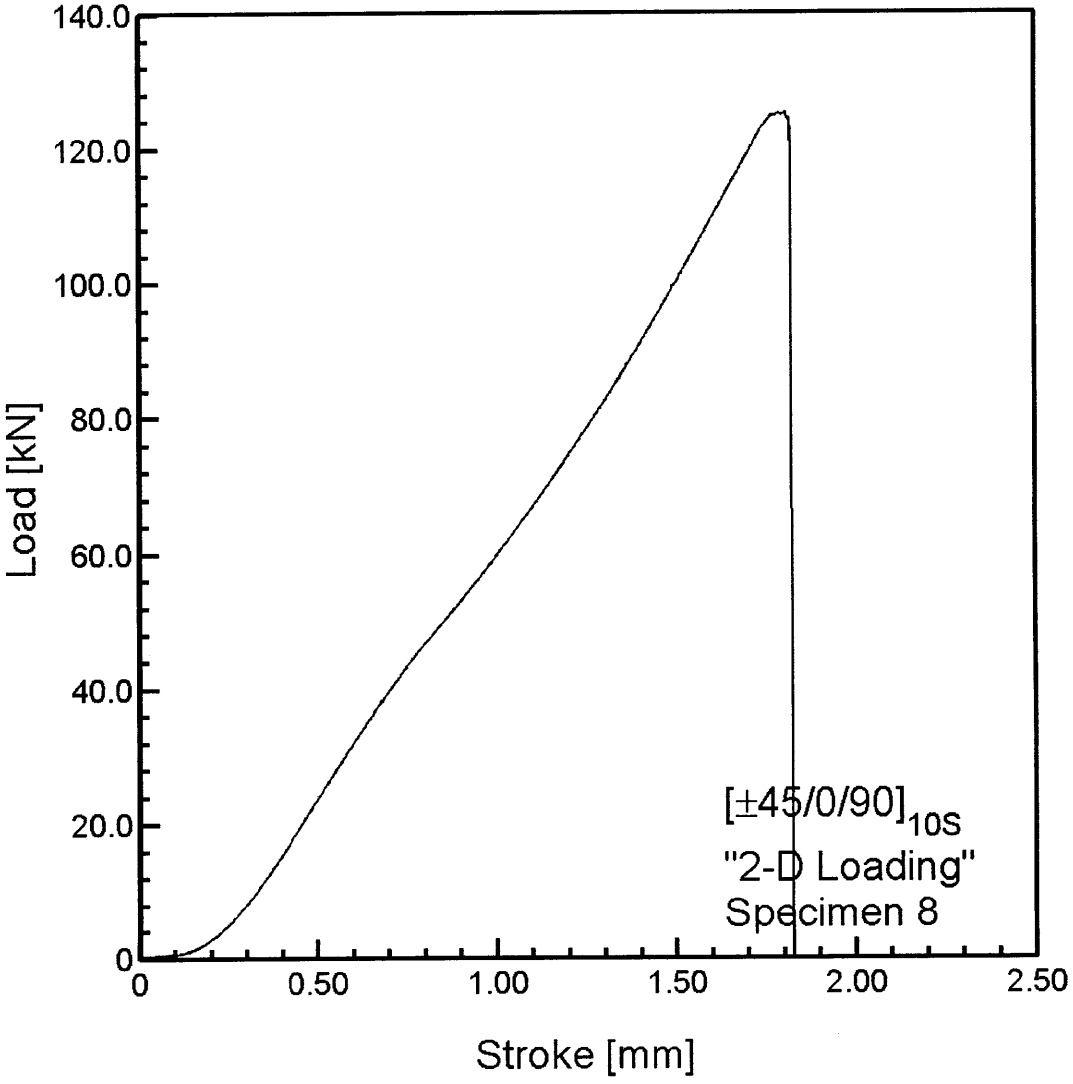

Figure A.8 Load versus stroke for $[\pm 45/0/90]_{10S}$ Specimen 8, from previous work [34], tested to failure in "two-dimensional loading".

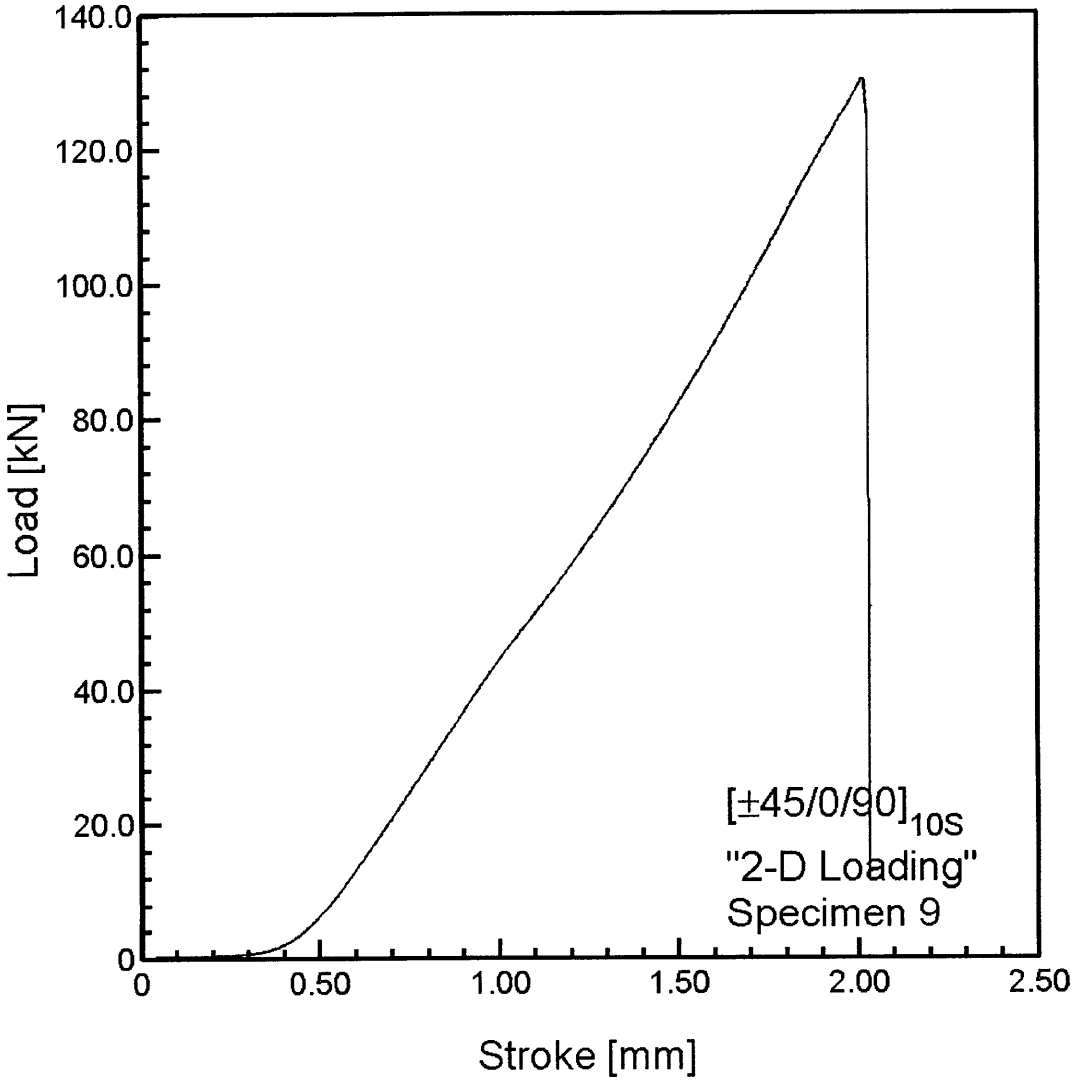

Figure A.9 Load versus stroke for $[\pm 45/0/90]_{10S}$ Specimen 9, from previous work [34], tested to failure in "two-dimensional loading".

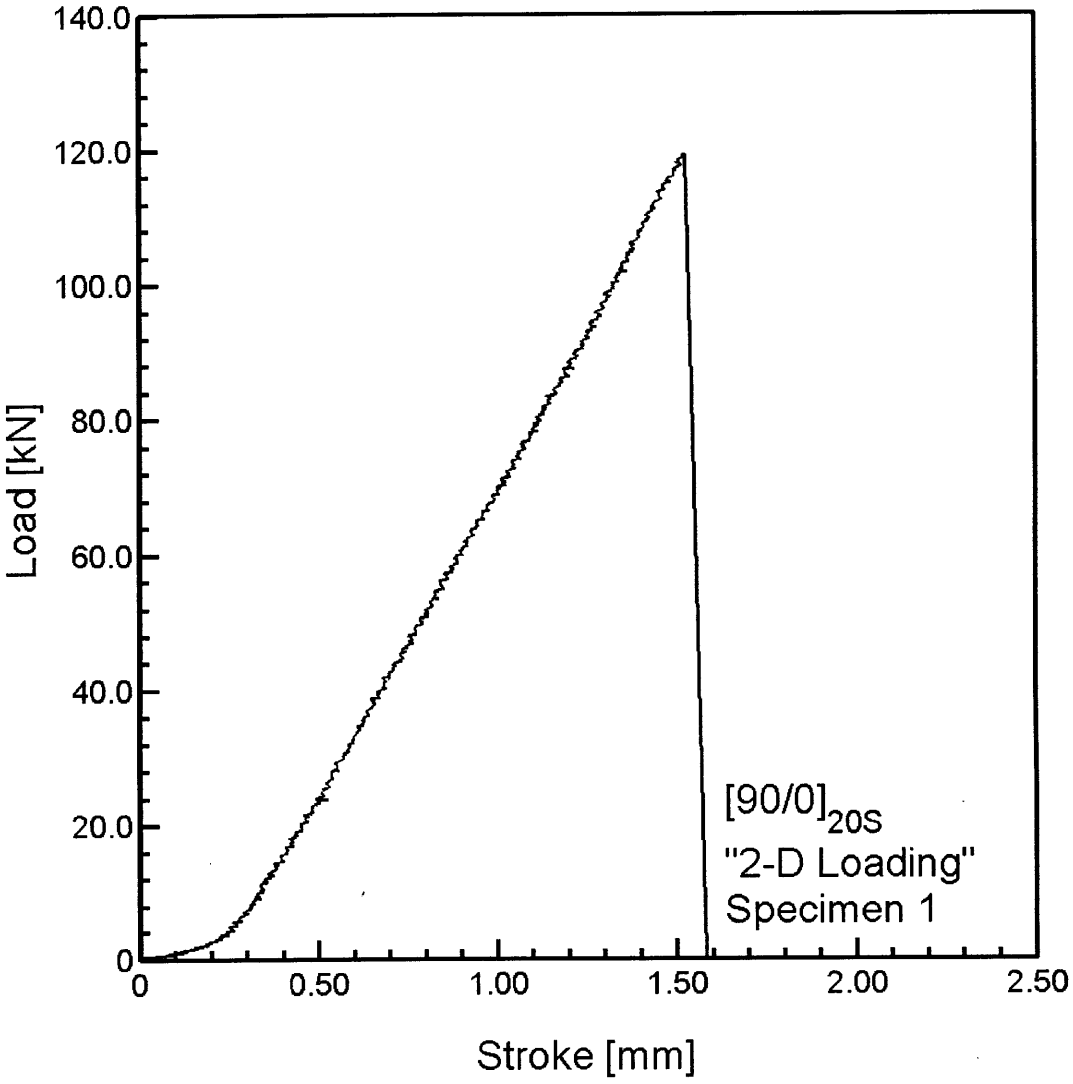

Figure A.10 Load versus stroke for $[90/0]_{20S}$ Specimen 1 tested to failure in "two-dimensional loading".

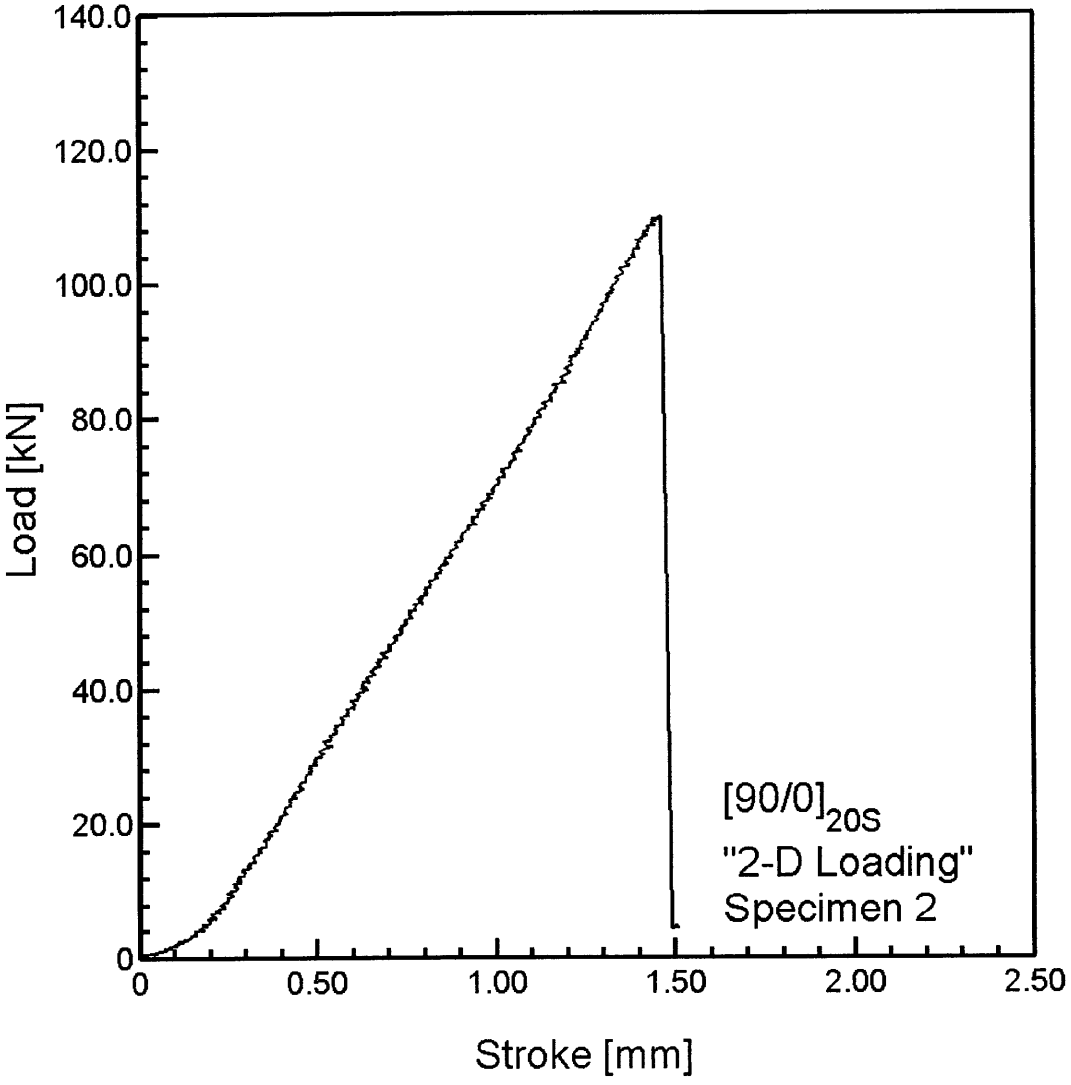

Figure A.11 Load versus stroke for $[90/0]_{20S}$ Specimen 2 tested to failure in "two-dimensional loading".

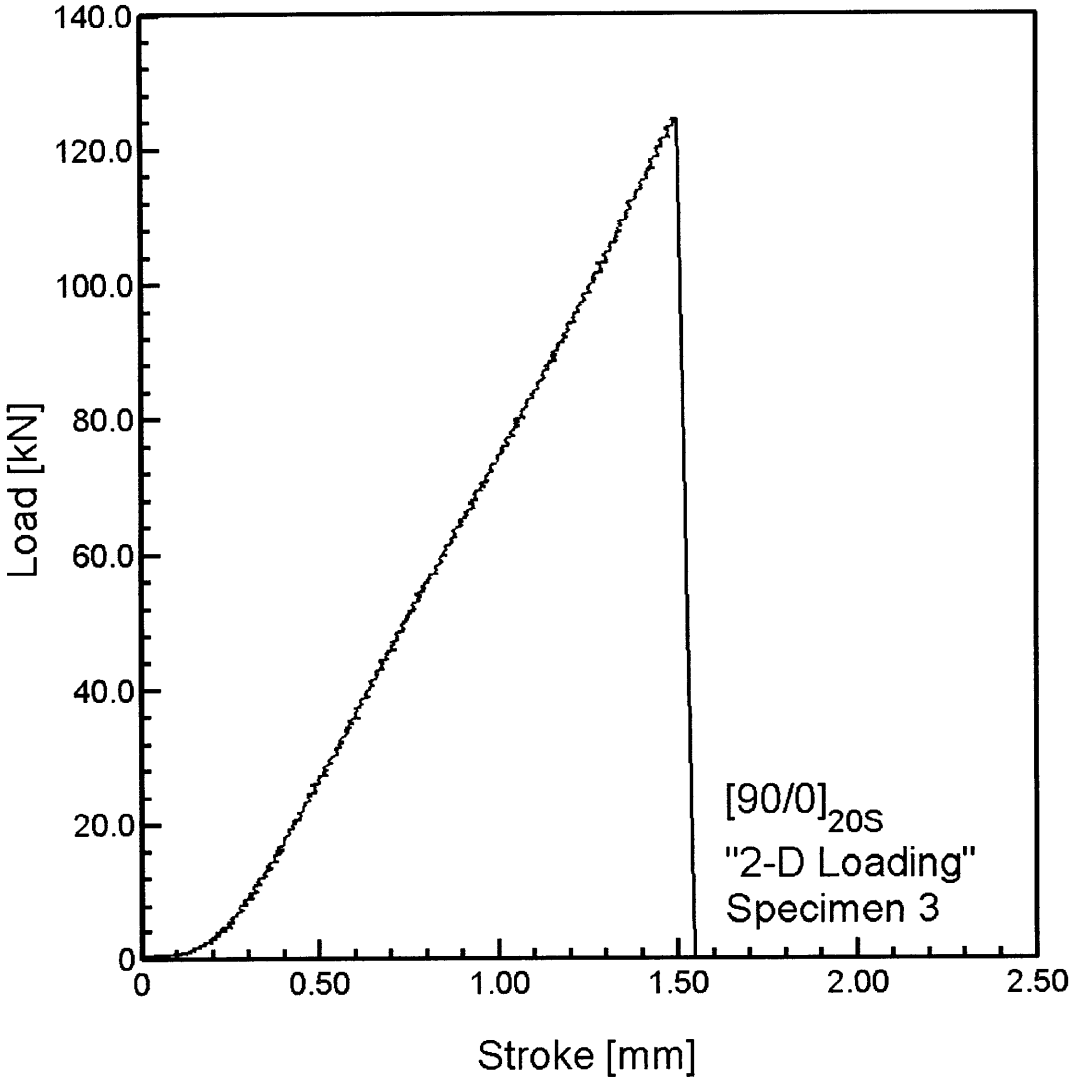

Figure A.12 Load versus stroke for $[90/0]_{20S}$ Specimen 3 tested to failure in "two-dimensional loading".

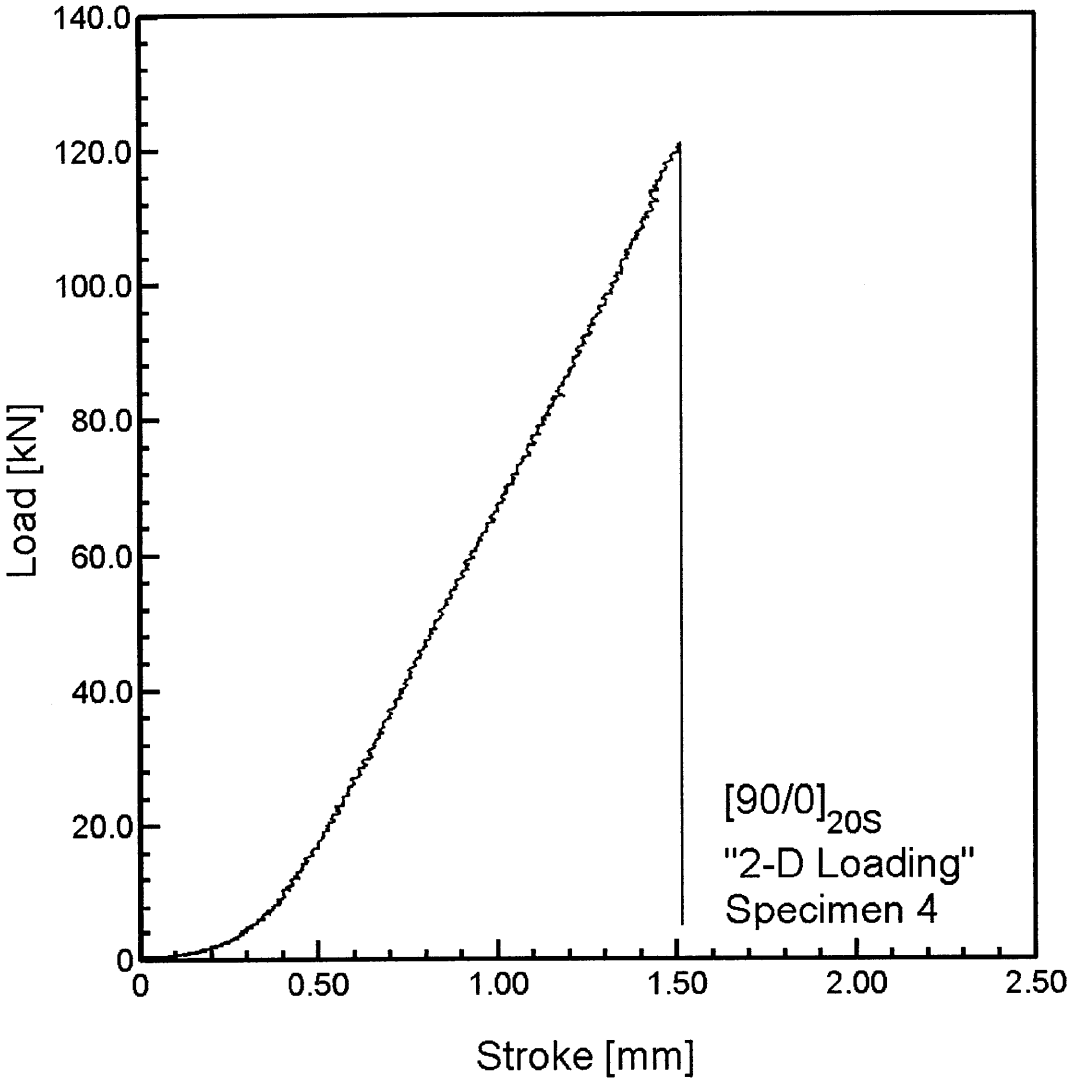

Figure A.13 Load versus stroke for $[90/0]_{20S}$ Specimen 4 tested to failure in "two-dimensional loading".

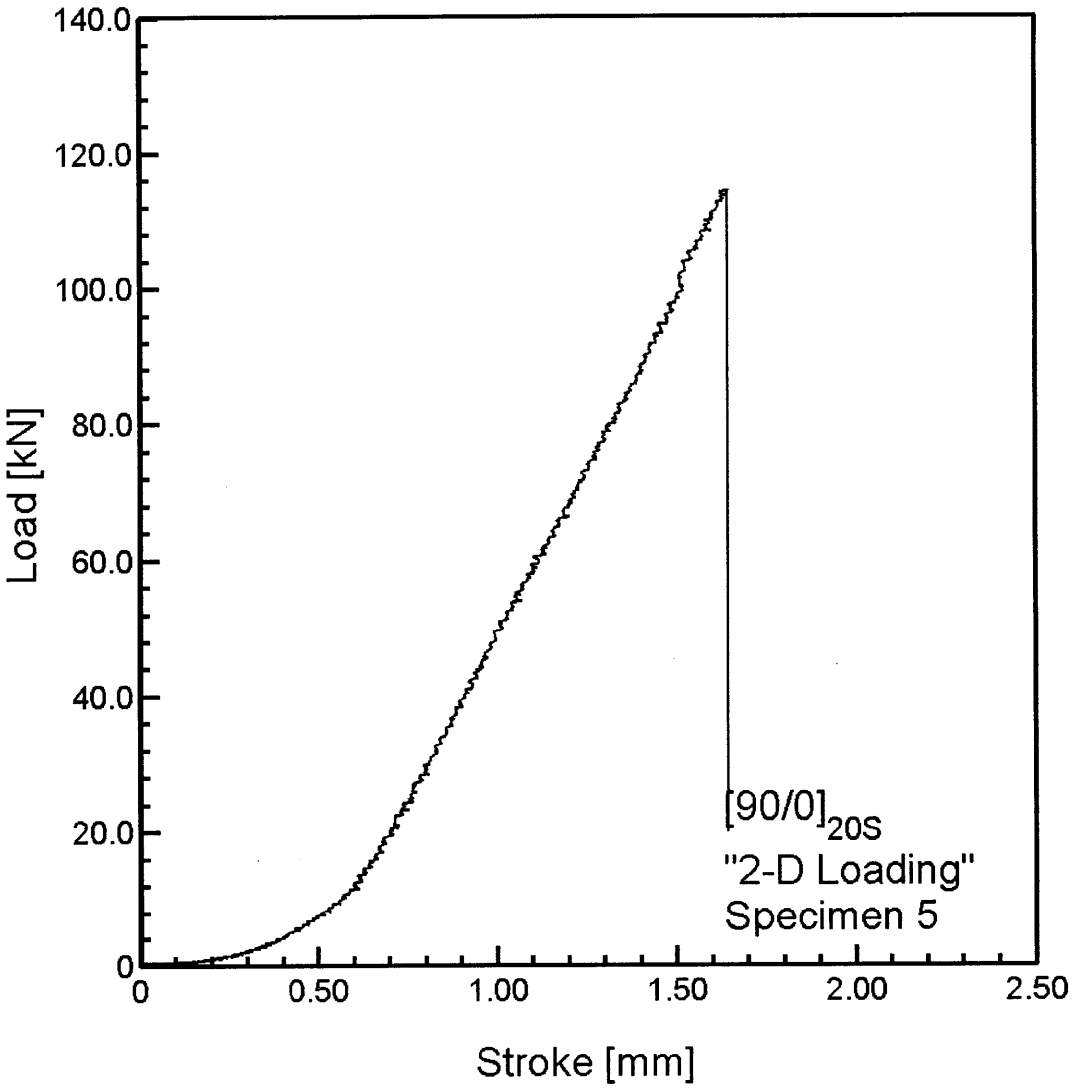

Figure A.14 Load versus stroke for $[90/0]_{20S}$ Specimen 5 tested to failure in "two-dimensional loading".

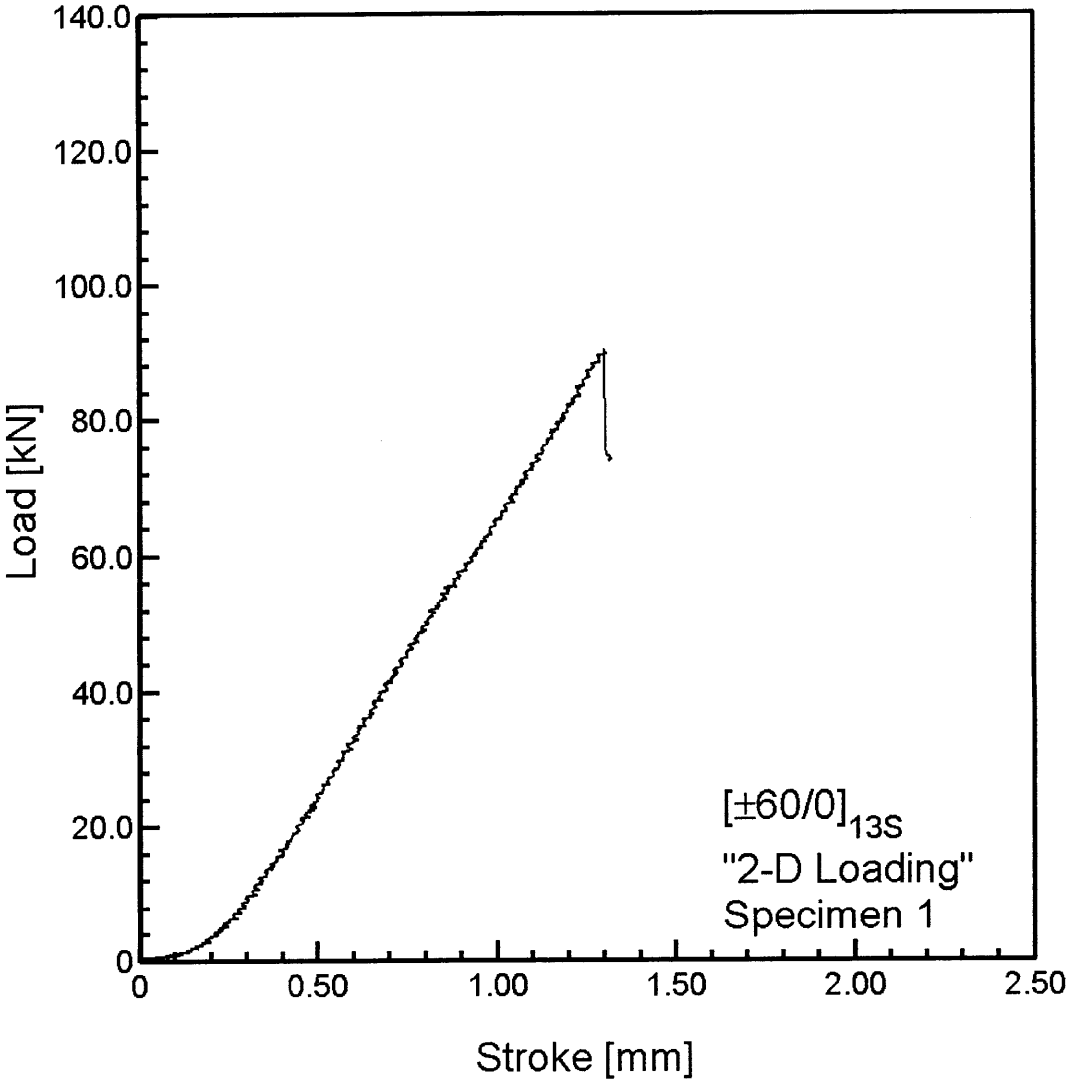

Figure A.15 Load versus stroke for $[\pm 60/0]_{13S}$ Specimen 1 tested to failure in "two-dimensional loading".

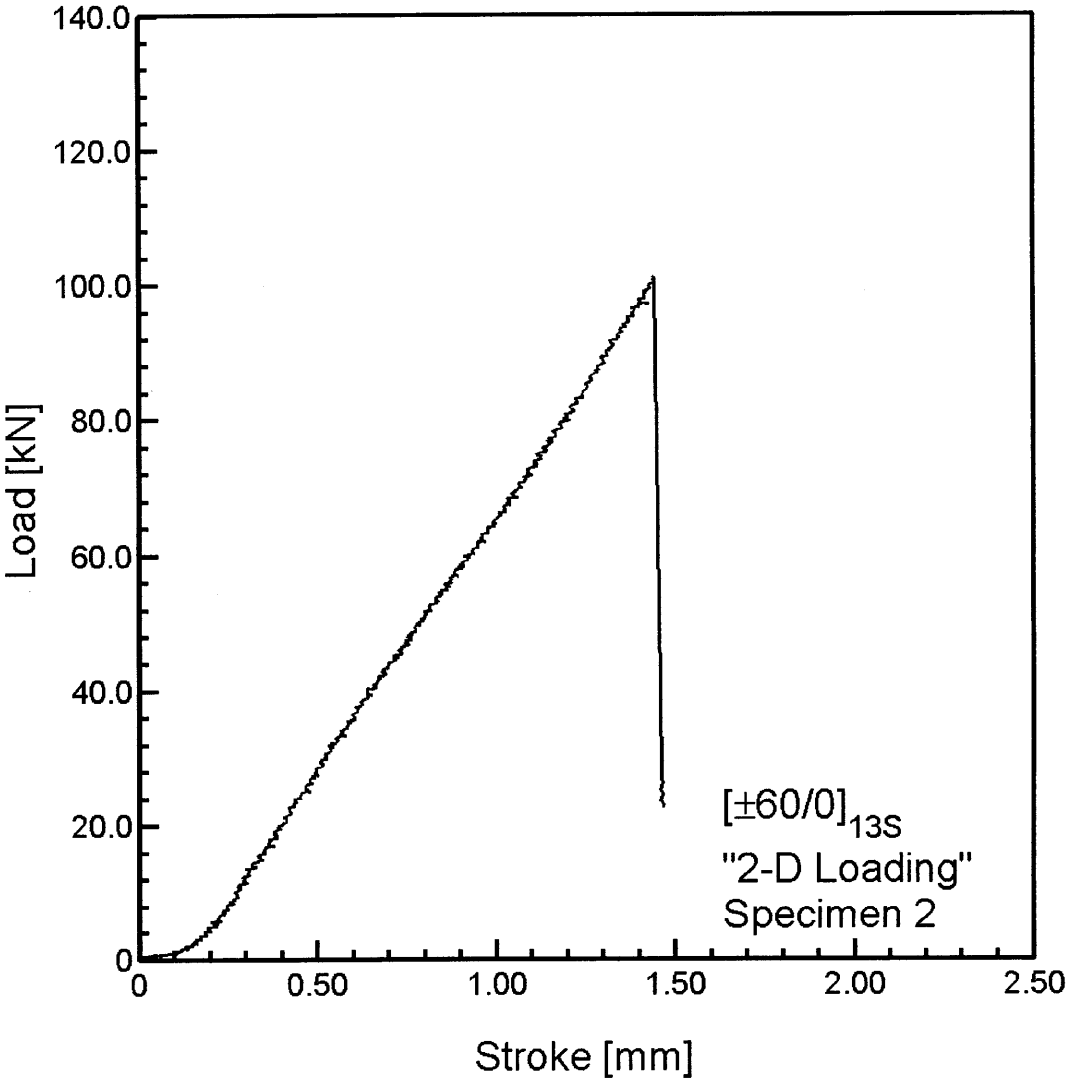

Figure A.16 Load versus stroke for $[\pm 60/0]_{13S}$ Specimen 2 tested to failure in "two-dimensional loading".

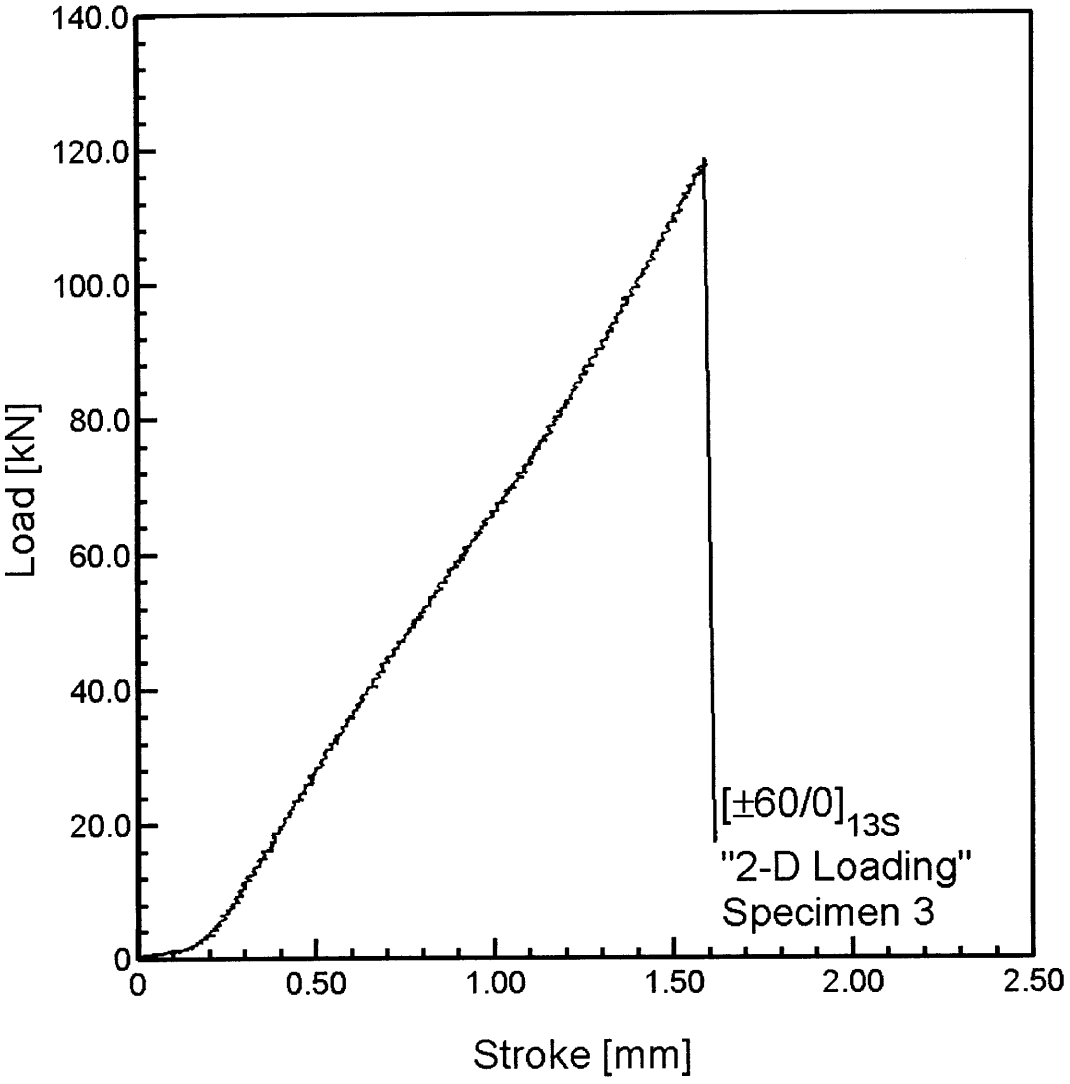

Figure A.17 Load versus stroke for $[\pm 60/0]_{13S}$ Specimen 3 tested to failure in "two-dimensional loading".

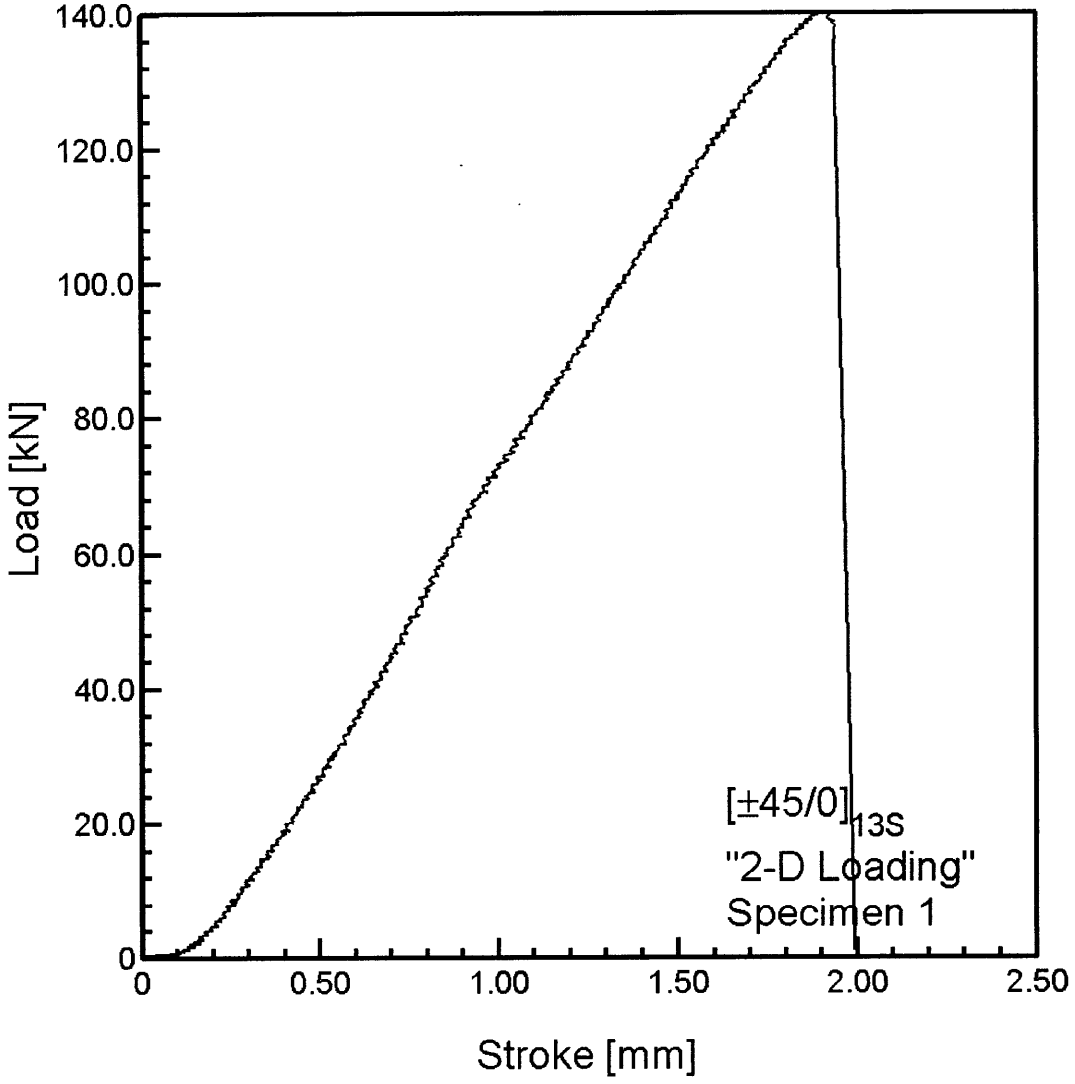

Figure A.18 Load versus stroke for $[\pm 45/0]_{13S}$ Specimen 1 tested to failure in "two-dimensional loading".

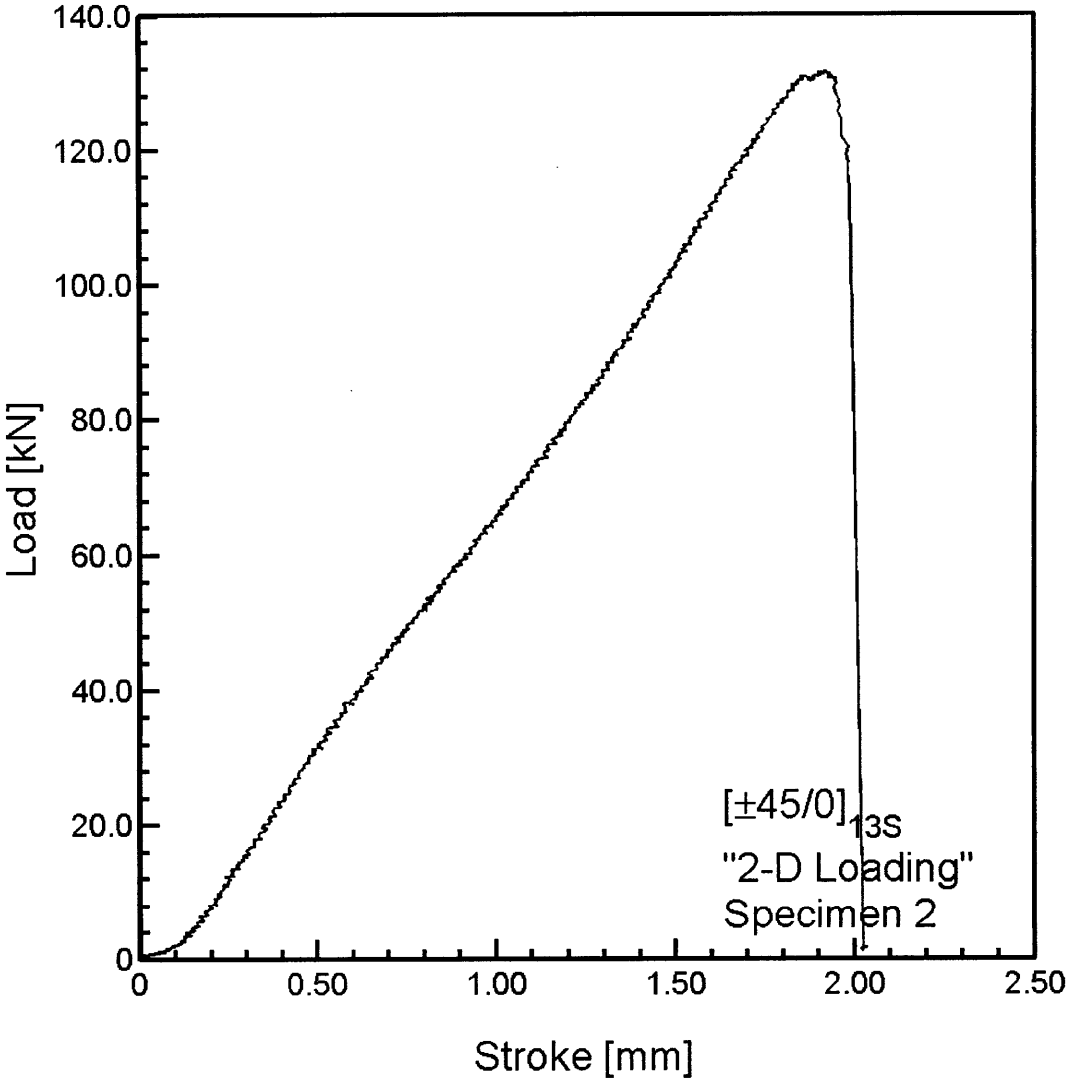

Figure A.19 Load versus stroke for $[\pm 45/0]_{13S}$ Specimen 2 tested to failure in "two-dimensional loading".

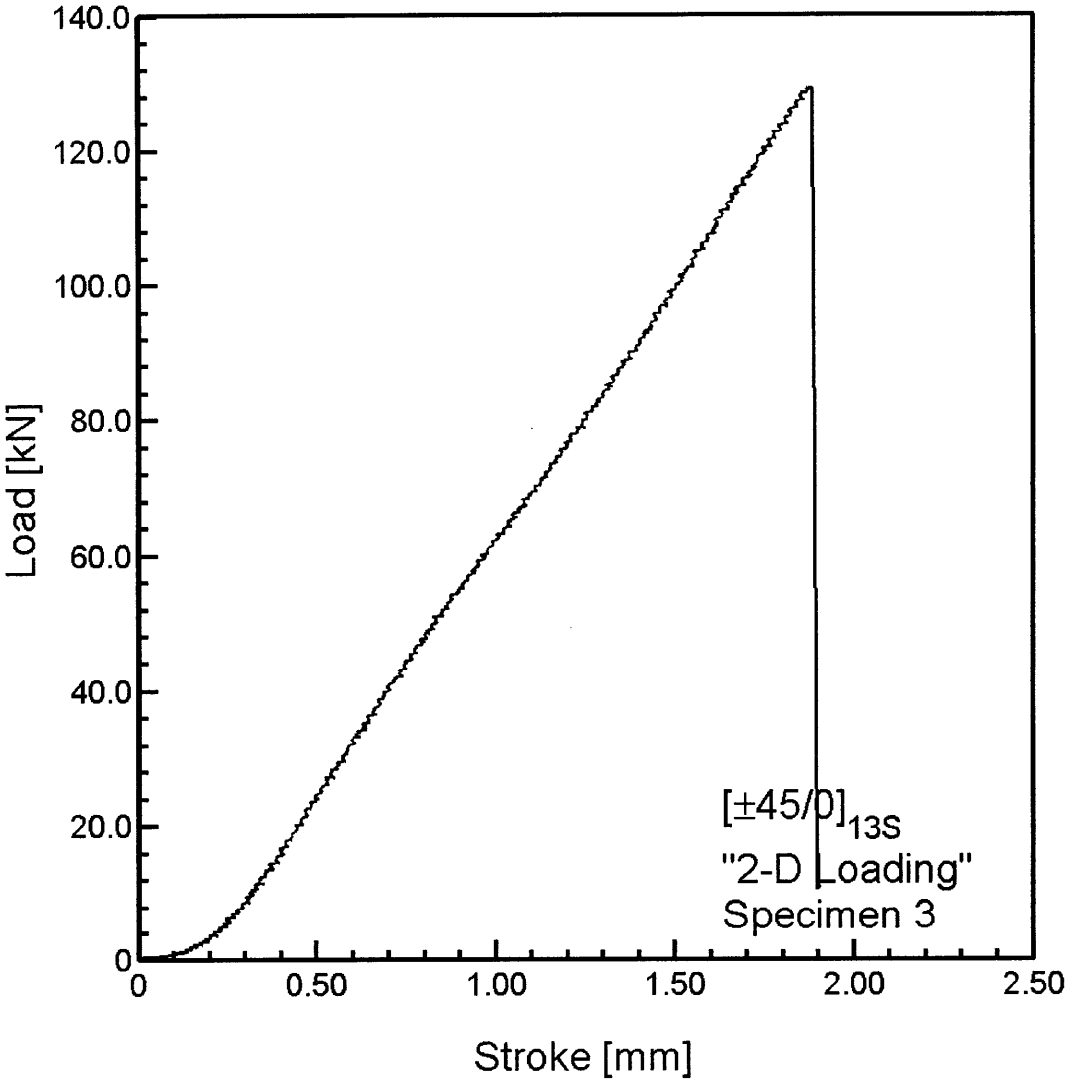

Figure A.20 Load versus stroke for $[\pm 45/0]_{13S}$ Specimen 3 tested to failure in "two-dimensional loading".

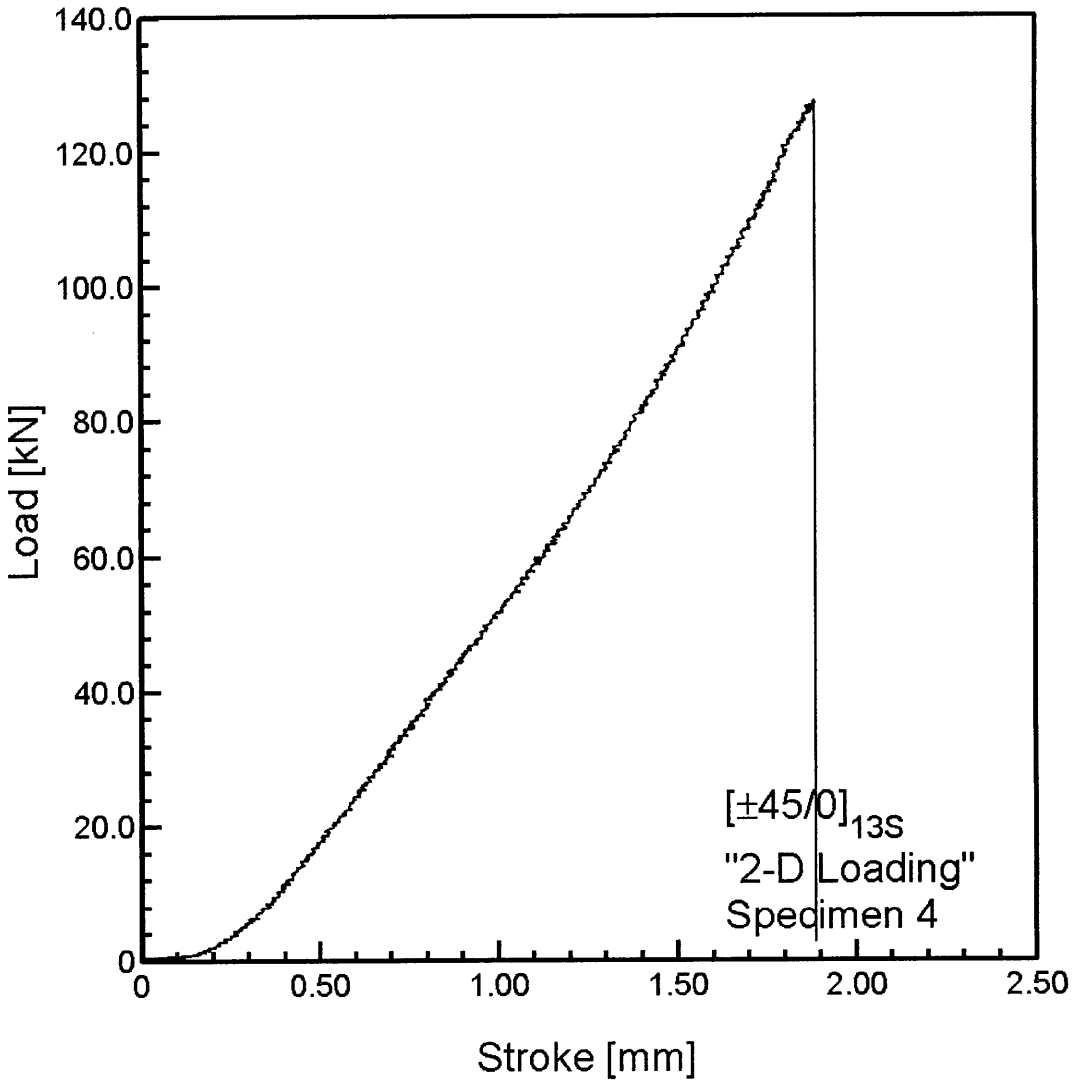

Figure A.21 Load versus stroke for $[\pm 45/0]_{13S}$ Specimen 4 tested to failure in "two-dimensional loading".

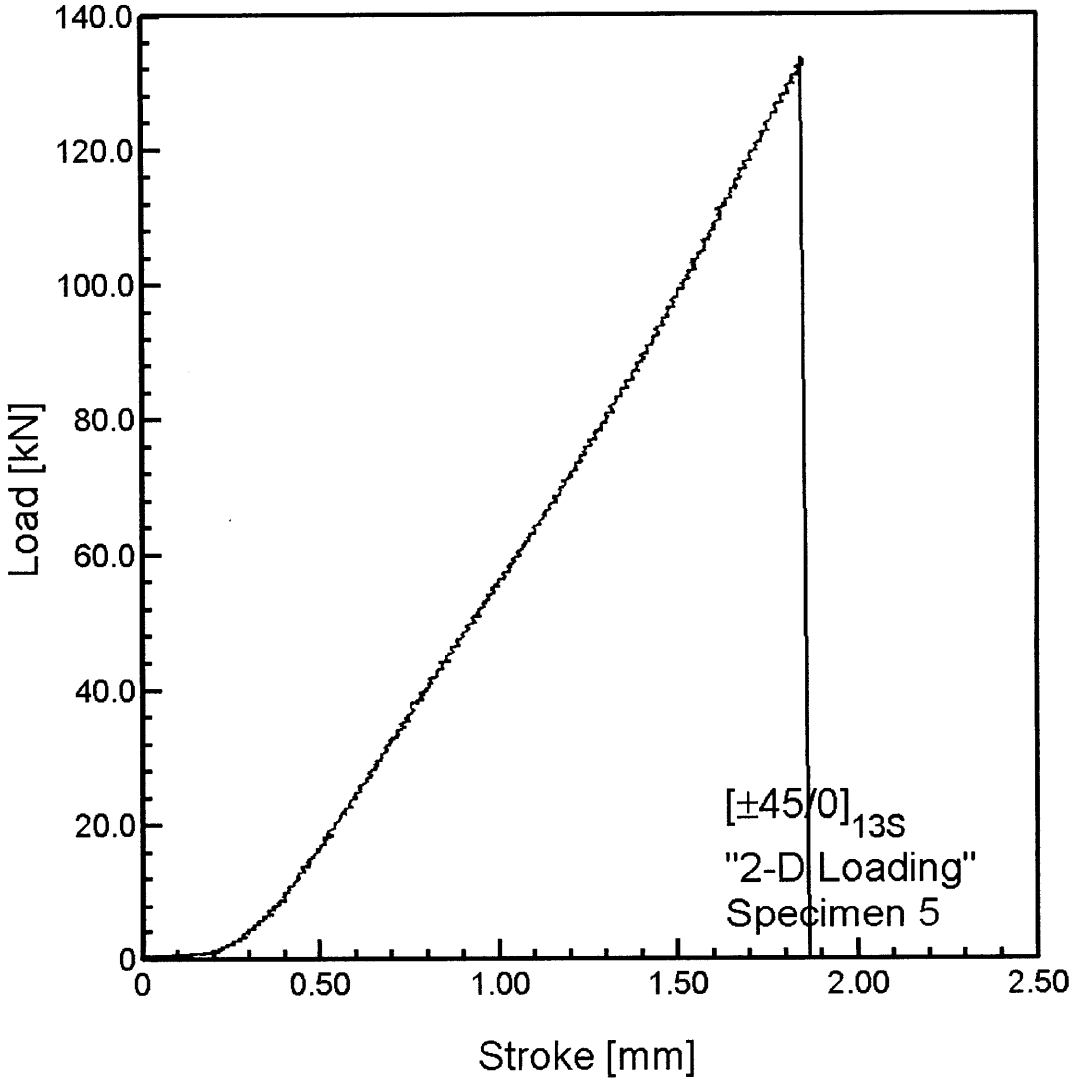

Figure A.22 Load versus stroke for $[\pm 45/0]_{13S}$ Specimen 5 tested to failure in "two-dimensional loading".

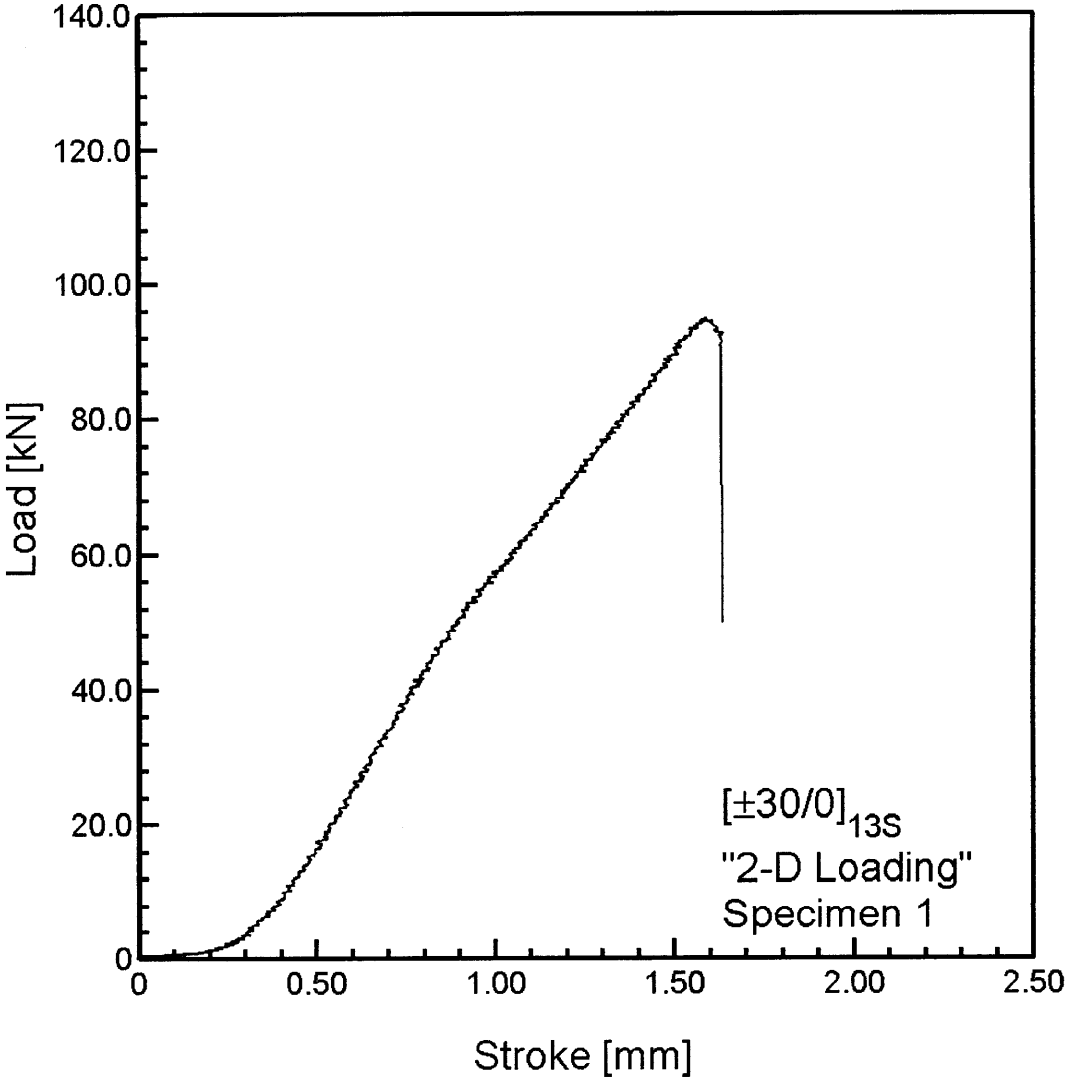

Figure A.23 Load versus stroke for $[\pm 30/0]_{13S}$ Specimen 1 tested to failure in "two-dimensional loading".

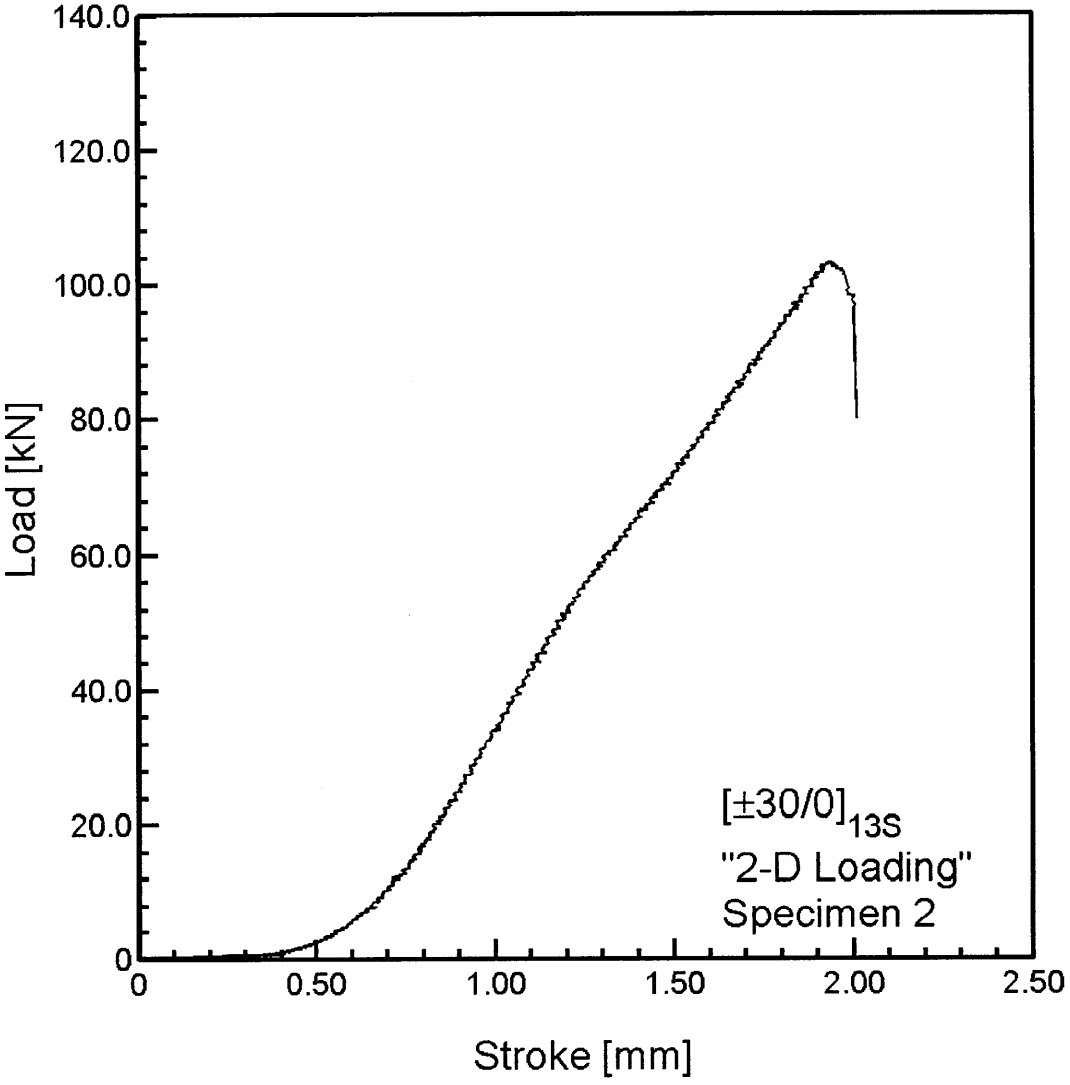

Figure A.24 Load versus stroke for $[\pm 30/0]_{13S}$ Specimen 2 tested to failure in "two-dimensional loading".

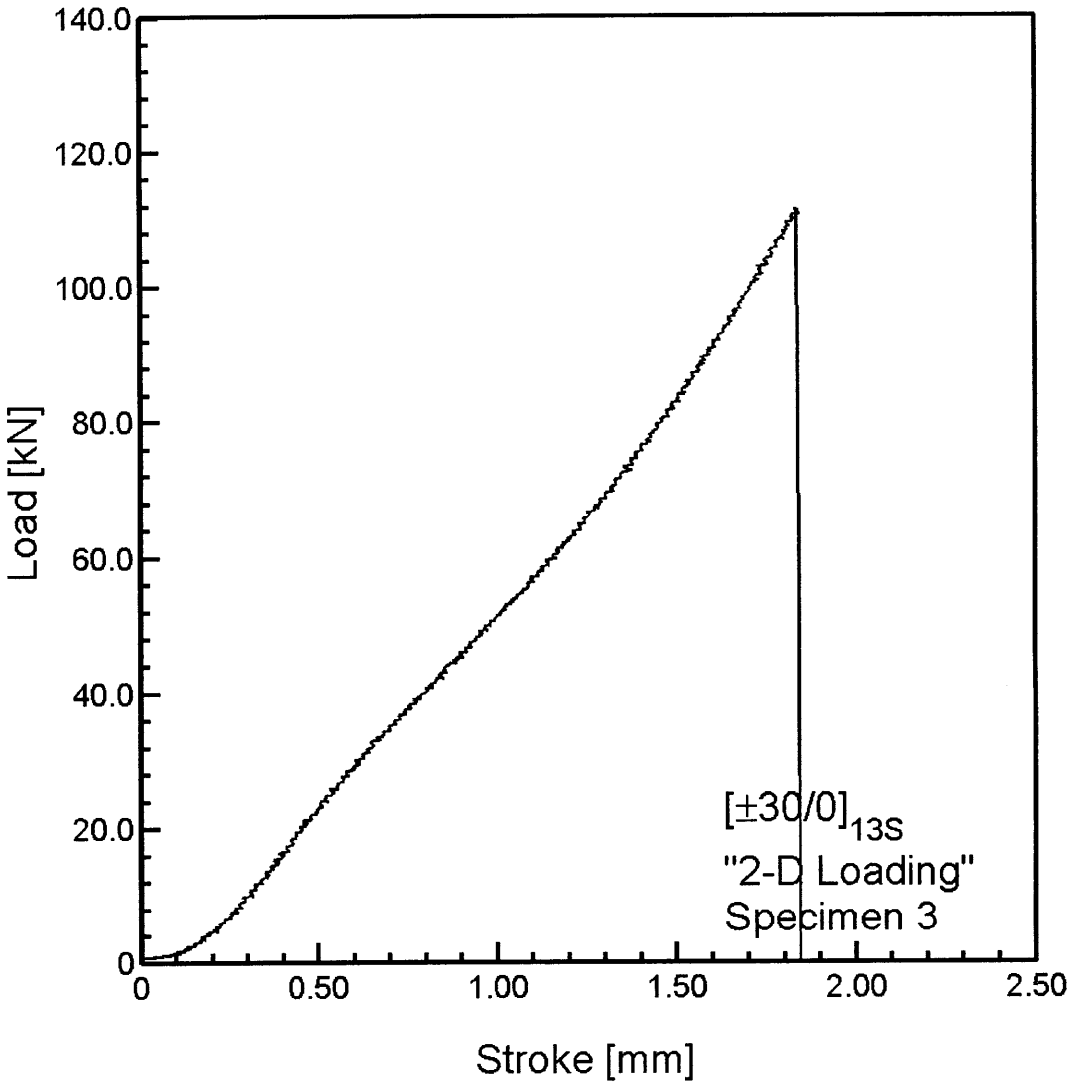

Figure A.25 Load versus stroke for $[\pm 30/0]_{13S}$ Specimen 3 tested to failure in "two-dimensional loading".

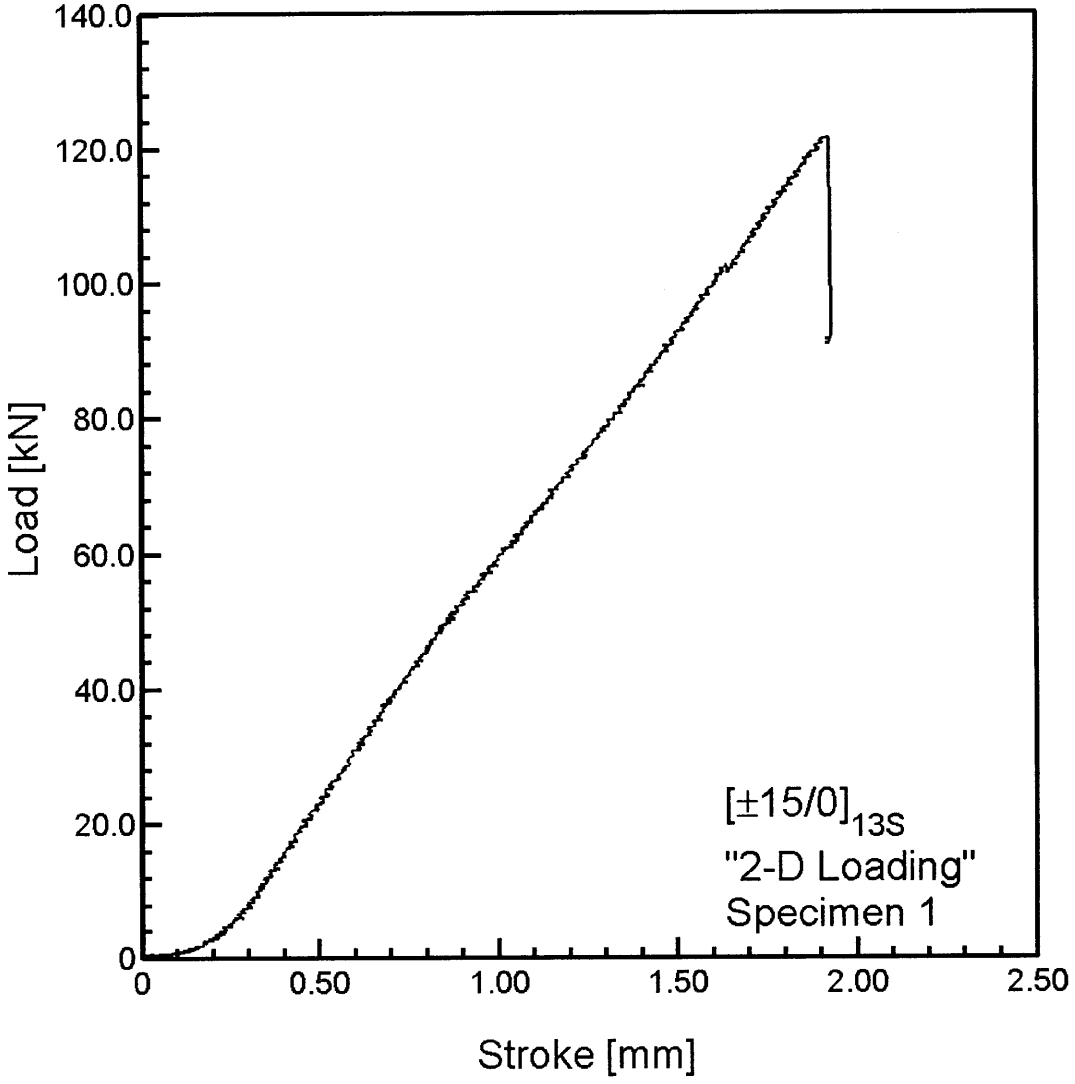

Figure A.26 Load versus stroke for $[\pm 15/0]_{13S}$ Specimen 1 tested to failure in "two-dimensional loading".

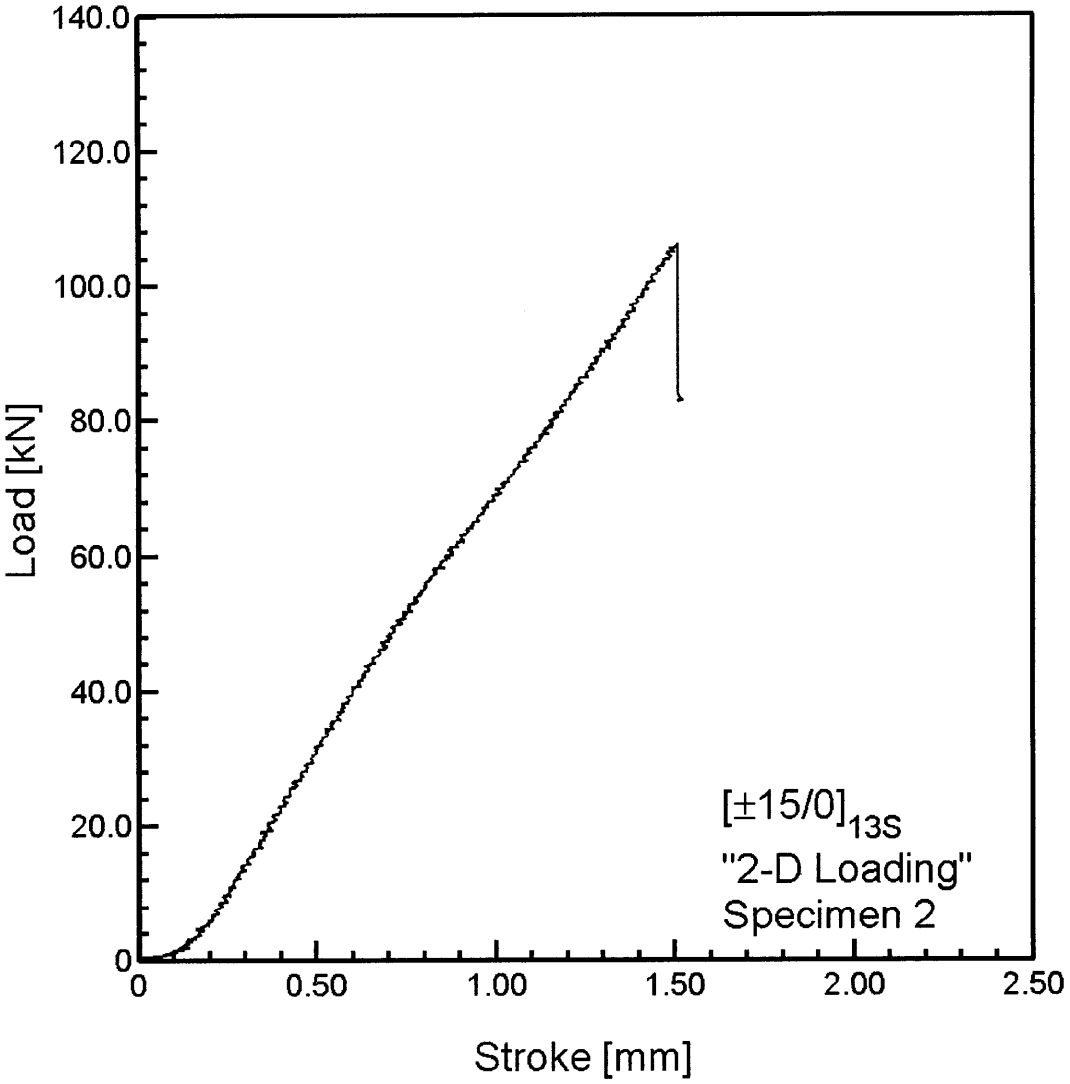

Figure A.27 Load versus stroke for $[\pm 15/0]_{13S}$ Specimen 2 tested to failure in "two-dimensional loading".

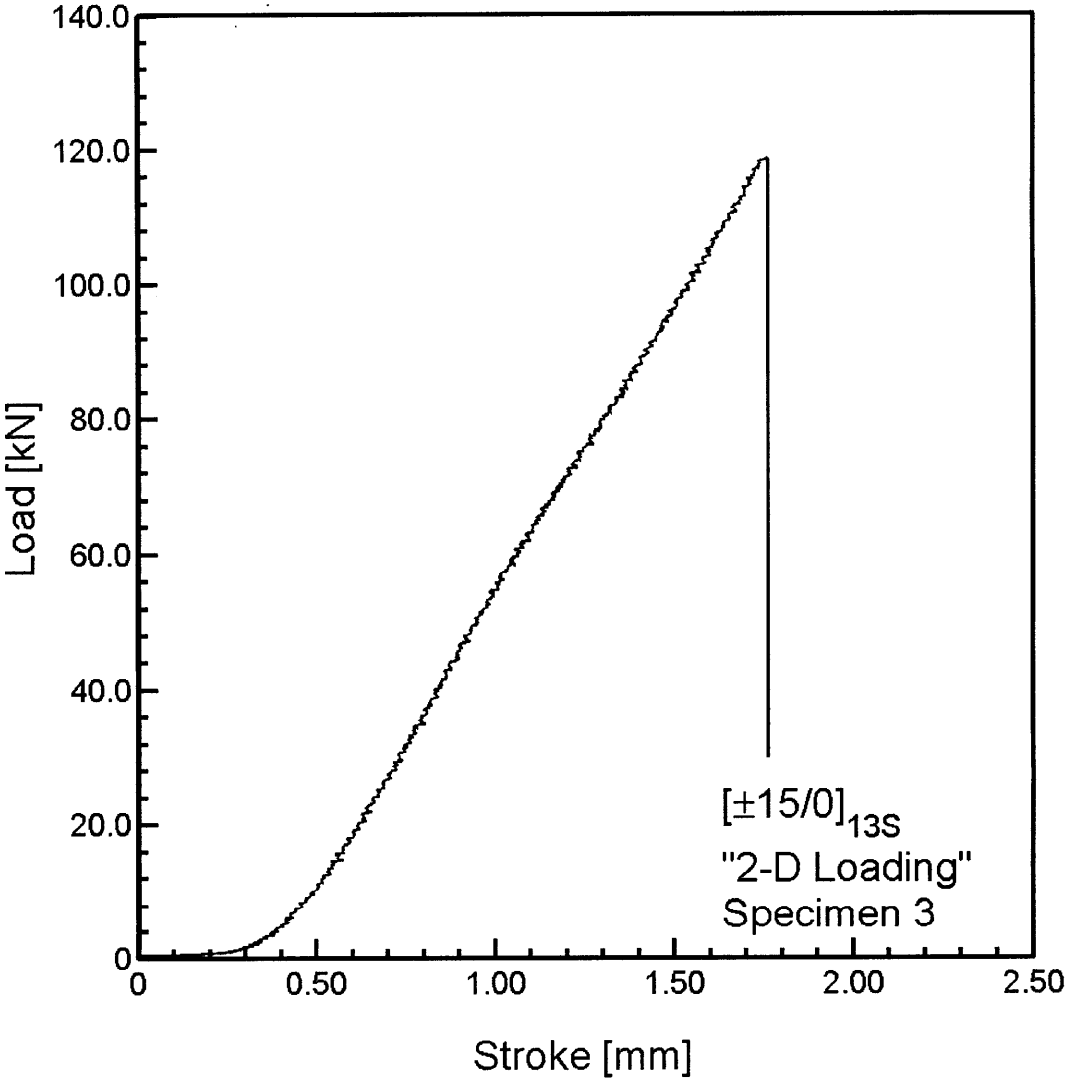

Figure A.28 Load versus stroke for $[\pm 15/0]_{13S}$ Specimen 3 tested to failure in "two-dimensional loading".

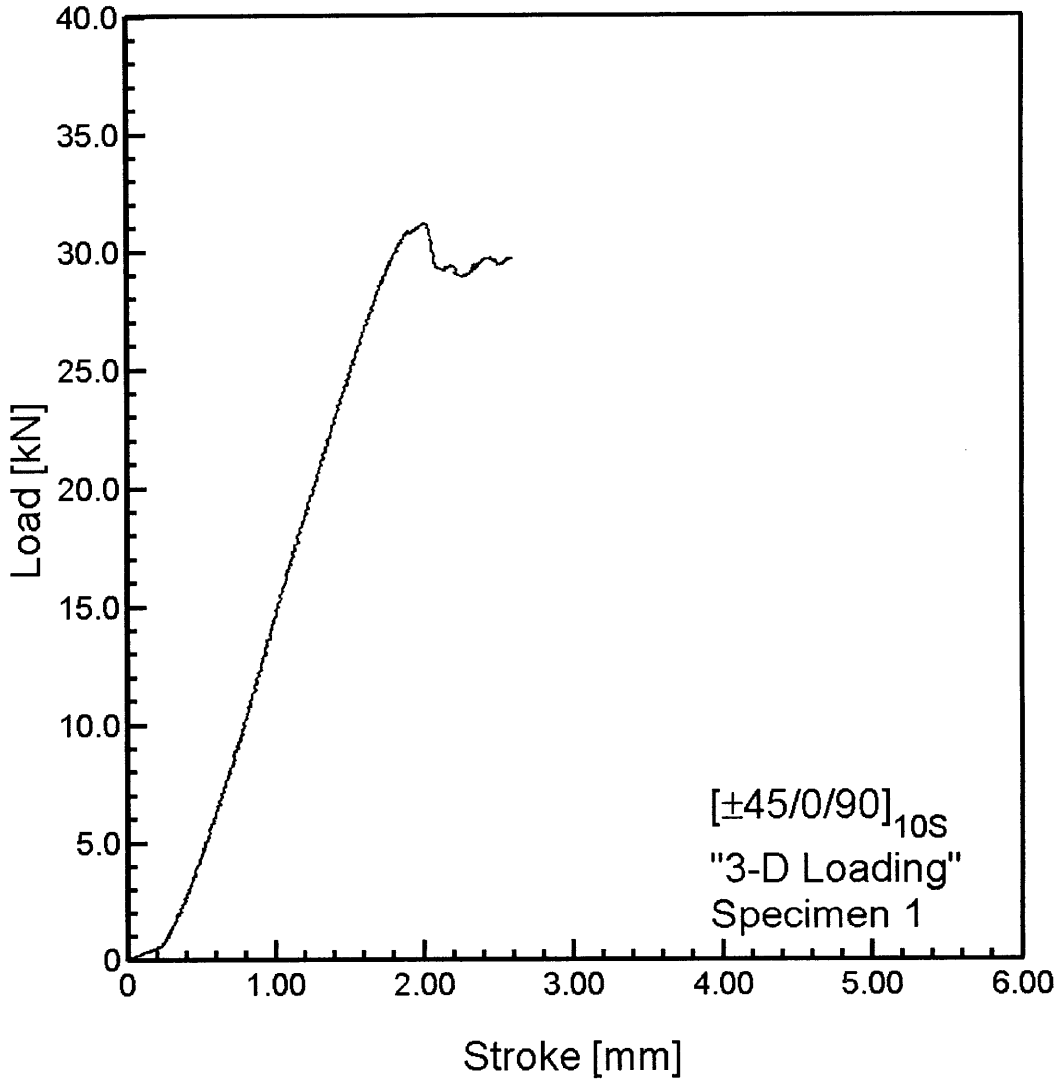

Figure A.29 Load versus stroke for $[\pm 45/0/90]_{10S}$ Specimen 1 tested to failure in "three-dimensional loading".

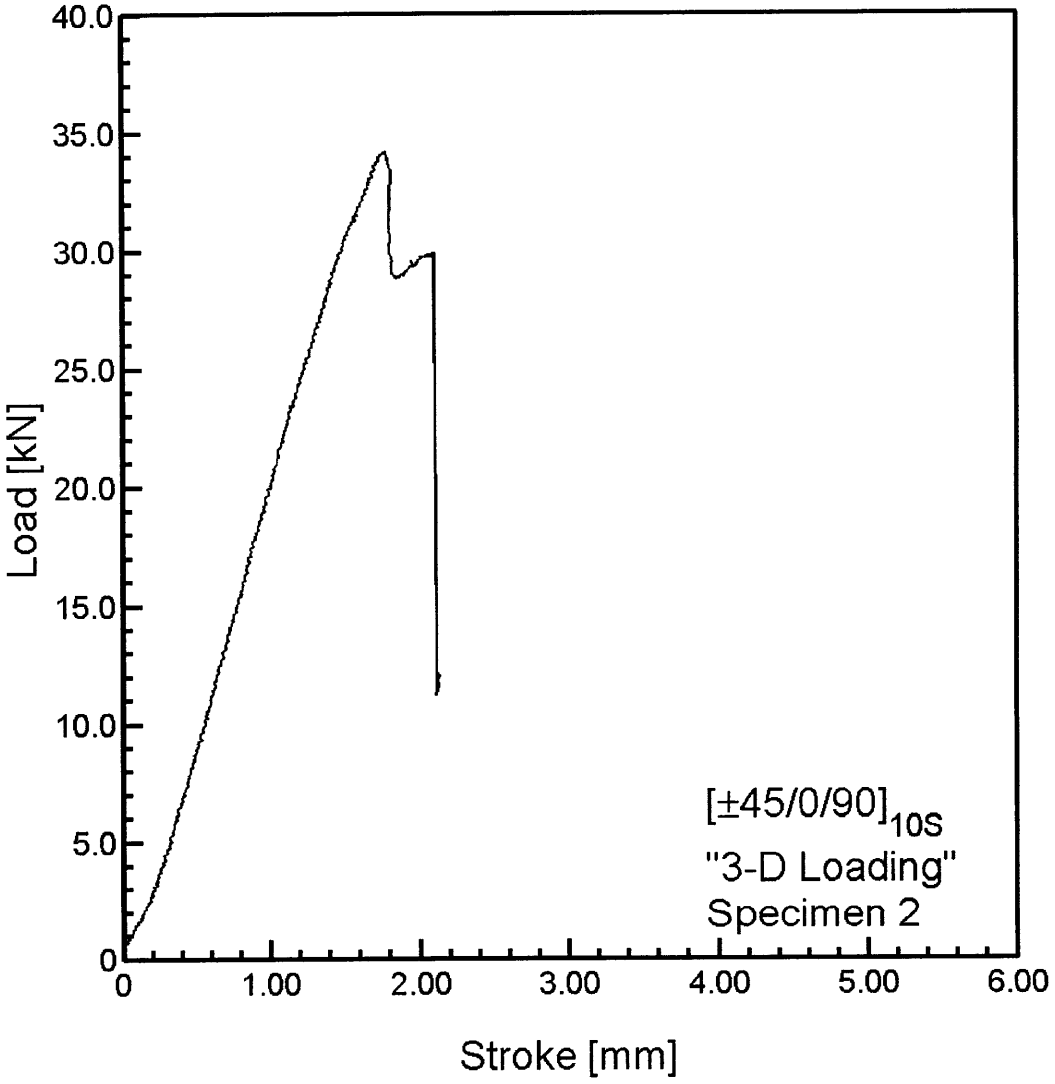

Figure A.30 Load versus stroke for $[\pm 45/0/90]_{10S}$ Specimen 2 tested to failure in "three-dimensional loading".

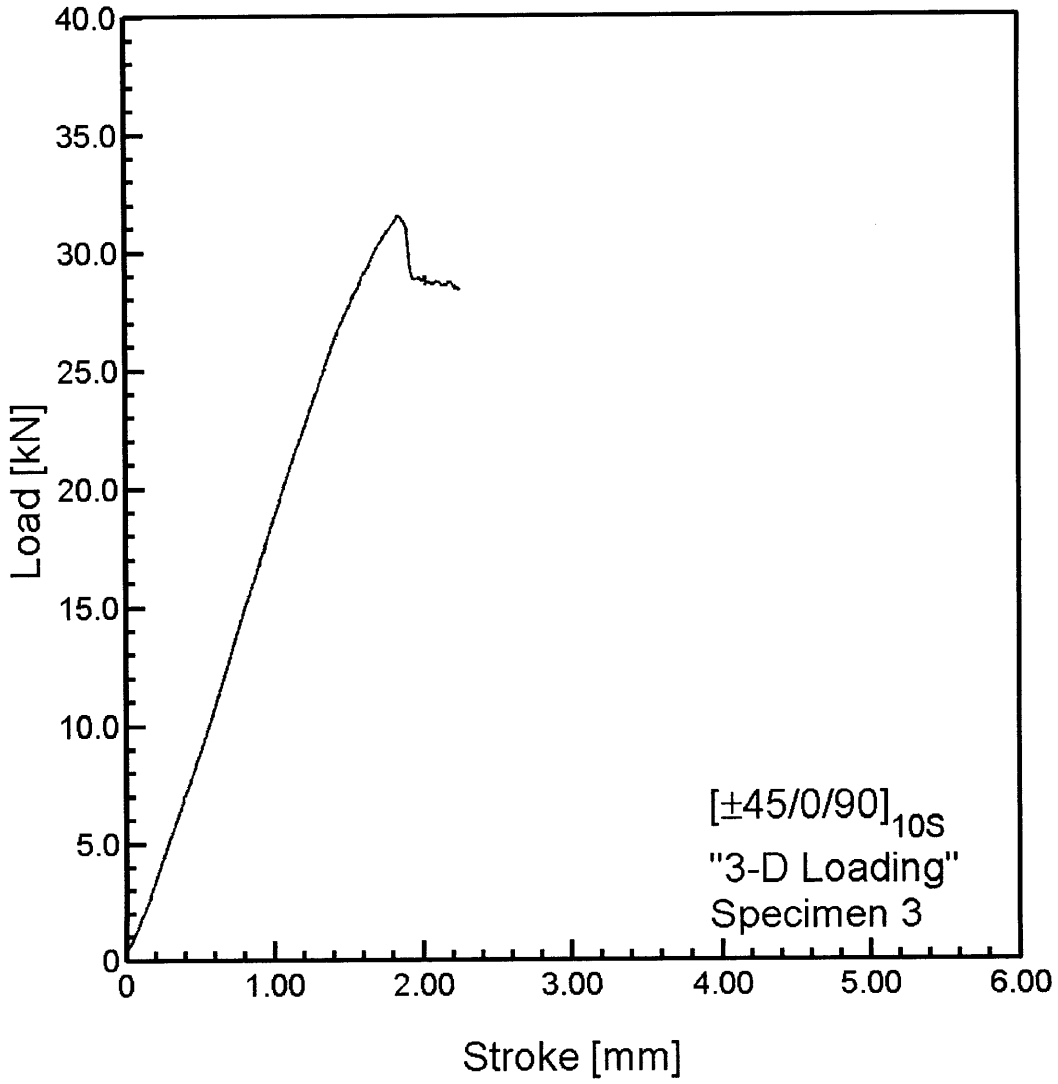

Figure A.31 Load versus stroke for $[\pm 45/0/90]_{10S}$ Specimen 3 tested to failure in "three-dimensional loading".

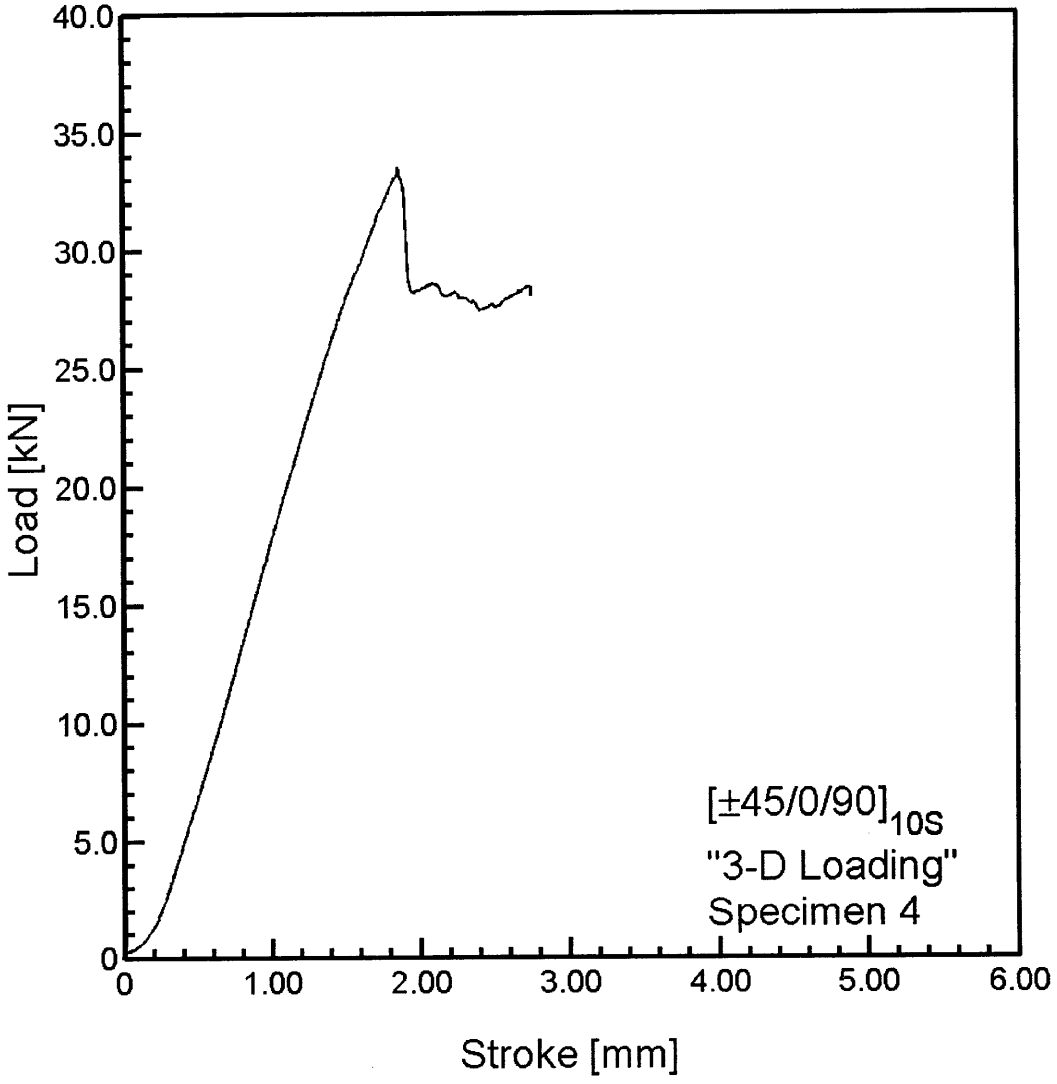

Figure A.32 Load versus stroke for $[\pm 45/0/90]_{10S}$ Specimen 4 tested to failure in "three-dimensional loading".

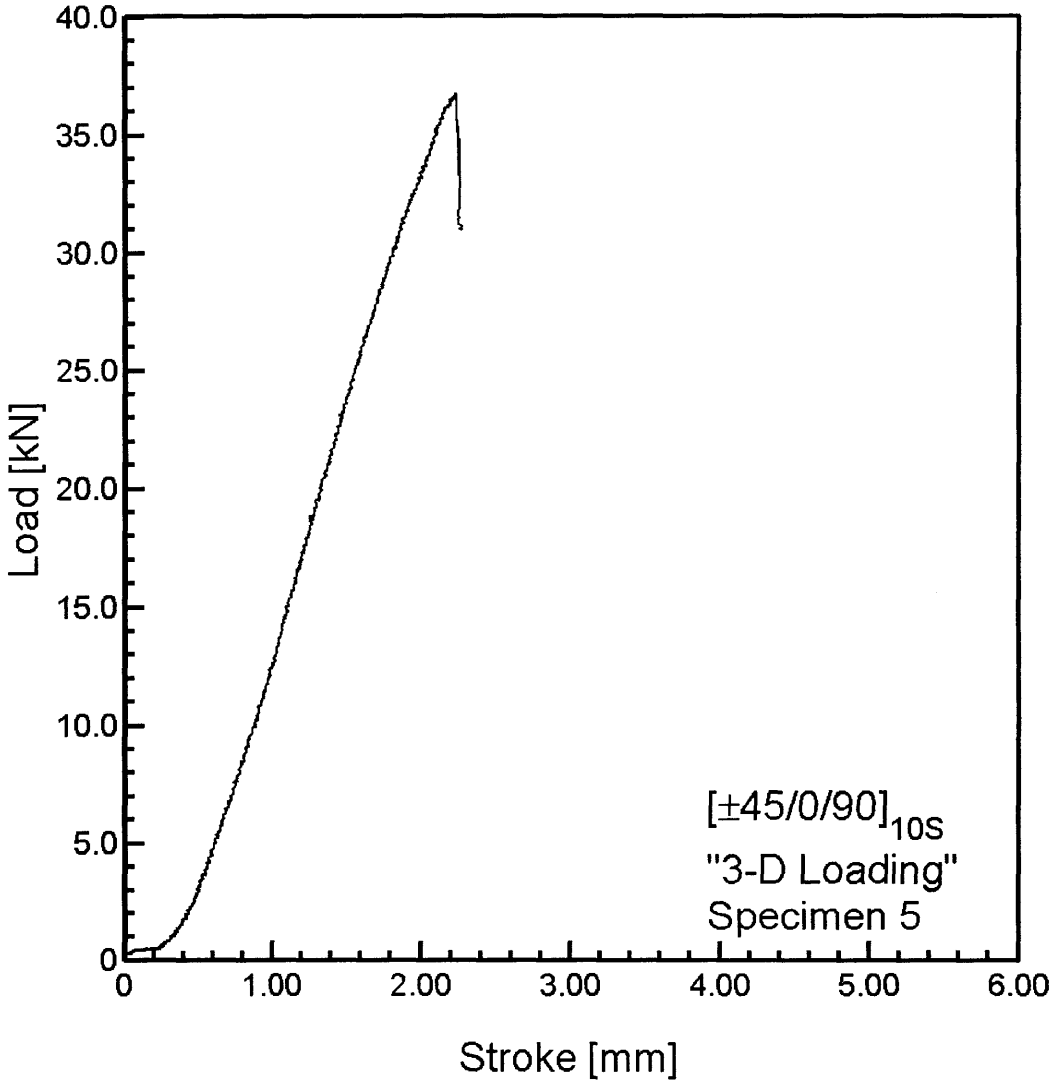

Figure A.33 Load versus stroke for $[\pm 45/0/90]_{10S}$ Specimen 5 tested to failure in "three-dimensional loading".

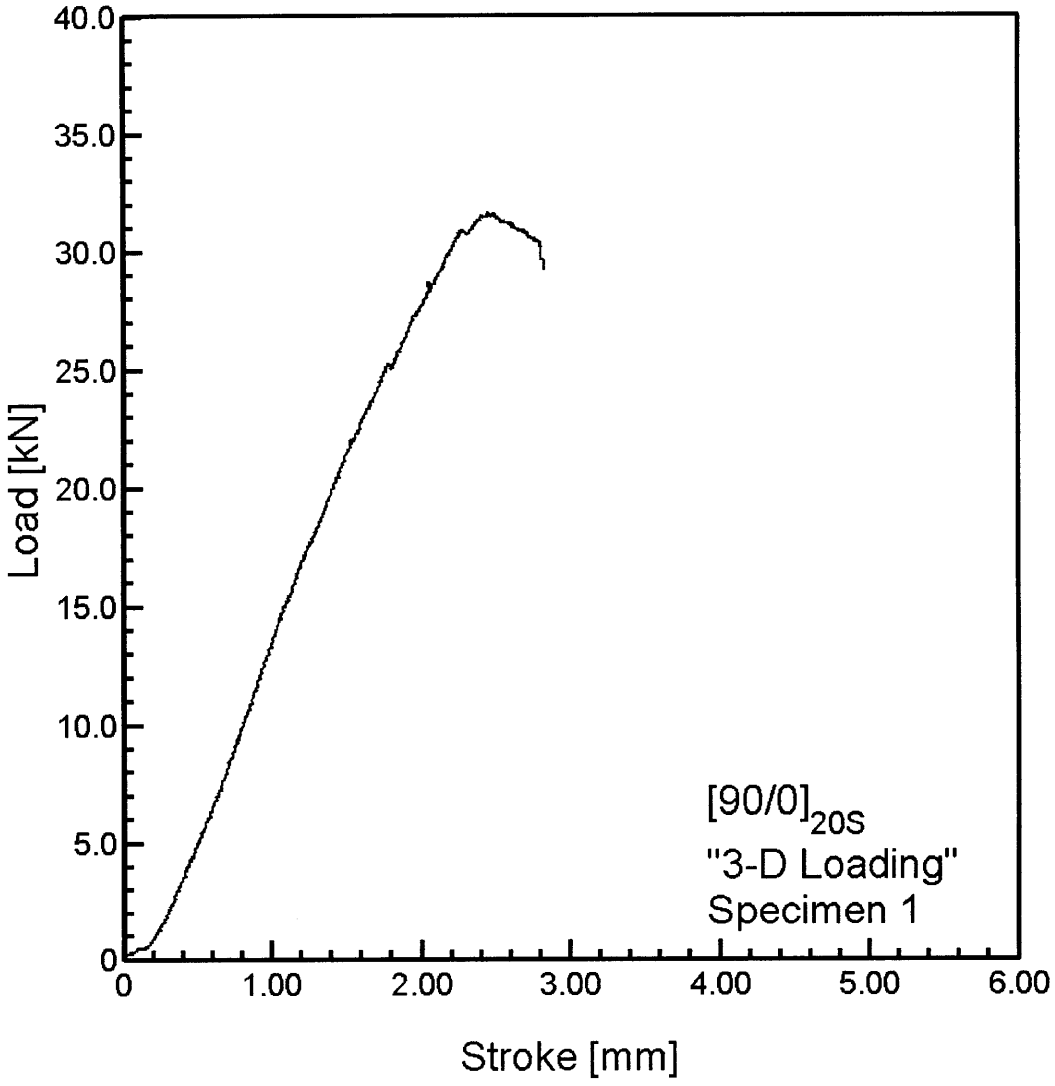

Figure A.34 Load versus stroke for $[90/0]_{10S}$ Specimen 1 tested to failure in "three-dimensional loading".

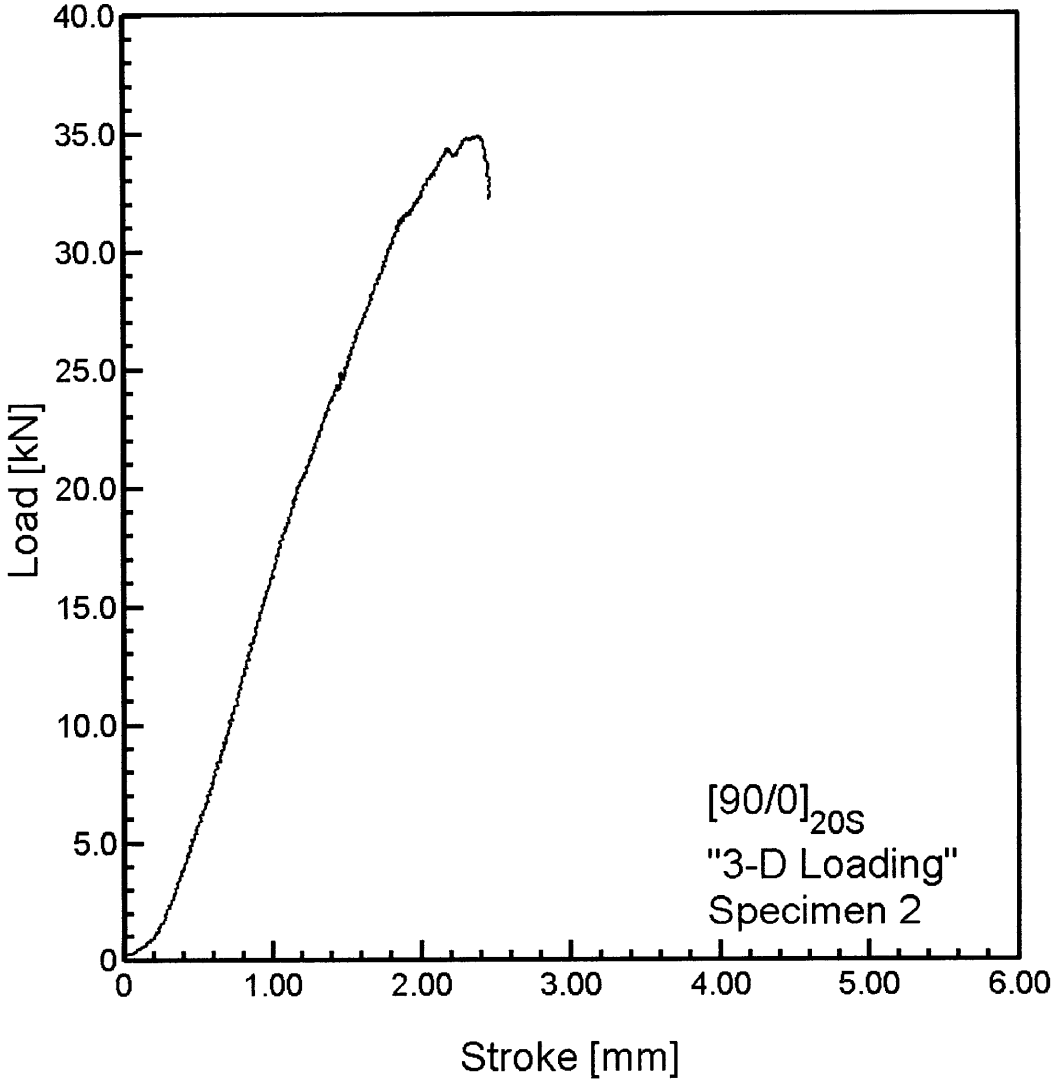

Figure A.35 Load versus stroke for $[90/0]_{10S}$ Specimen 2 tested to failure in "three-dimensional loading".

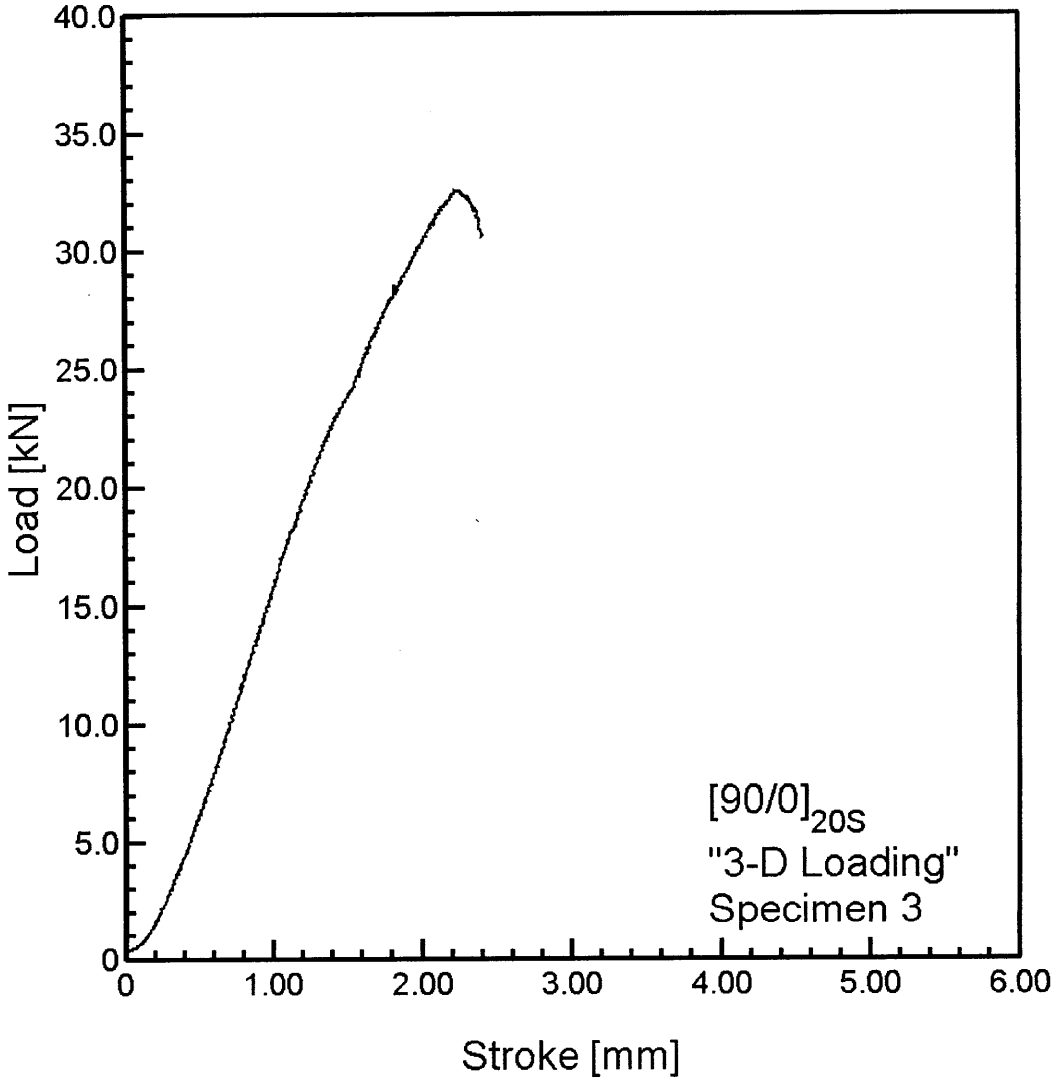

Figure A.36 Load versus stroke for $[90/0]_{10S}$ Specimen 3 tested to failure in "three-dimensional loading".

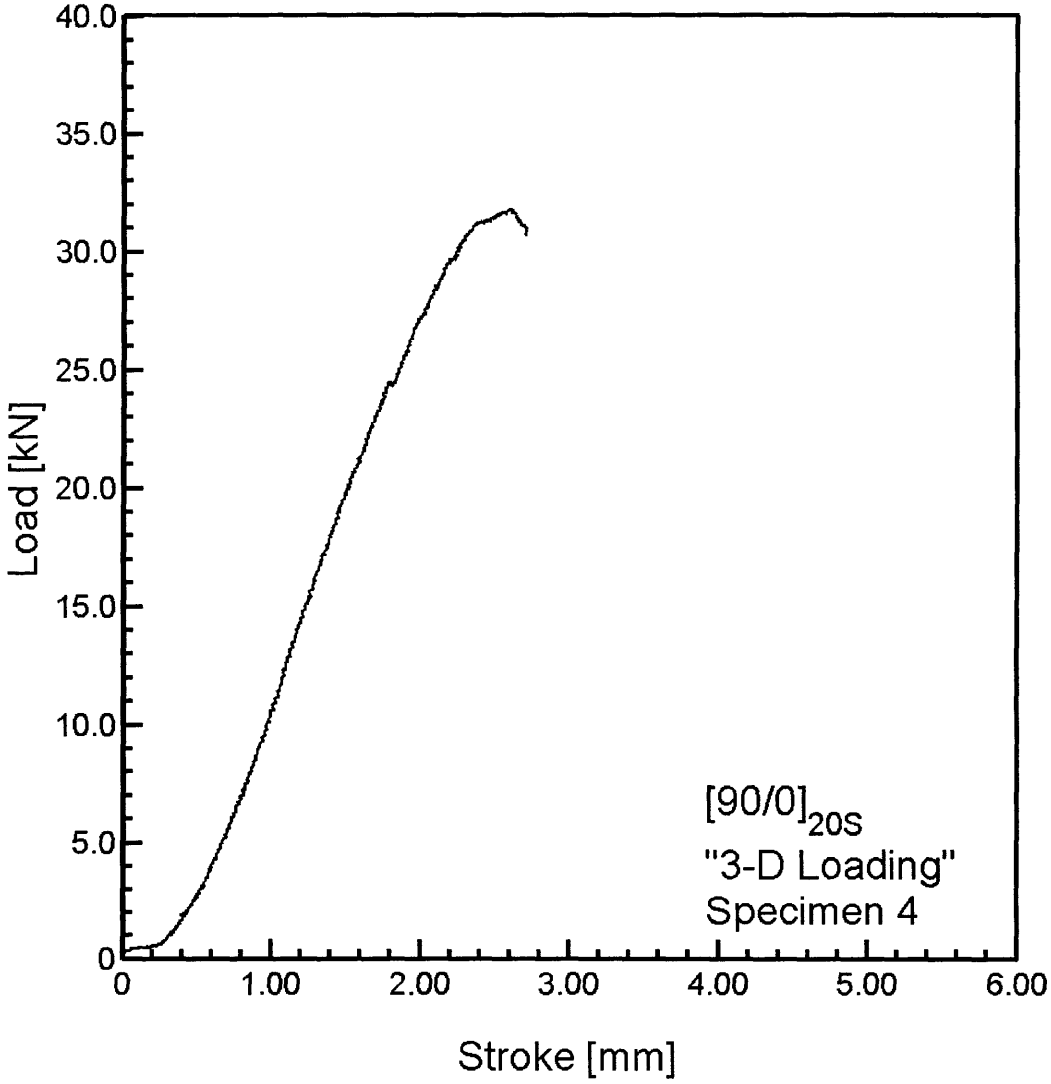

Figure A.37 Load versus stroke for $[90/0]_{10S}$ Specimen 4 tested to failure in "three-dimensional loading".

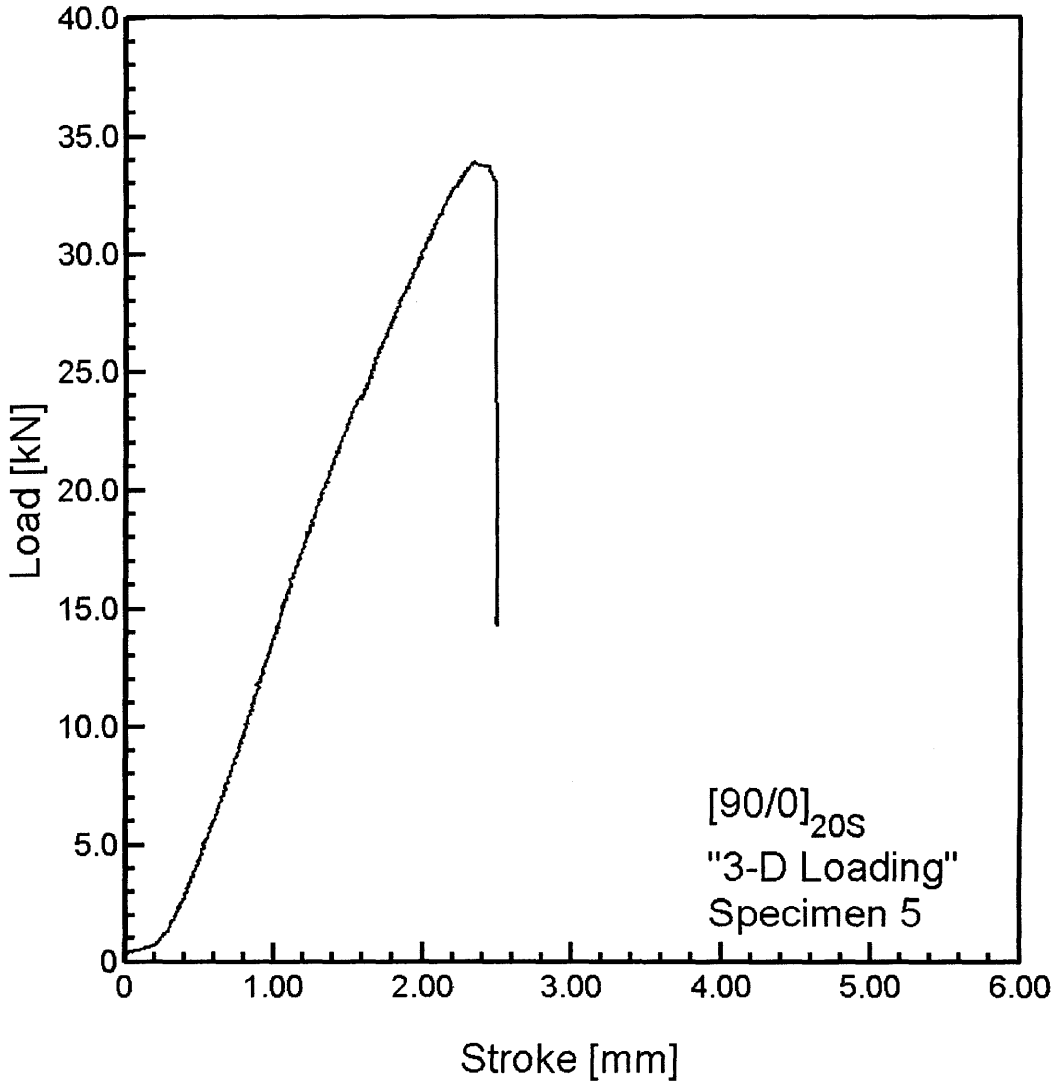

Figure A.38 Load versus stroke for $[90/0]_{10S}$ Specimen 5 tested to failure in "three-dimensional loading".

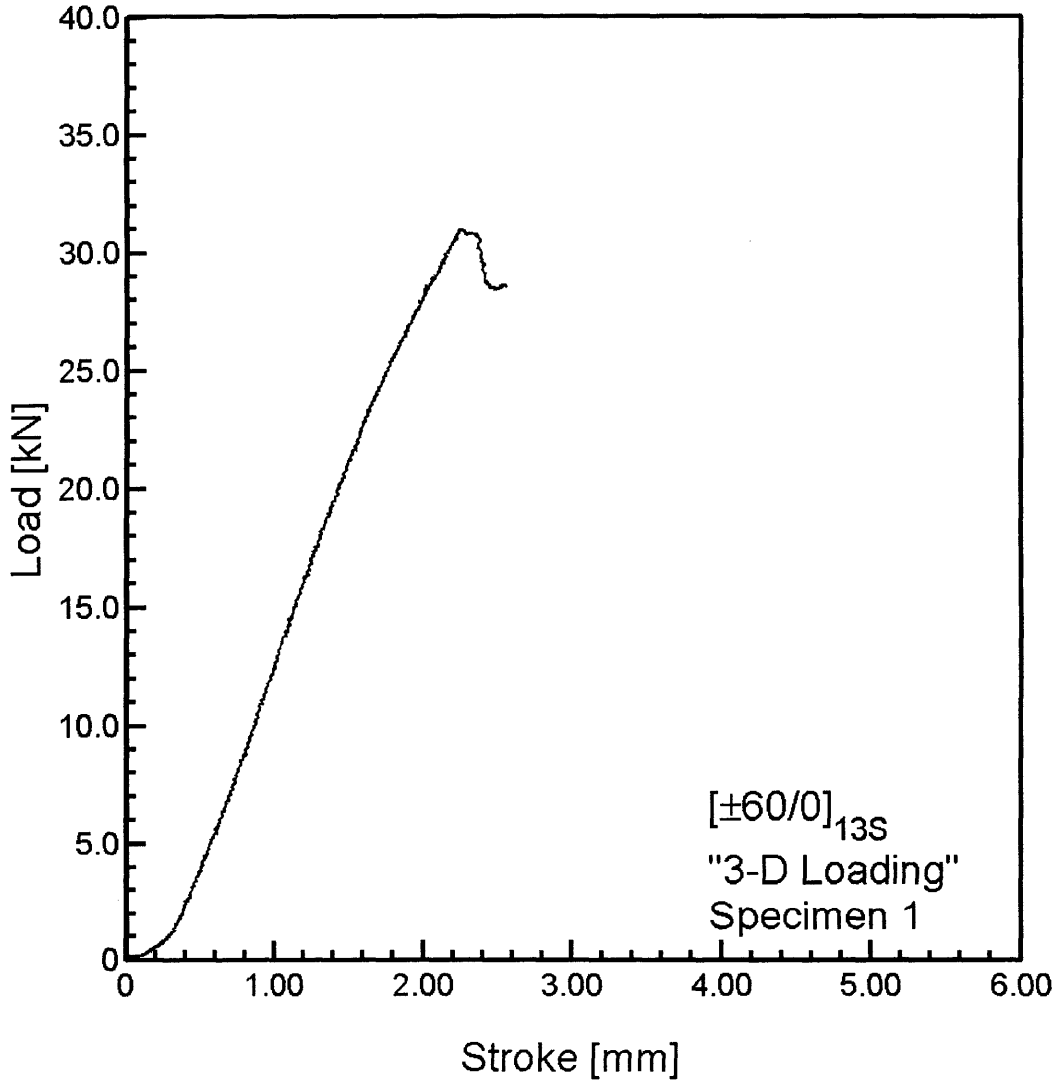

Figure A.39 Load versus stroke for $[\pm 60/0]_{13S}$ Specimen 1 tested to failure in "three-dimensional loading".

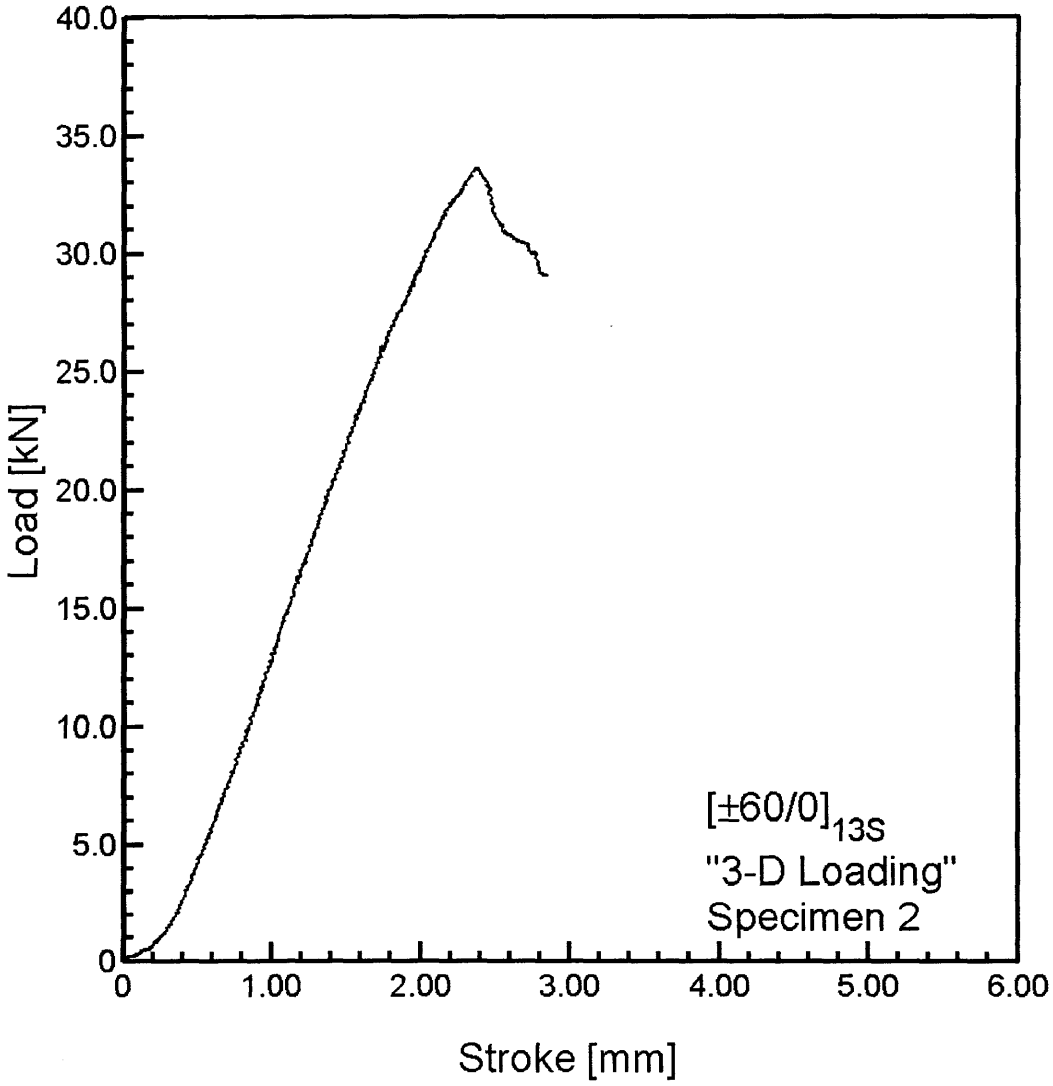

Figure A.40 Load versus stroke for $[\pm 60/0]_{13S}$ Specimen 2 tested to failure in "three-dimensional loading".

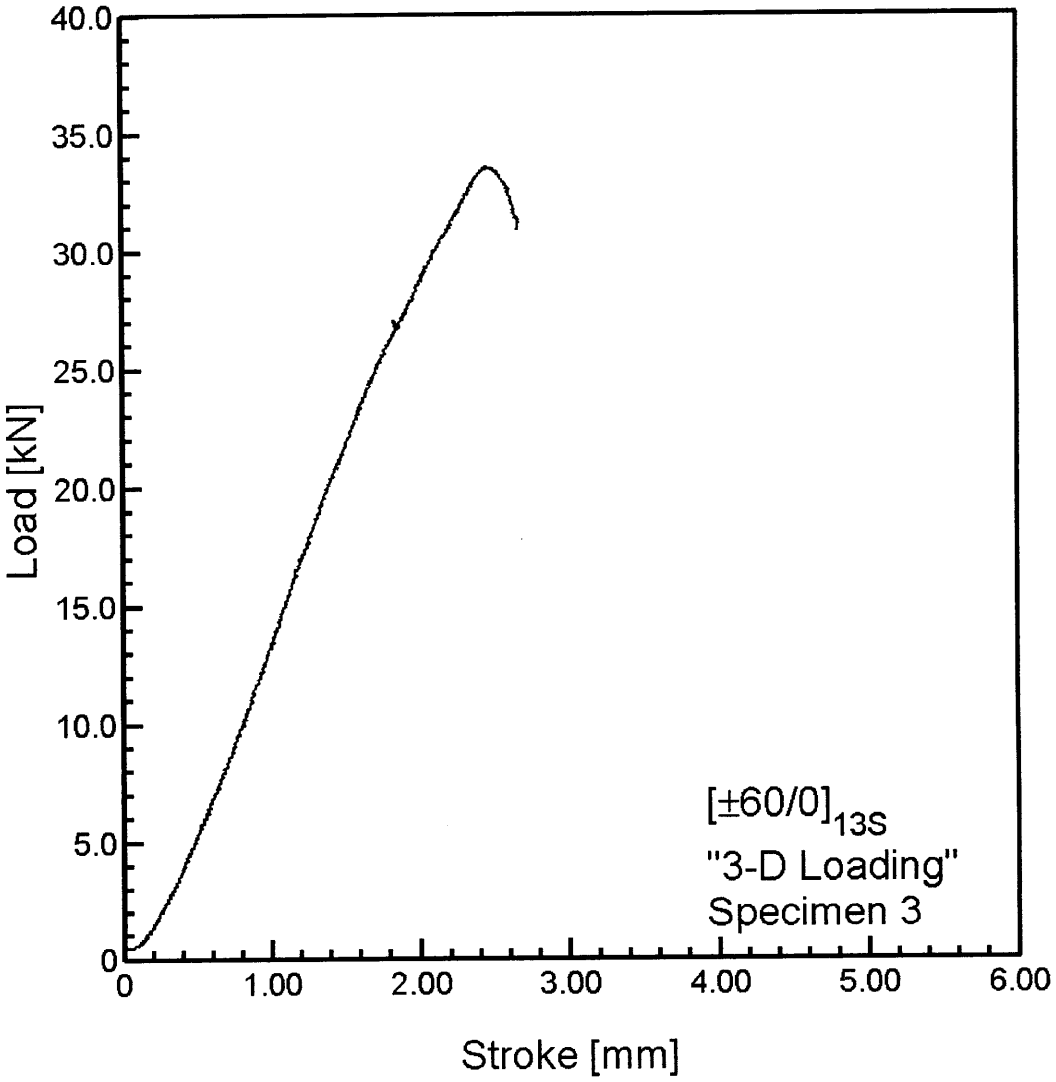

Figure A.41 Load versus stroke for $[\pm 60/0]_{13S}$ Specimen 3 tested to failure in "three-dimensional loading".

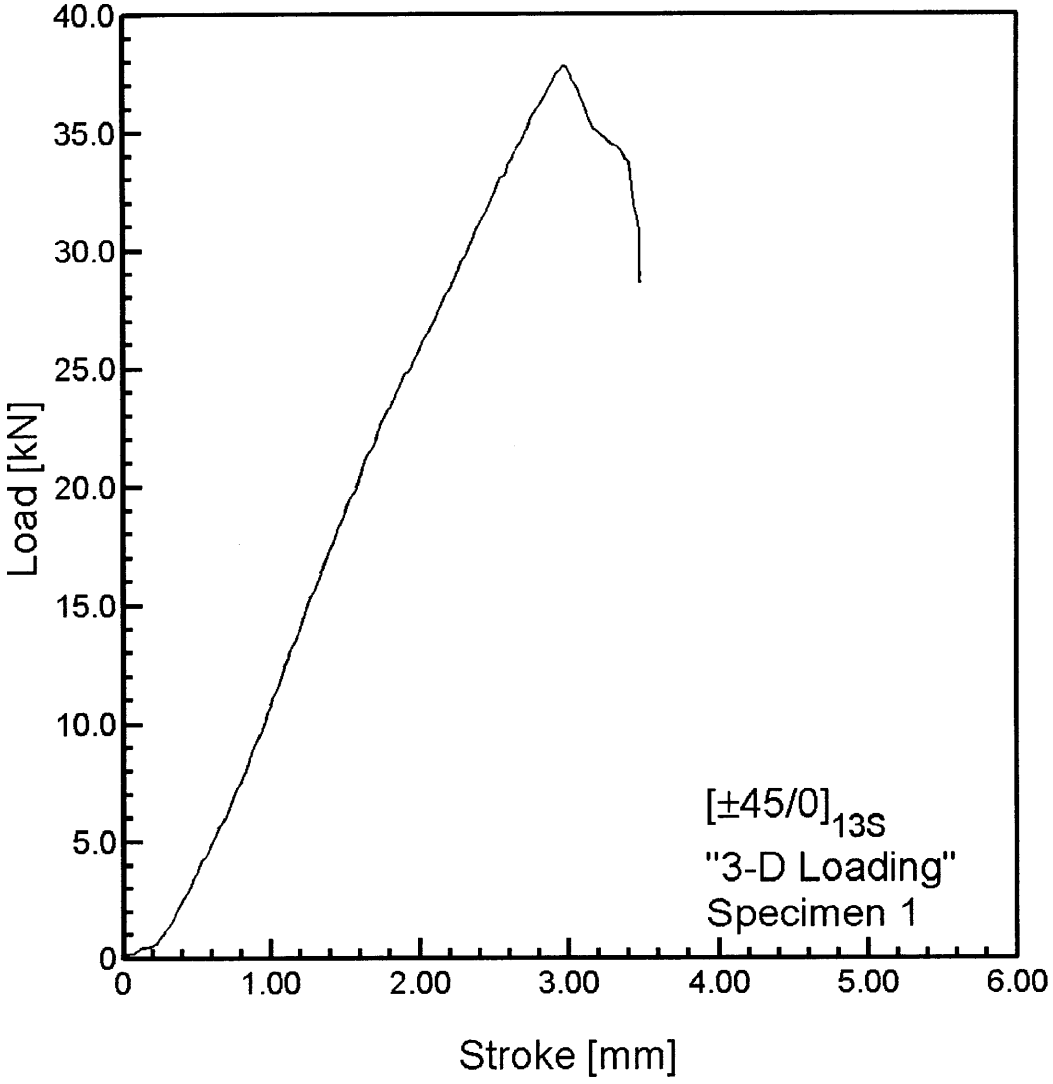

Figure A.42 Load versus stroke for $[\pm 45/0]_{13S}$ Specimen 1 tested to failure in "three-dimensional loading".

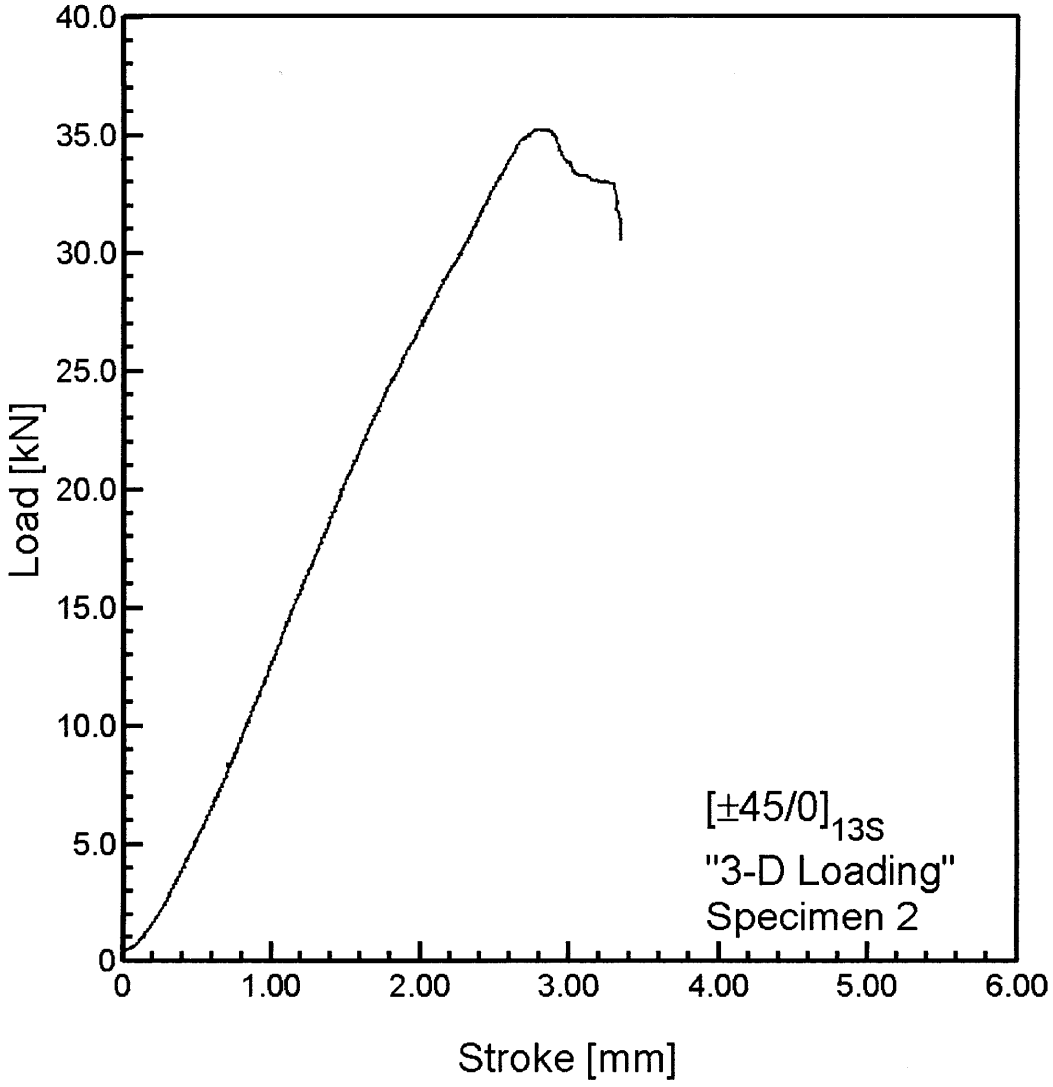

Figure A.43 Load versus stroke for $[\pm 45/0]_{13S}$ Specimen 2 tested to failure in "three-dimensional loading".

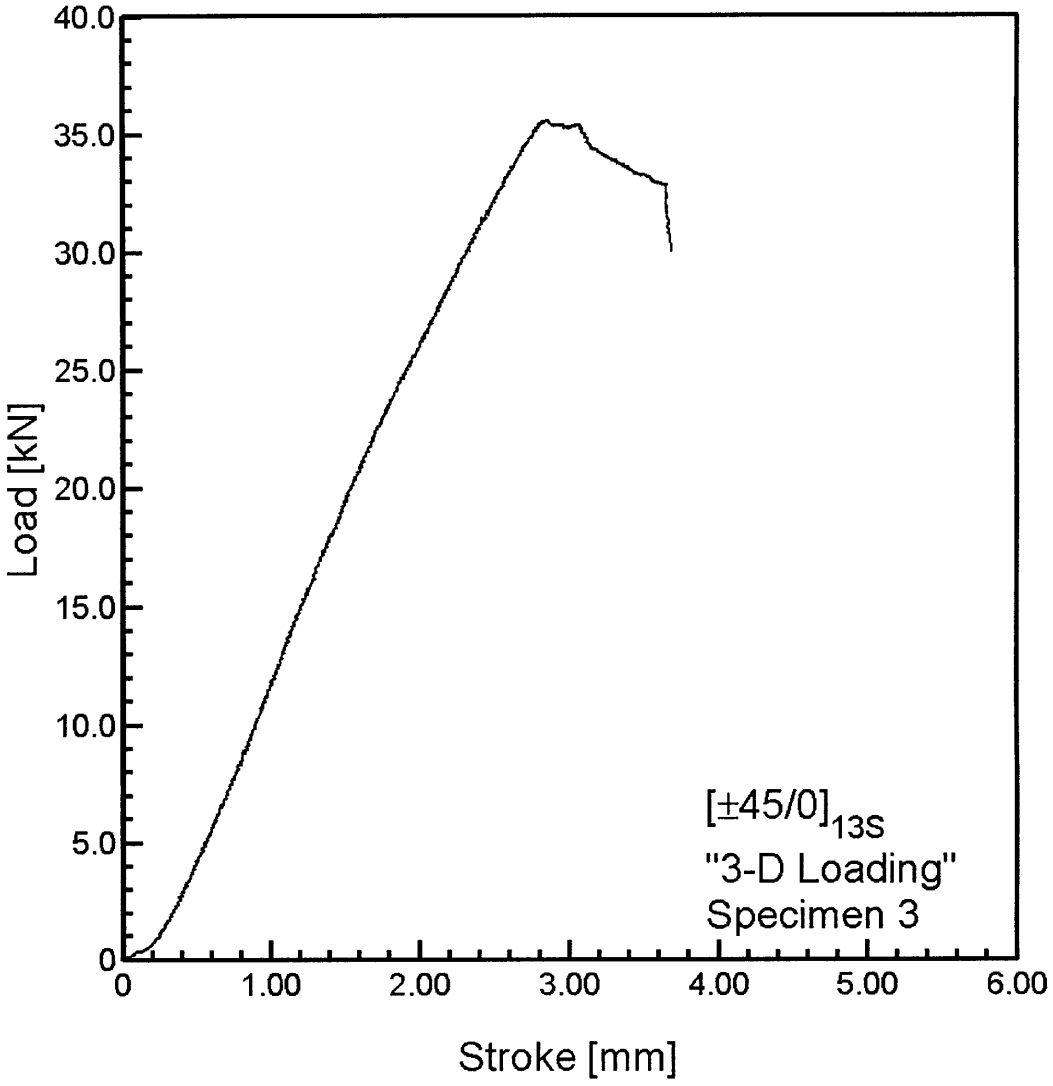

Figure A.44 Load versus stroke for $[\pm 45/0]_{13S}$ Specimen 3 tested to failure in "three-dimensional loading".

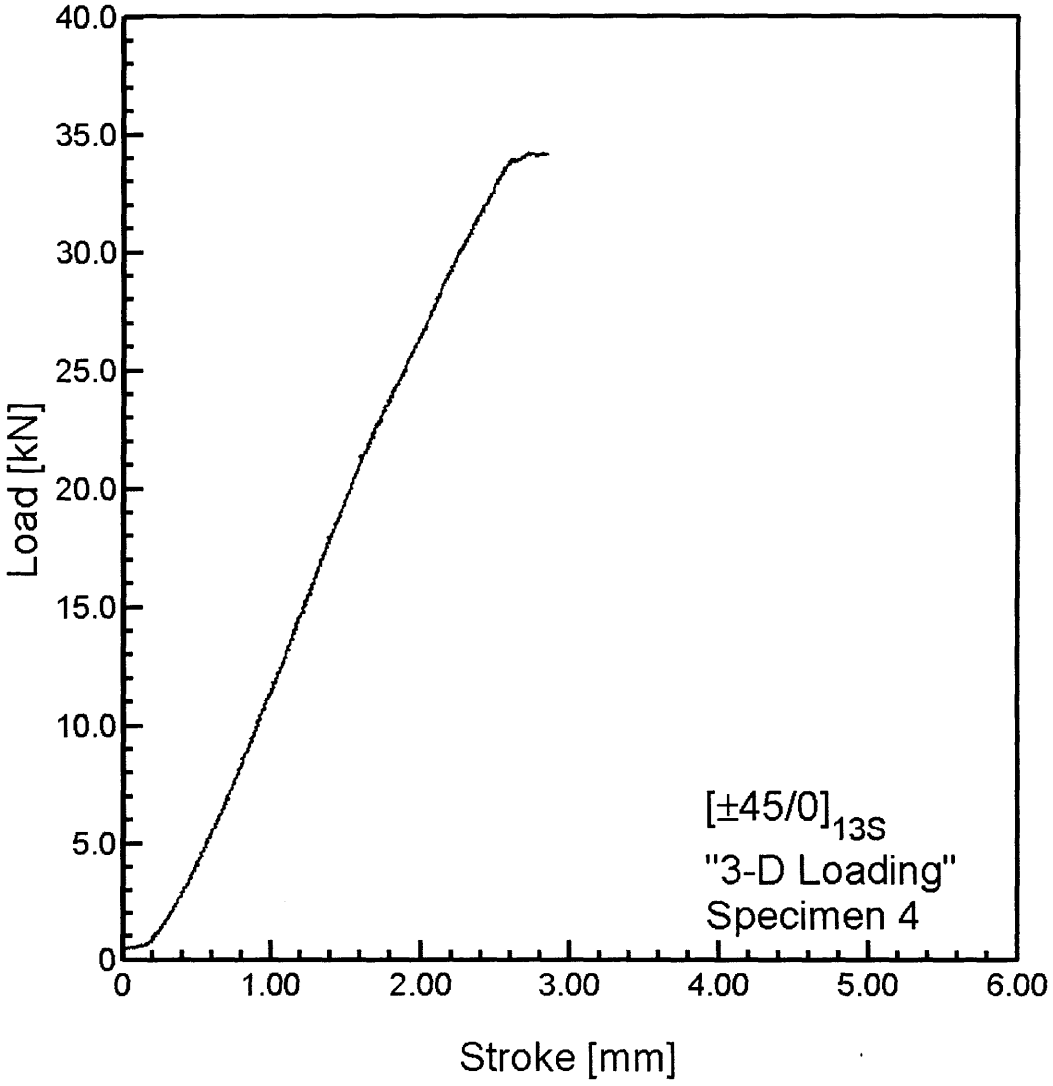

Figure A.45 Load versus stroke for $[\pm 45/0]_{13S}$ Specimen 4 tested to failure in "three-dimensional loading".

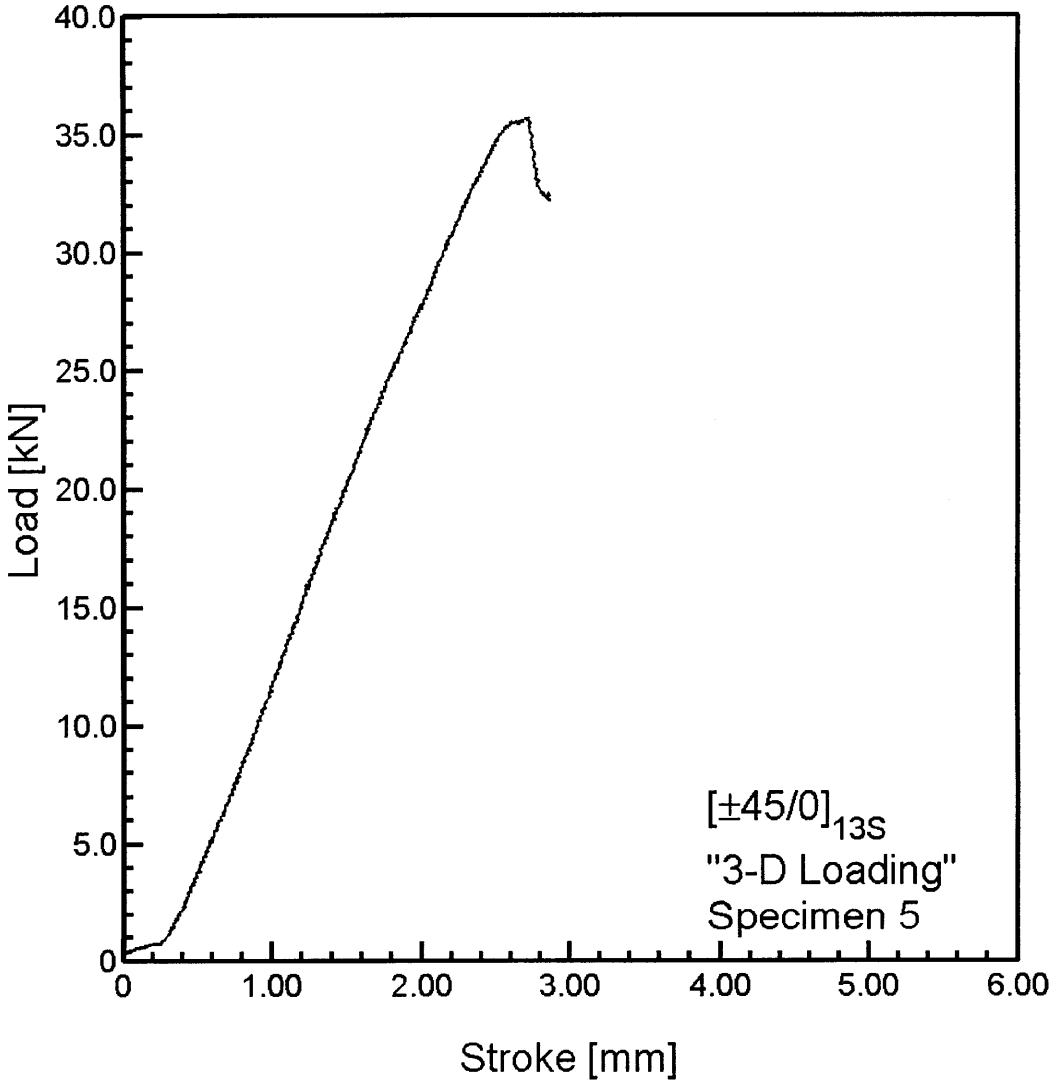

Figure A.46 Load versus stroke for $[\pm 45/0]_{13S}$ Specimen 5 tested to failure in "three-dimensional loading".

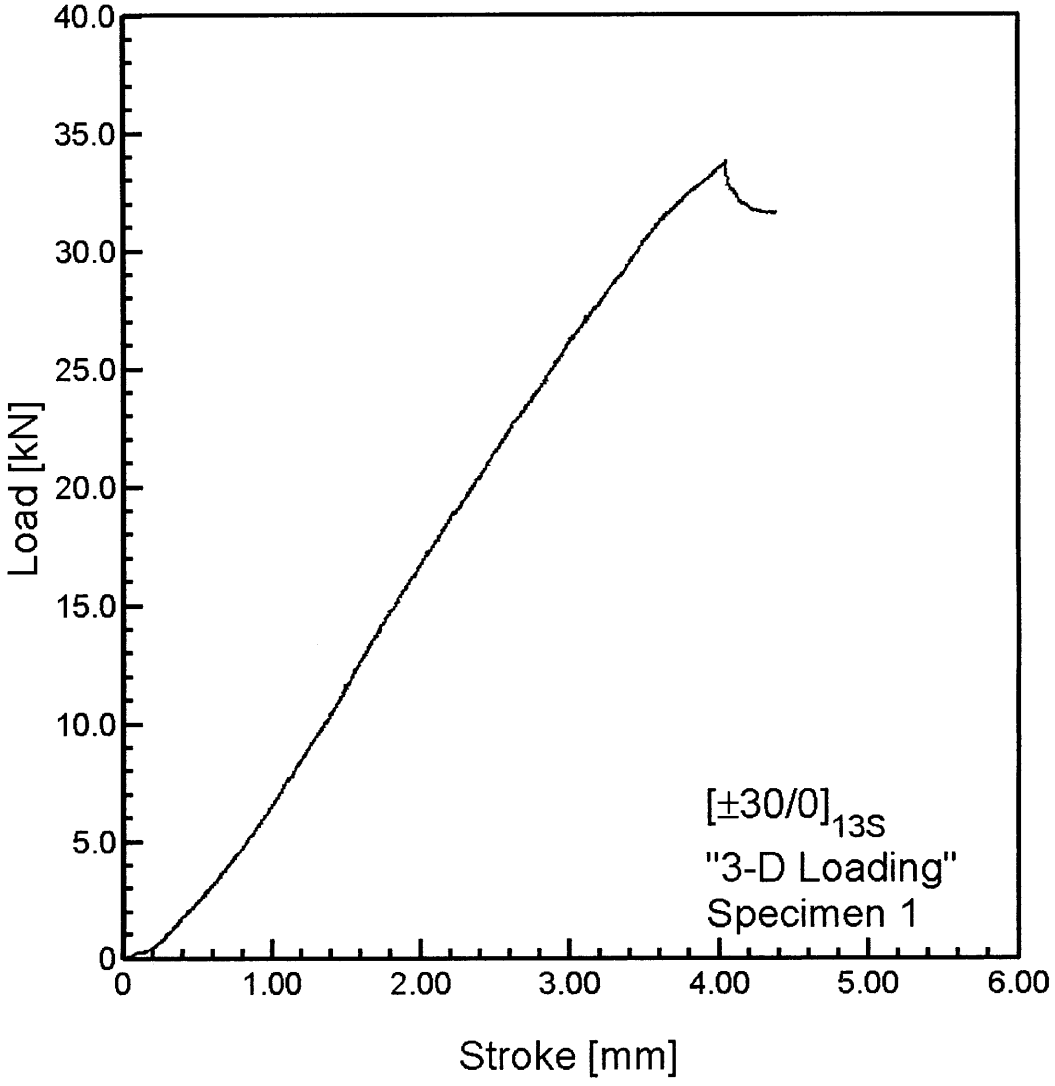

Figure A.47 Load versus stroke for $[\pm 30/0]_{13S}$ Specimen 1 tested to failure in "three-dimensional loading".

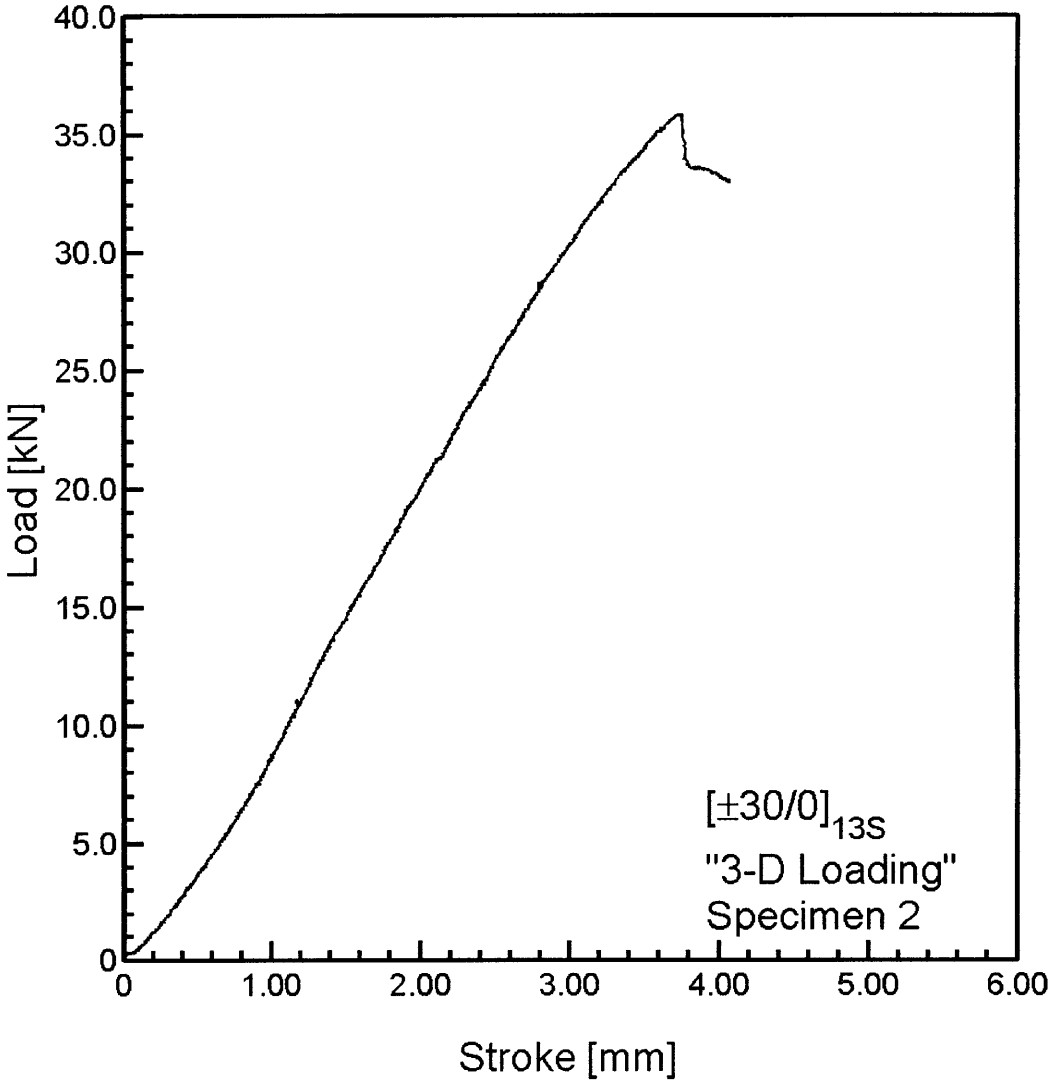

Figure A.48 Load versus stroke for $[\pm 30/0]_{13S}$ Specimen 2 tested to failure in "three-dimensional loading".

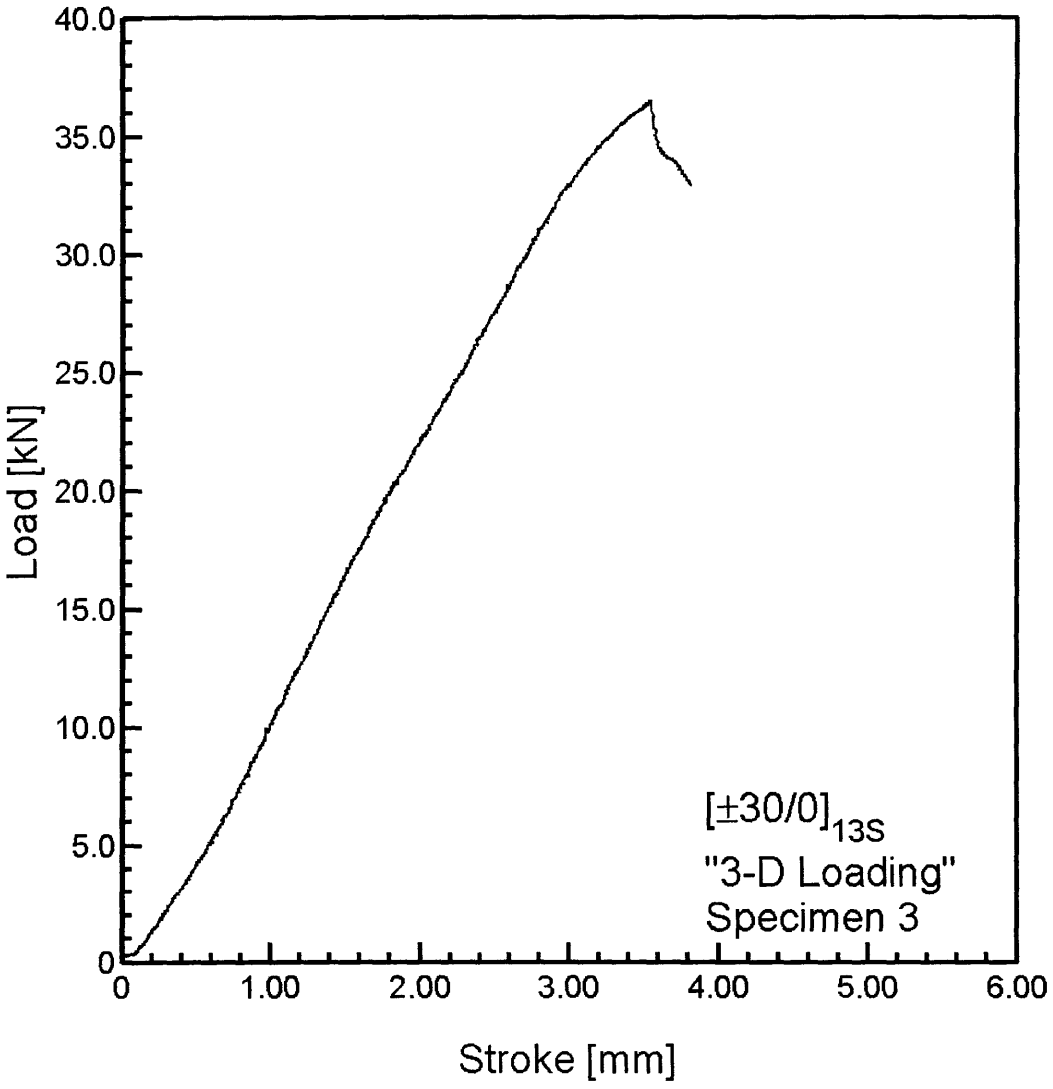

Figure A.49 Load versus stroke for $[\pm 30/0]_{13S}$ Specimen 3 tested to failure in "three-dimensional loading".

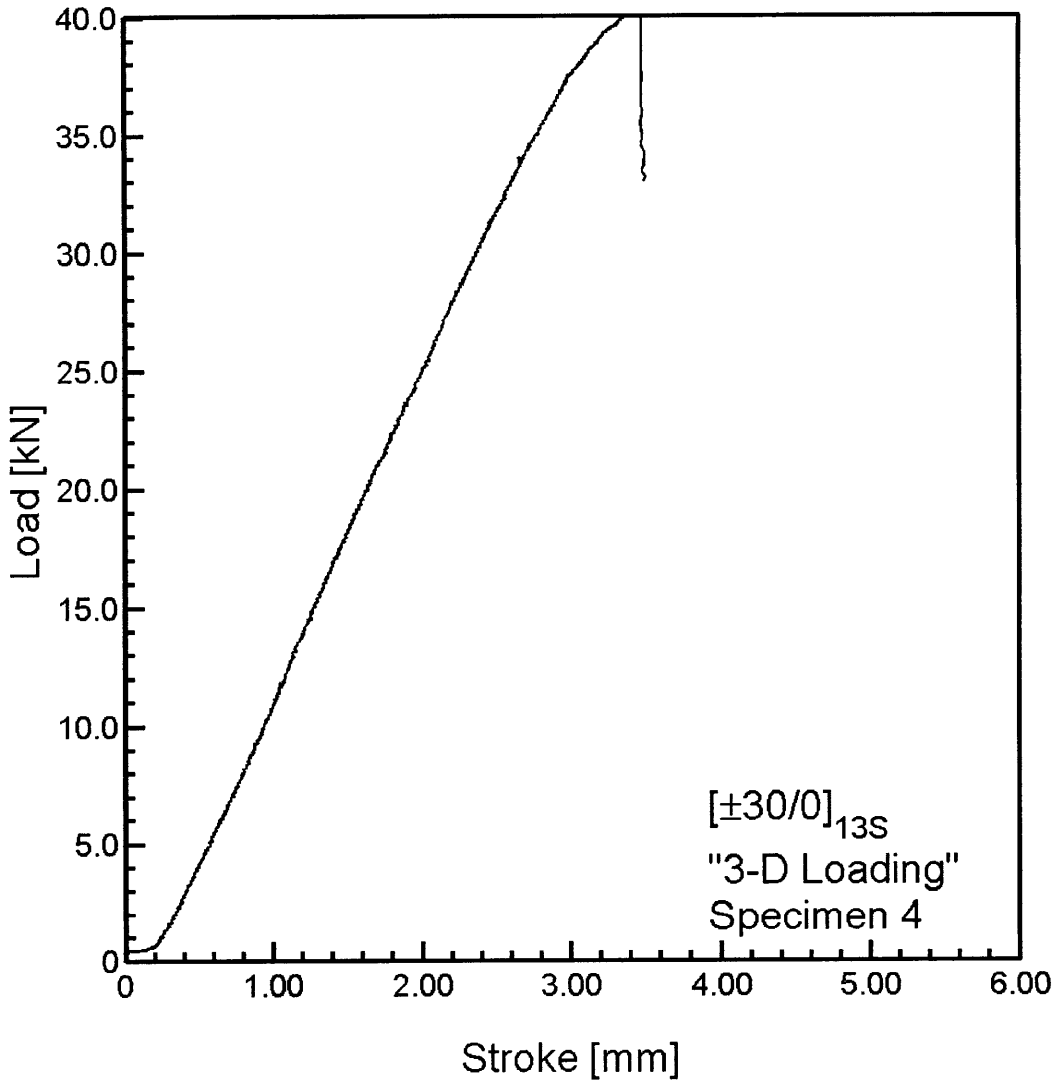

Figure A.50 Load versus stroke for $[\pm 30/0]_{13S}$ Specimen 4 tested to failure in "three-dimensional loading".

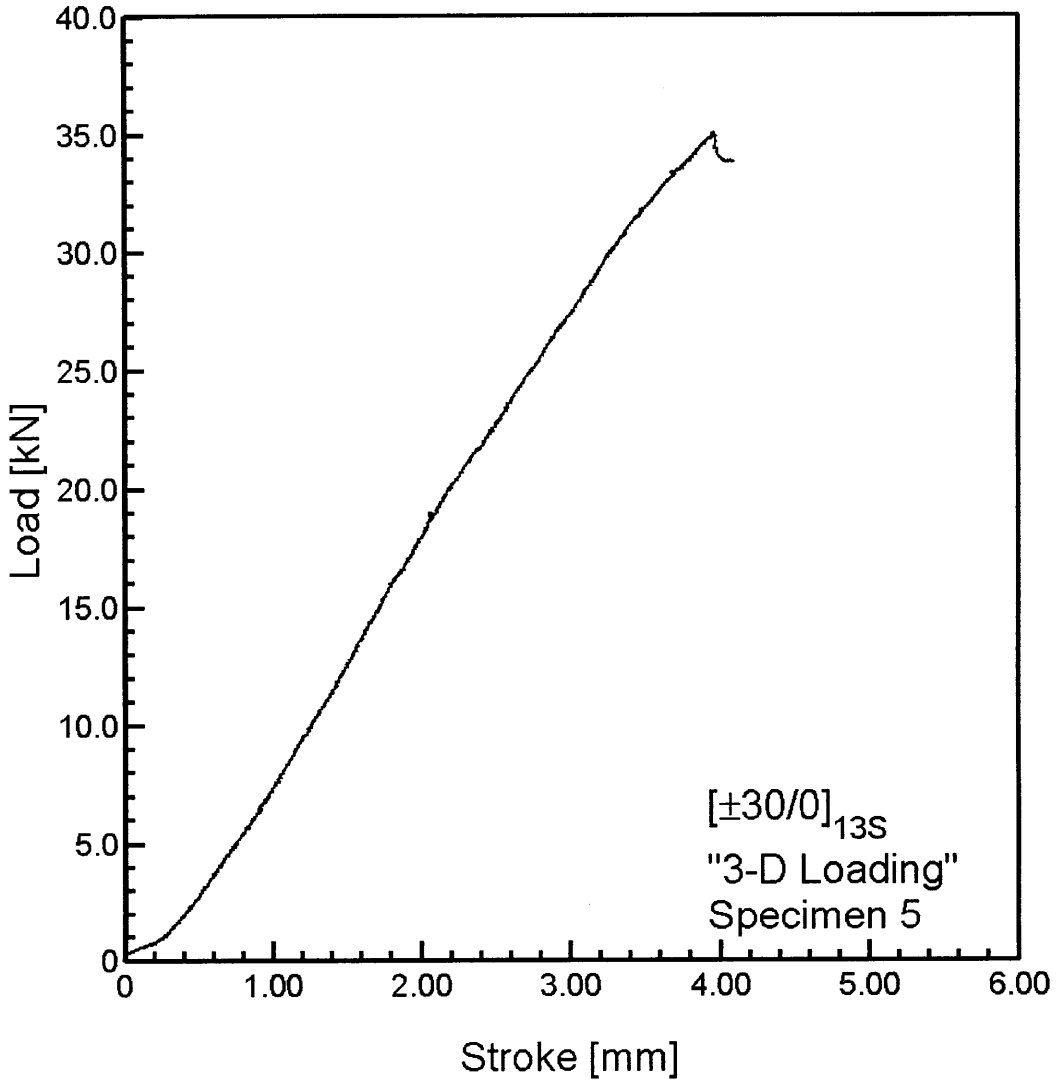

Figure A.51 Load versus stroke for $[\pm 30/0]_{13S}$ Specimen 5 tested to failure in "three-dimensional loading".

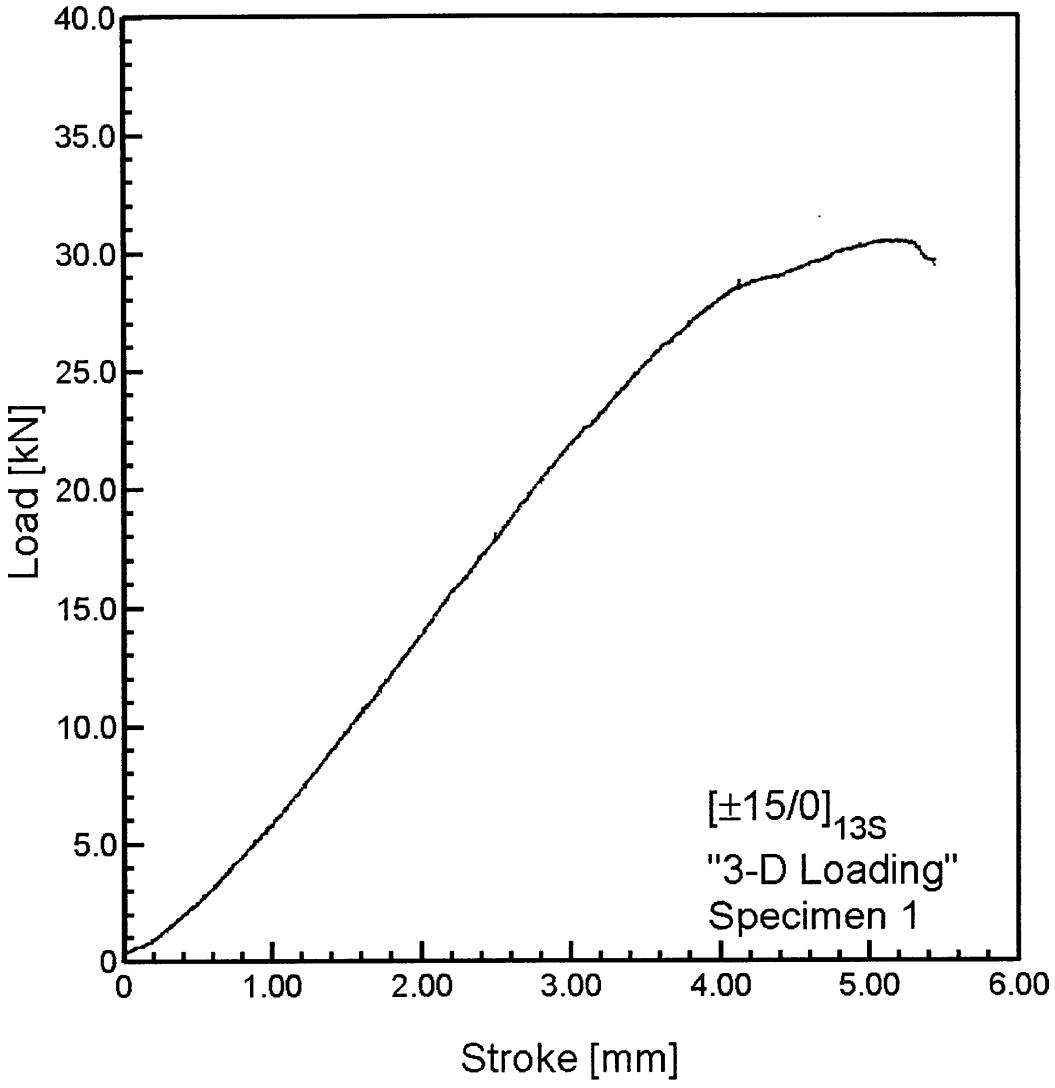

Figure A.52 Load versus stroke for $[\pm 15/0]_{13S}$ Specimen 1 tested to failure in "three-dimensional loading".

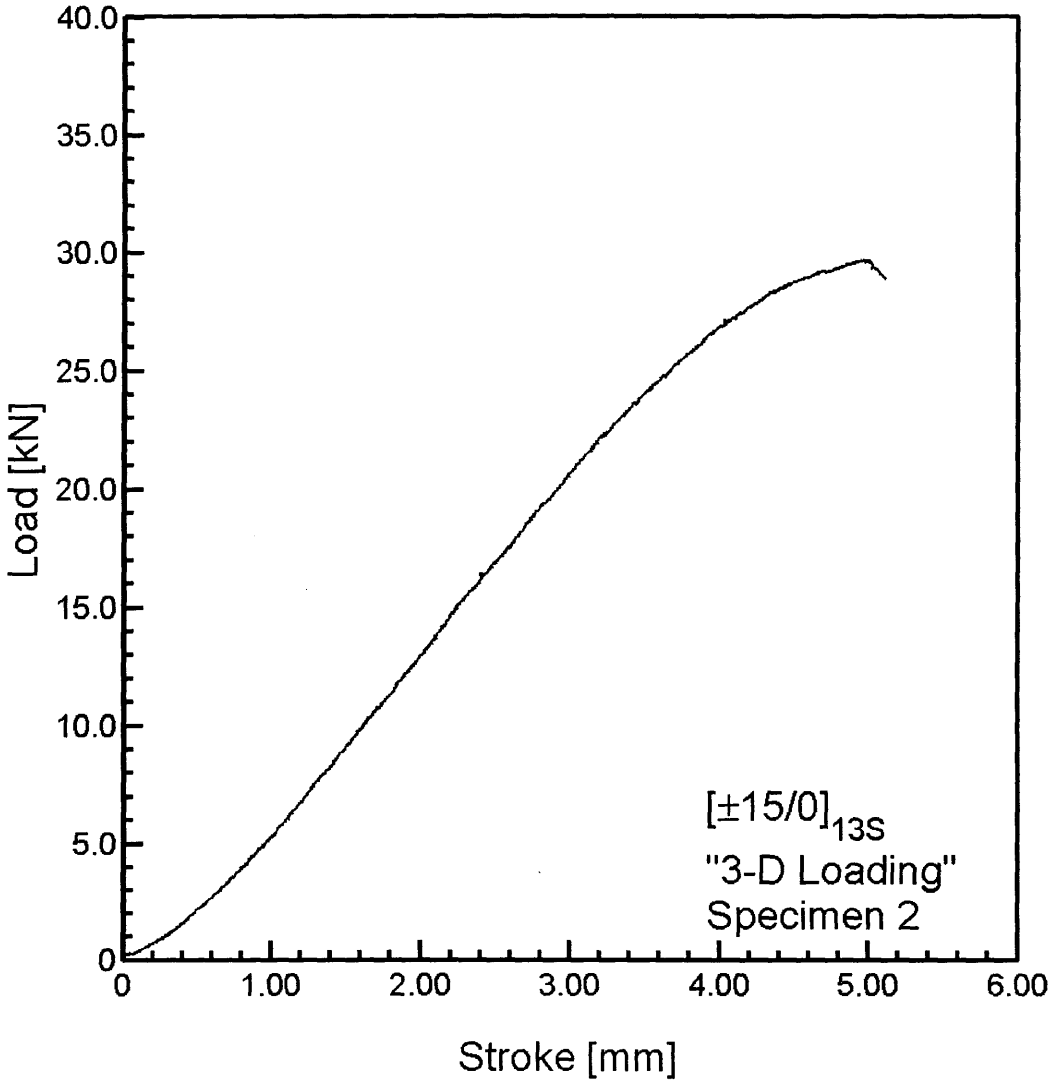

Figure A.53 Load versus stroke for $[\pm 15/0]_{13S}$ Specimen 2 tested to failure in "three-dimensional loading".

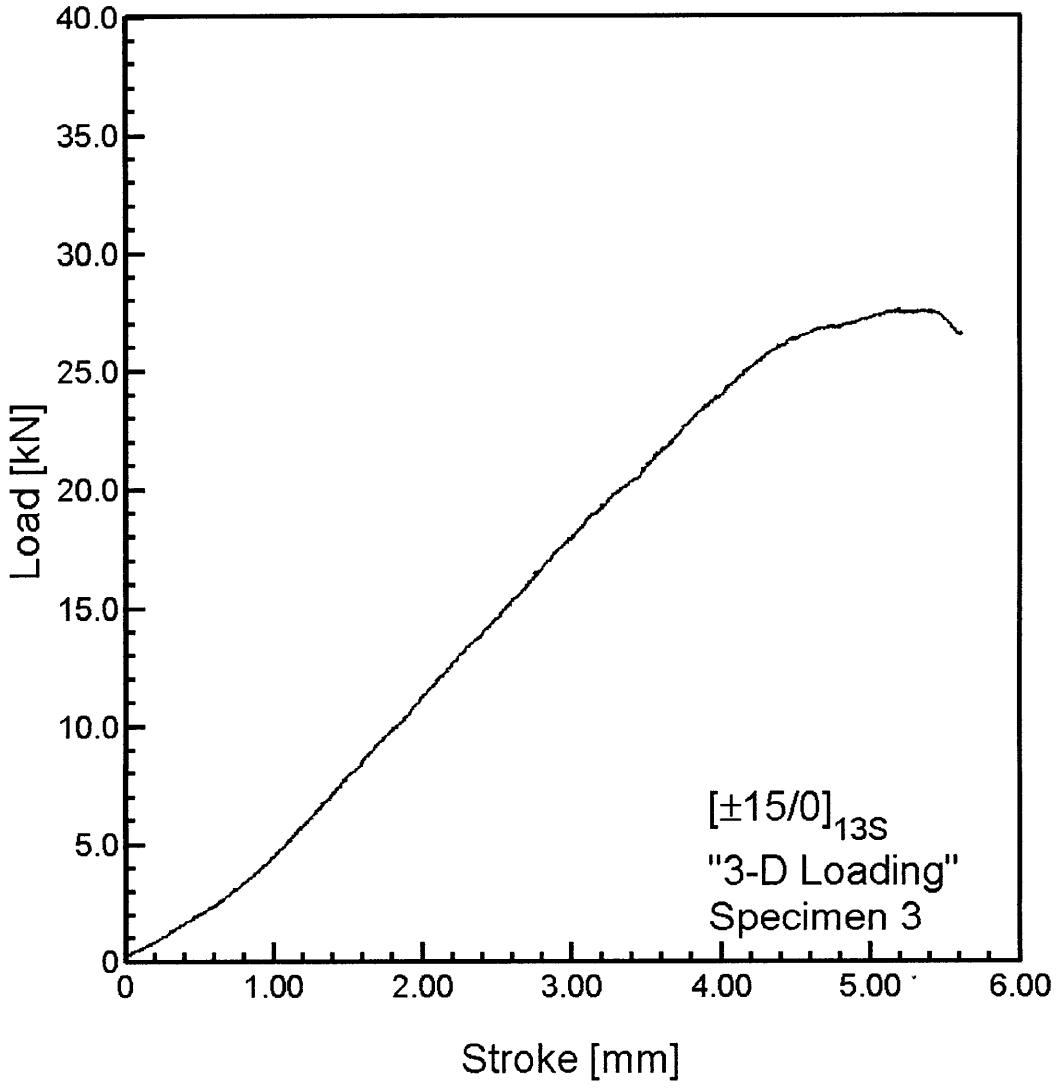

Figure A.54 Load versus stroke for $[\pm 15/0]_{13S}$ Specimen 3 tested to failure in "three-dimensional loading".

Appendix B

Photographs of "Two-Dimensional Loading" Specimens After Failure

Photographs of all specimens tested to final failure with the "two-dimensional loading" configuration (as discussed in Chapter 5) are presented in this appendix. The photographs are a top view and side view of each specimen. The testing procedures are those discussed in Chapter 4.

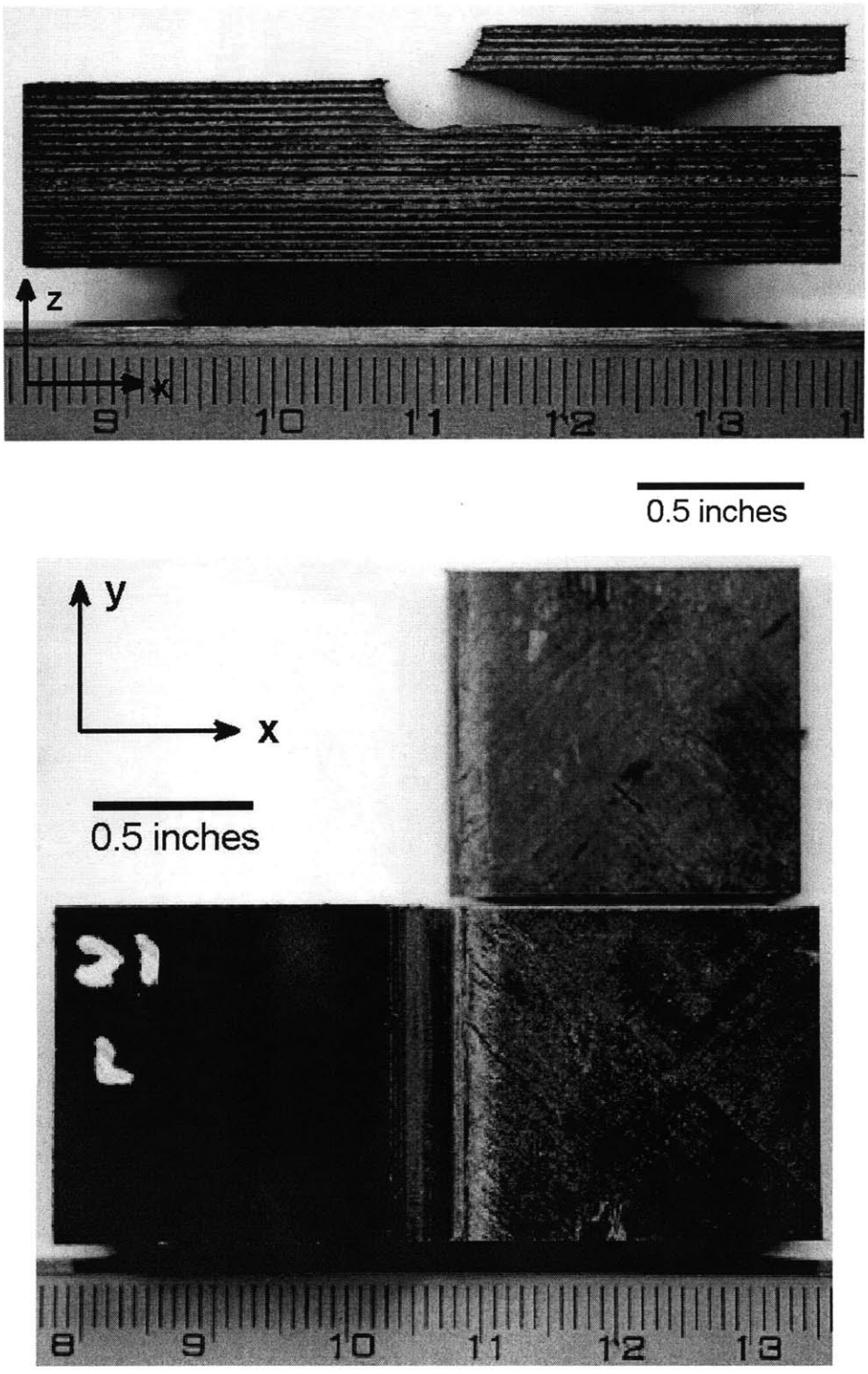

Figure B.1 Photographs of $[\pm 45/90/0]_{10S}$ Specimen 1, from previous work [34], tested to failure in "two-dimensional loading", shown via (*top*) side view, and (*bottom*) top view with delamination surfaces exposed.

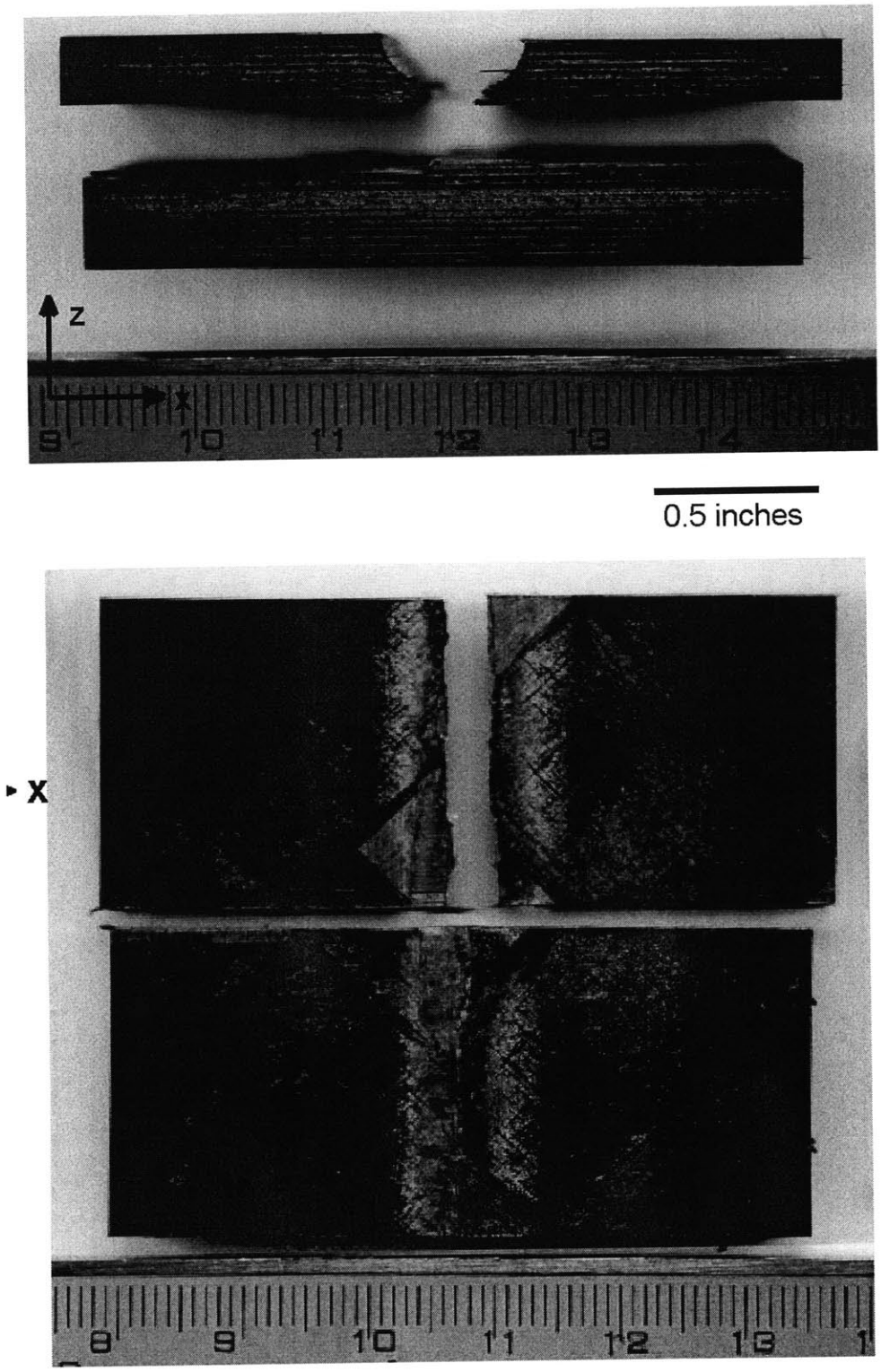

Figure B.2 Photographs of $[\pm 45/90/0]_{10S}$ Specimen 2, from previous work [34], tested to failure in "two-dimensional loading", shown via (*top*) side view, and (*bottom*) top view with delamination surfaces exposed.

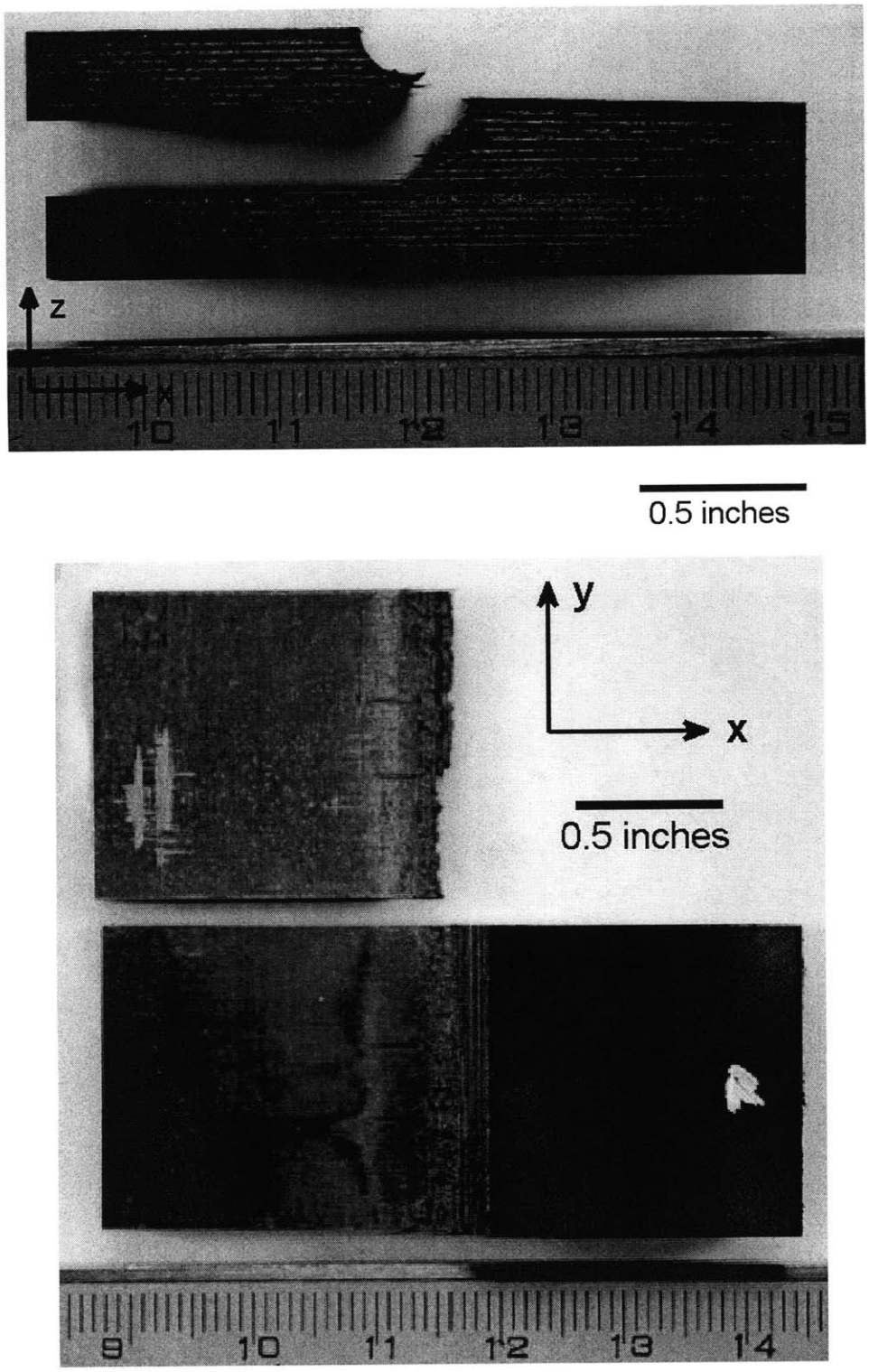

Figure B.3 Photographs of $[\pm 45/90/0]_{10S}$ Specimen 3, from previous work [34], tested to failure in "two-dimensional loading", shown via (*top*) side view, and (*bottom*) top view with delamination surfaces exposed.

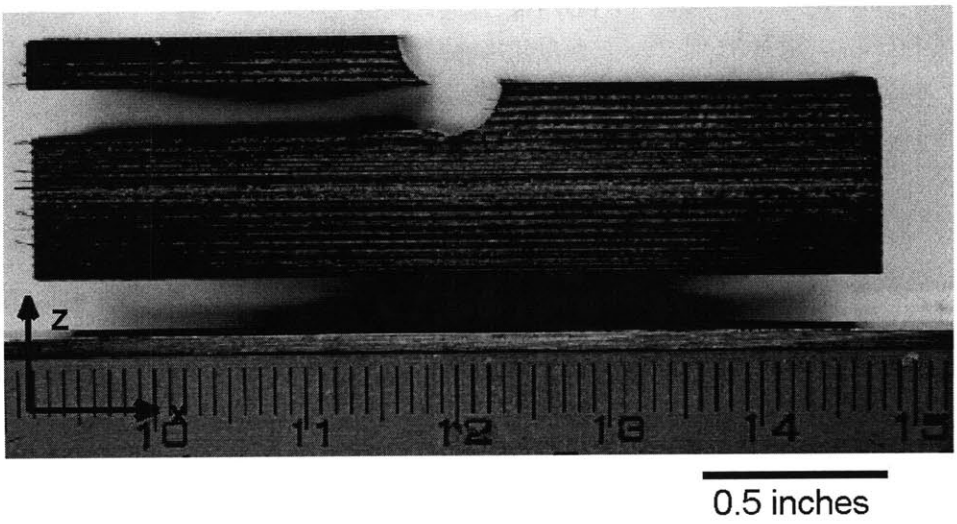

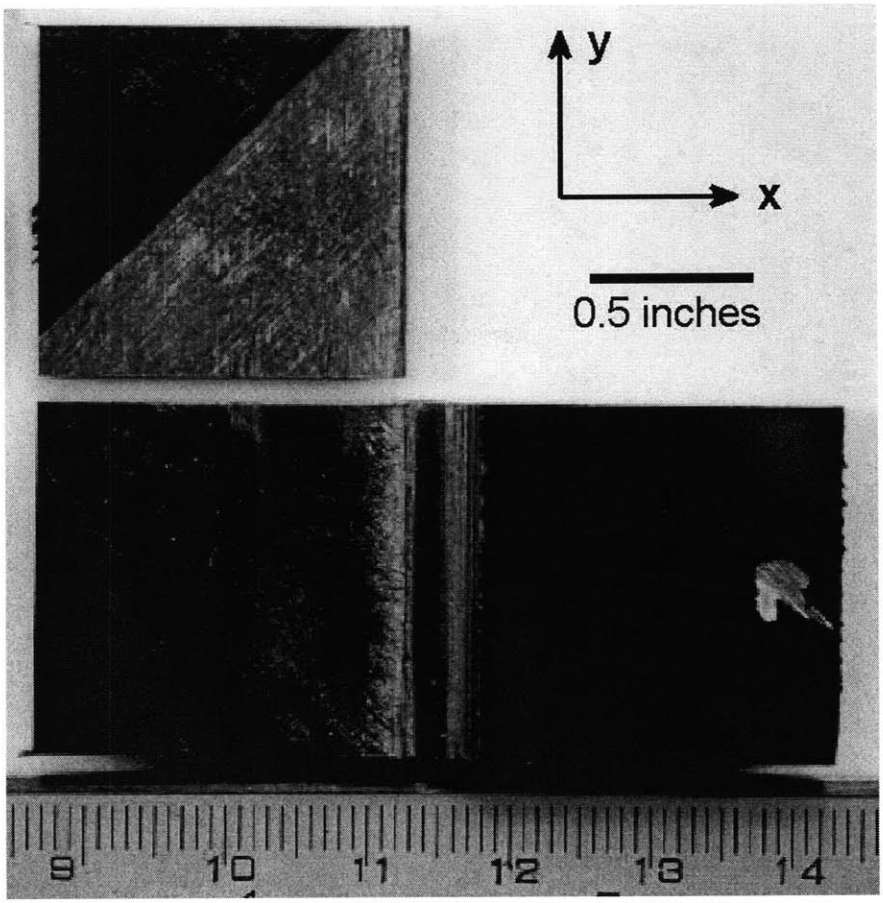

Figure B.4 Photographs of $[\pm 45/90/0]_{10S}$ Specimen 4, from previous work [34], tested to failure in "two-dimensional loading", shown via (*top*) side view, and (*bottom*) top view with delamination surfaces exposed.

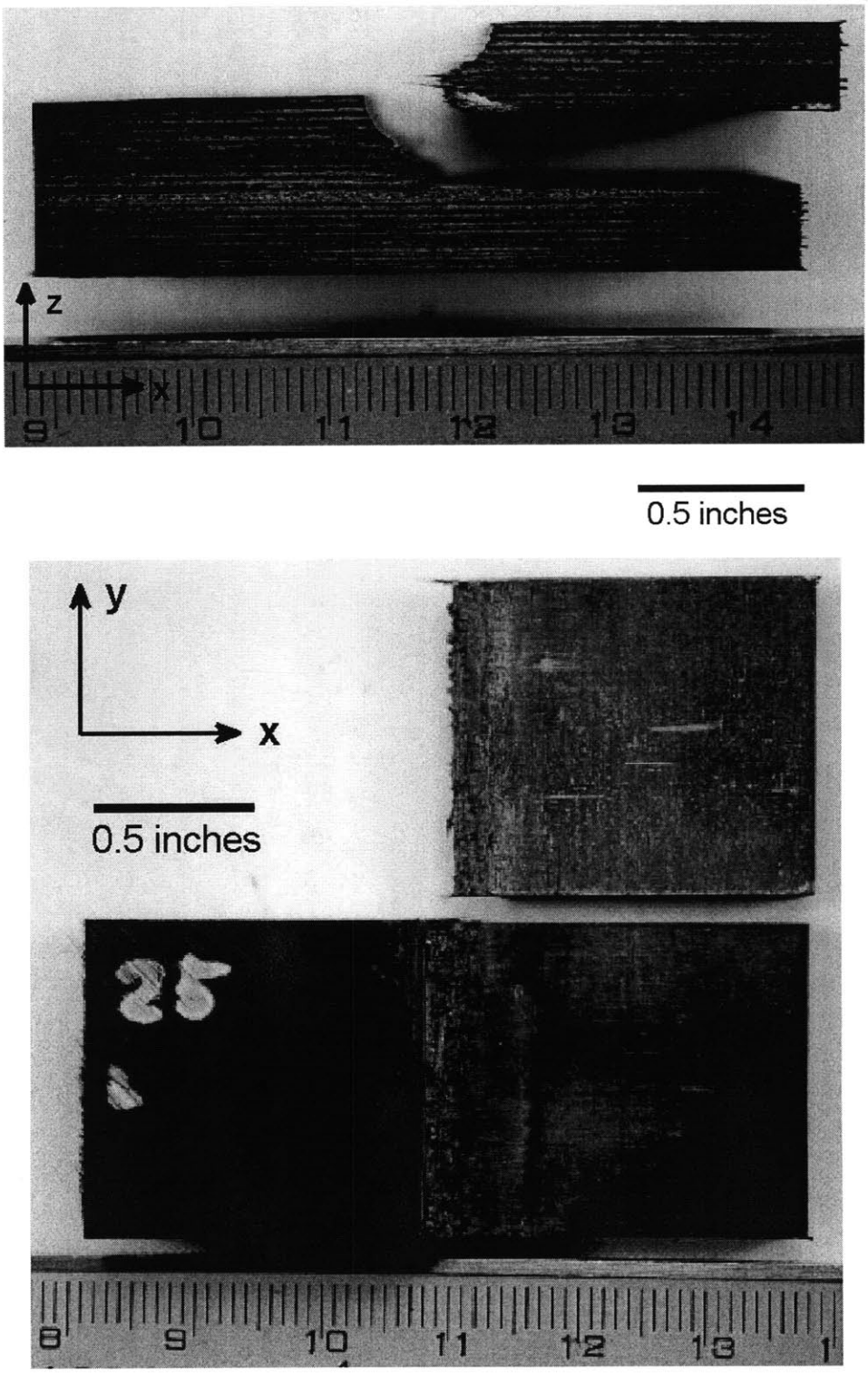

Figure B.5 Photographs of $[\pm 45/90/0]_{10S}$ Specimen 5, from previous work [34], tested to failure in "two-dimensional loading", shown via (*top*) side view, and (*bottom*) top view with delamination surfaces exposed.

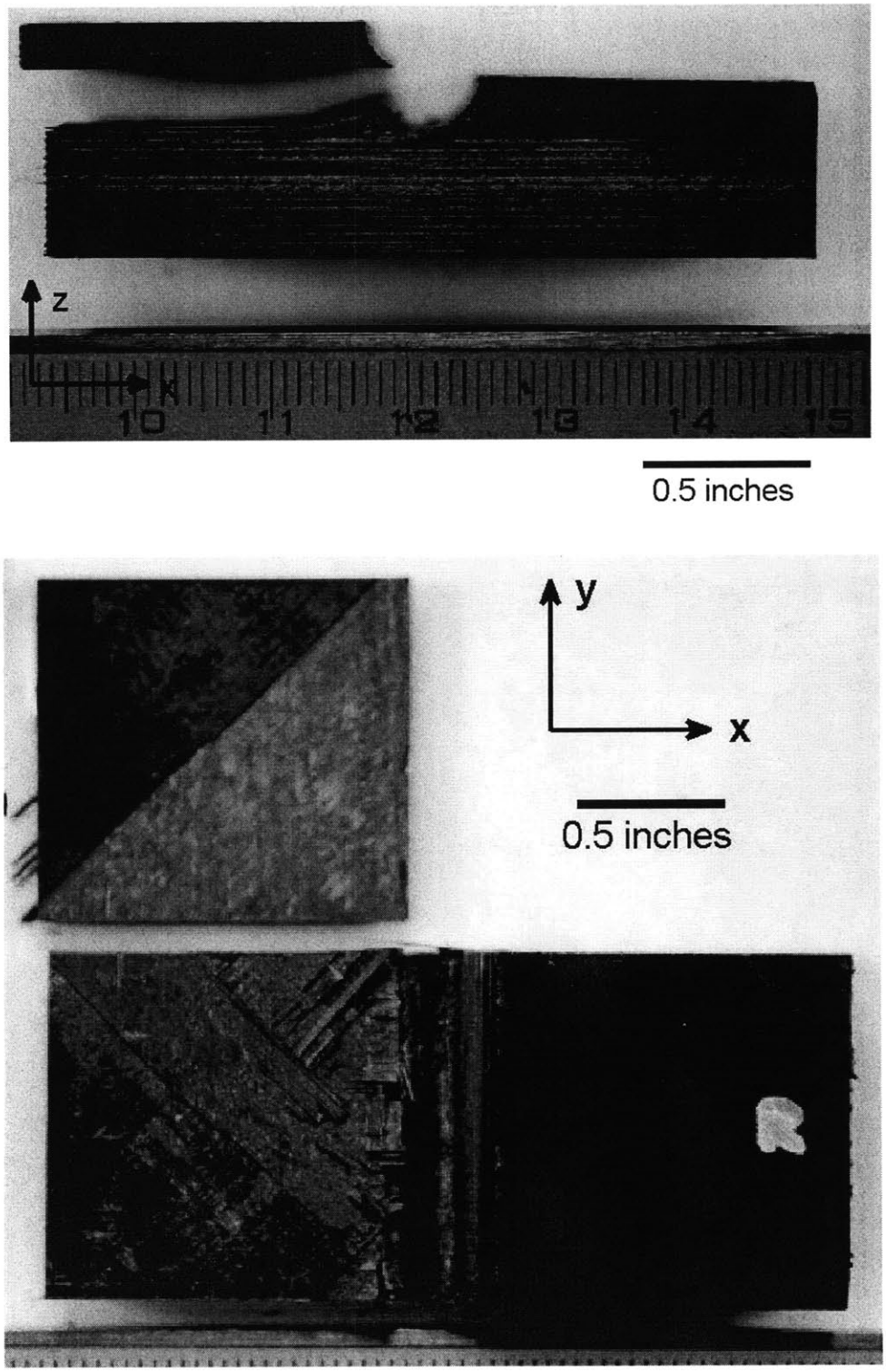

Figure B.6 Photographs of $[\pm 45/90/0]_{10S}$ Specimen 6, from previous work [34], tested to failure in "two-dimensional loading", shown via (*top*) side view, and (*bottom*) top view with delamination surfaces exposed.

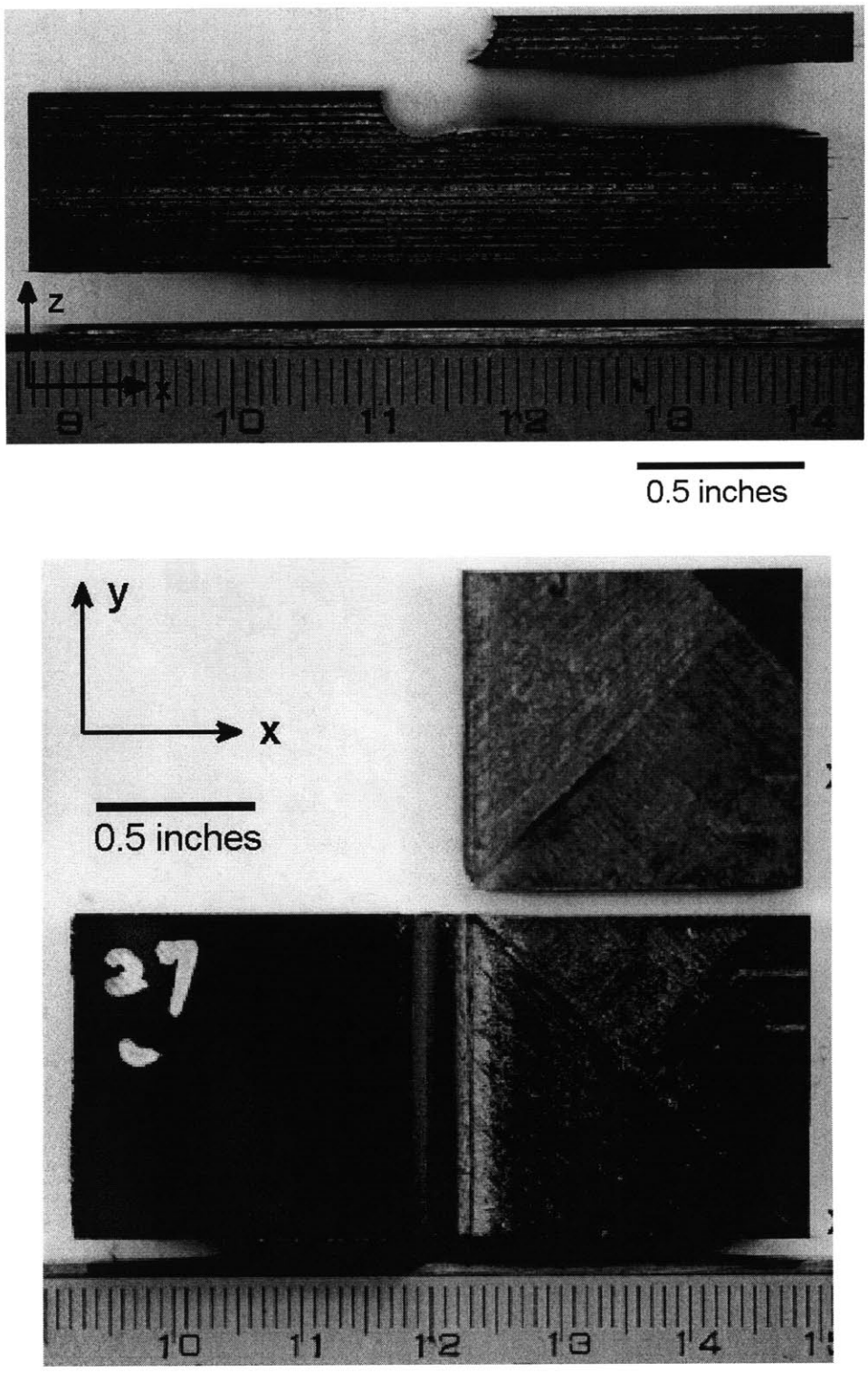

Figure B.7 Photographs of $[\pm 45/90/0]_{10S}$ Specimen 7, from previous work [34], tested to failure in "two-dimensional loading", shown via (*top*) side view, and (*bottom*) top view with delamination surfaces exposed.

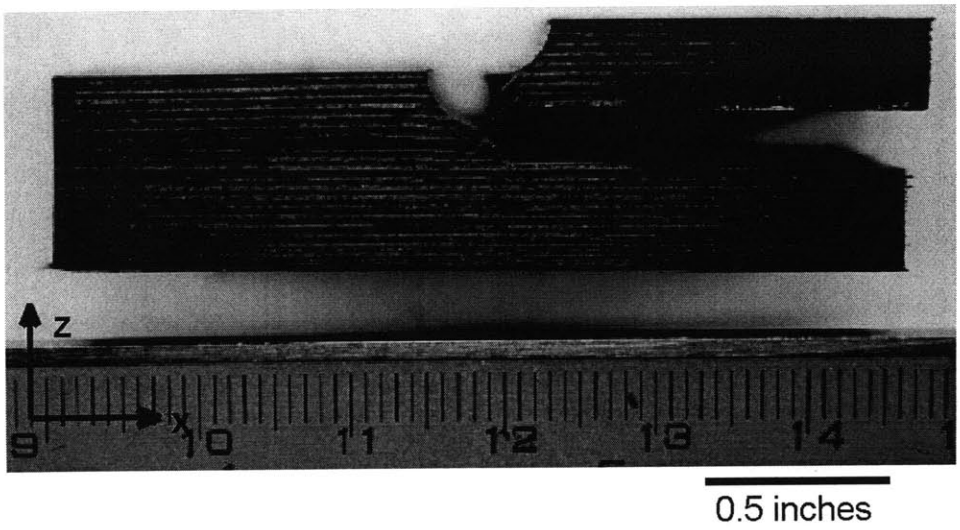

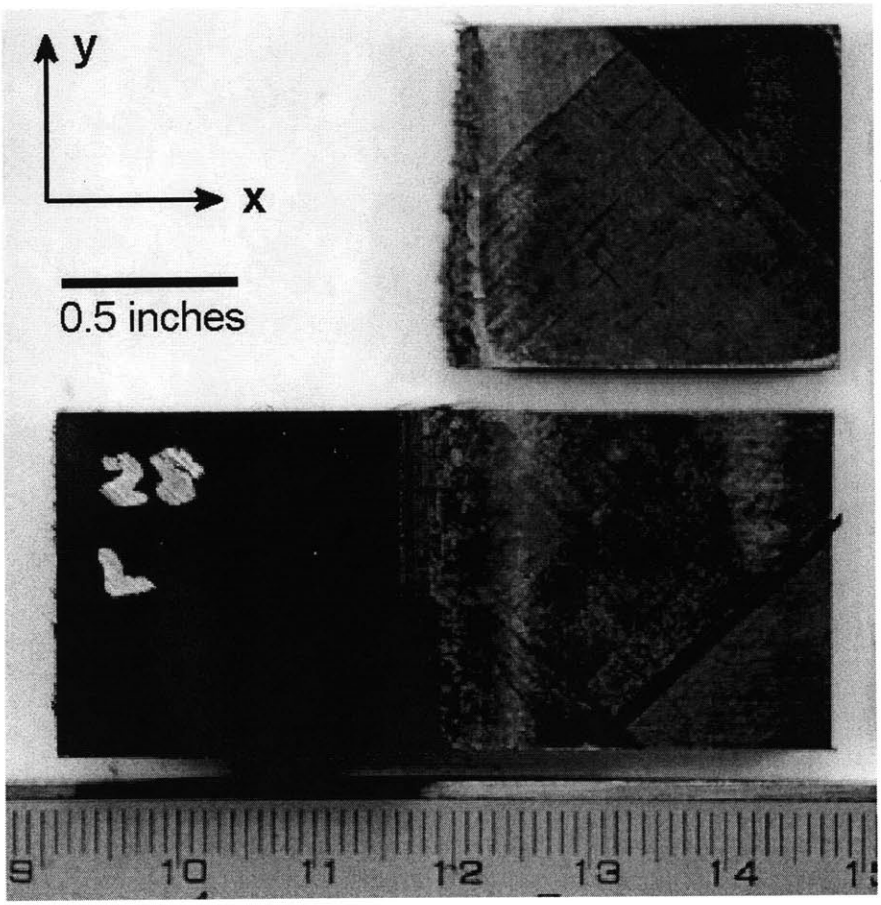

Figure B.8 Photographs of $[\pm 45/90/0]_{10S}$ Specimen 8, from previous work [34], tested to failure in "two-dimensional loading", shown via (*top*) side view, and (*bottom*) top view with delamination surfaces exposed.

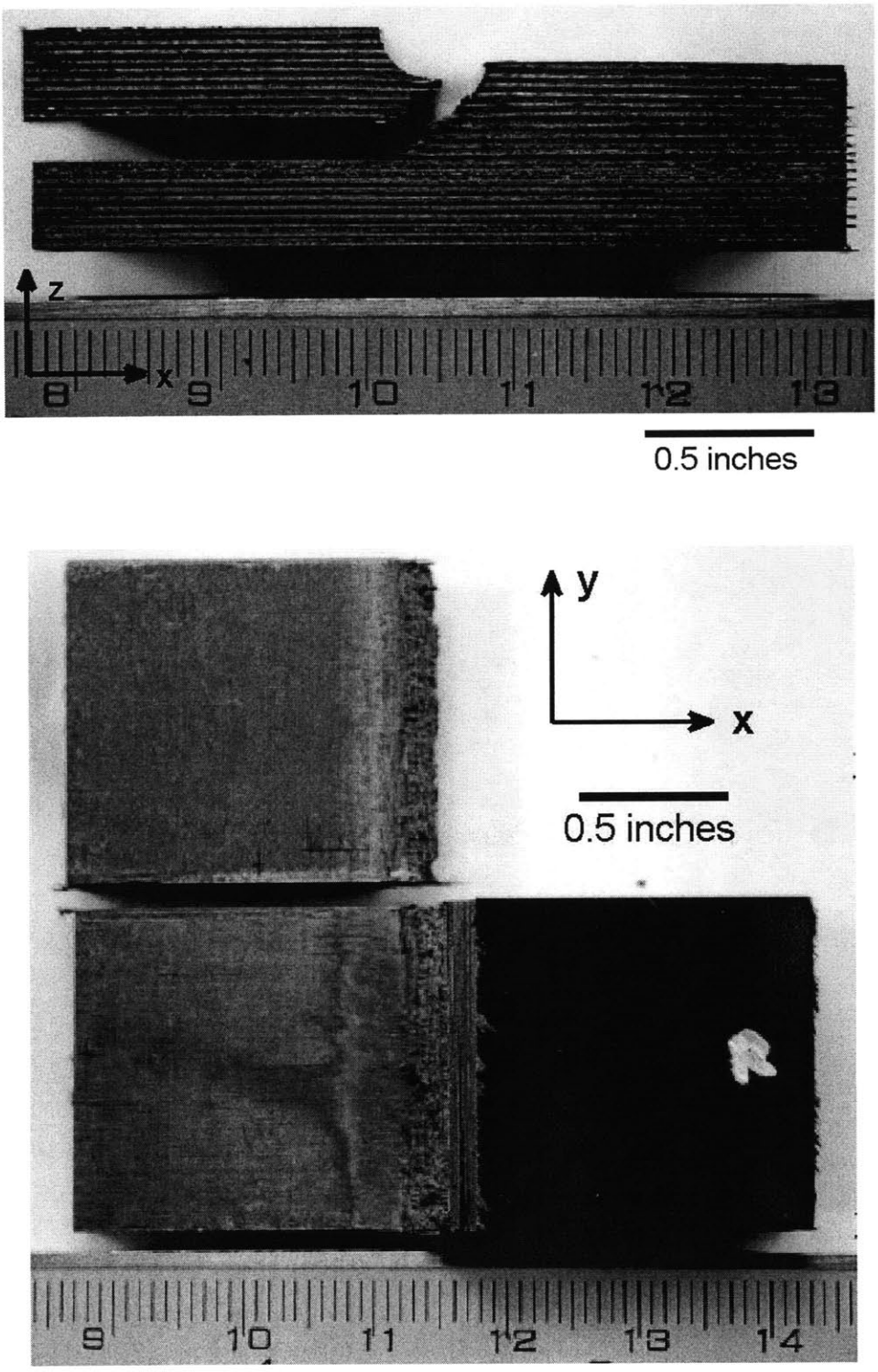

Figure B.9 Photographs of $[\pm 45/90/0]_{10S}$ Specimen 9, from previous work [34], tested to failure in "two-dimensional loading", shown via (*top*) side view, and (*bottom*) top view with delamination surfaces exposed.

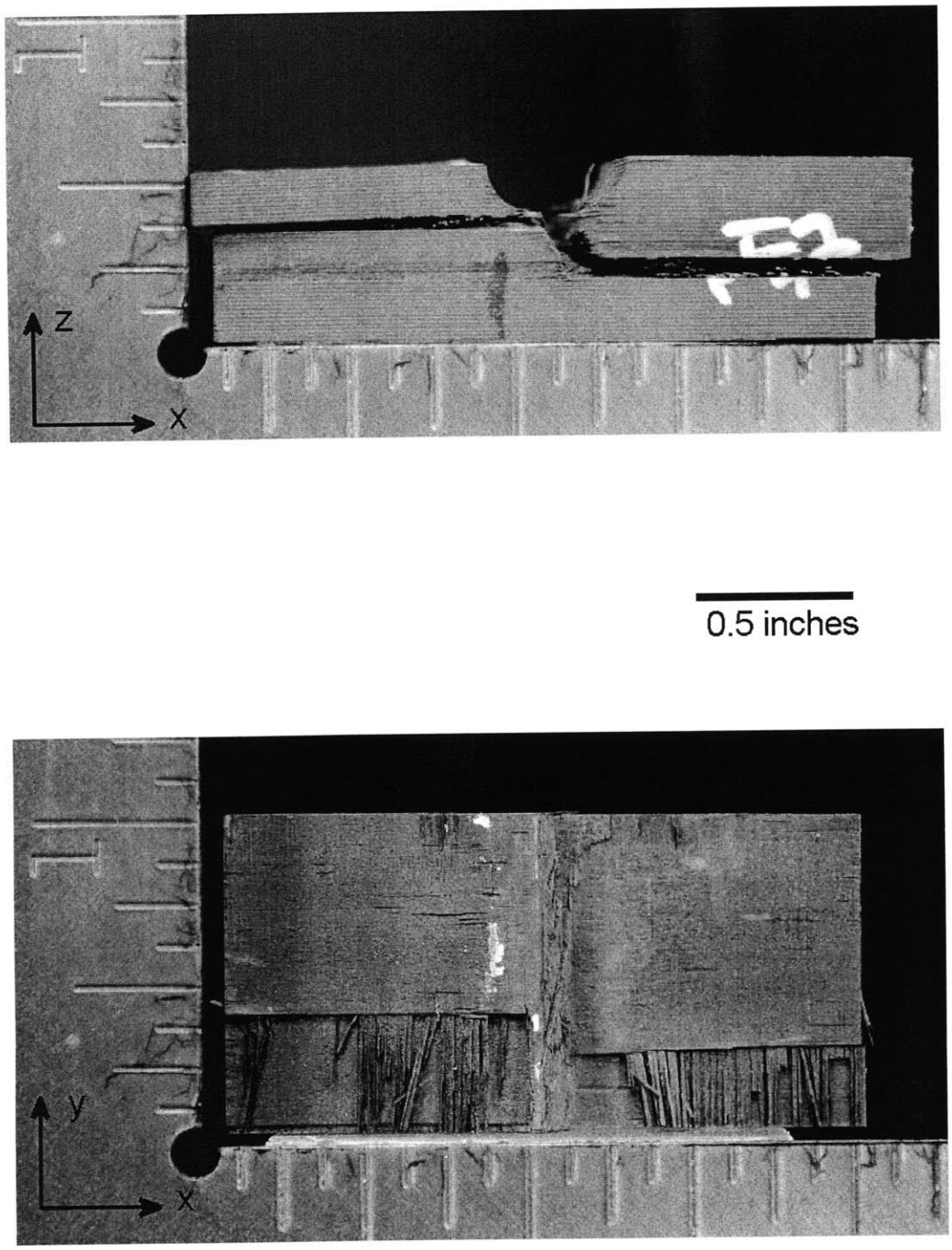

Figure B.10 Photographs of $[90/0]_{20S}$ Specimen 1, tested to failure in "two-dimensional loading", shown via (*top*) side view, and (*bottom*) top view with delamination surfaces exposed.

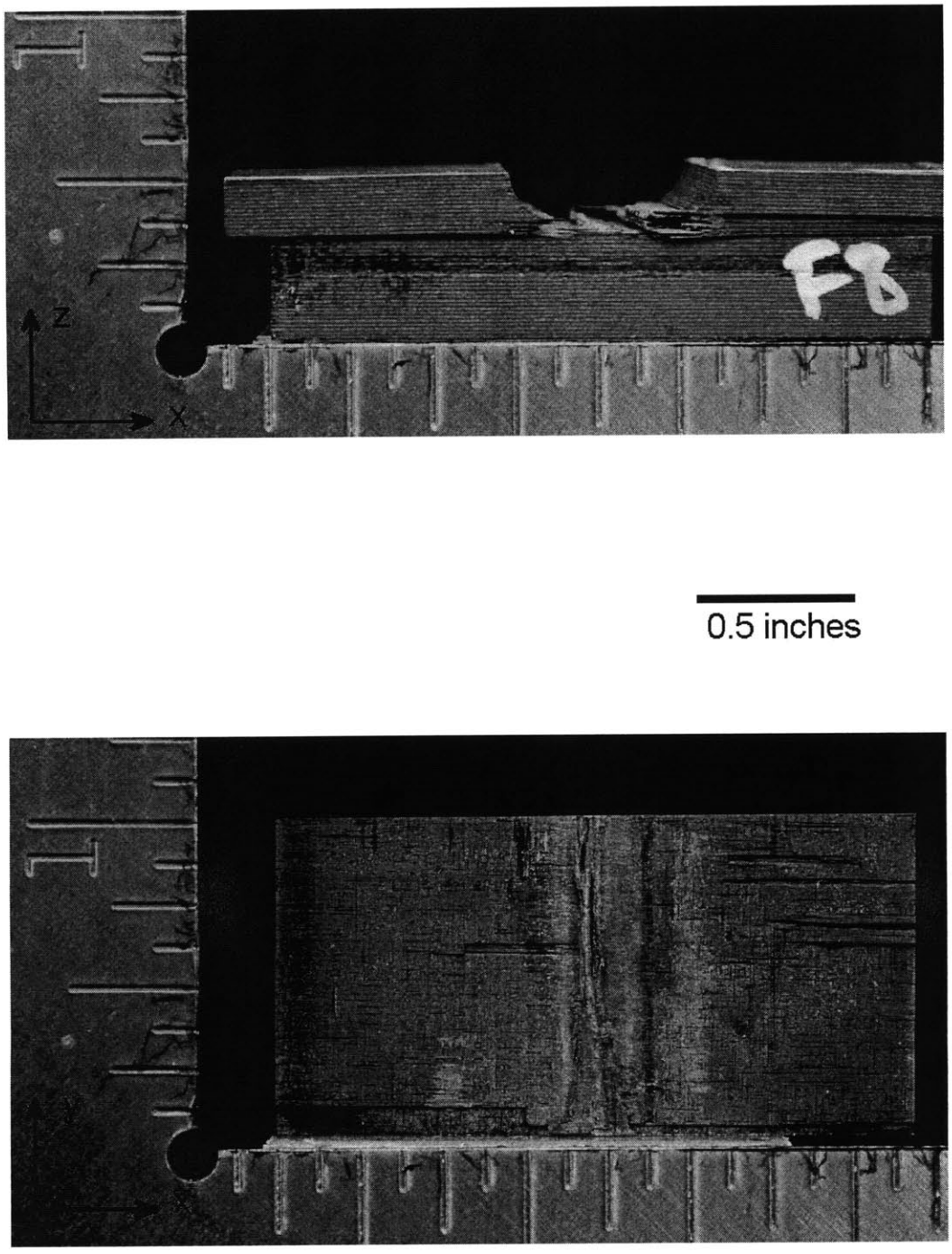

Figure B.11 Photographs of $[90/0]_{20S}$ Specimen 2, tested to failure in "two-dimensional loading", shown via (*top*) side view, and (*bottom*) top view with delamination surfaces exposed.

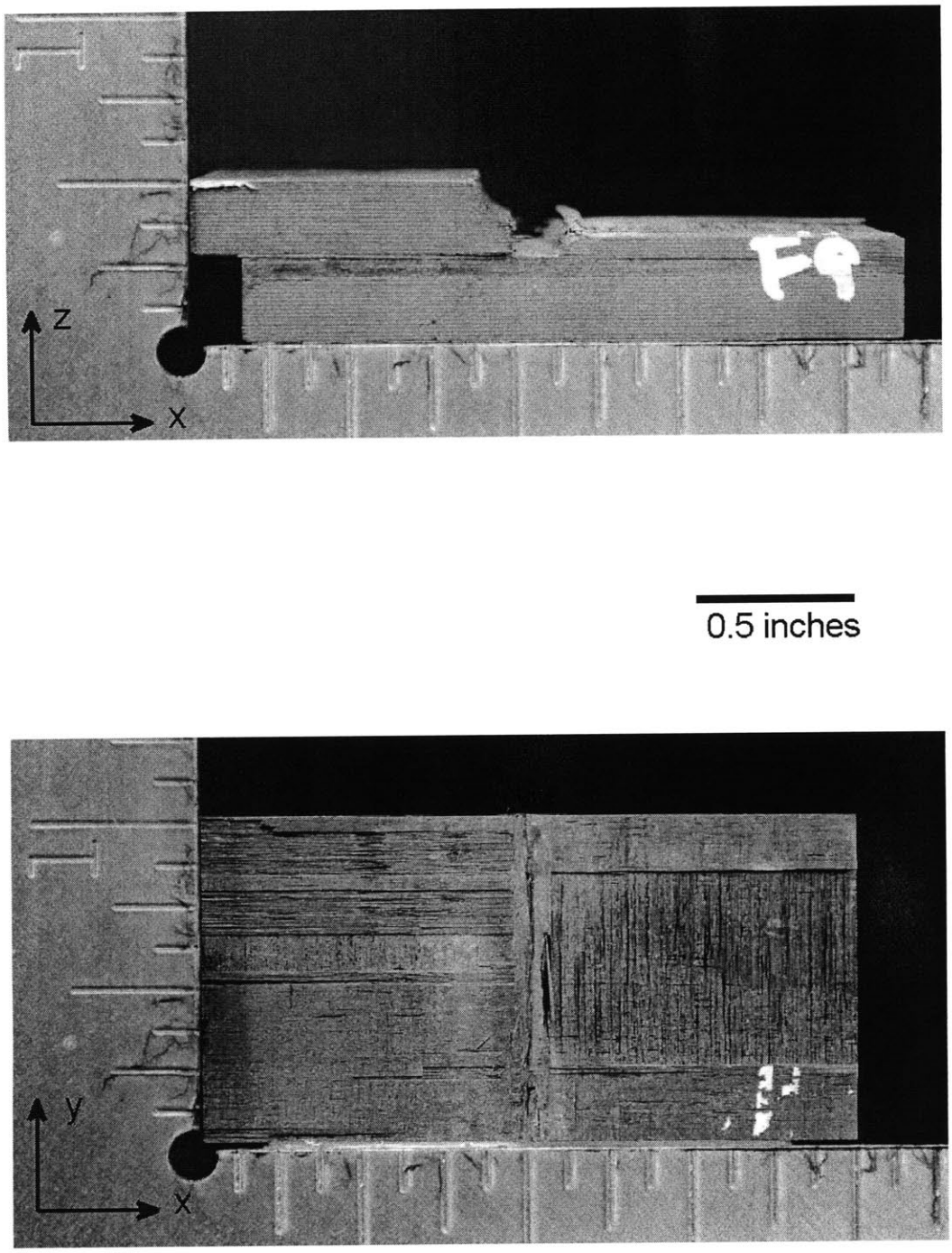

Figure B.12 Photographs of $[90/0]_{20S}$ Specimen 3, tested to failure in "two-dimensional loading", shown via (*top*) side view, and (*bottom*) top view with delamination surfaces exposed.

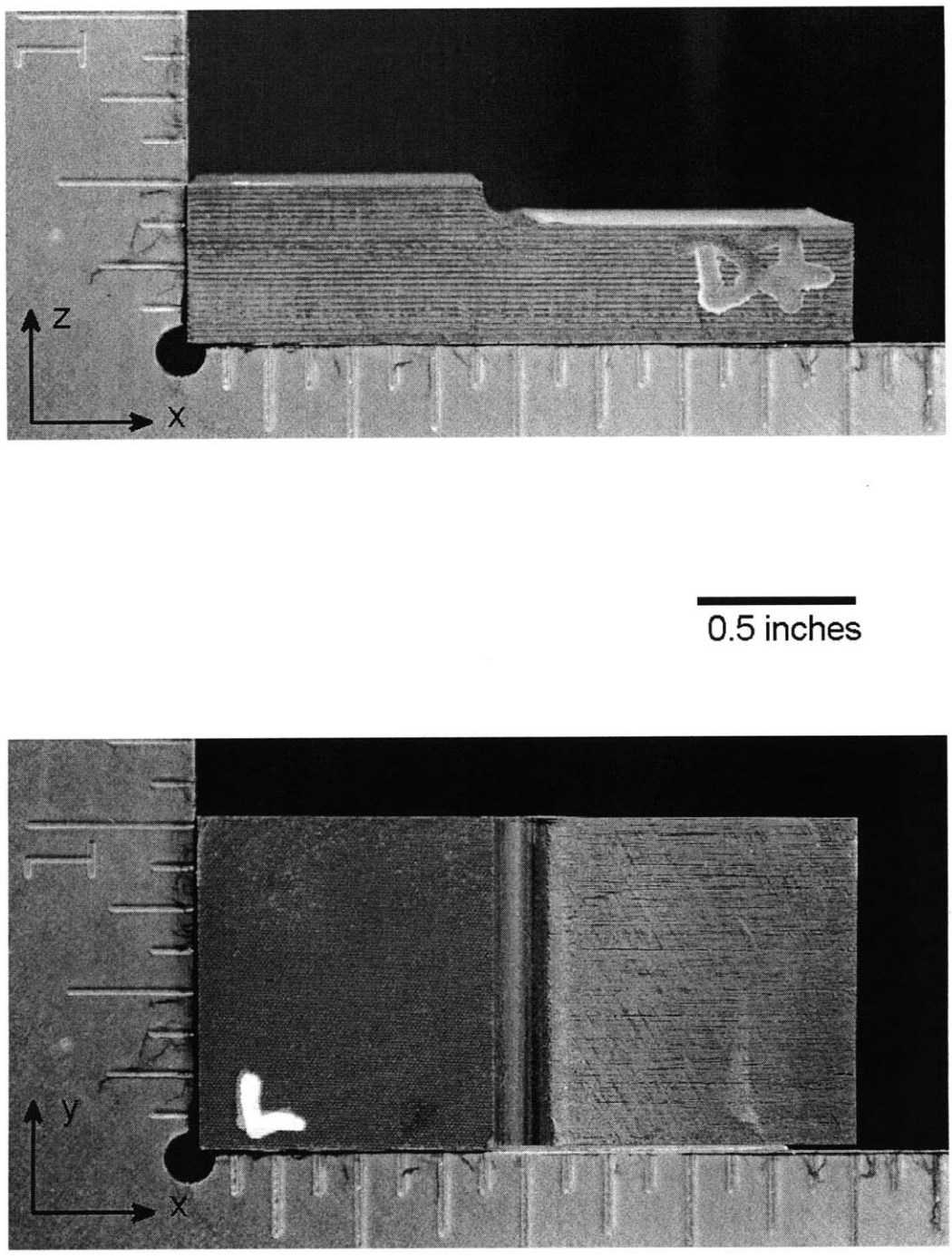

Figure B.13 Photographs of $[\pm 60/0]_{13S}$ Specimen 1, tested to failure in "two-dimensional loading", shown via (*top*) side view, and (*bottom*) top view with delamination surfaces exposed.

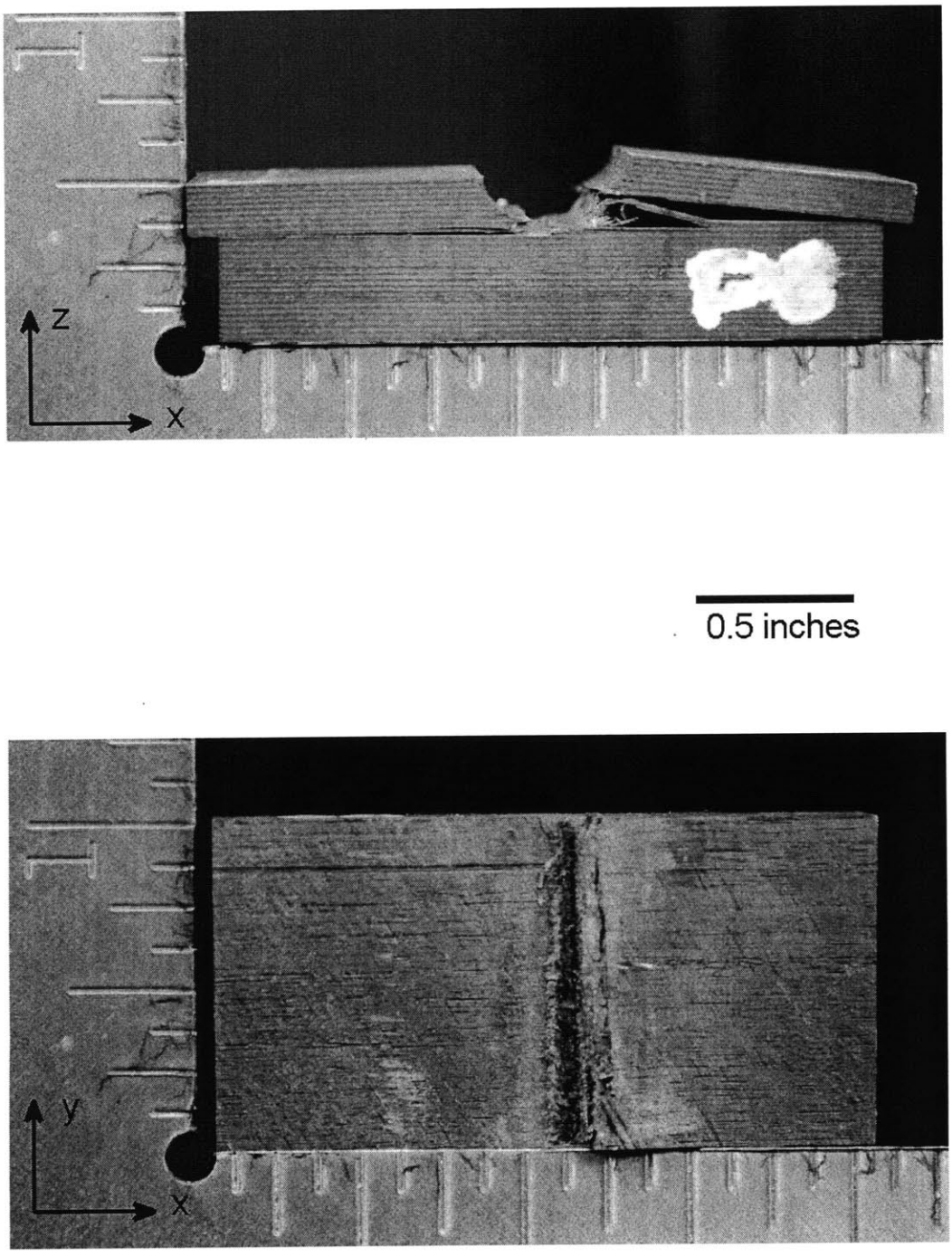

Figure B.14 Photographs of $[\pm 60/0]_{13S}$ Specimen 2, tested to failure in "two-dimensional loading", shown via (*top*) side view, and (*bottom*) top view with delamination surfaces exposed.

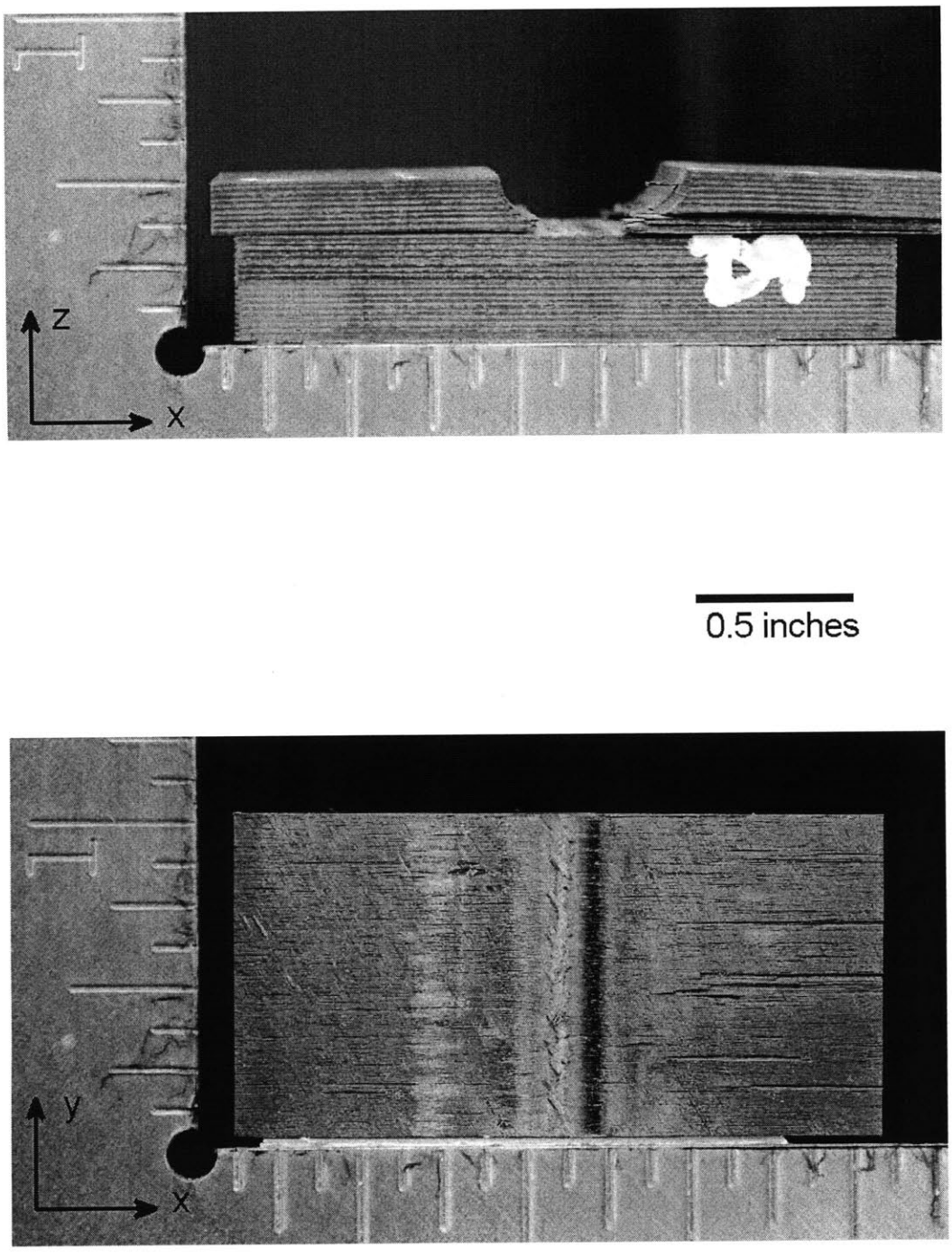

Figure B.15 Photographs of $[\pm 60/0]_{13S}$ Specimen 3, tested to failure in "two-dimensional loading", shown via (*top*) side view, and (*bottom*) top view with delamination surfaces exposed.

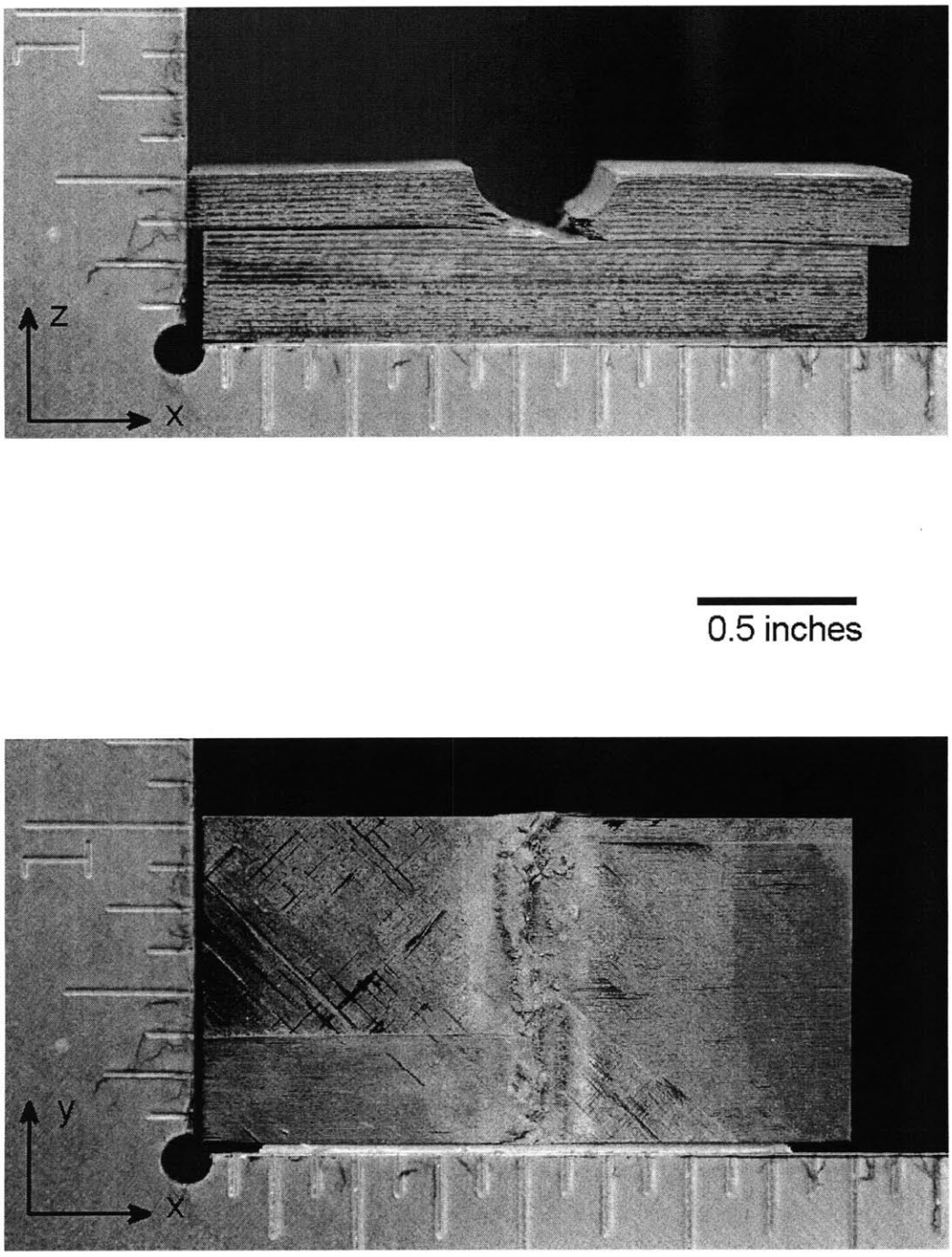

Figure B.16 Photographs of $[\pm 45/0]_{13S}$ Specimen 1, tested to failure in "two-dimensional loading", shown via (*top*) side view, and (*bottom*) top view with delamination surfaces exposed.

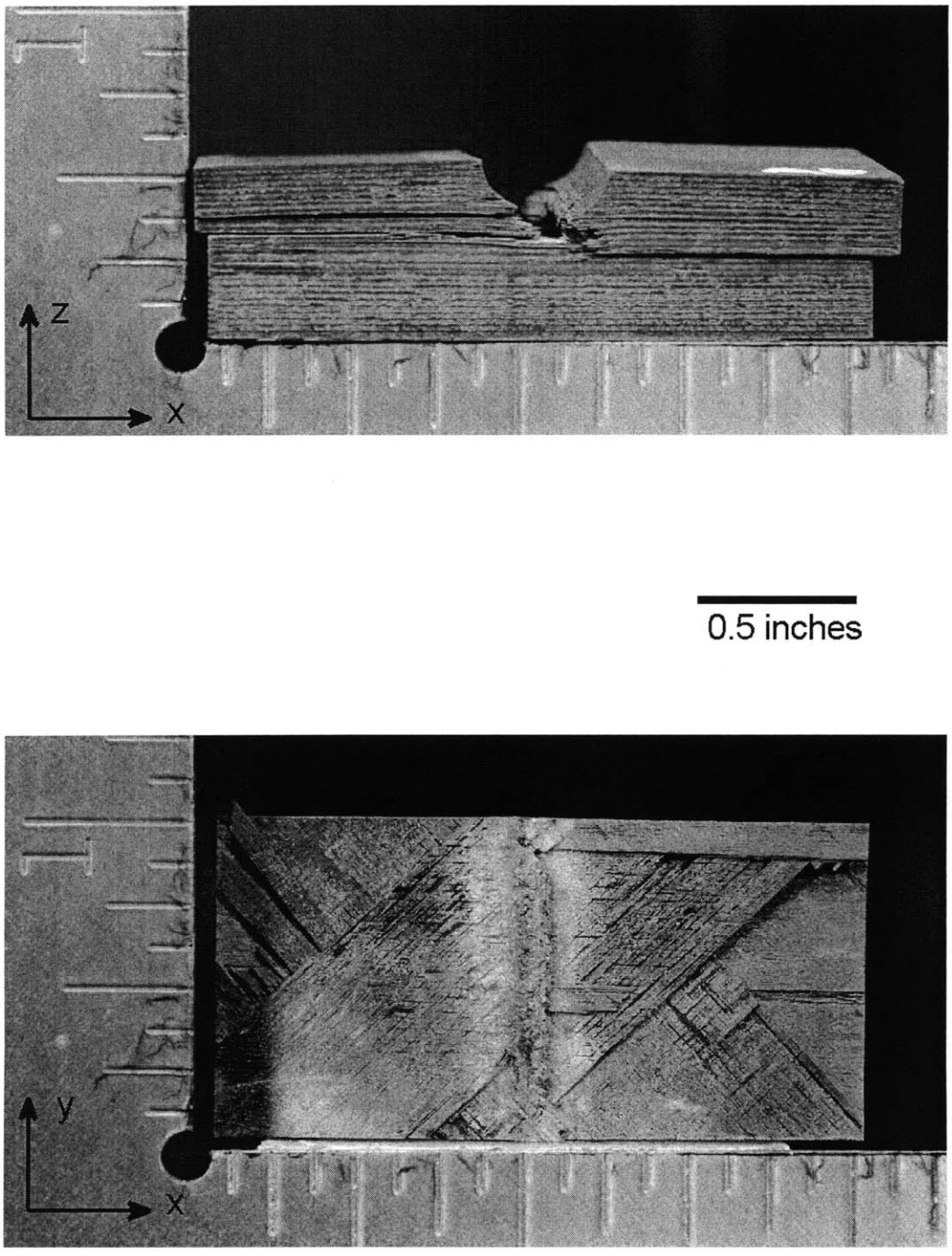

Figure B.17 Photographs of $[\pm 45/0]_{13S}$ Specimen 2, tested to failure in "two-dimensional loading", shown via (*top*) side view, and (*bottom*) top view with delamination surfaces exposed.

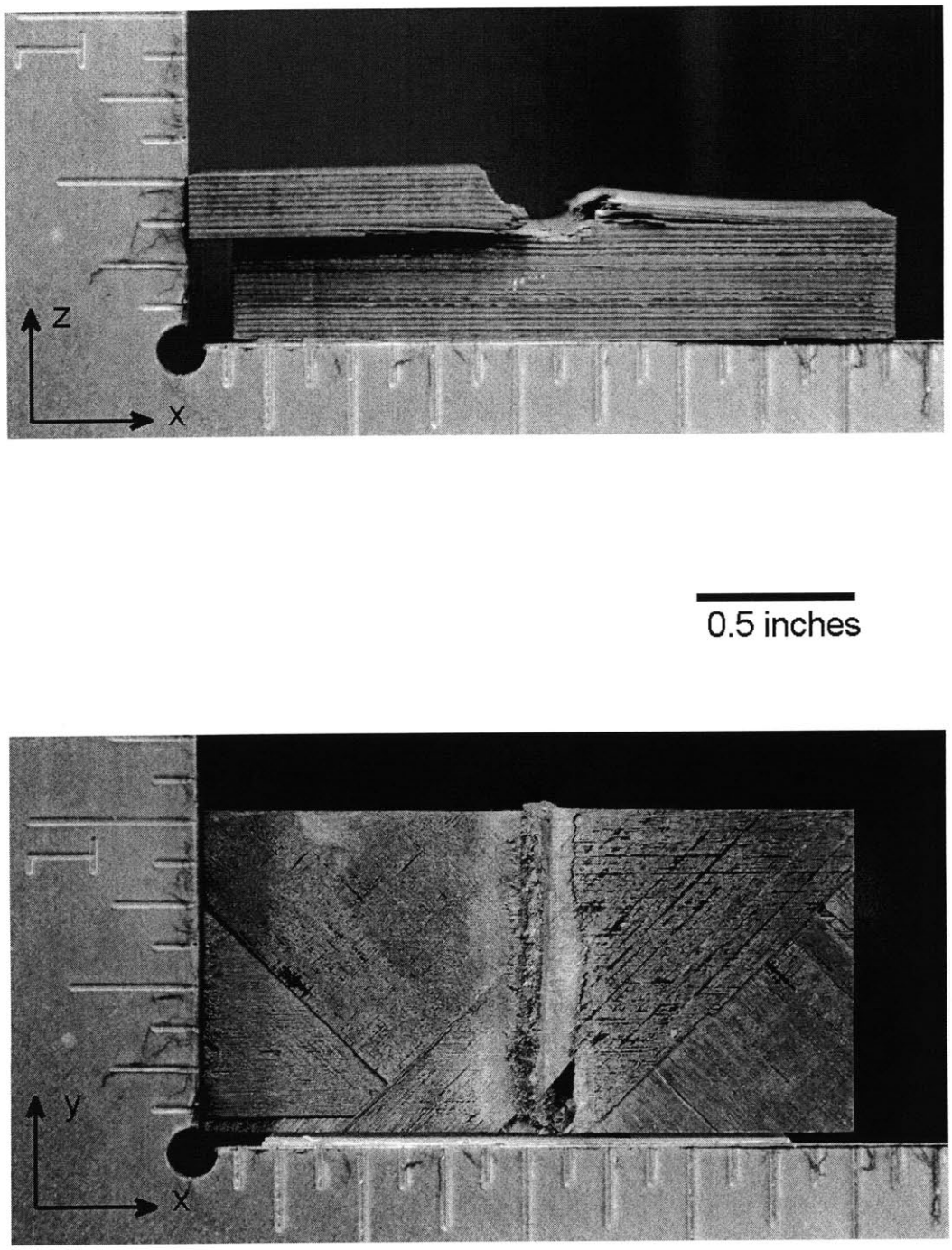

Figure B.18 Photographs of $[\pm 45/0]_{13S}$ Specimen 3, tested to failure in "two-dimensional loading", shown via (*top*) side view, and (*bottom*) top view with delamination surfaces exposed.

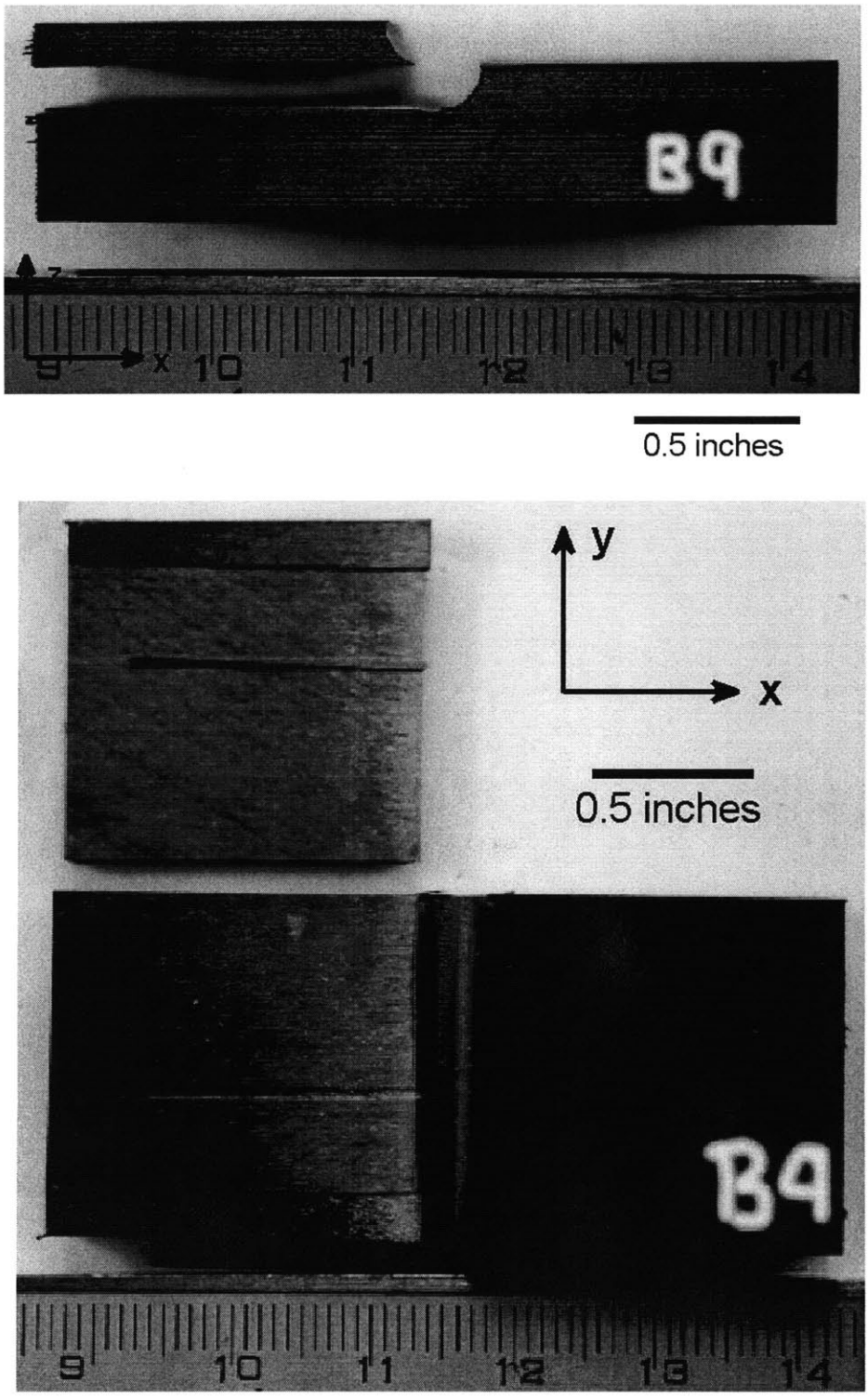

Figure B.19 Photographs of $[\pm 30/0]_{10S}$ Specimen 1, tested to failure in "two-dimensional loading", shown via (*top*) side view, and (*bottom*) top view with delamination surfaces exposed.

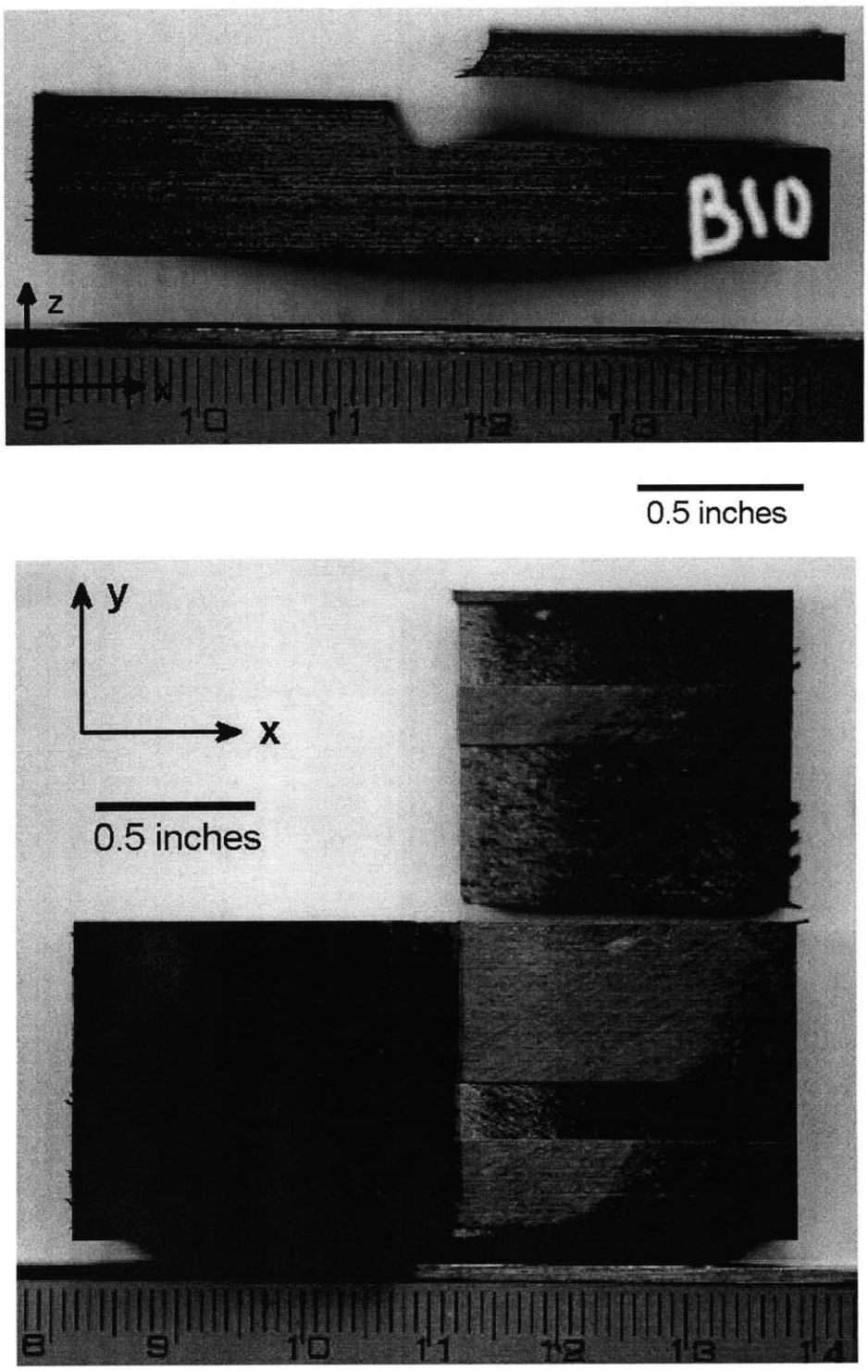

Figure B.20 Photographs of $[\pm 30/0]_{10S}$ Specimen 2, tested to failure in "two-dimensional loading", shown via (*top*) side view, and (*bottom*) top view with delamination surfaces exposed.

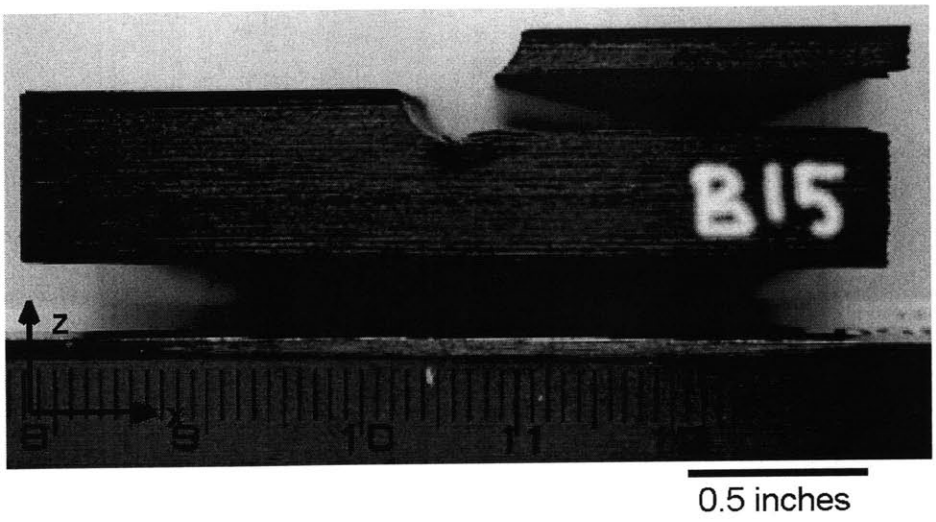

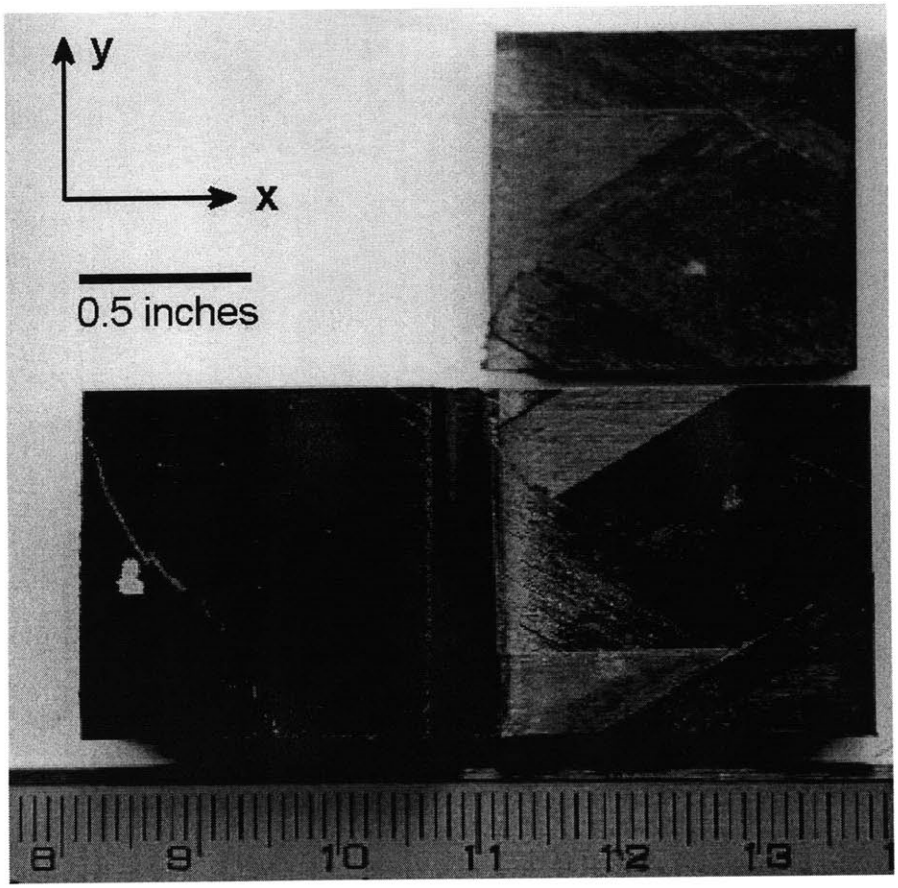

Figure B.21 Photographs of $[\pm 30/0]_{10S}$ Specimen 3, tested to failure in "two-dimensional loading", shown via (*top*) side view, and (*bottom*) top view with delamination surfaces exposed.

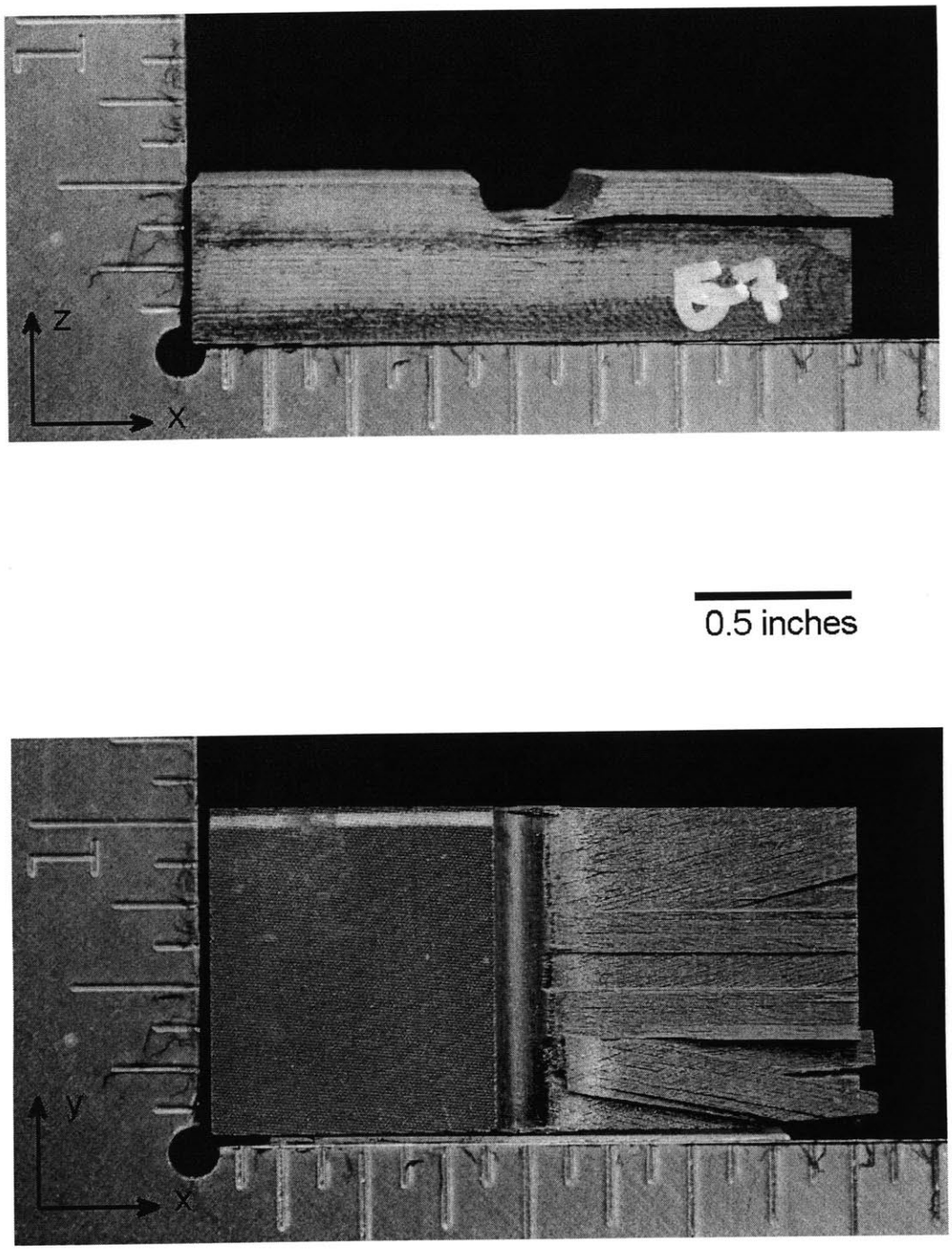

Figure B.22 Photographs of $[\pm 15/0]_{13S}$ Specimen 1, tested to failure in "two-dimensional loading", shown via (*top*) side view, and (*bottom*) top view with delamination surfaces exposed.

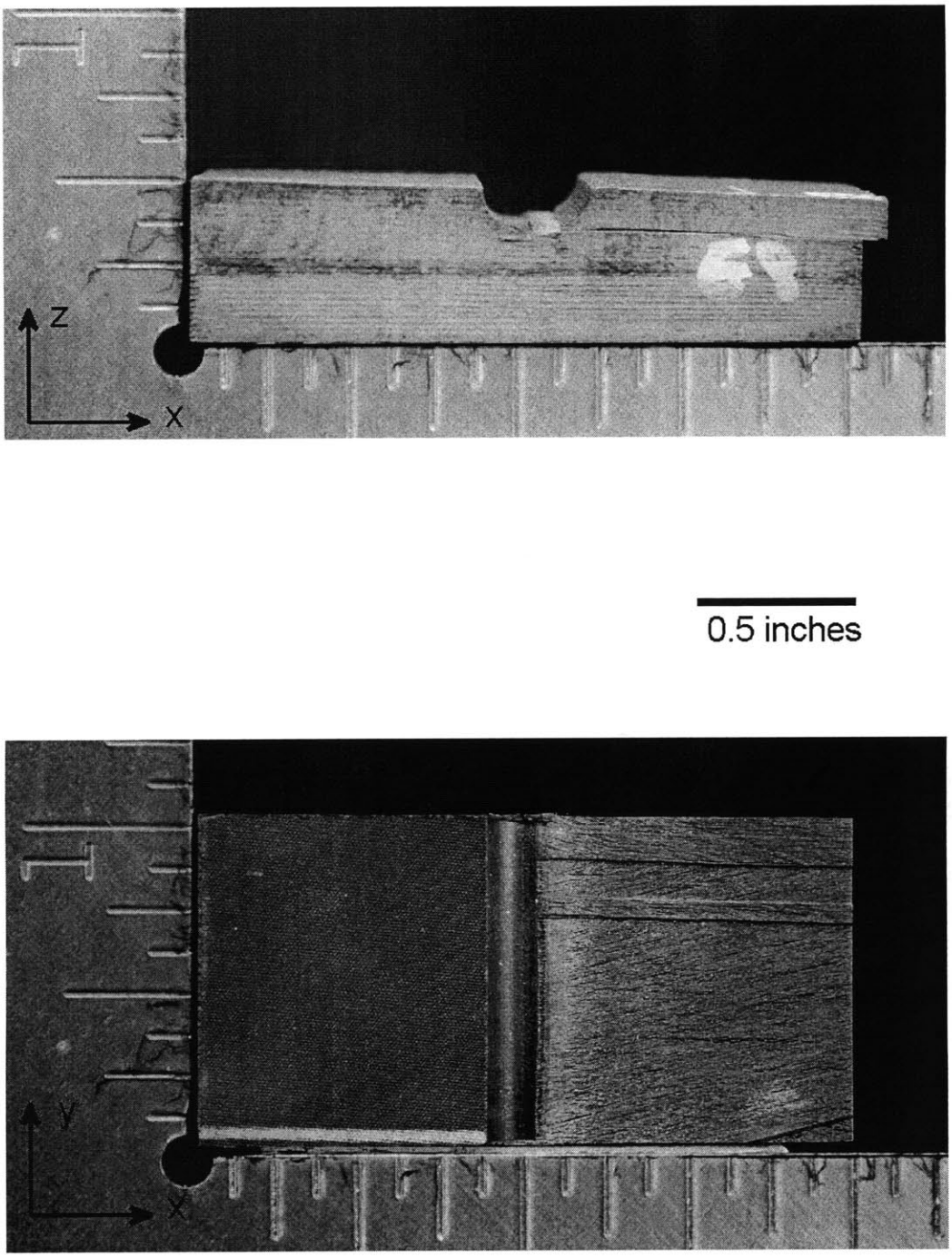

Figure B.23 Photographs of $[\pm 15/0]_{13S}$ Specimen 2, tested to failure in "two-dimensional loading", shown via (*top*) side view, and (*bottom*) top view with delamination surfaces exposed.

Appendix C

Photographs of "Three-Dimensional Loading" Specimens After Failure

Photographs of all specimens tested to final failure with the "three-dimensional loading" configuration (as discussed in Chapter 5) are presented in this appendix. The photographs are a top view and side view of each specimen. The testing procedures are those discussed in Chapter 4.

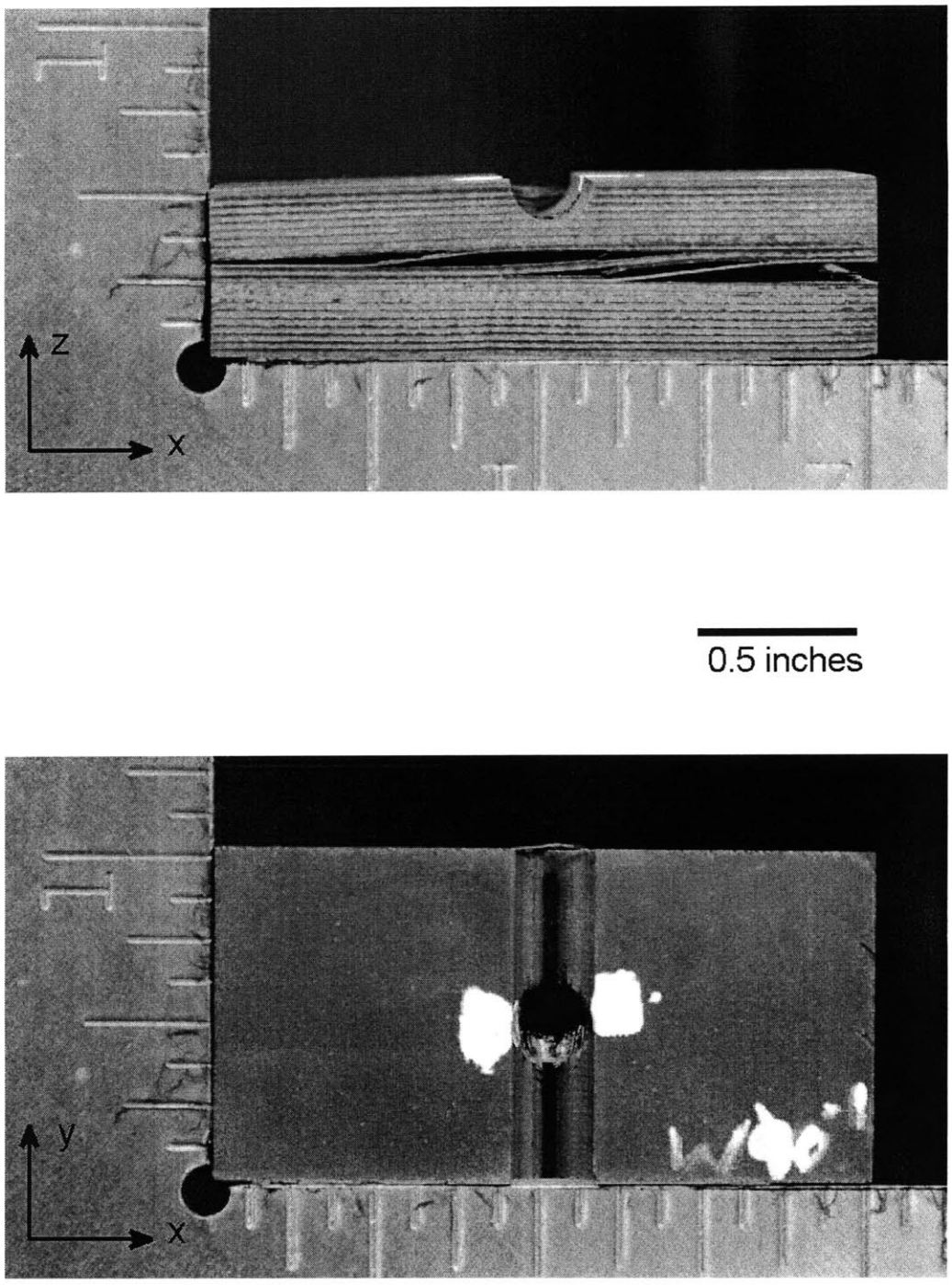

Figure C.1 Photographs of $[\pm 45/0/90]_{20S}$ Specimen 1, tested to failure in "three-dimensional loading" shown via (*top*) side view, and (*bottom*) top view with crater from indenter visible.

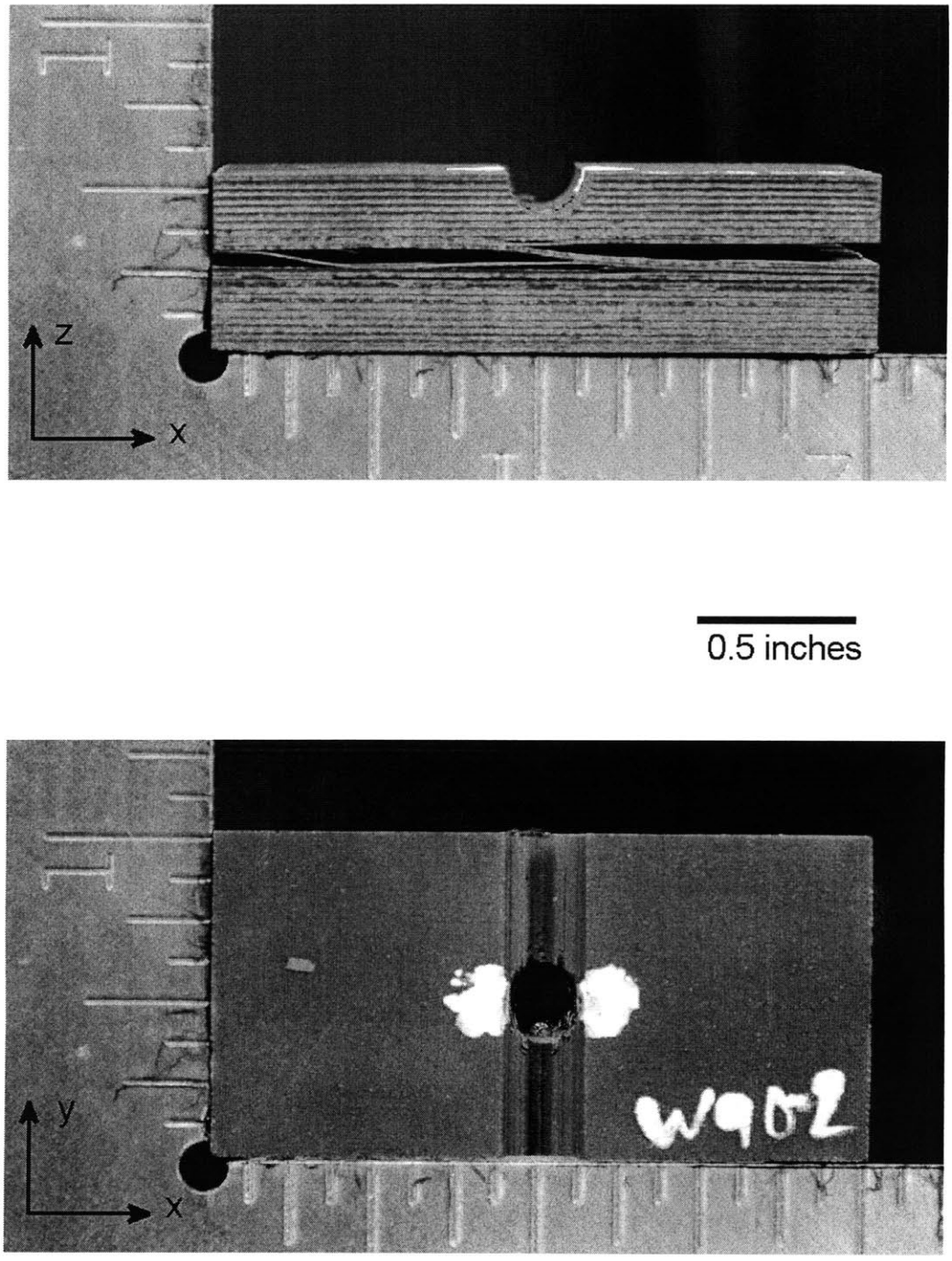

Figure C.2 Photographs of $[\pm 45/0/90]_{20S}$ Specimen 2, tested to failure in "three-dimensional loading" shown via (*top*) side view, and (*bottom*) top view with crater from indenter visible.

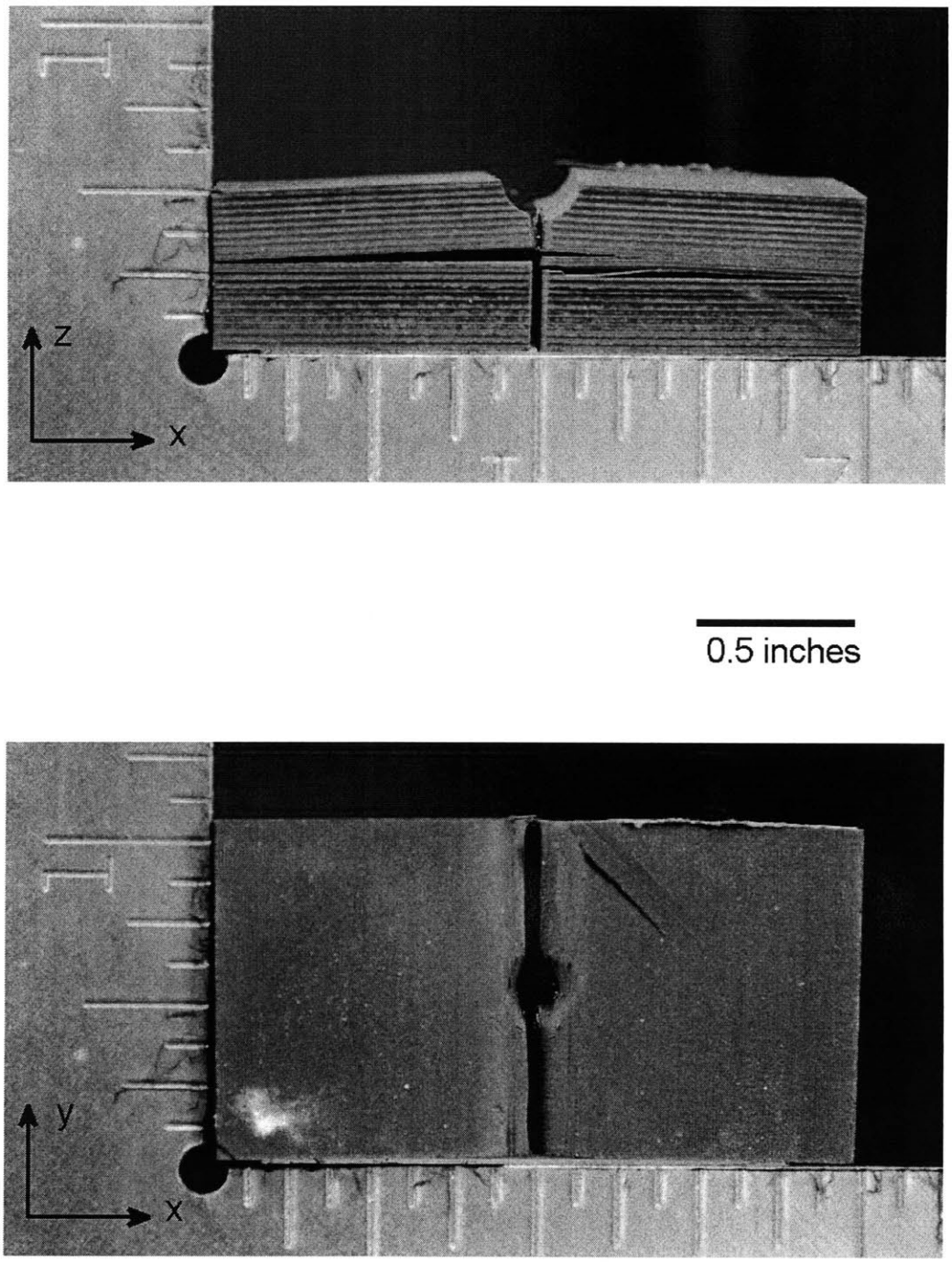

Figure C.3 Photographs of $[\pm 45/0/90]_{20S}$ Specimen 3, tested to failure in "three-dimensional loading" shown via (*top*) side view, and (*bottom*) top view with crater from indenter visible.

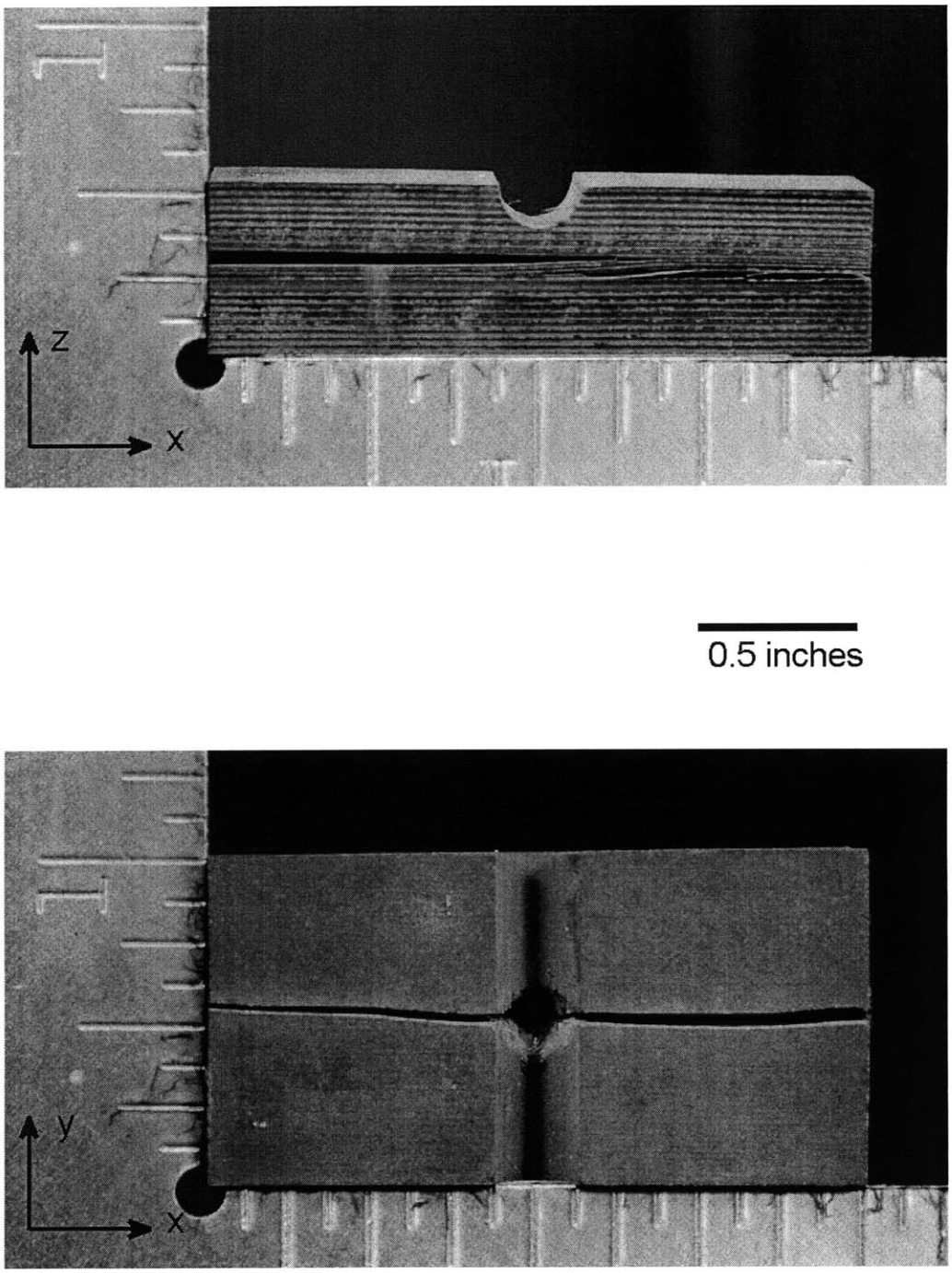

Figure C.4 Photographs of $[\pm 45/0/90]_{20S}$ Specimen 4, tested to failure in "three-dimensional loading" shown via (*top*) side view, and (*bottom*) top view with crater from indenter visible.

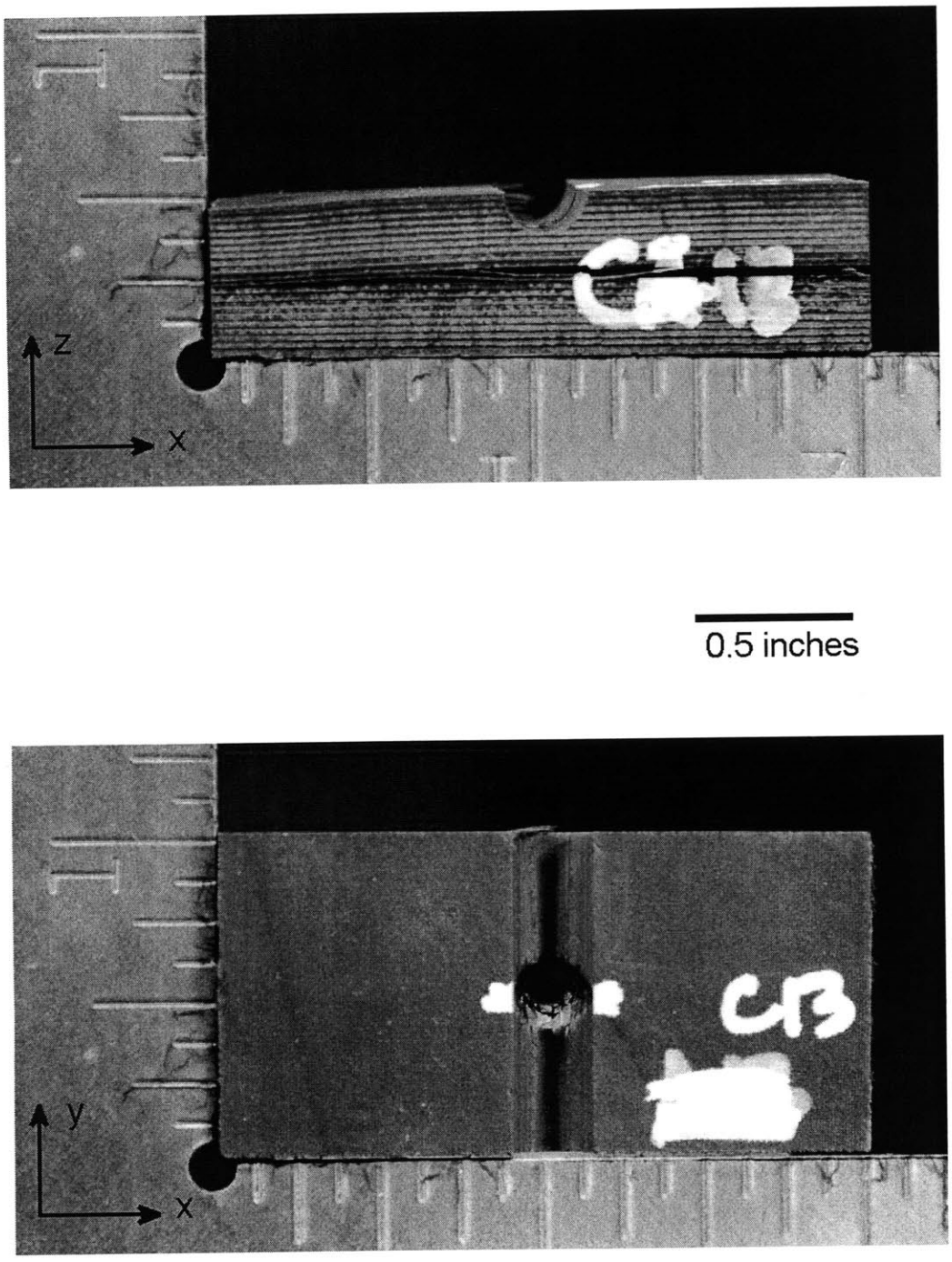

Figure C.5 Photographs of $[\pm 45/0/90]_{20S}$ Specimen 5, tested to failure in "three-dimensional loading" shown via (*top*) side view, and (*bottom*) top view with crater from indenter visible.

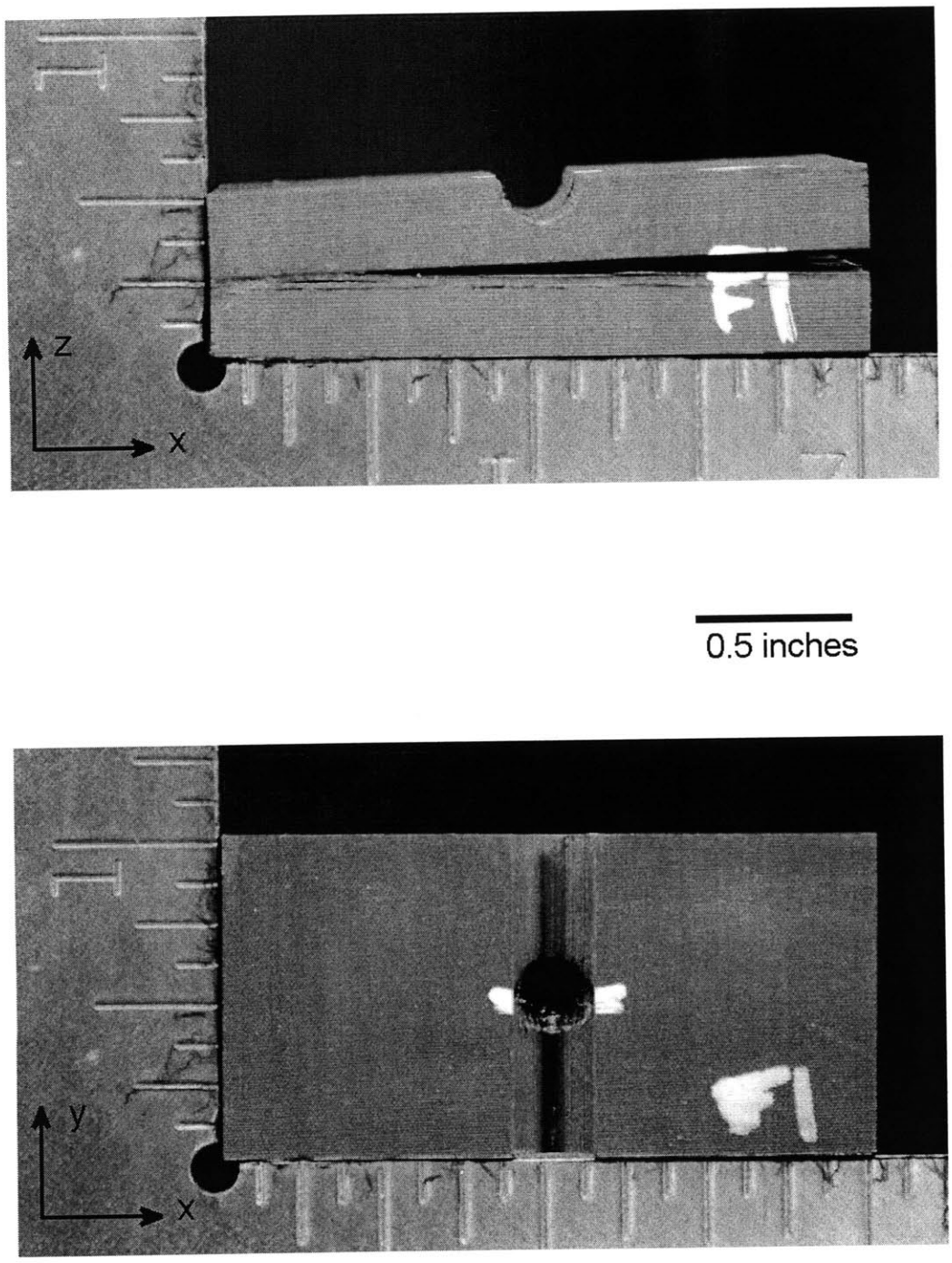

Figure C.6 Photographs of $[90/0]_{20S}$ Specimen 1, tested to failure in "three-dimensional loading" shown via (*top*) side view, and (*bottom*) top view with crater from indenter visible.

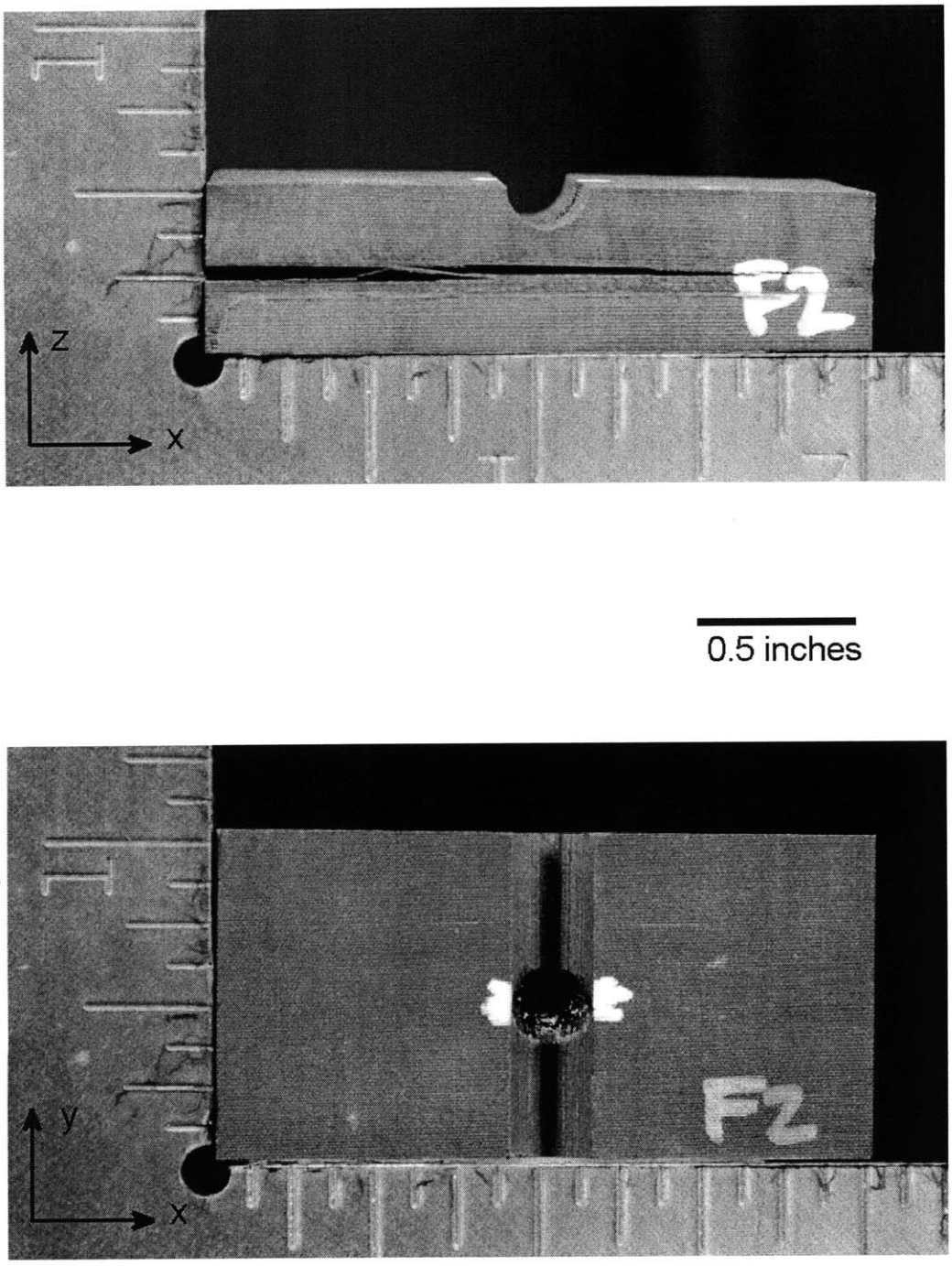

Figure C.7 Photographs of $[90/0]_{20S}$ Specimen 2, tested to failure in "three-dimensional loading" shown via (*top*) side view, and (*bottom*) top view with crater from indenter visible.

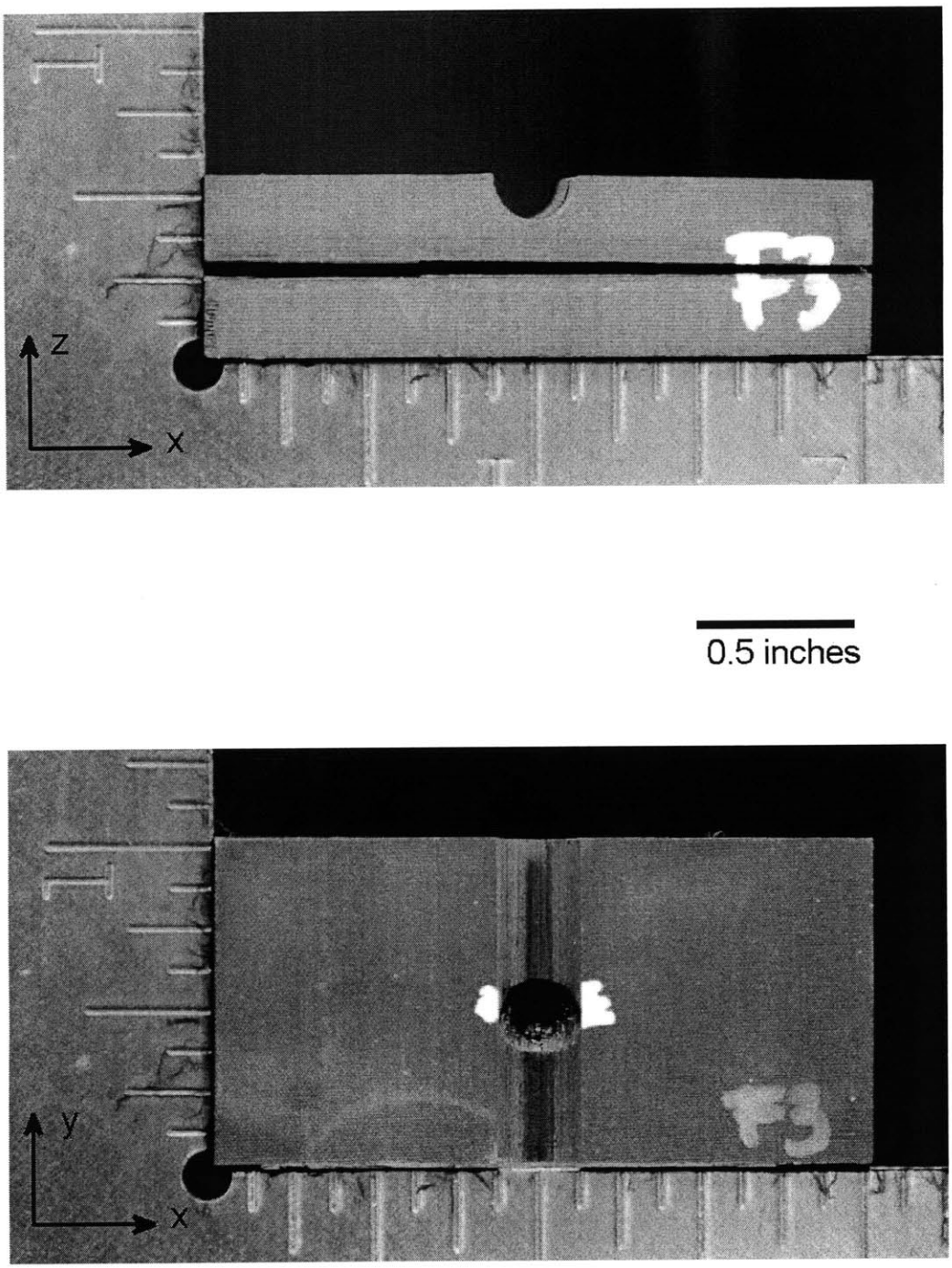

Figure C.8 Photographs of $[90/0]_{20S}$ Specimen 3, tested to failure in "three-dimensional loading" shown via (*top*) side view, and (*bottom*) top view with crater from indenter visible.

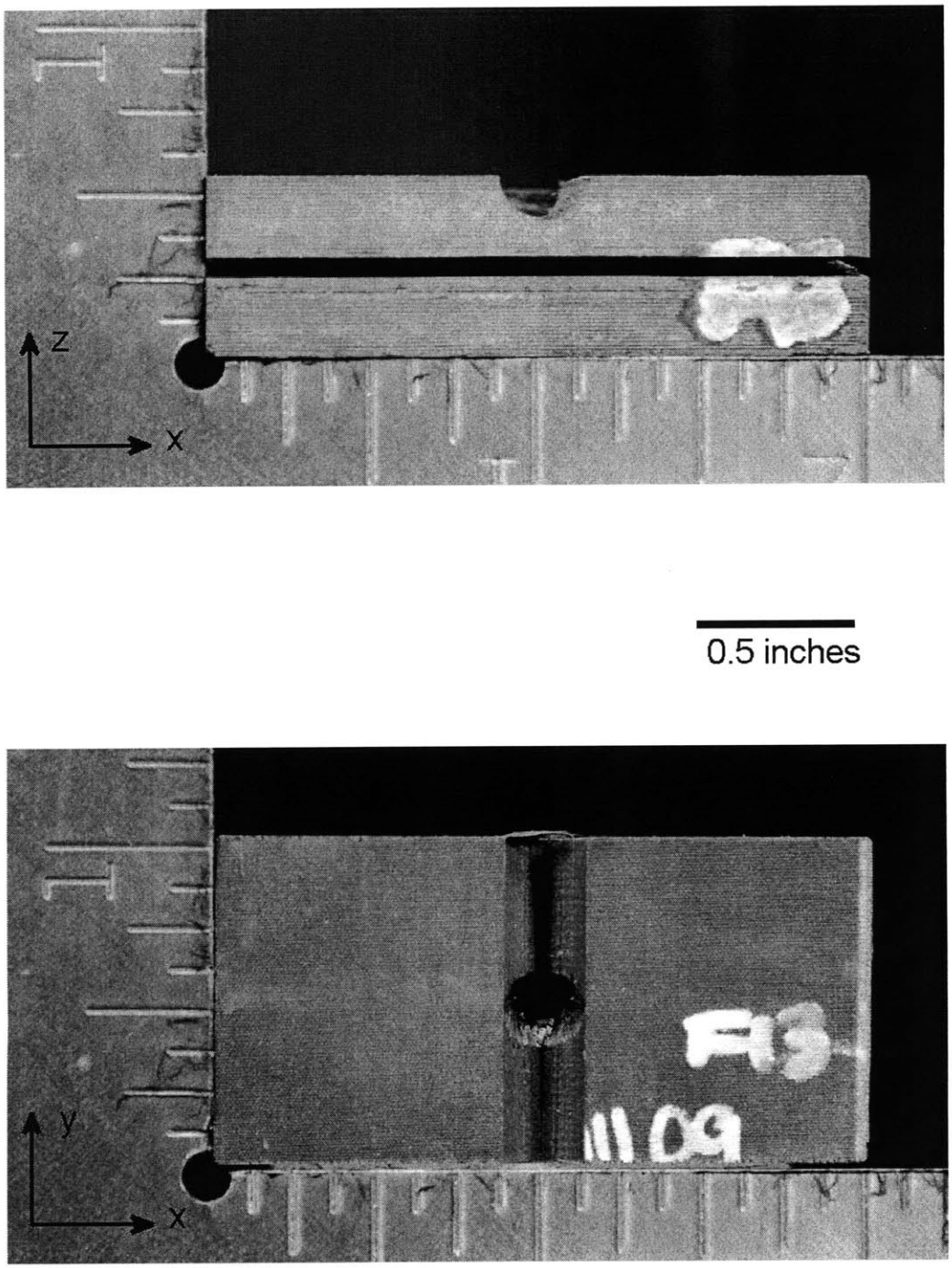

Figure C.9 Photographs of $[90/0]_{20S}$ Specimen 4, tested to failure in "three-dimensional loading" shown via (*top*) side view, and (*bottom*) top view with crater from indenter visible.

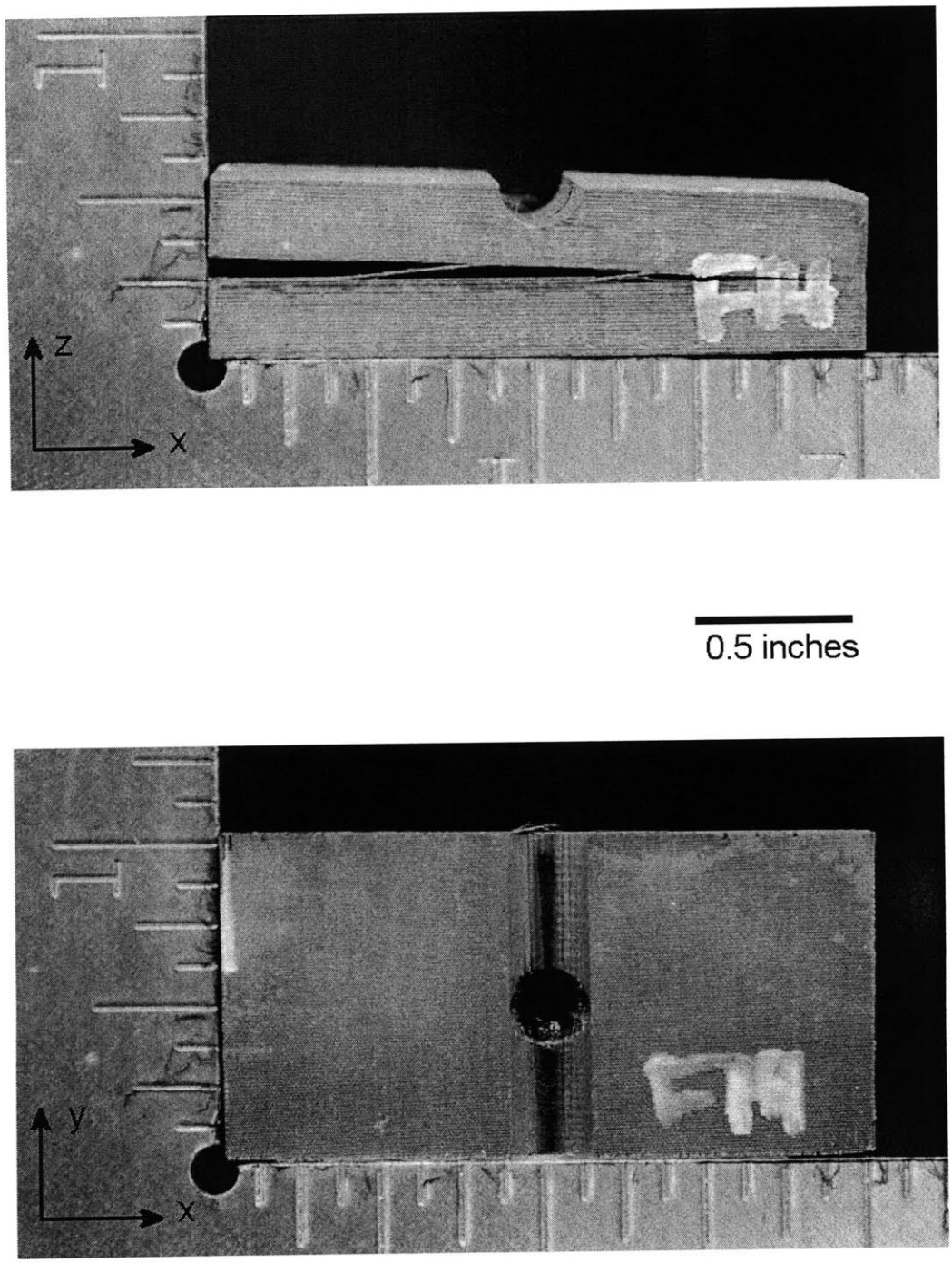

Figure C.10 Photographs of $[90/0]_{20S}$ Specimen 5, tested to failure in "three-dimensional loading" shown via (*top*) side view, and (*bottom*) top view with crater from indenter visible.

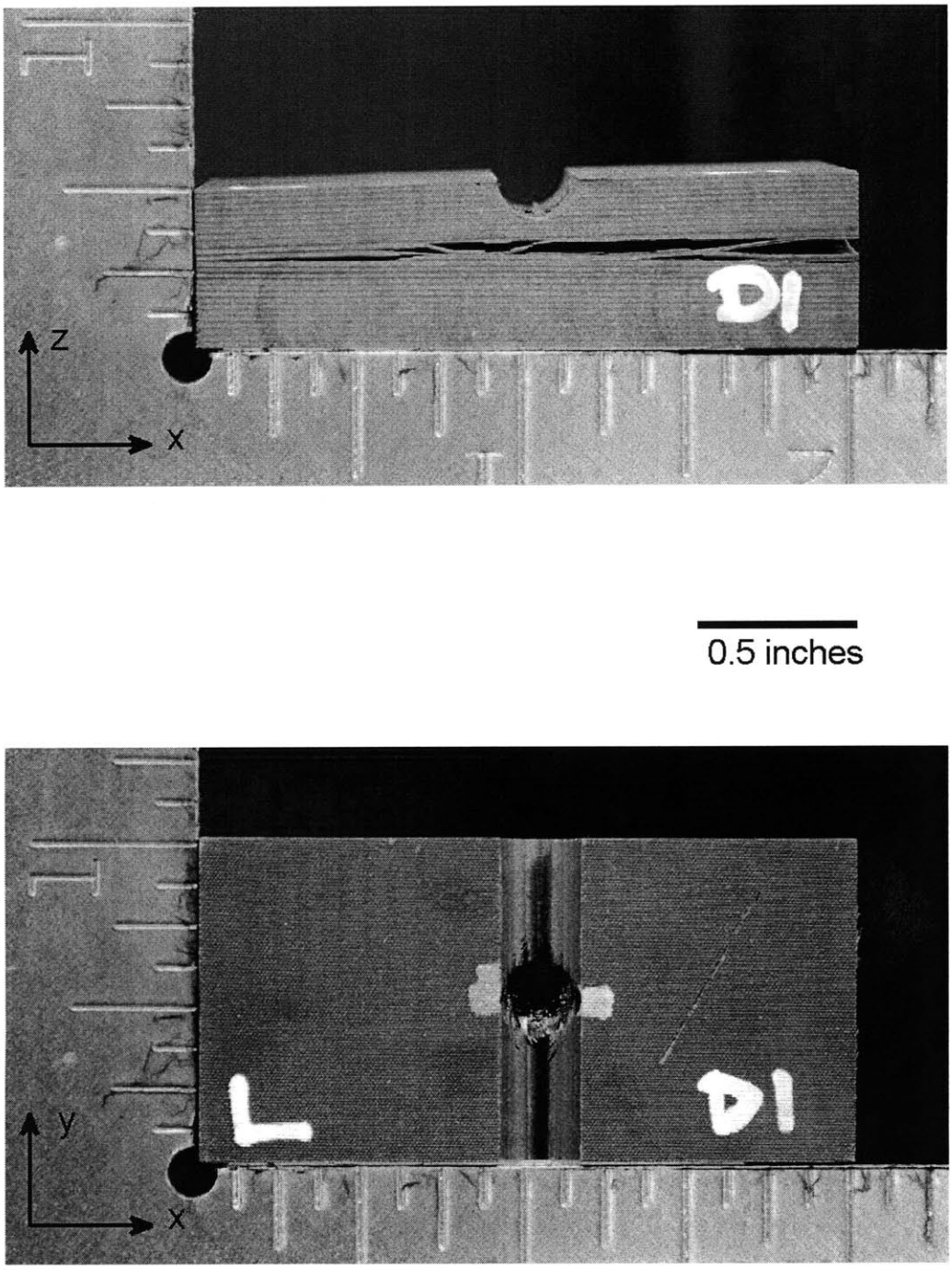

Figure C.11 Photographs of $[\pm 60/0]_{13S}$ Specimen 1, tested to failure in "three-dimensional loading" shown via (*top*) side view, and (*bottom*) top view with crater from indenter visible.

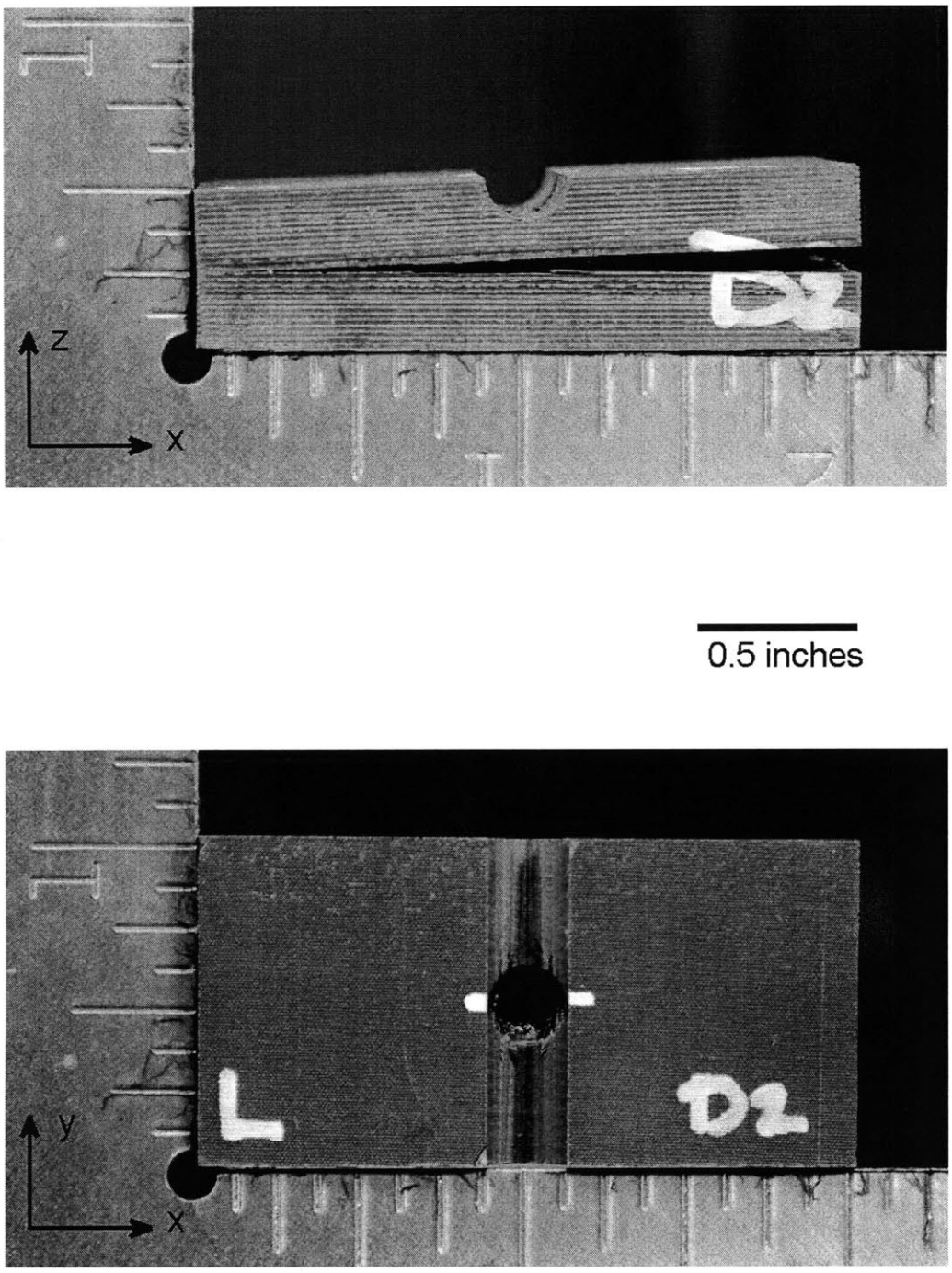

Figure C.12 Photographs of $[\pm 60/0]_{13S}$ Specimen 2, tested to failure in "three-dimensional loading" shown via (*top*) side view, and (*bottom*) top view with crater from indenter visible.

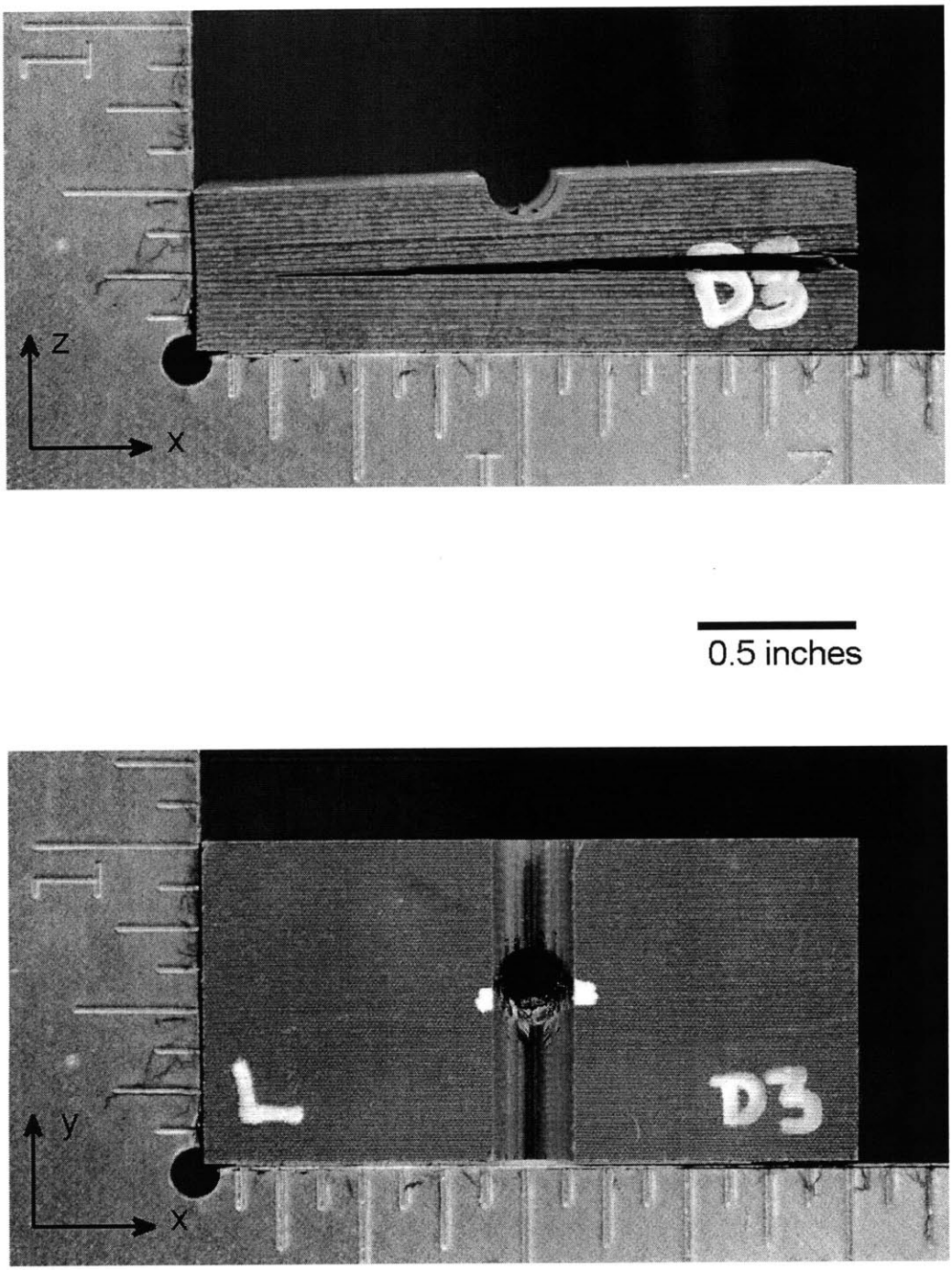

Figure C.13 Photographs of $[\pm 60/0]_{13S}$ Specimen 3, tested to failure in "three-dimensional loading" shown via (*top*) side view, and (*bottom*) top view with crater from indenter visible.

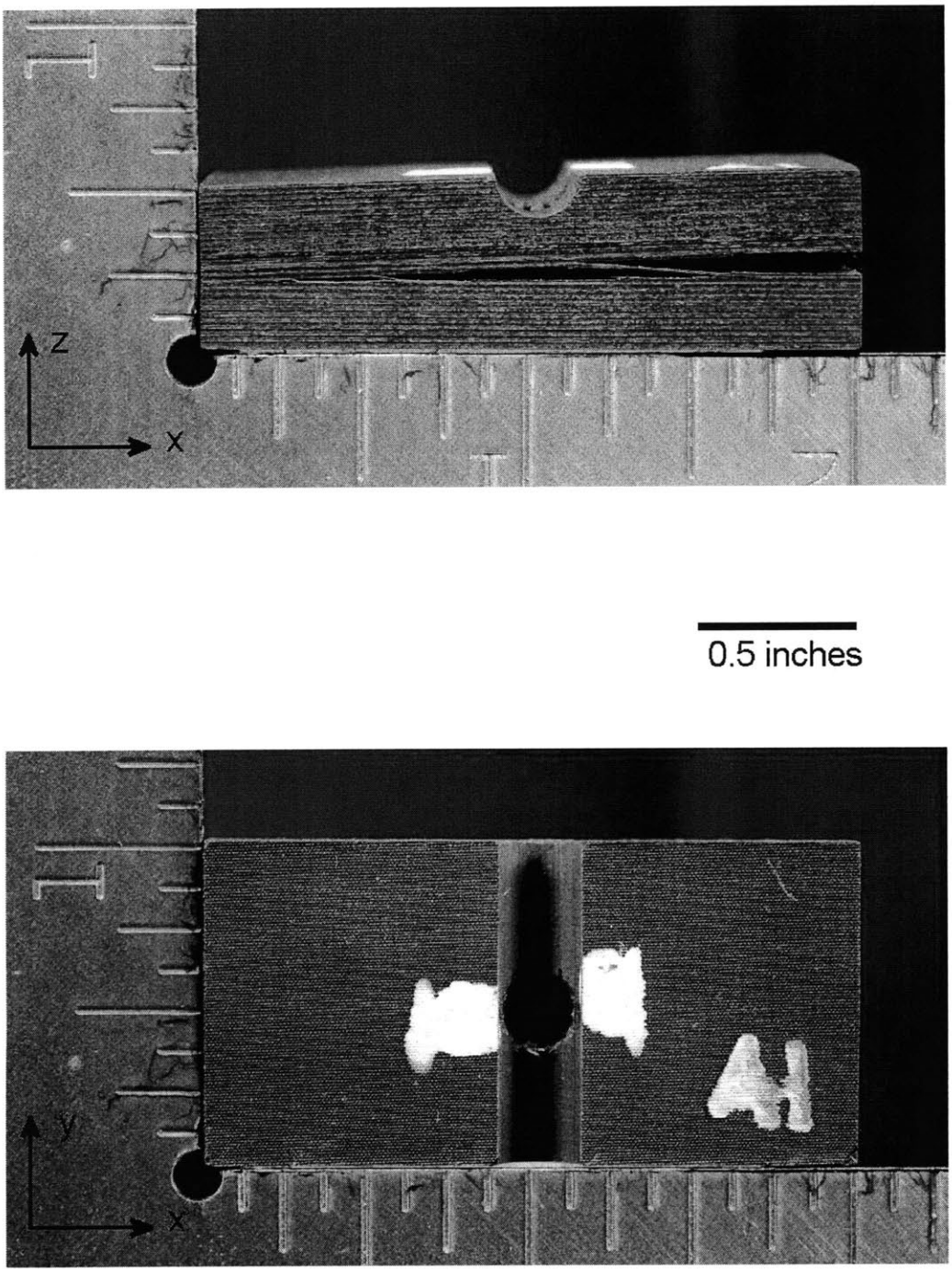

Figure C.14 Photographs of $[\pm 45/0]_{13S}$ Specimen 1, tested to failure in "three-dimensional loading" shown via (*top*) side view, and (*bottom*) top view with crater from indenter visible.

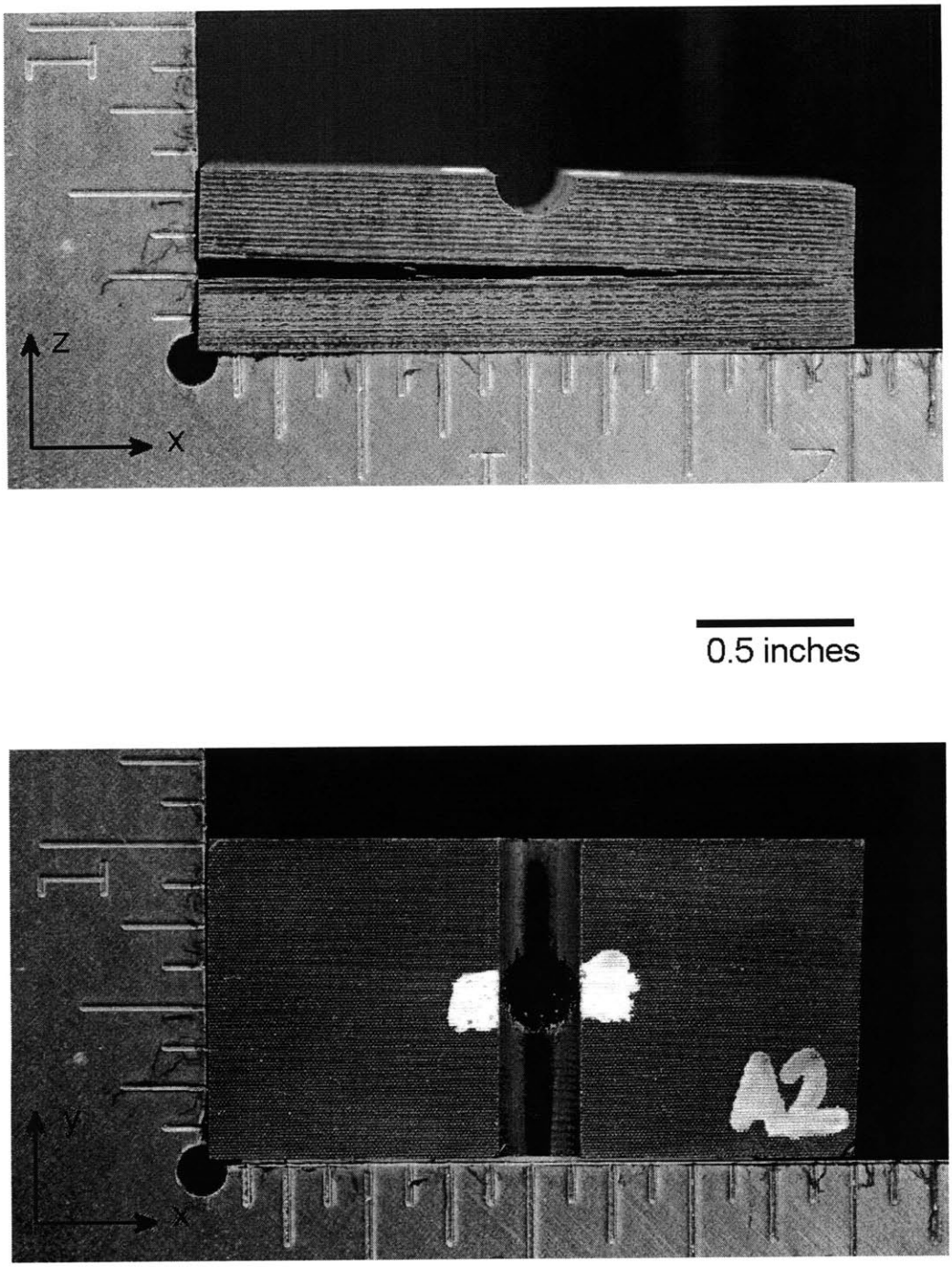

Figure C.15 Photographs of $[\pm 45/0]_{13S}$ Specimen 2, tested to failure in "three-dimensional loading" shown via (*top*) side view, and (*bottom*) top view with crater from indenter visible.

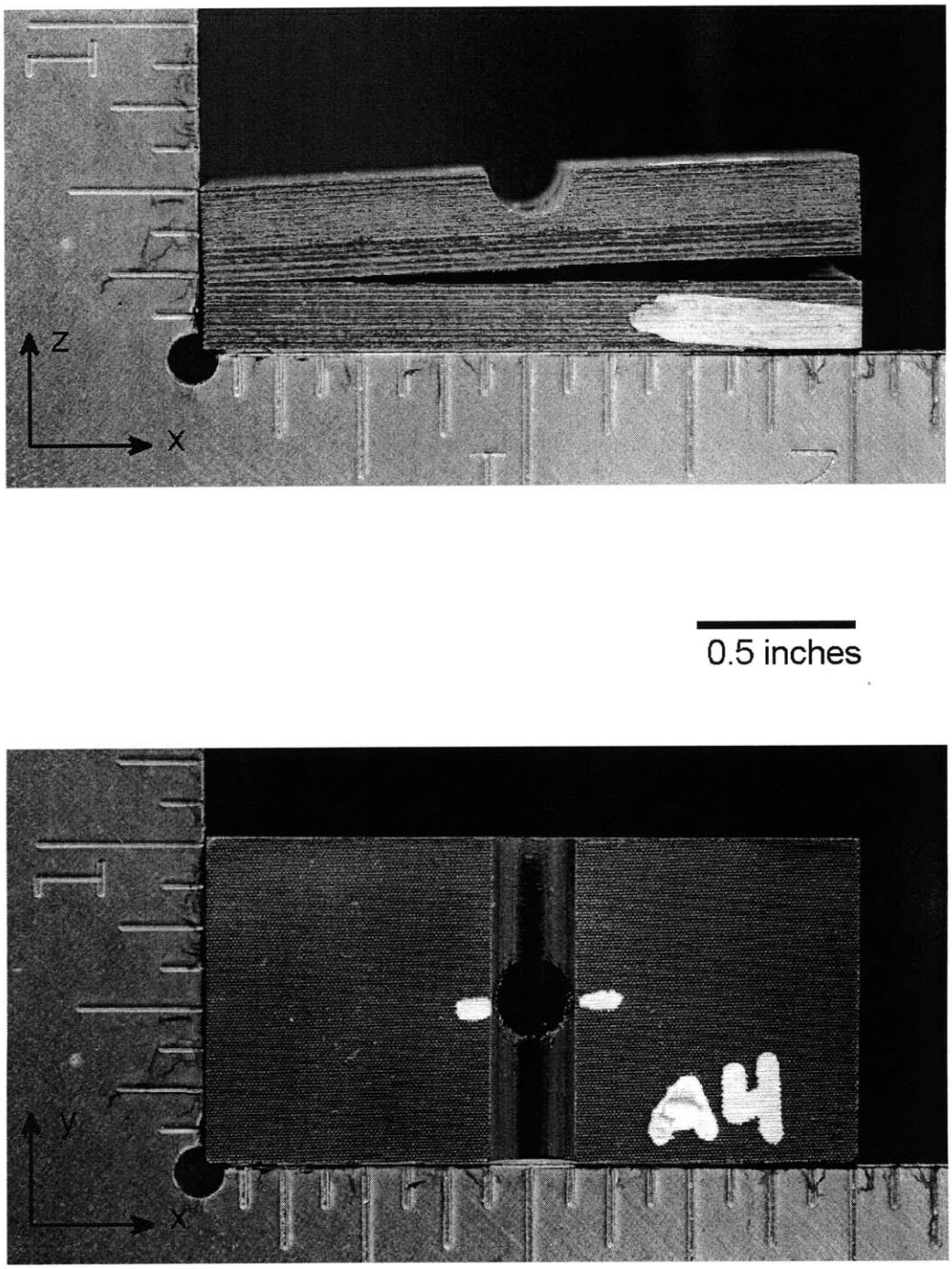

Figure C.16 Photographs of $[\pm 45/0]_{13S}$ Specimen 3, tested to failure in "three-dimensional loading" shown via (*top*) side view, and (*bottom*) top view with crater from indenter visible.

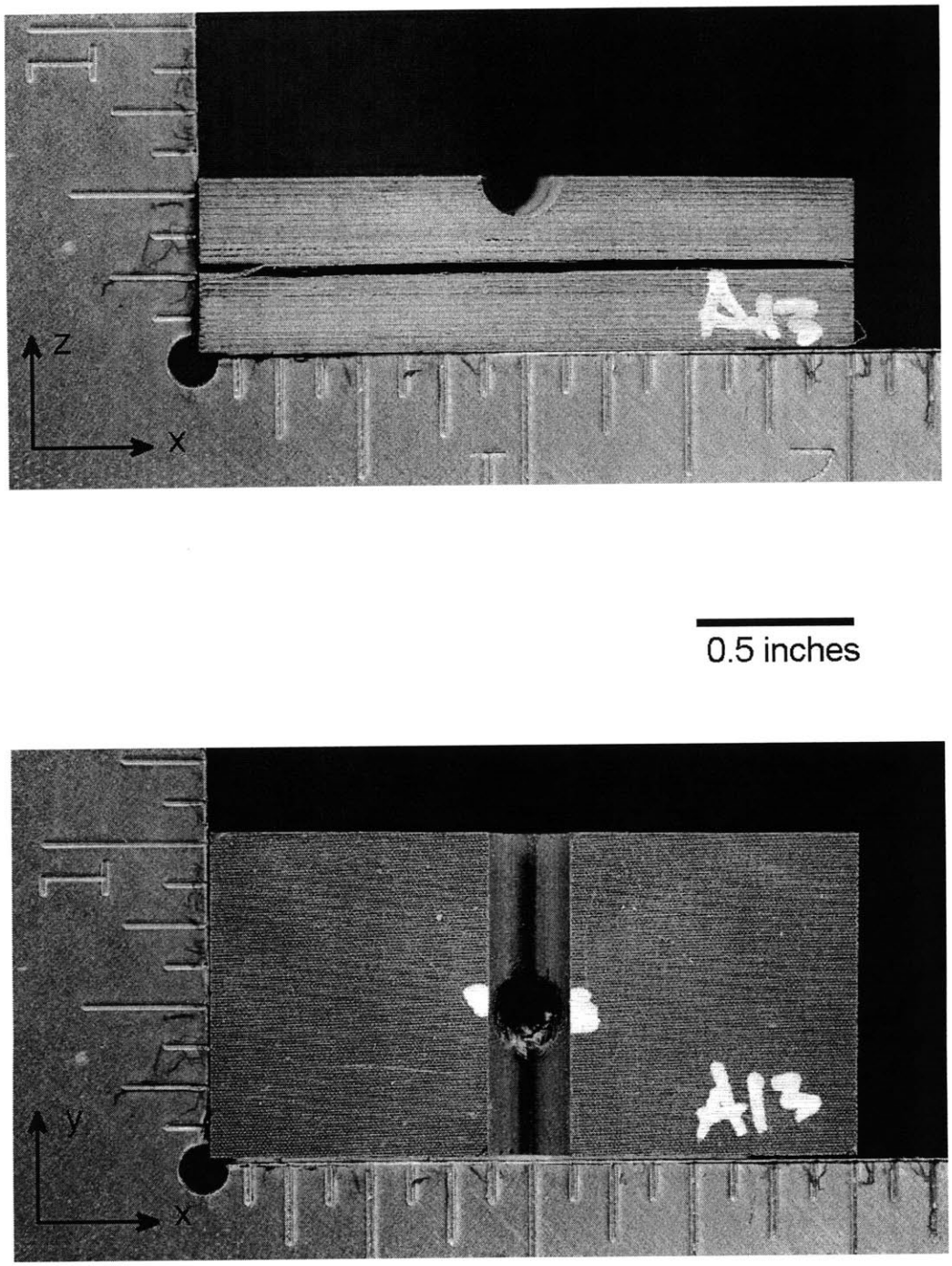

Figure C.17 Photographs of $[\pm 45/0]_{13S}$ Specimen 4, tested to failure in "three-dimensional loading" shown via (*top*) side view, and (*bottom*) top view with crater from indenter visible.

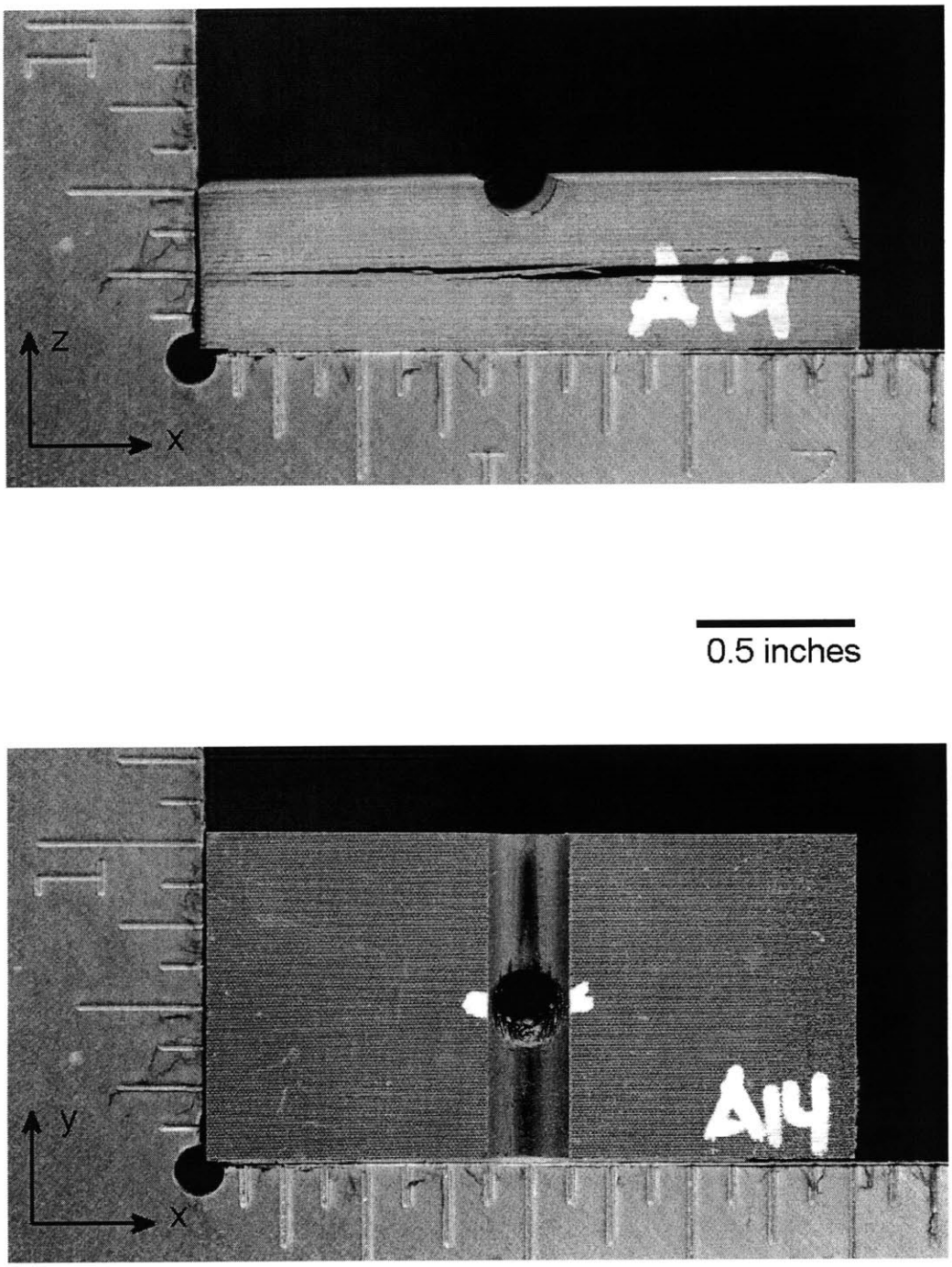

Figure C.18 Photographs of $[\pm 45/0]_{13S}$ Specimen 5, tested to failure in "three-dimensional loading" shown via (*top*) side view, and (*bottom*) top view with crater from indenter visible.

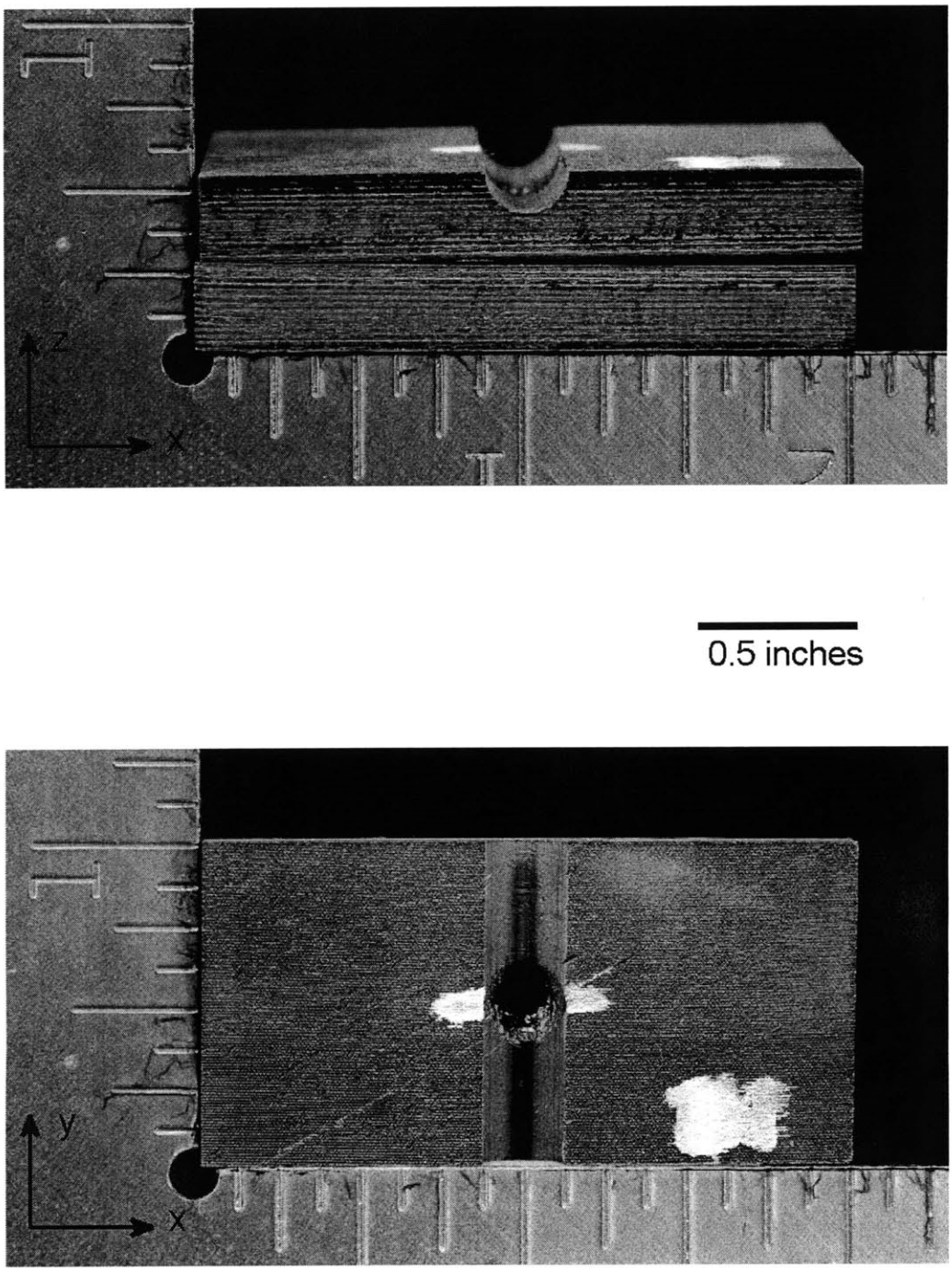

Figure C.19 Photographs of $[\pm 30/0]_{13S}$ Specimen 1, tested to failure in "three-dimensional loading" shown via (*top*) side view, and (*bottom*) top view with crater from indenter visible.

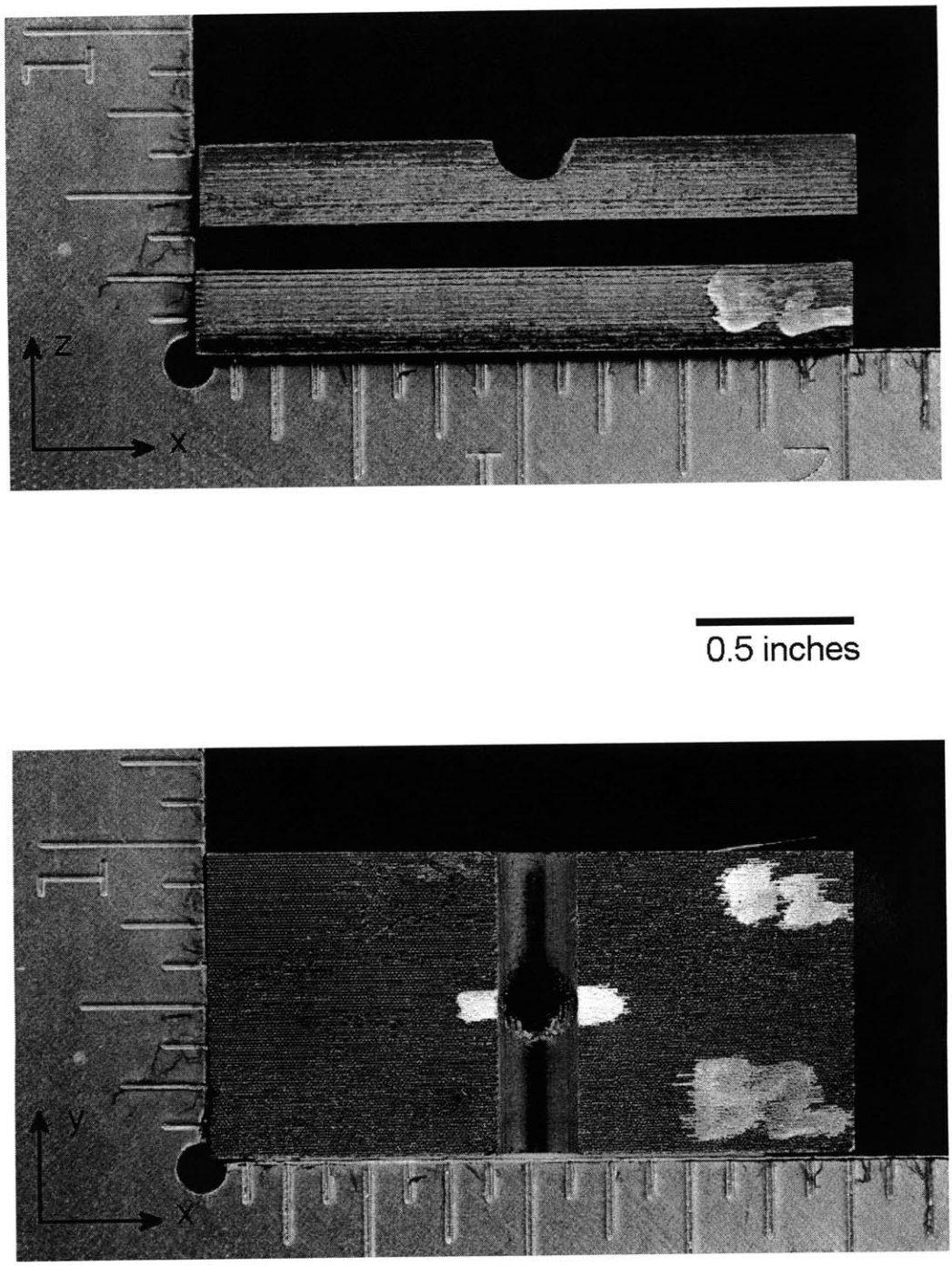

Figure C.20 Photographs of $[\pm 30/0]_{13S}$ Specimen 2, tested to failure in "three-dimensional loading" shown via (*top*) side view, and (*bottom*) top view with crater from indenter visible.

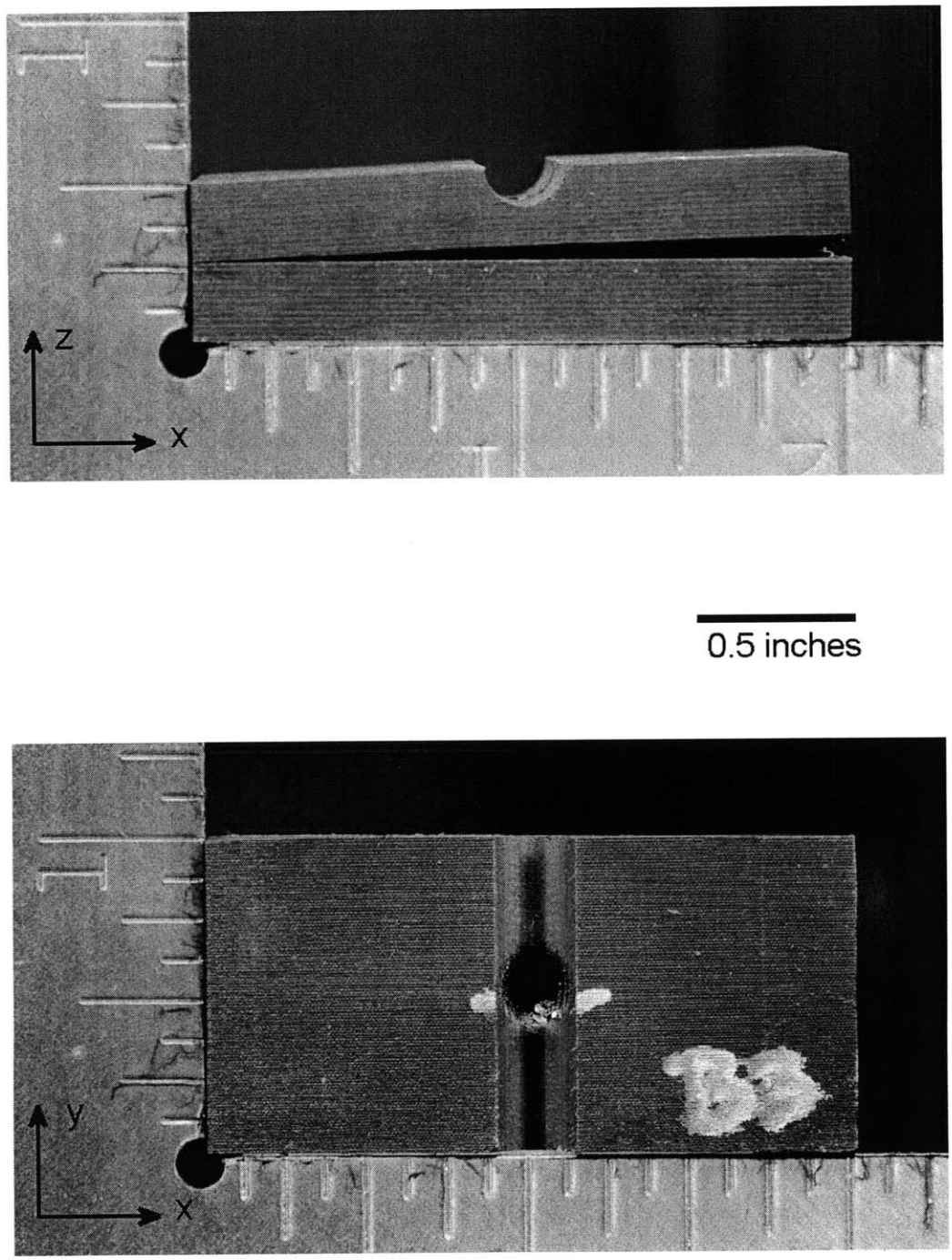

Figure C.21 Photographs of $[\pm 30/0]_{13S}$ Specimen 3, tested to failure in "three-dimensional loading" shown via (*top*) side view, and (*bottom*) top view with crater from indenter visible.

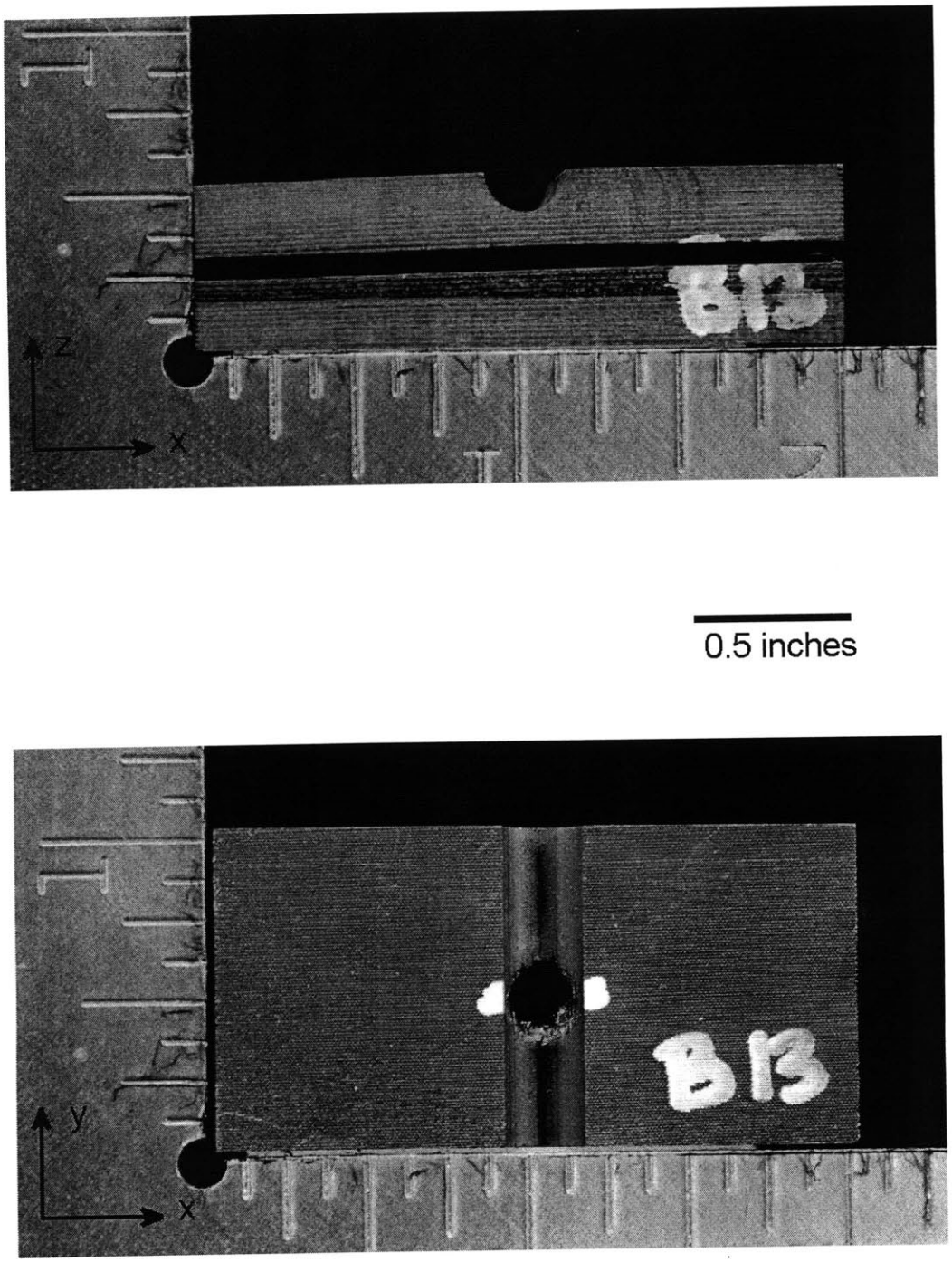

Figure C.22 Photographs of $[\pm 30/0]_{13S}$ Specimen 4, tested to failure in "three-dimensional loading" shown via (*top*) side view, and (*bottom*) top view with crater from indenter visible.

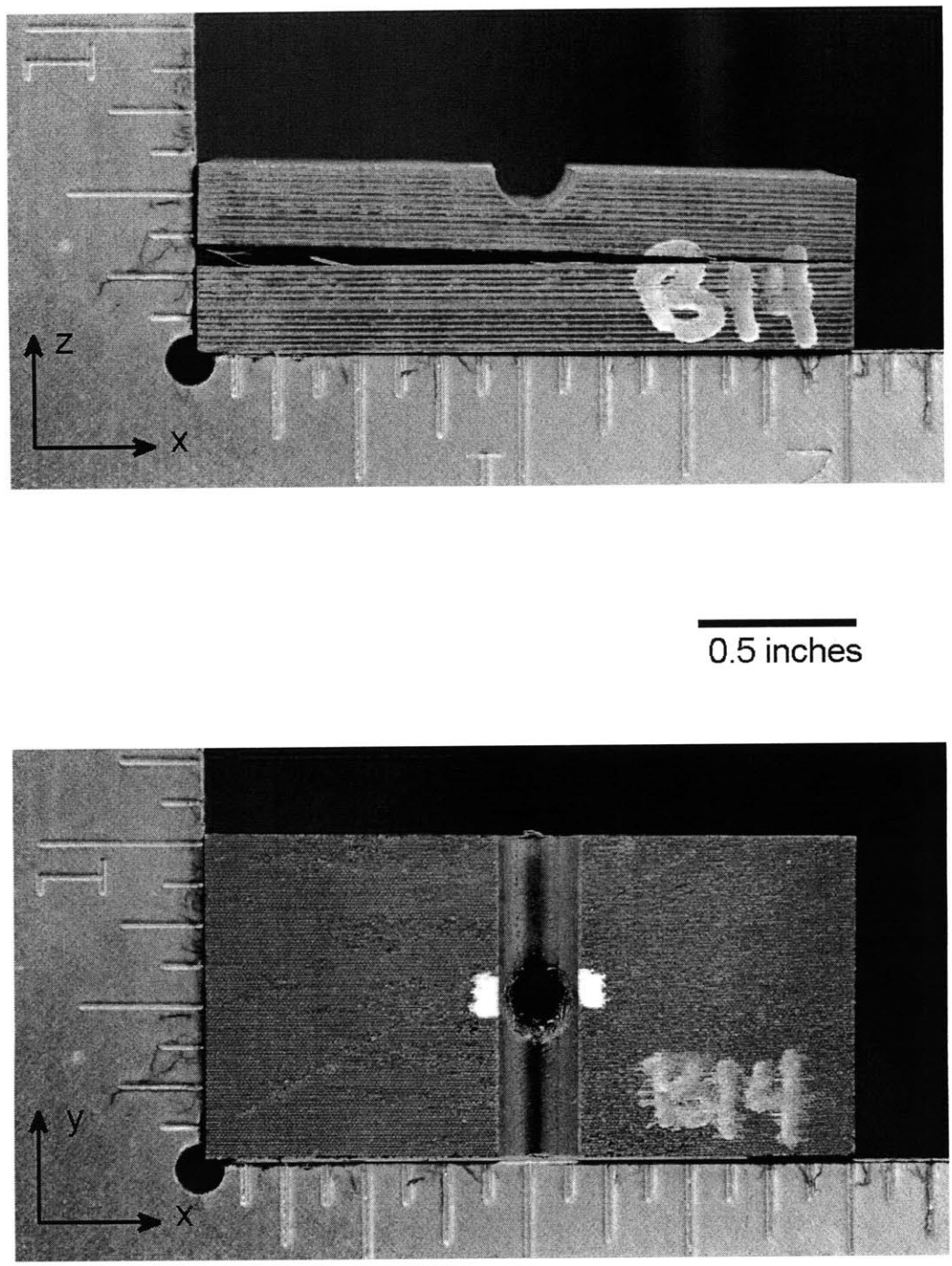

Figure C.23 Photographs of $[\pm 30/0]_{13S}$ Specimen 5, tested to failure in "three-dimensional loading" shown via (*top*) side view, and (*bottom*) top view with crater from indenter visible.

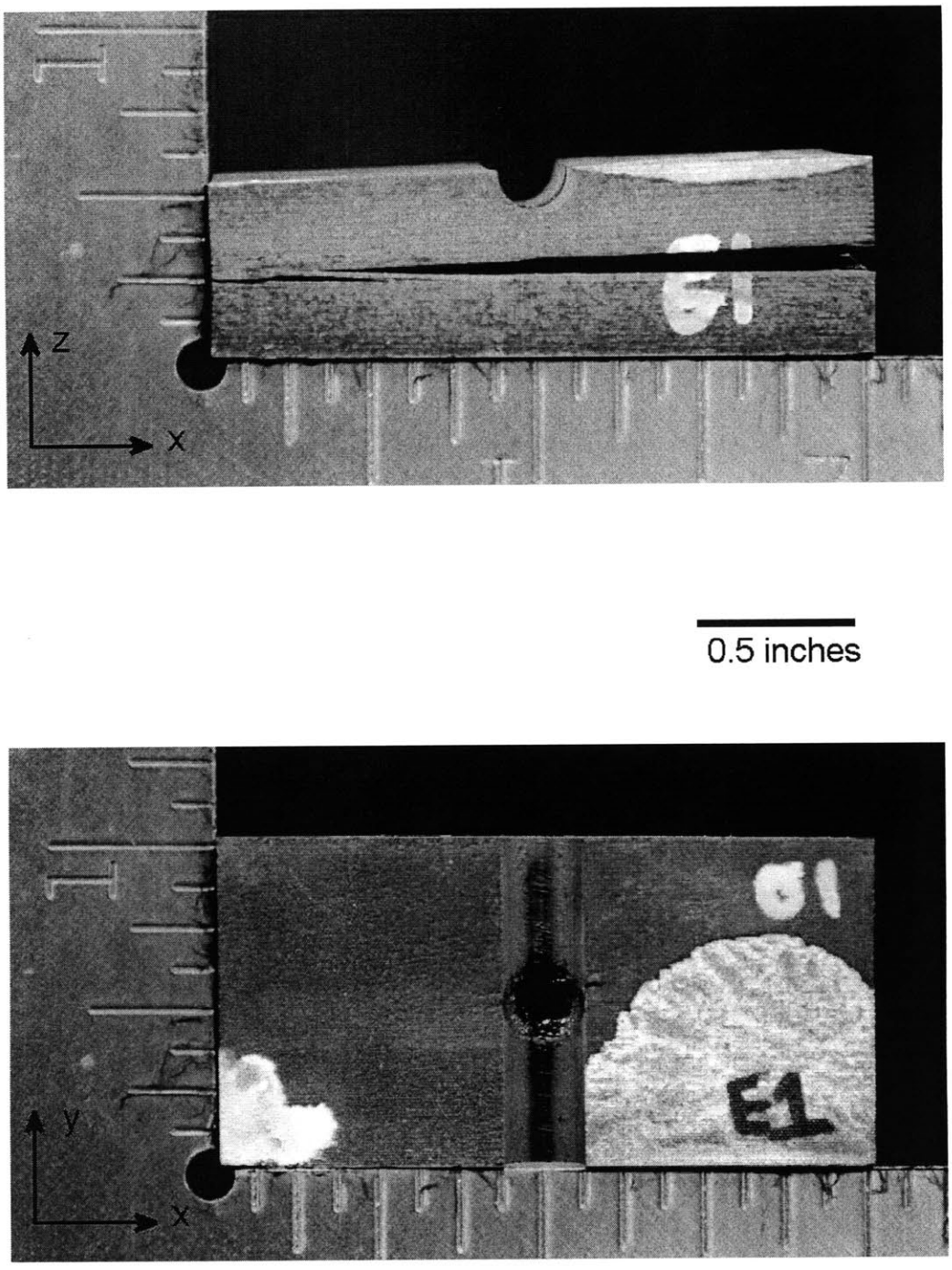

Figure C.24 Photographs of $[\pm 15/0]_{13S}$ Specimen 1, tested to failure in "three-dimensional loading" shown via (*top*) side view, and (*bottom*) top view with crater from indenter visible.

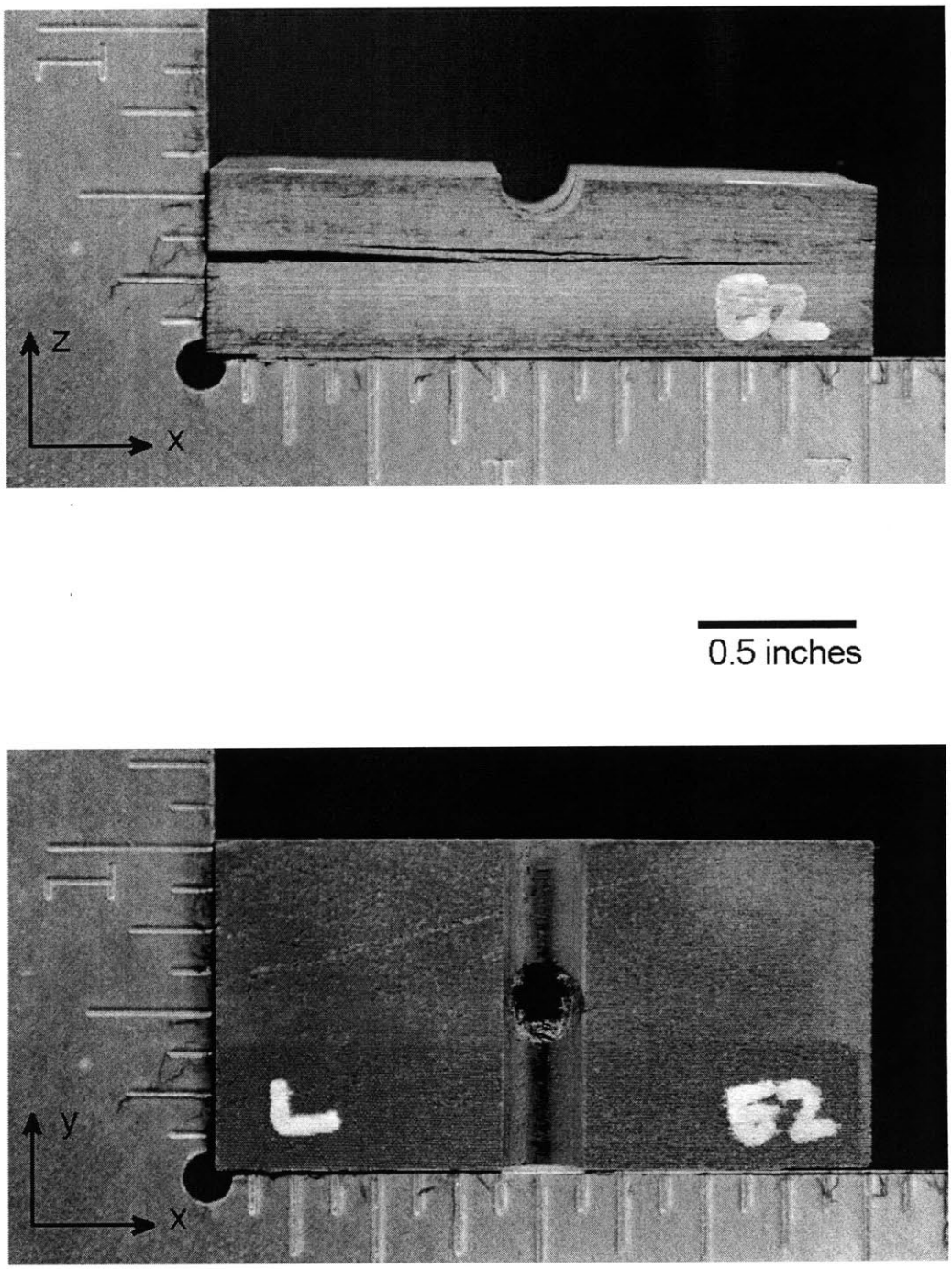

Figure C.25 Photographs of $[\pm 15/0]_{13S}$ Specimen 2, tested to failure in "three-dimensional loading" shown via (*top*) side view, and (*bottom*) top view with crater from indenter visible.

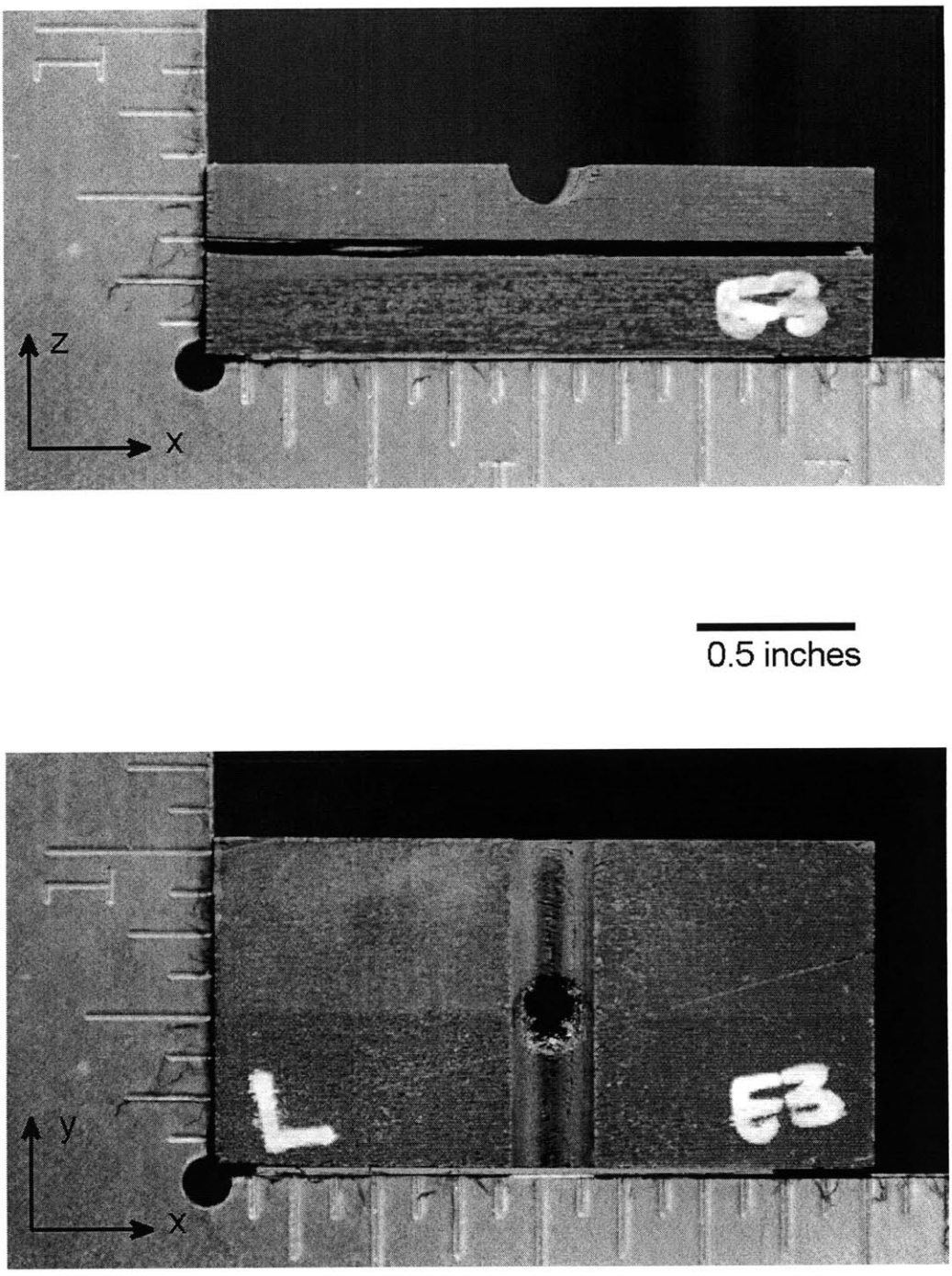

Figure C.26 Photographs of $[\pm 15/0]_{13S}$ Specimen 3, tested to failure in "three-dimensional loading" shown via (*top*) side view, and (*bottom*) top view with crater from indenter visible.

Appendix D

Photographs of "Two-Dimensional Loading" Specimens After Crushing

Photographs of all specimens tested to the crushing bound with the "two-dimensional loading" configuration (as discussed in Chapter 5) are presented in this appendix. The photographs are a top view and side view of each specimen. The testing procedures are those discussed in Chapter 4.

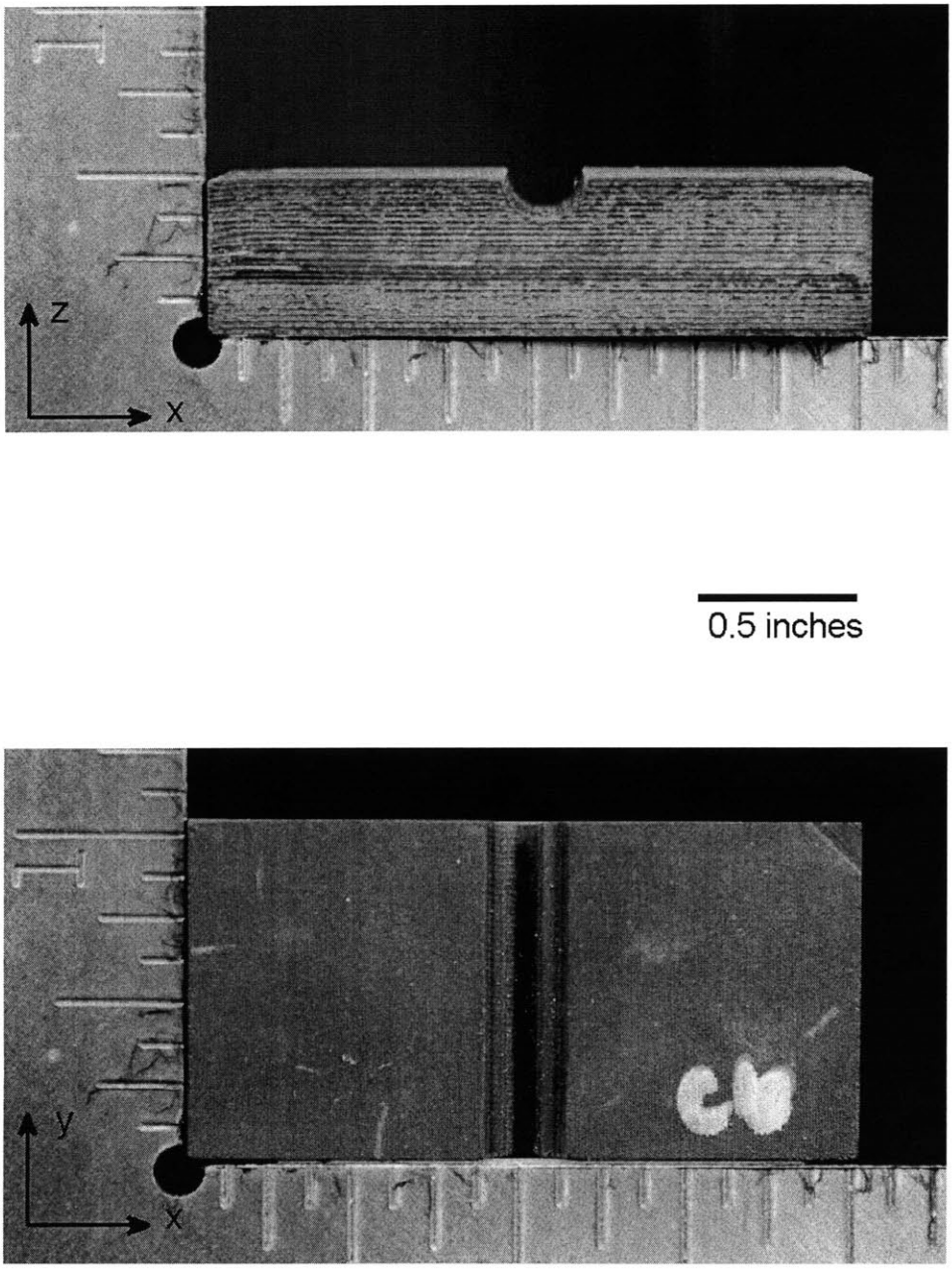

Figure D.1 Photographs of $[\pm 45/90/0]_{10S}$ specimen, tested to crushing in "two-dimensional loading", shown via (*top*) side view, and (*bottom*) top view.

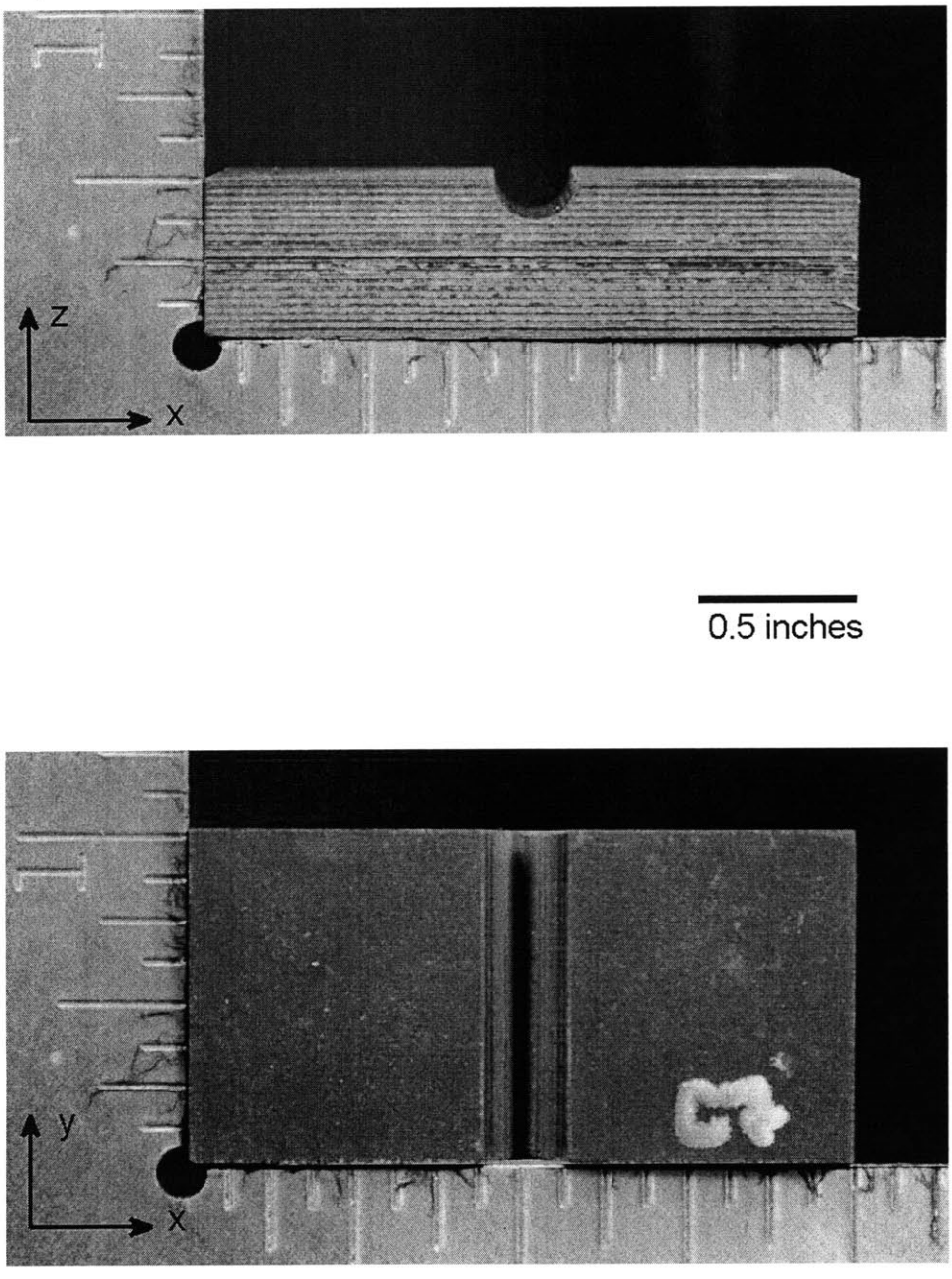

Figure D.2 Photographs of $[\pm 45/90/0]_{10S}$ specimen, tested to crushing in "two-dimensional loading", shown via (*top*) side view, and (*bottom*) top view.

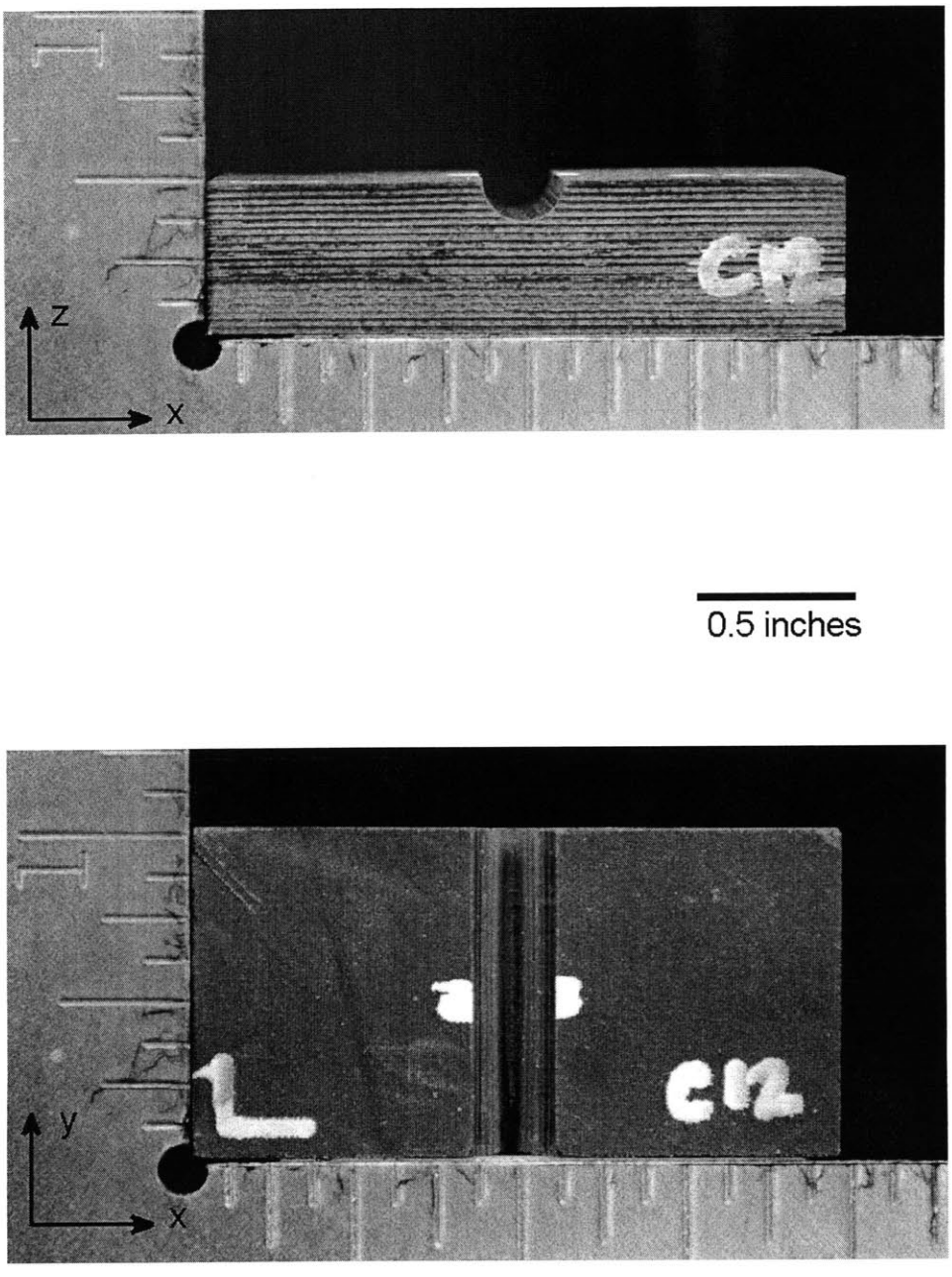

Figure D.3 Photographs of $[\pm 45/90/0]_{10S}$ specimen, tested to crushing in "two-dimensional loading", shown via (*top*) side view, and (*bottom*) top view.

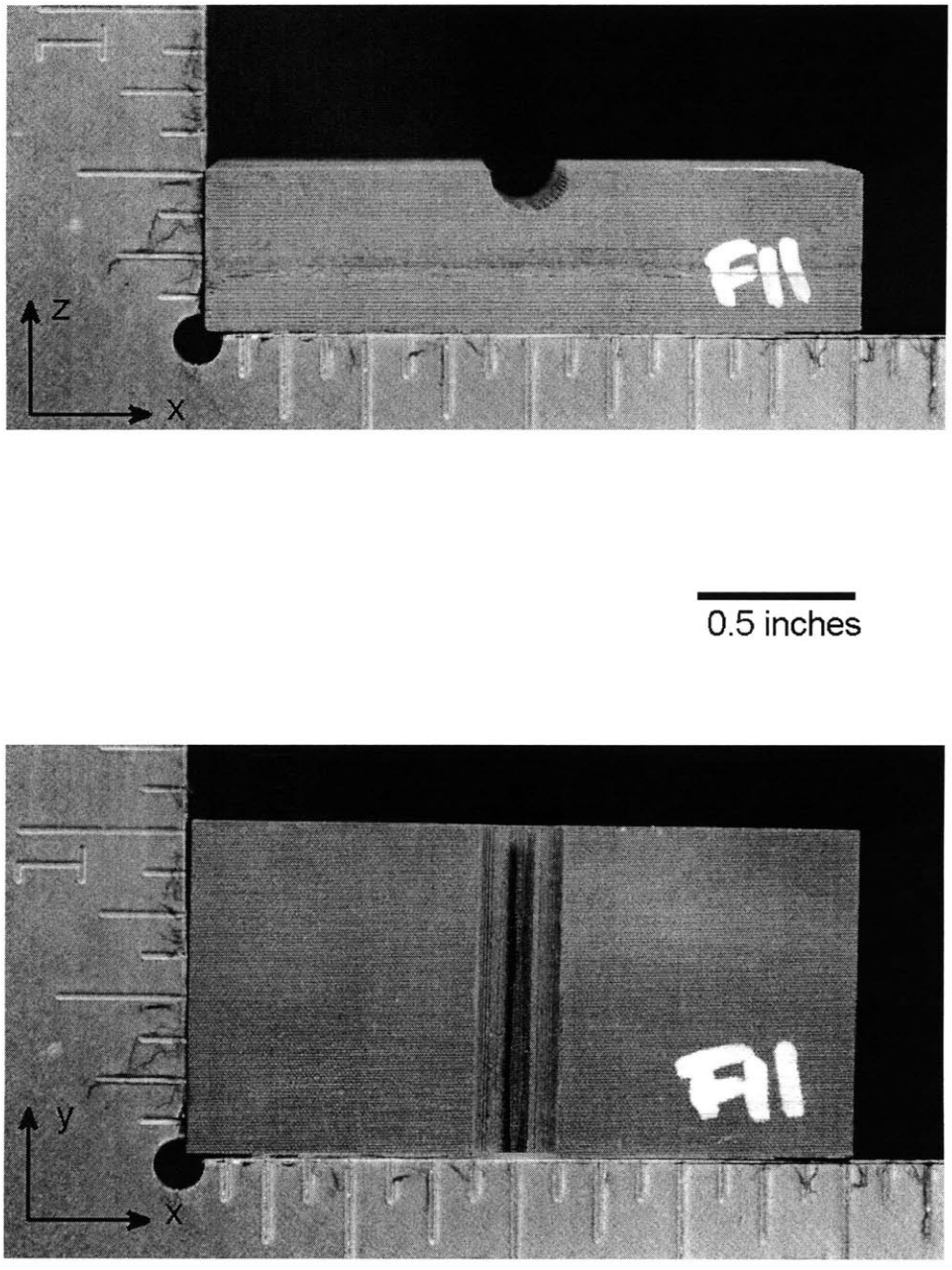

Figure D.4 Photographs of $[90/0]_{20S}$ specimen, tested to crushing in "two-dimensional loading", shown via (*top*) side view, and (*bottom*) top view.

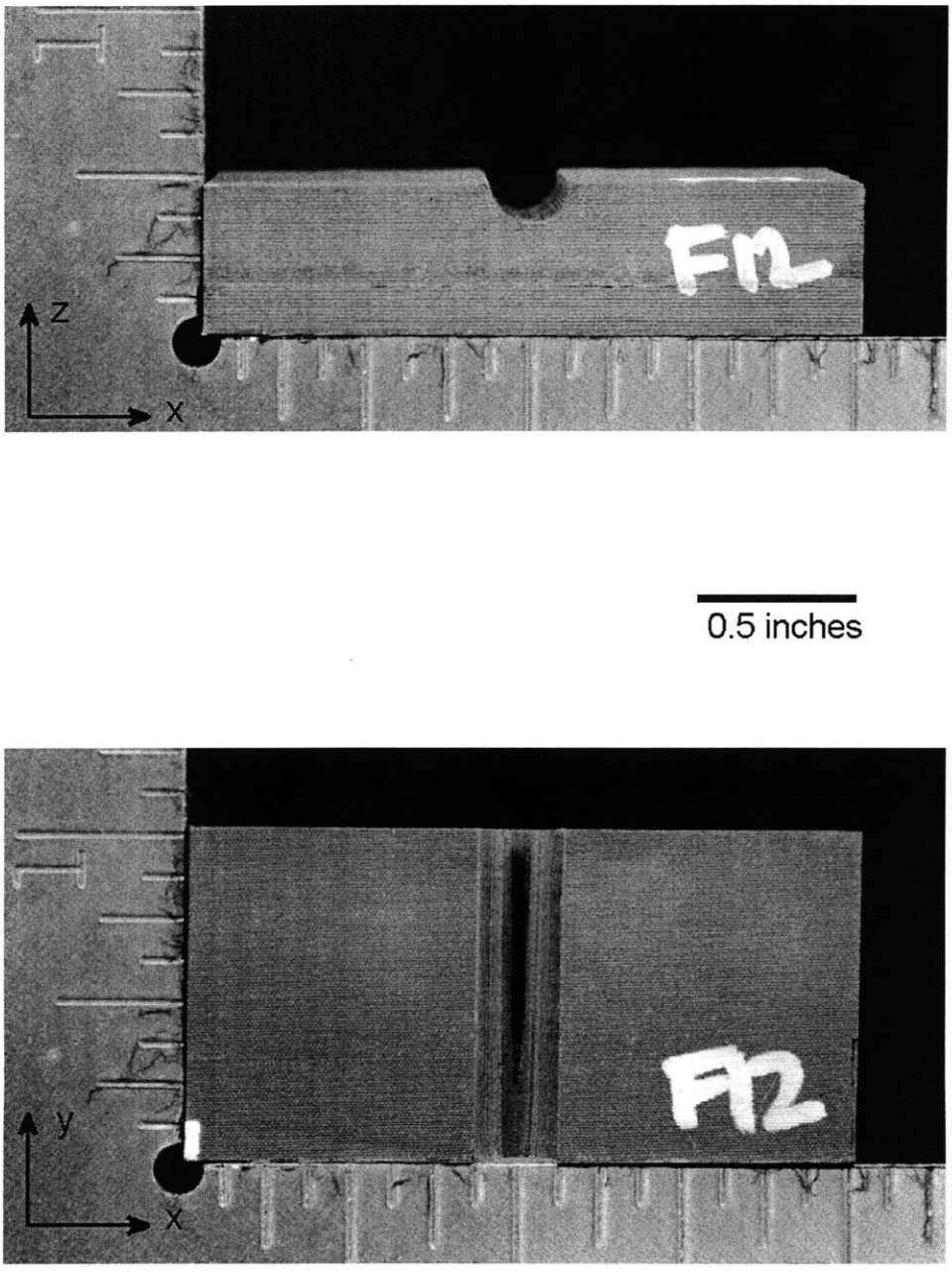

Figure D.5 Photographs of $[90/0]_{20S}$ specimen, tested to crushing in "two-dimensional loading", shown via (*top*) side view, and (*bottom*) top view.

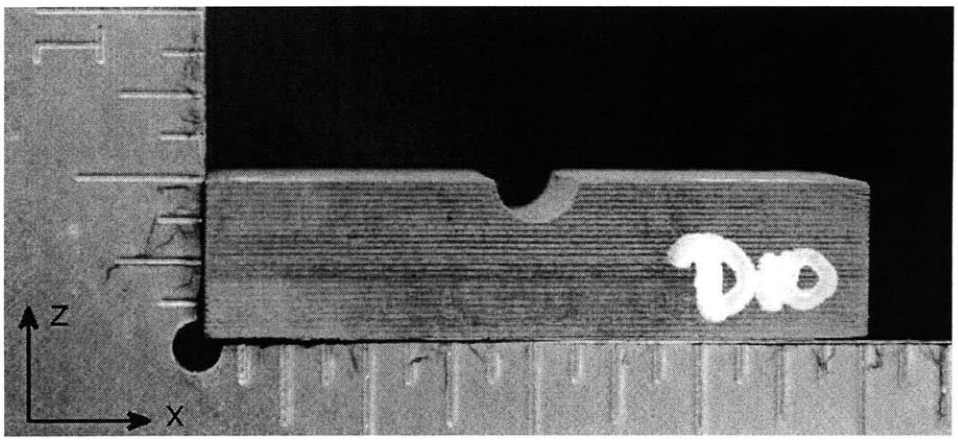

Figure D.6 Photographs of $[\pm 60/0]_{13S}$ specimen, tested to crushing in "two-dimensional loading", shown via (*top*) side view, and (*bottom*) top view.

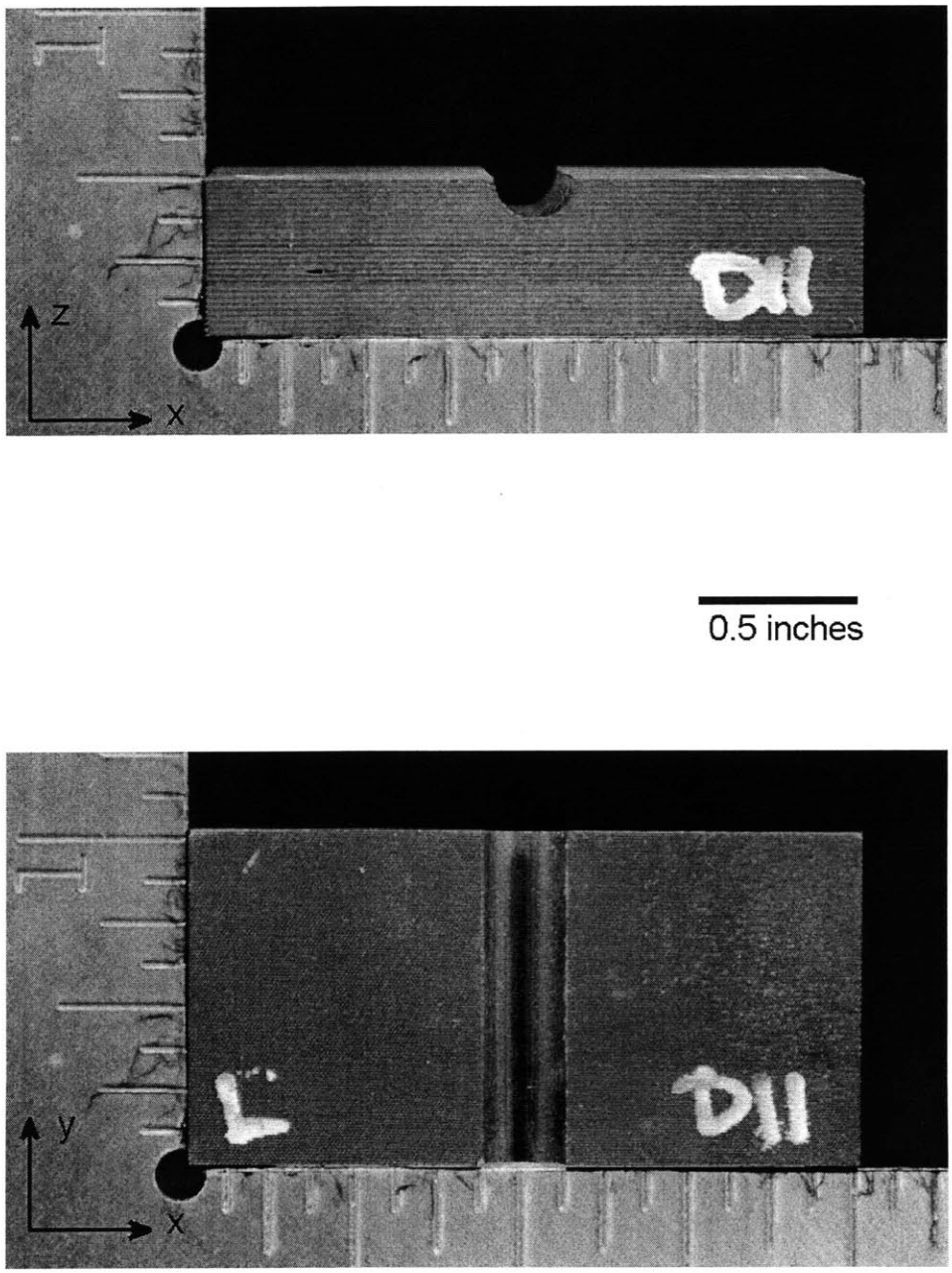

Figure D.7 Photographs of $[\pm 60/0]_{13S}$ specimen, tested to crushing in "two-dimensional loading", shown via (*top*) side view, and (*bottom*) top view.

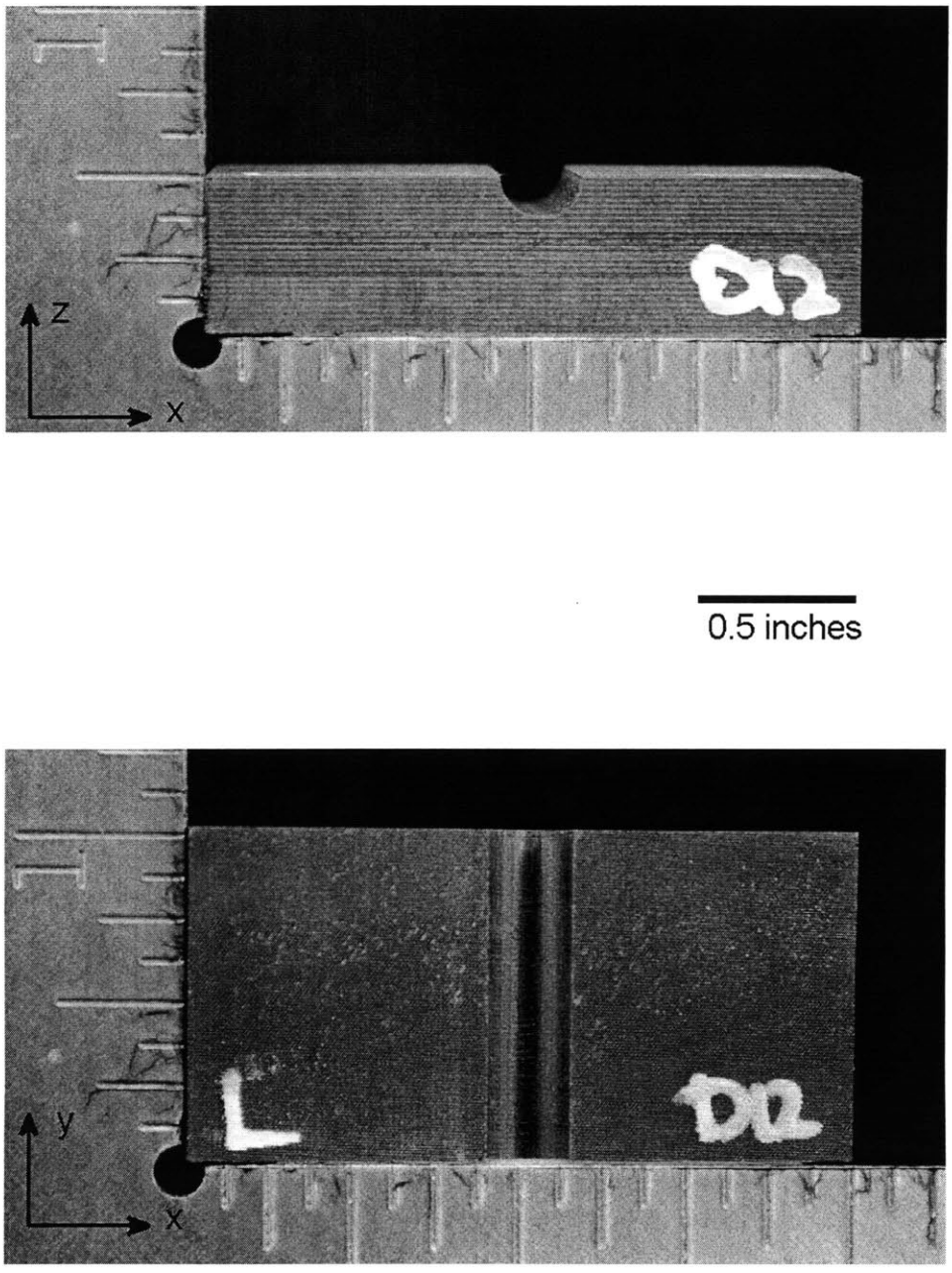

Figure D.8 Photographs of $[\pm 60/0]_{13S}$ specimen, tested to crushing in "two-dimensional loading", shown via (*top*) side view, and (*bottom*) top view.

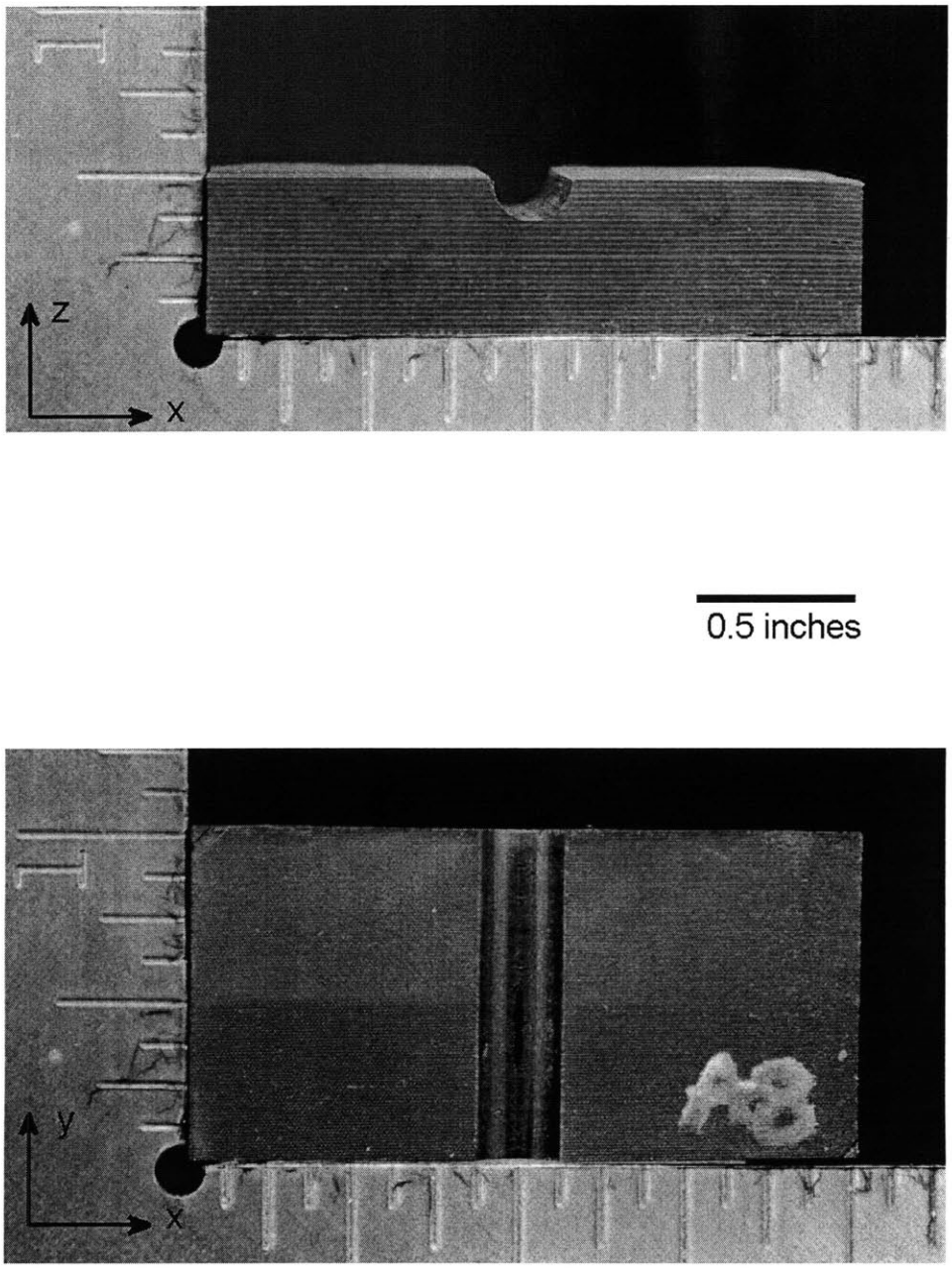

Figure D.9 Photographs of $[\pm 45/0]_{13S}$ specimen, tested to crushing in "two-dimensional loading", shown via (*top*) side view, and (*bottom*) top view.

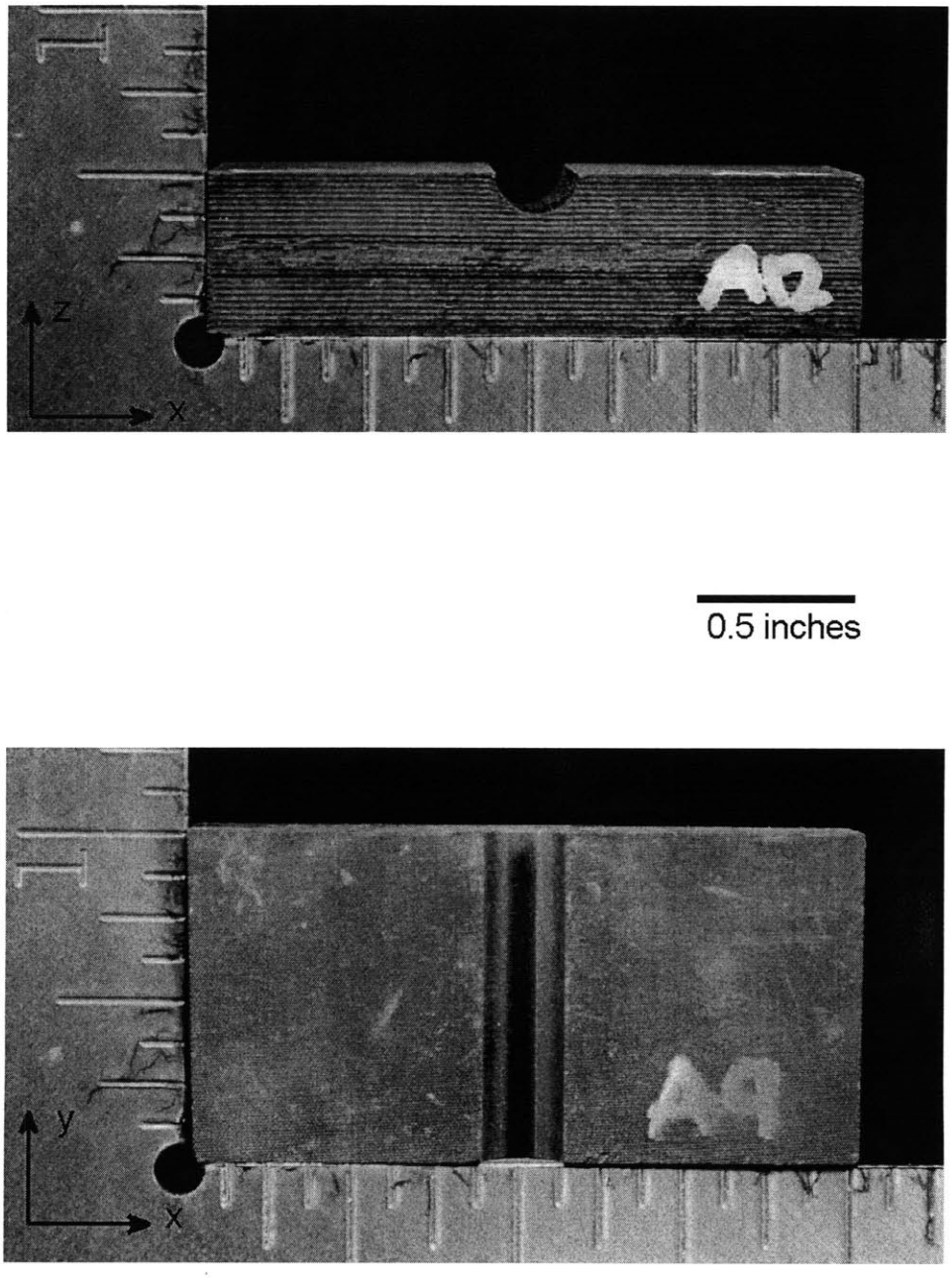

Figure D.10 Photographs of $[\pm 45/0]_{13S}$ specimen, tested to crushing in "two-dimensional loading", shown via (*top*) side view, and (*bottom*) top view.

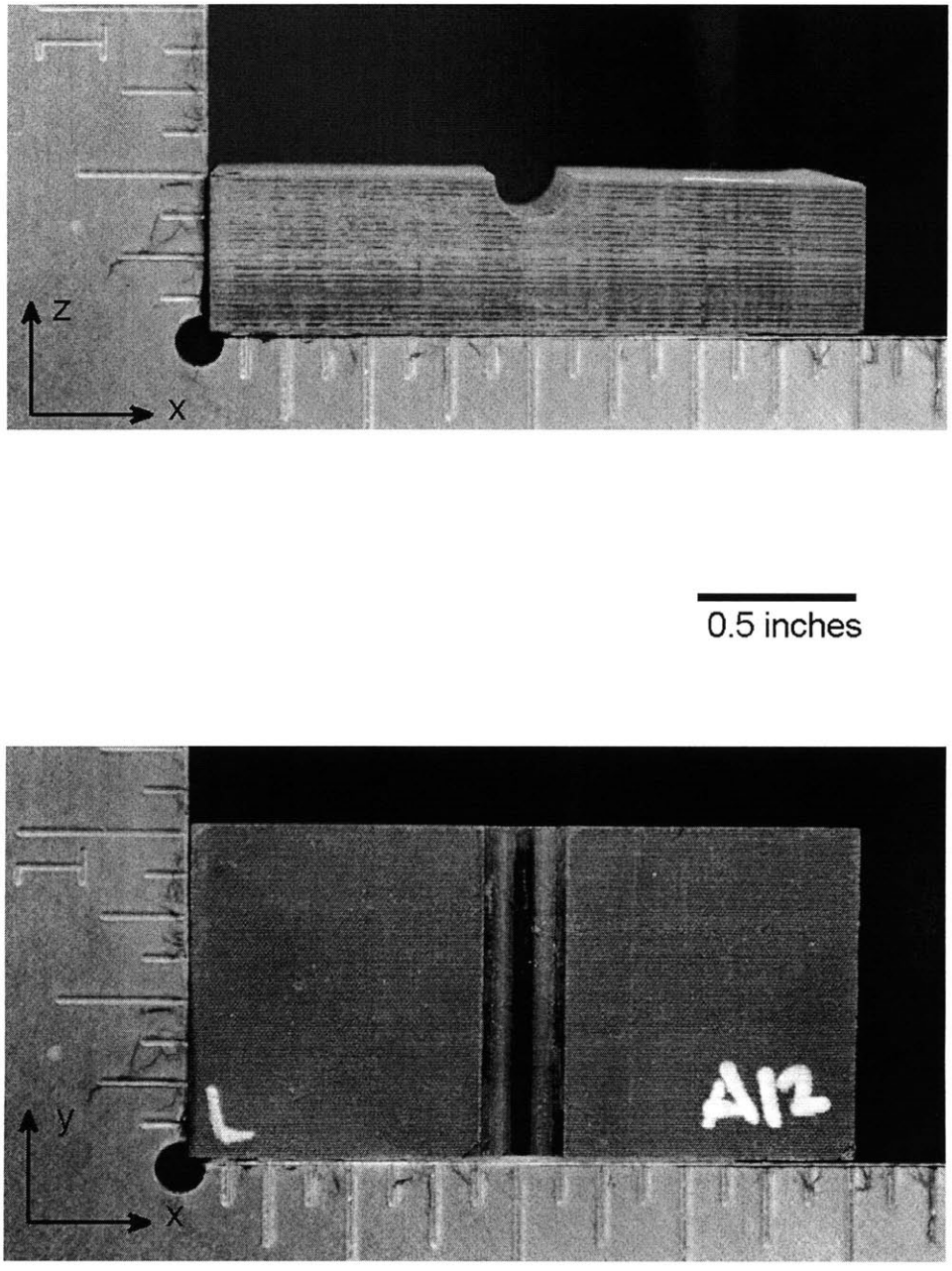

Figure D.11 Photographs of $[\pm 45/0]_{13S}$ specimen, tested to crushing in "two-dimensional loading", shown via (*top*) side view, and (*bottom*) top view.

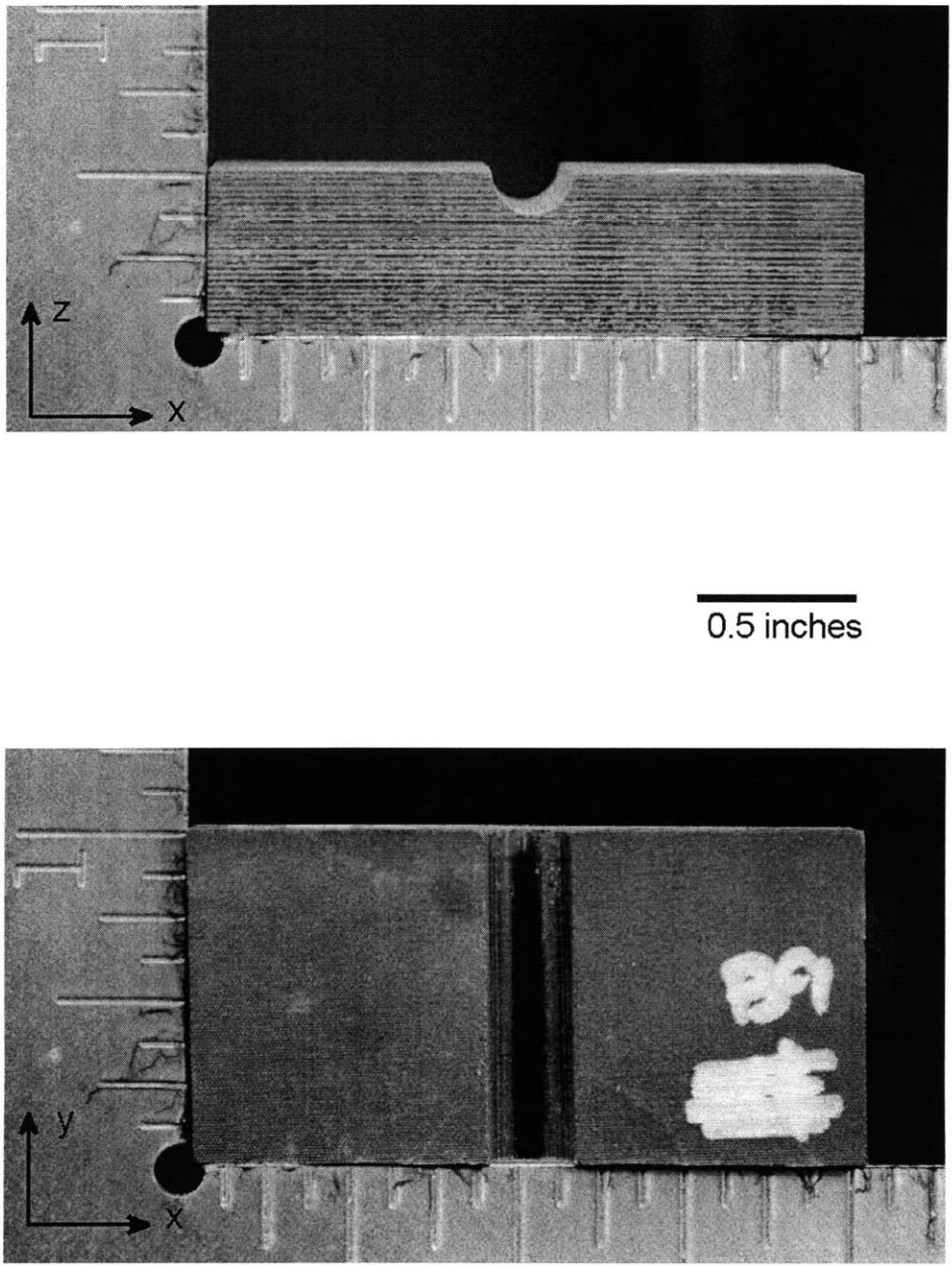

Figure D.12 Photographs of $[\pm 30/0]_{13S}$ specimen, tested to crushing in "two-dimensional loading", shown via (*top*) side view, and (*bottom*) top view.

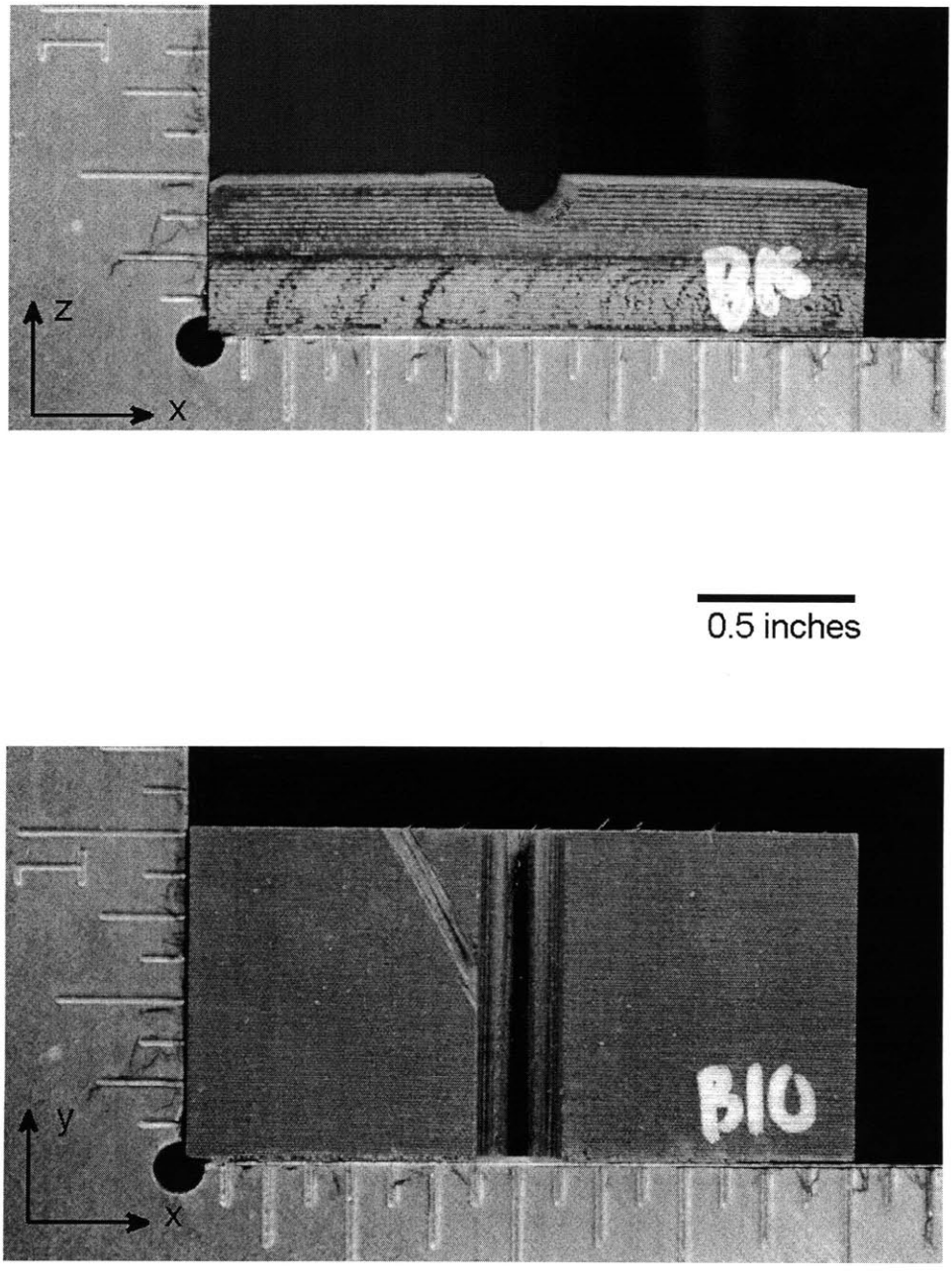

Figure D.13 Photographs of $[\pm 30/0]_{13S}$ specimen, tested to crushing in "two-dimensional loading", shown via (*top*) side view, and (*bottom*) top view.

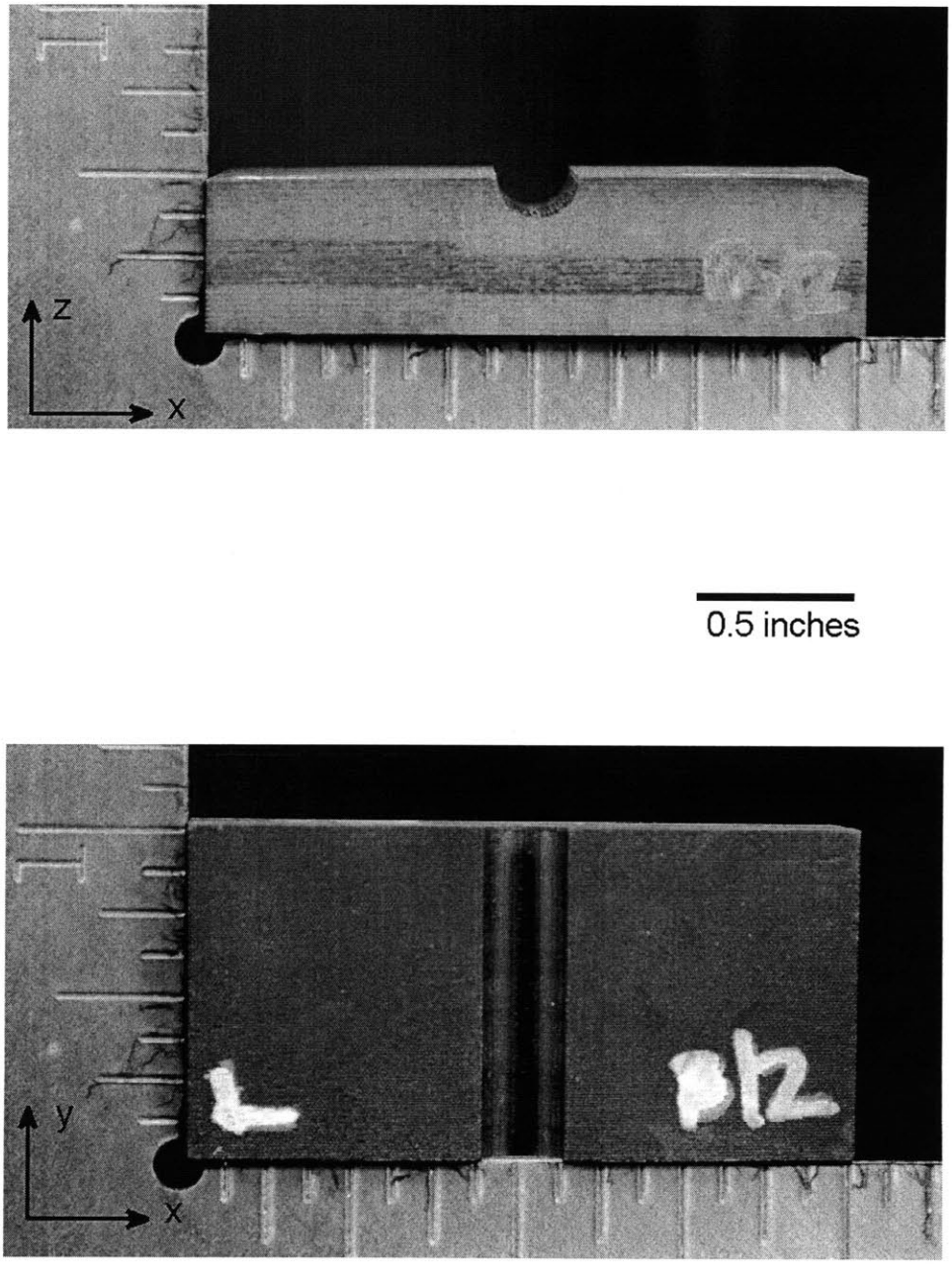

Figure D.14 Photographs of $[\pm 30/0]_{13S}$ specimen, tested to crushing in "two-dimensional loading", shown via (*top*) side view, and (*bottom*) top view.

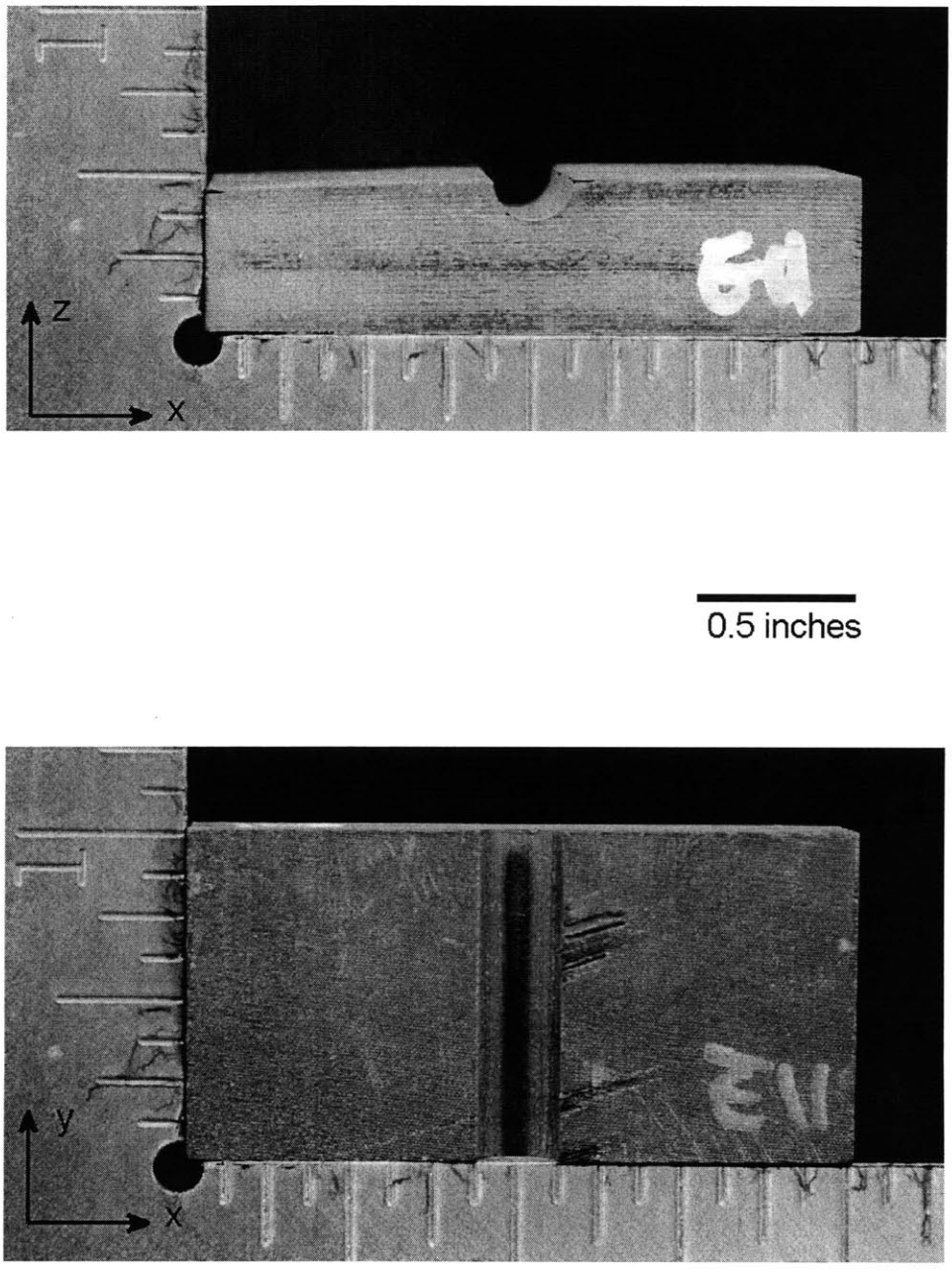

Figure D.15 Photographs of $[\pm 15/0]_{13S}$ specimen, tested to crushing in "two-dimensional loading", shown via (*top*) side view, and (*bottom*) top view.

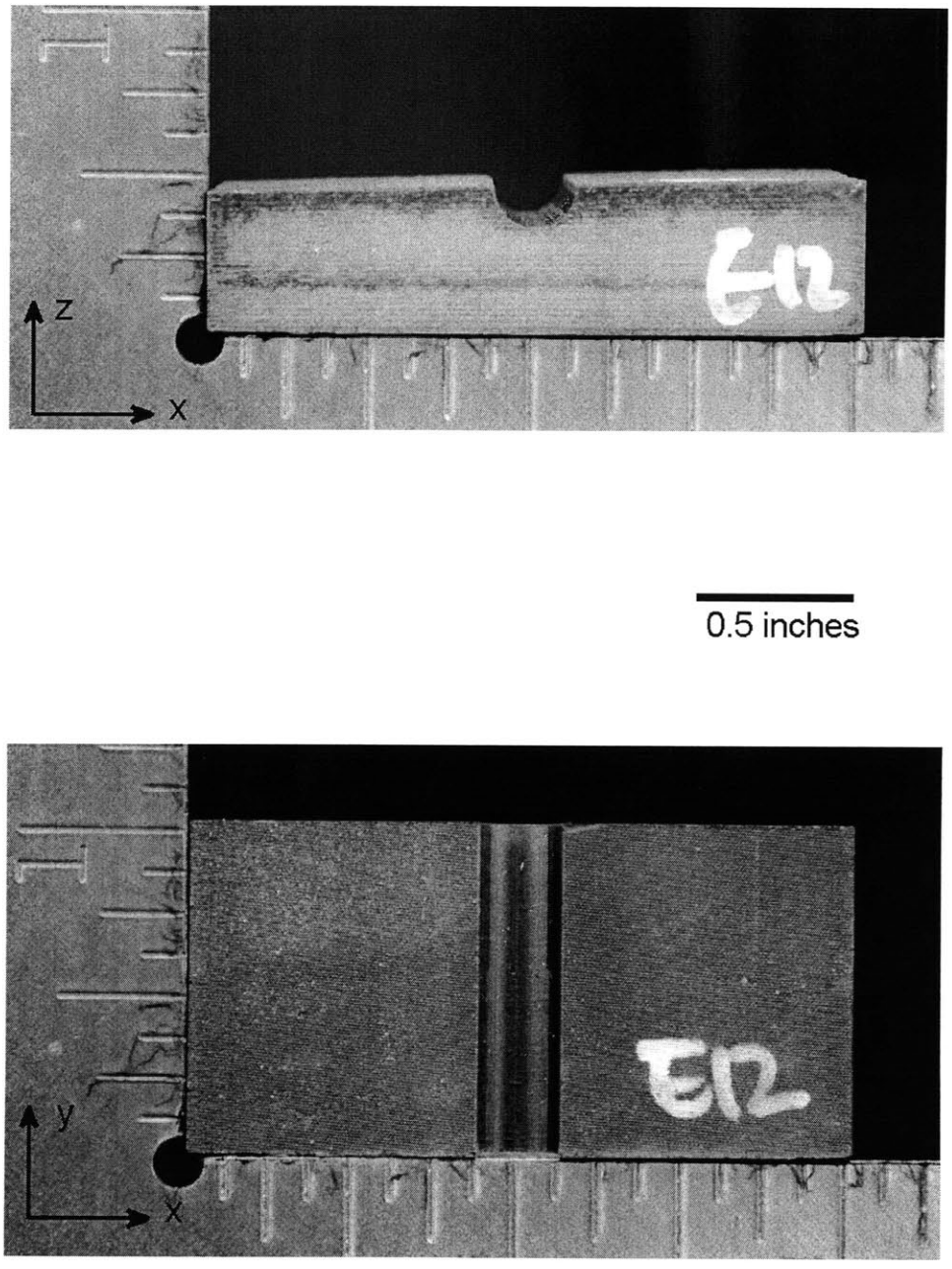

Figure D.16 Photographs of $[\pm 15/0]_{13S}$ specimen, tested to crushing in "two-dimensional loading", shown via (*top*) side view, and (*bottom*) top view.

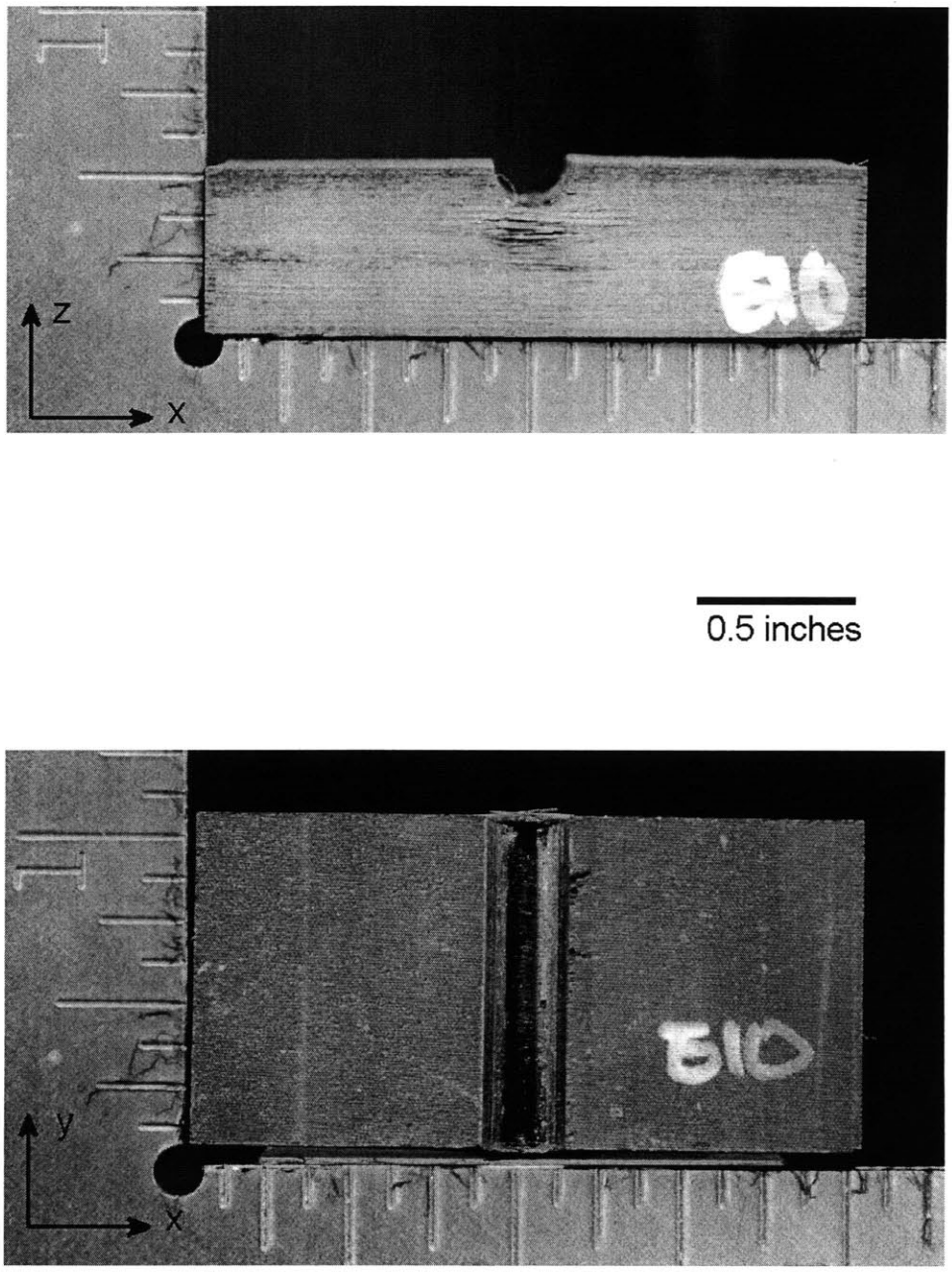

Figure D.17 Photographs of $[\pm 15/0]_{13S}$ specimen, tested to crushing in "two-dimensional loading", shown via (*top*) side view, and (*bottom*) top view.

Appendix E

Photographs of "Three-Dimensional Loading" Specimens After Crushing

Photographs of all specimens tested to the crushing bound with the "three-dimensional loading" configuration (as discussed in Chapter 5) are presented in this appendix. The photographs are a top view and side view of each specimen. The testing procedures are those discussed in Chapter 4.

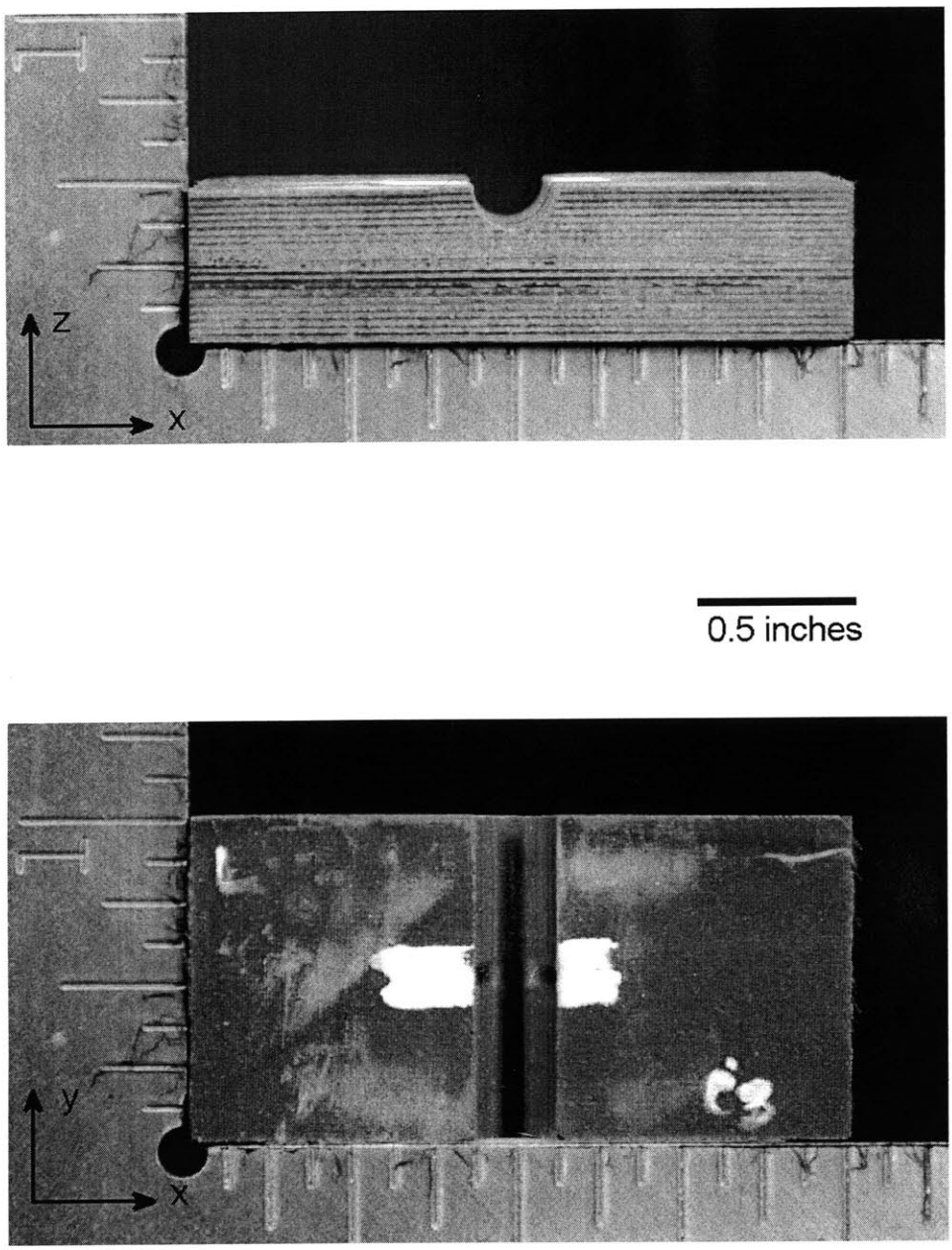

Figure E.1 Photographs of $[\pm 45/90/0]_{10S}$ specimen, tested to crushing in "three-dimensional loading", shown via (*top*) side view, and (*bottom*) top view.

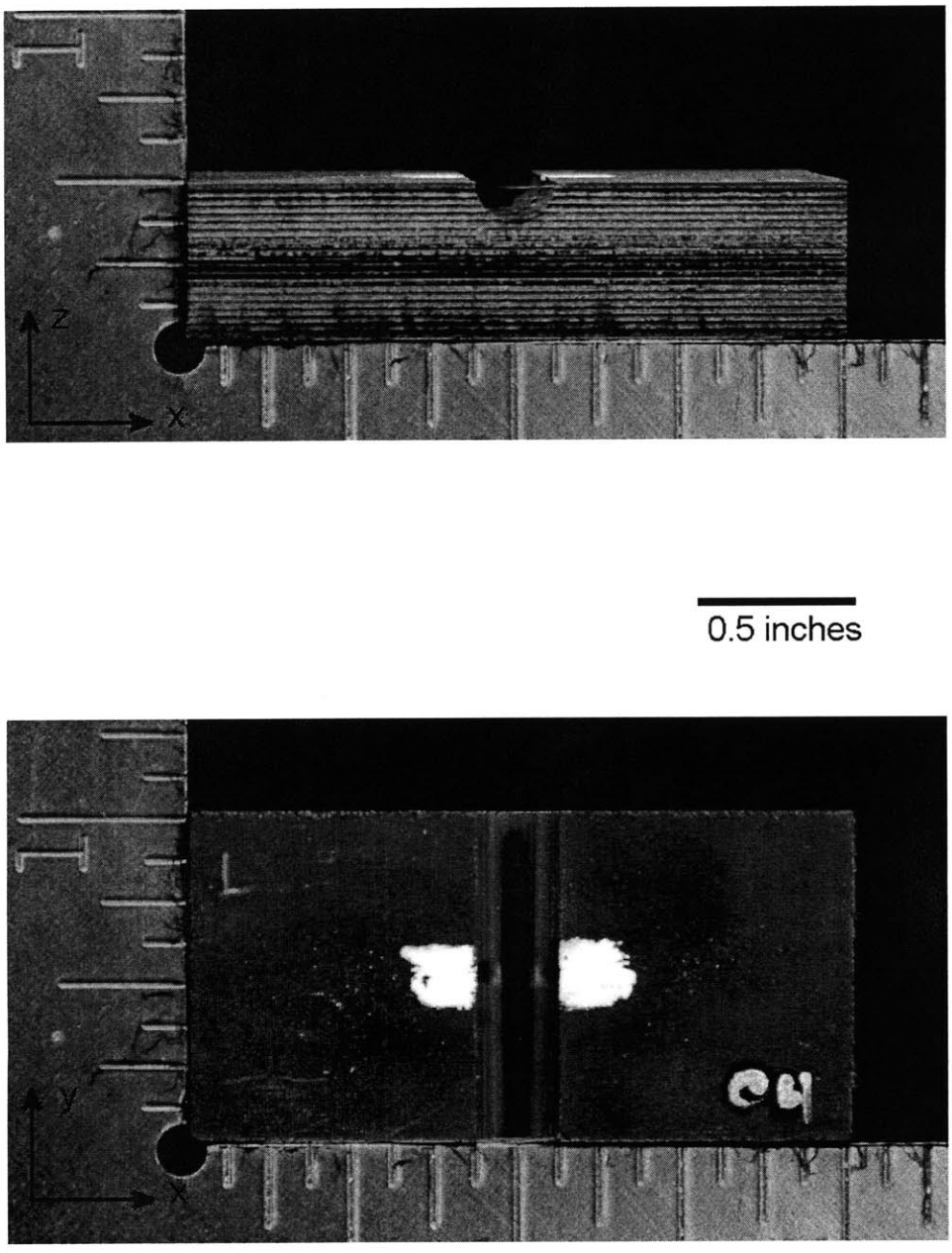

Figure E.2 Photographs of $[\pm 45/90/0]_{10S}$ specimen, tested to crushing in "three-dimensional loading", shown via (*top*) side view, and (*bottom*) top view.

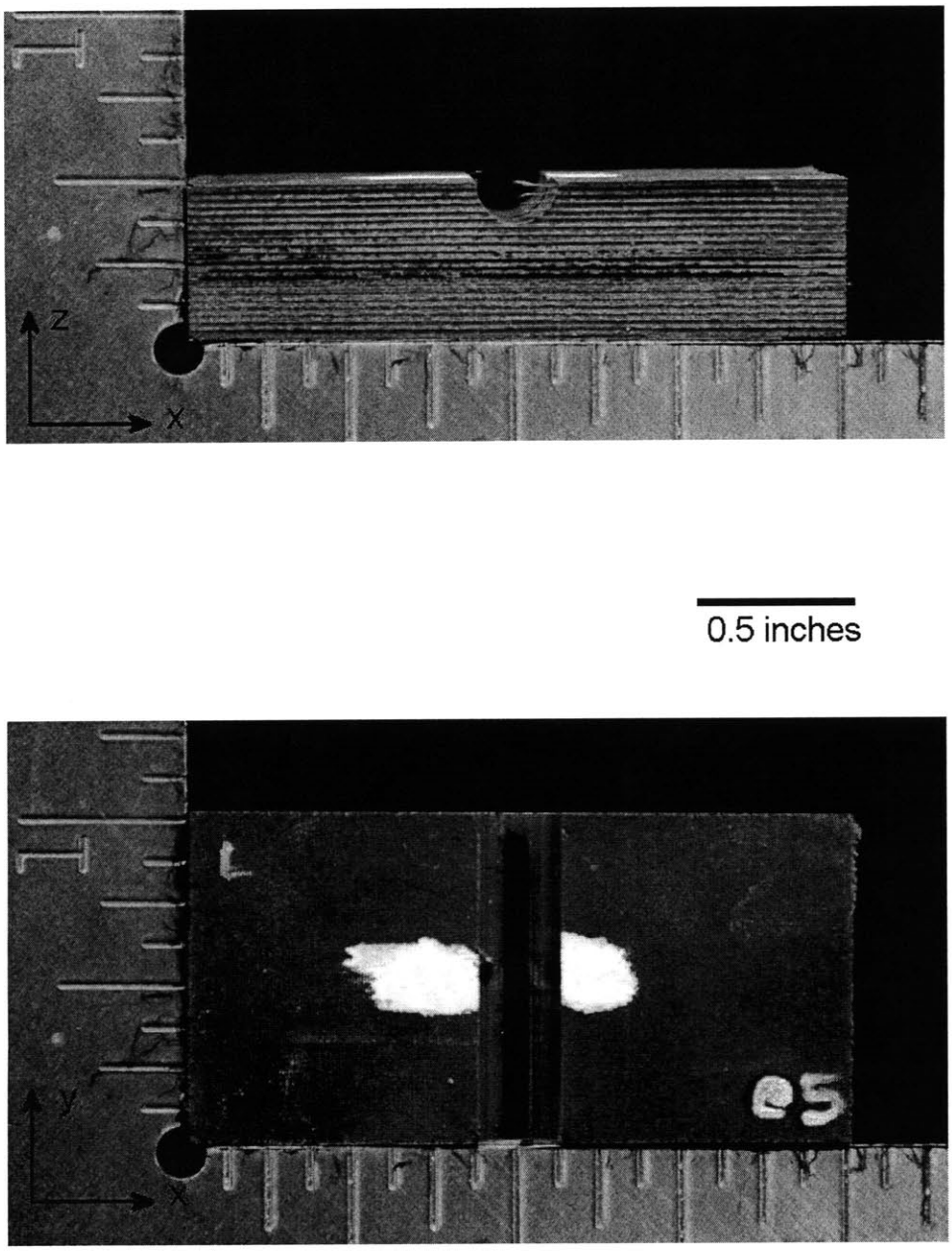

Figure E.3 Photographs of $[\pm 45/90/0]_{10S}$ specimen, tested to crushing in "three-dimensional loading", shown via (*top*) side view, and (*bottom*) top view.

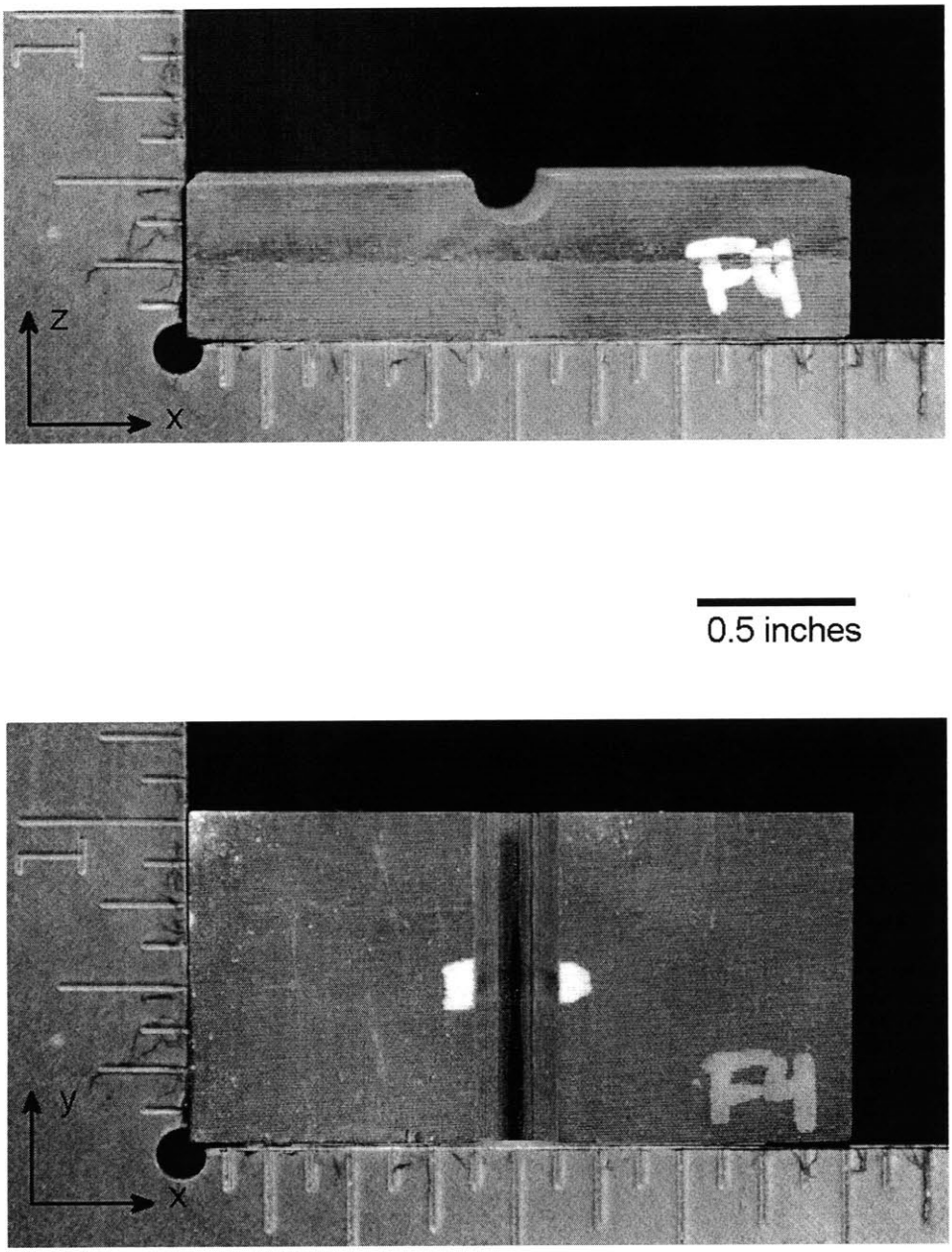

Figure E.4 Photographs of $[90/0]_{20S}$ specimen, tested to crushing in "three-dimensional loading", shown via (*top*) side view, and (*bottom*) top view.

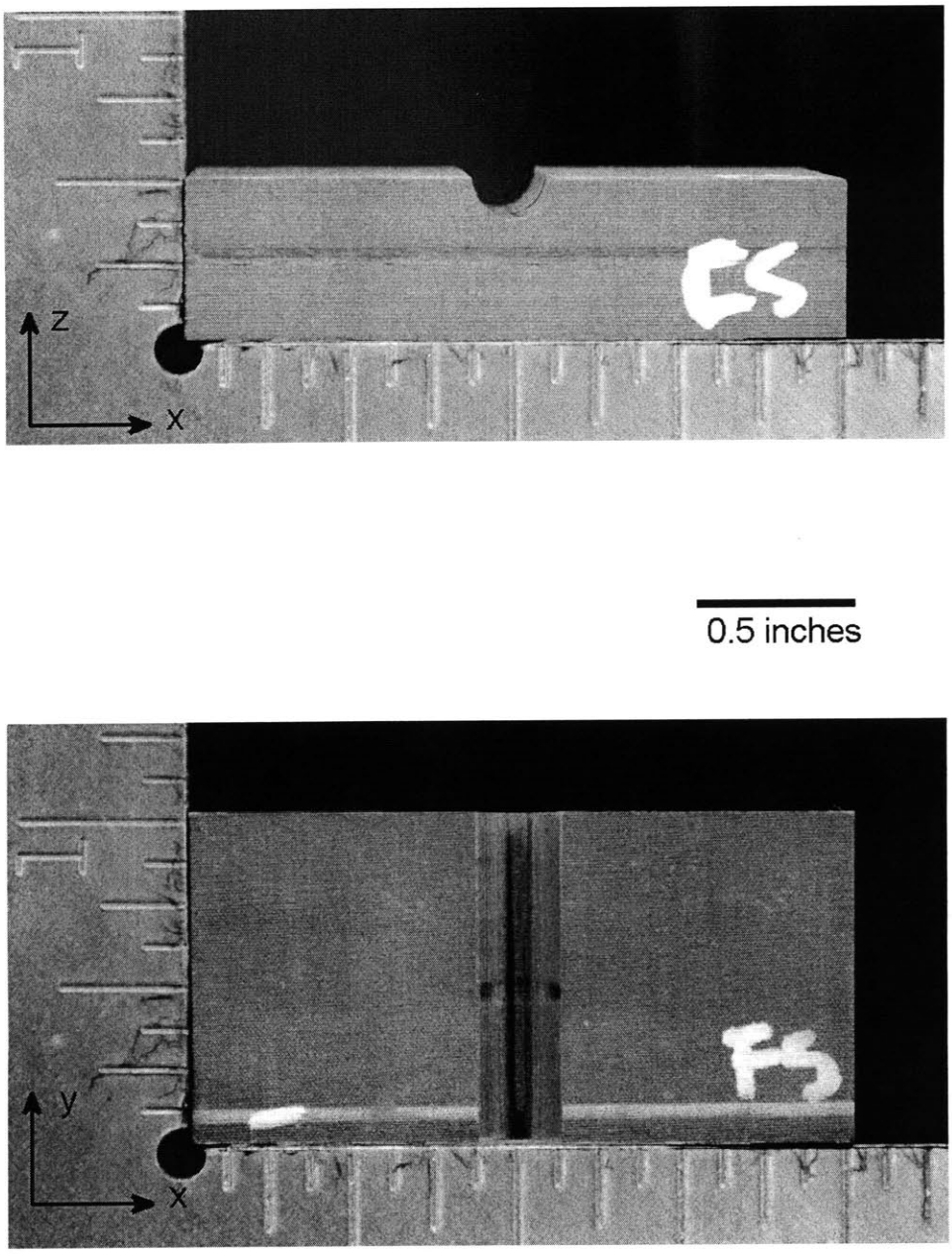

Figure E.5 Photographs of $[90/0]_{20S}$ specimen, tested to crushing in "three-dimensional loading", shown via (*top*) side view, and (*bottom*) top view.

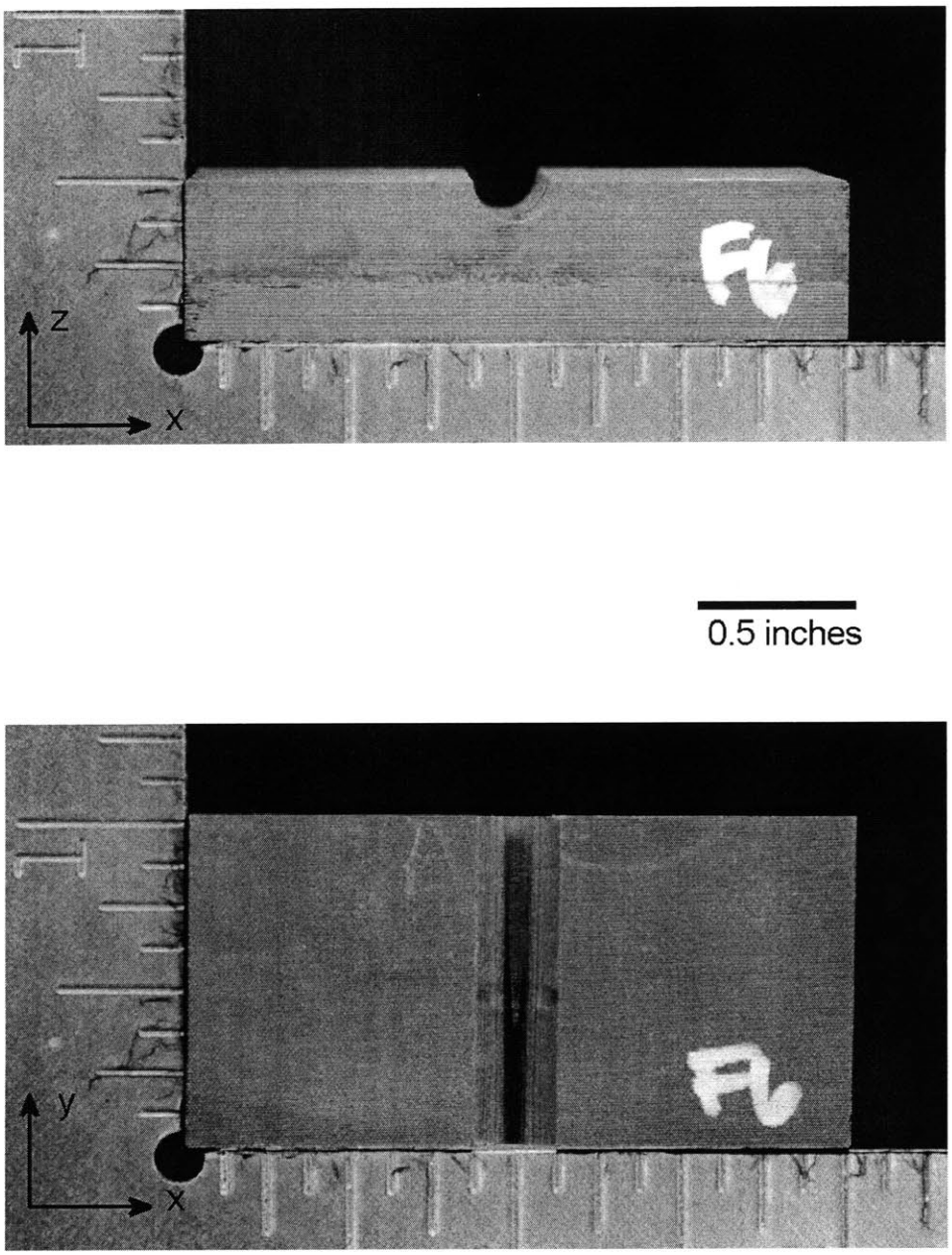

Figure E.6 Photographs of $[90/0]_{20S}$ specimen, tested to crushing in "three-dimensional loading", shown via (*top*) side view, and (*bottom*) top view.

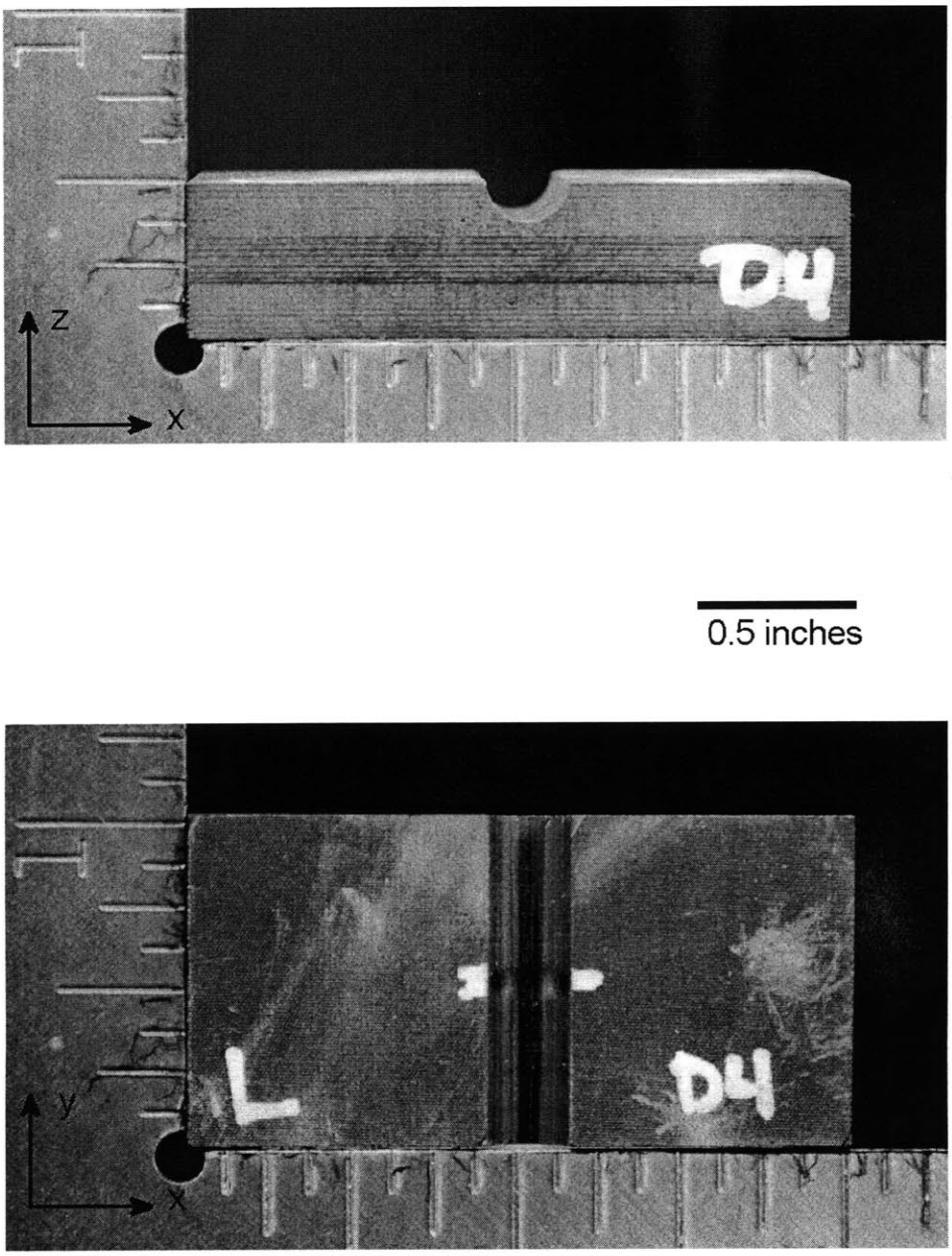

Figure E.7 Photographs of $[\pm 60/0]_{13S}$ specimen, tested to crushing in "three-dimensional loading", shown via (*top*) side view, and (*bottom*) top view.

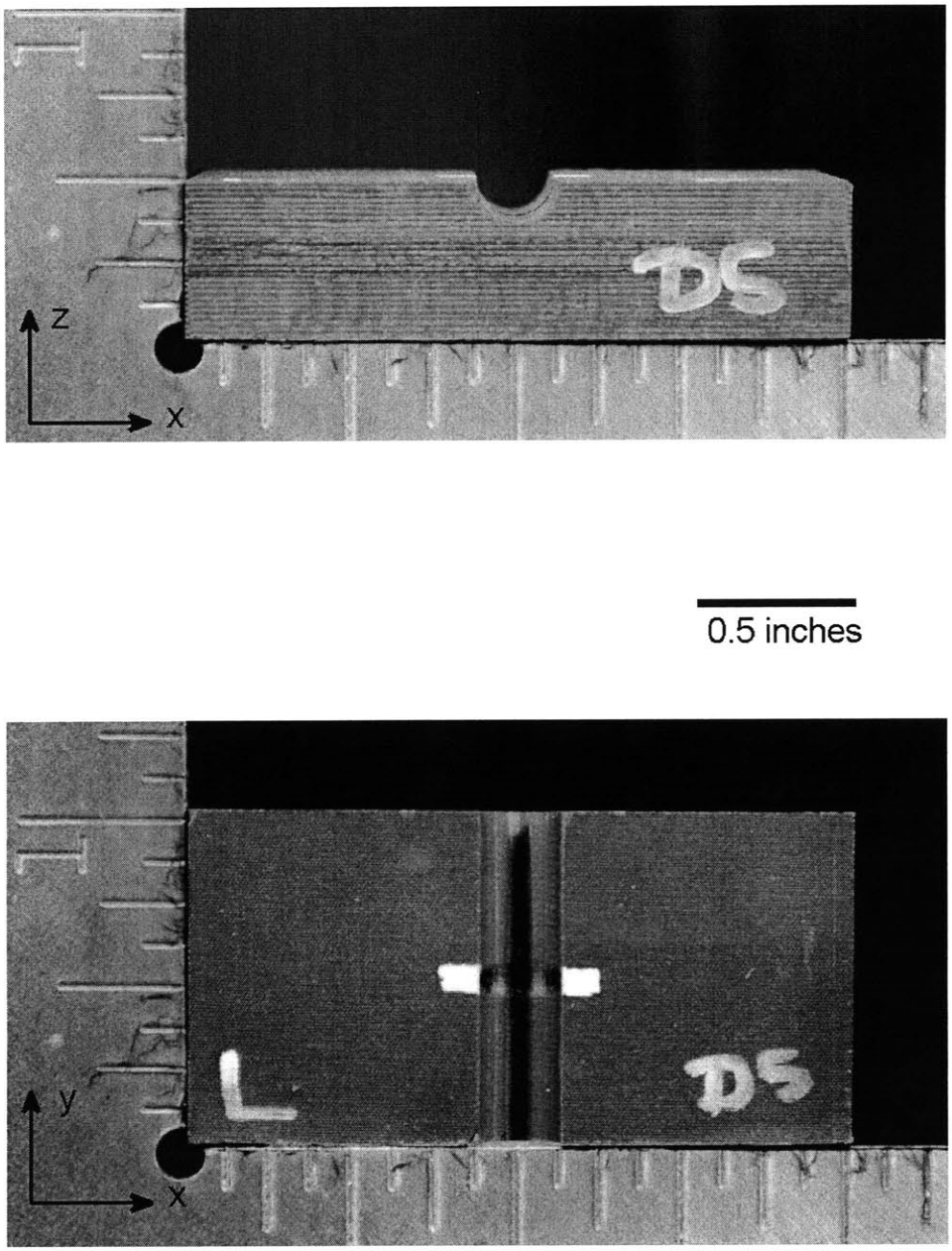

Figure E.8 Photographs of $[\pm 60/0]_{13S}$ specimen, tested to crushing in "three-dimensional loading", shown via (*top*) side view, and (*bottom*) top view.

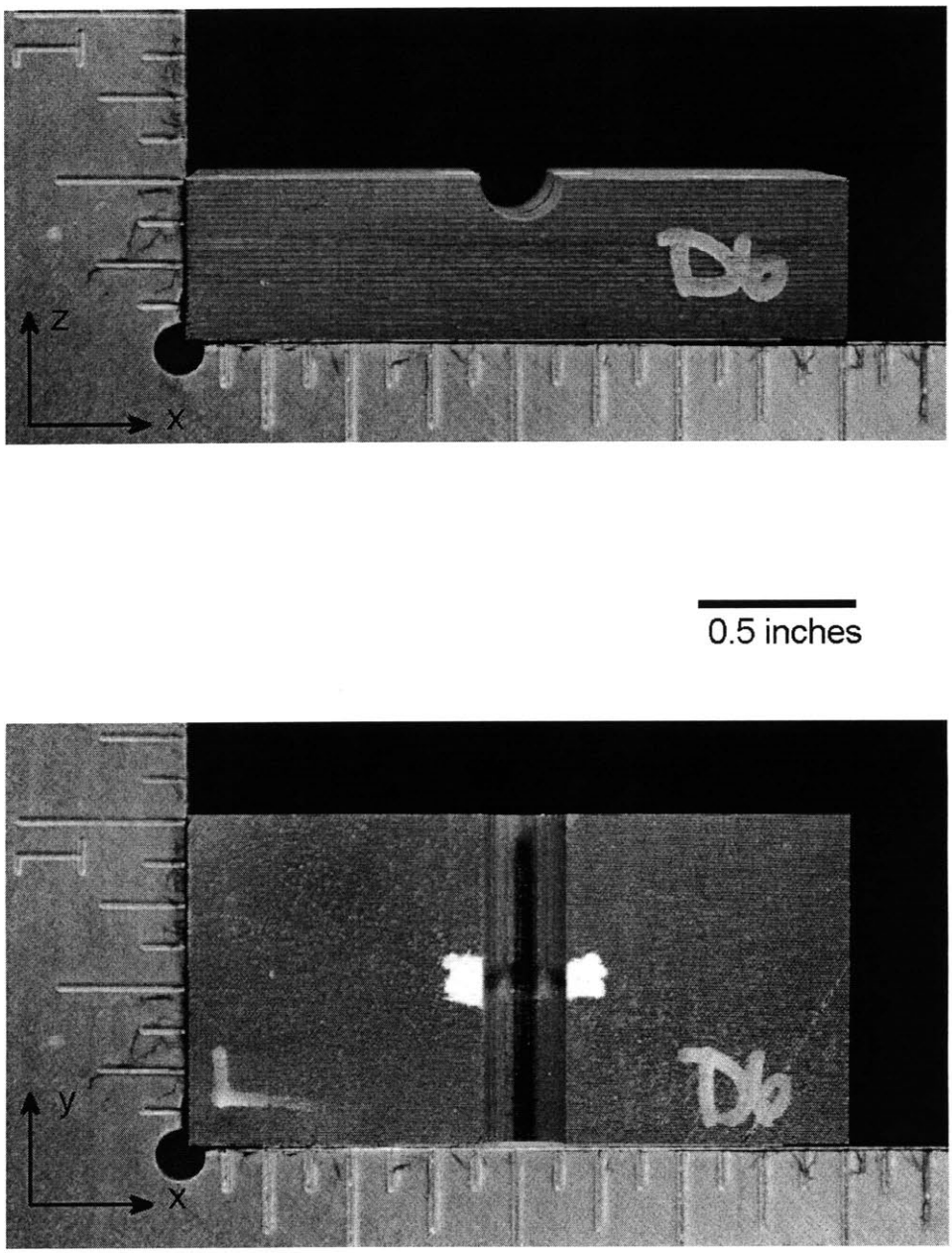

Figure E.9 Photographs of $[\pm 60/0]_{13S}$ specimen, tested to crushing in "three-dimensional loading", shown via (*top*) side view, and (*bottom*) top view.

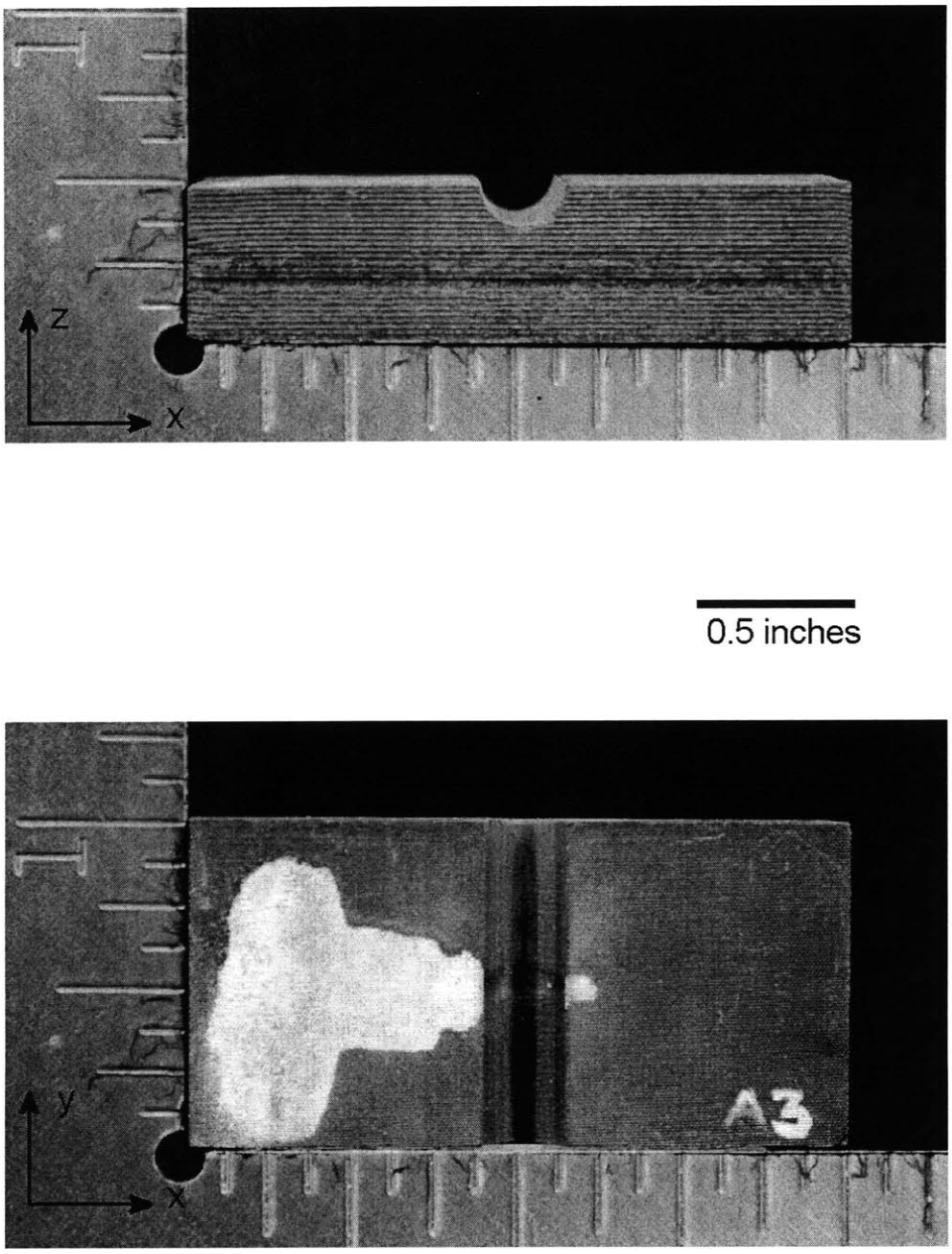

Figure E.10 Photographs of $[\pm 45/0]_{13S}$ specimen, tested to crushing in "three-dimensional loading", shown via (*top*) side view, and (*bottom*) top view.

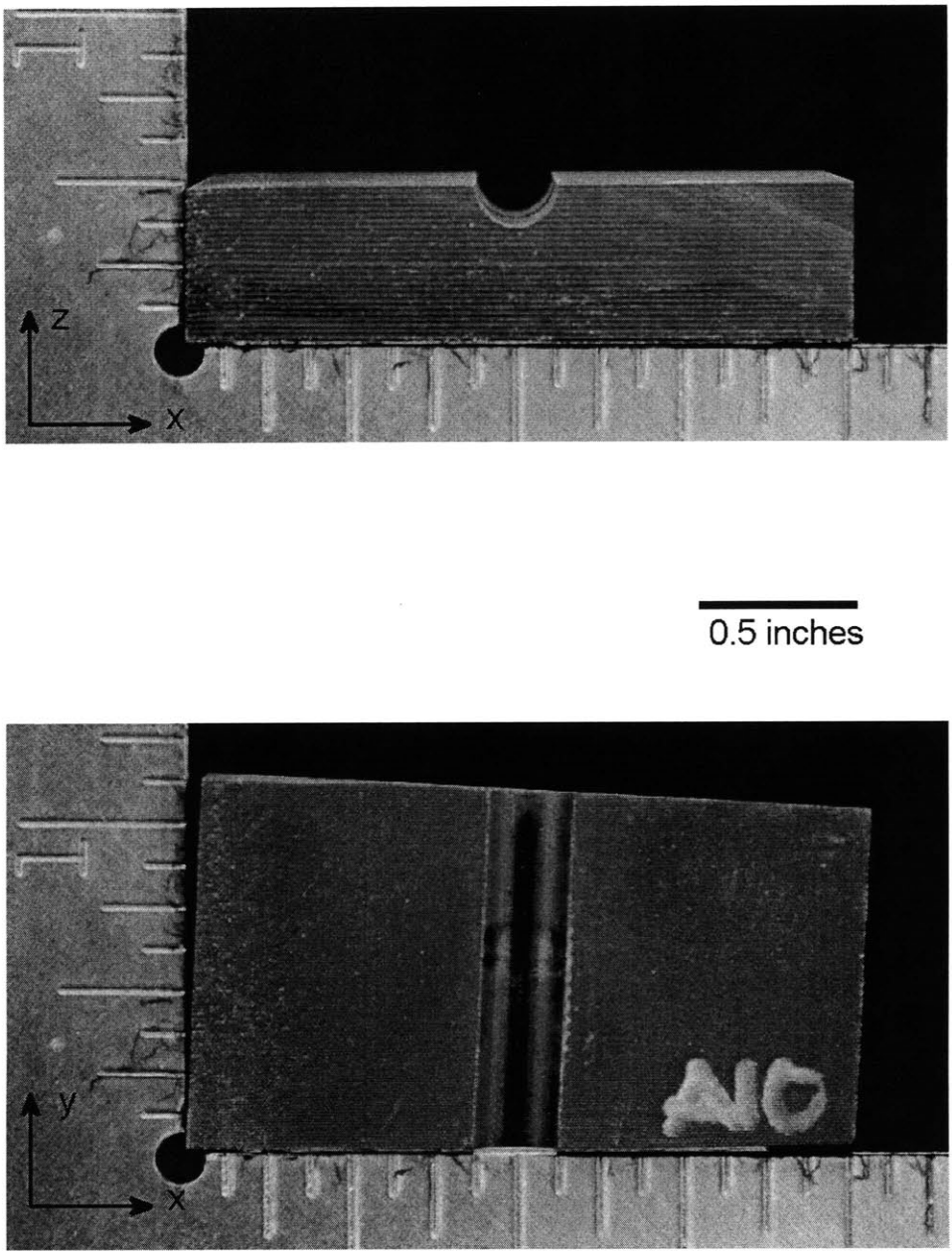

Figure E.11 Photographs of $[\pm 45/0]_{13S}$ specimen, tested to crushing in "three-dimensional loading", shown via (*top*) side view, and (*bottom*) top view.

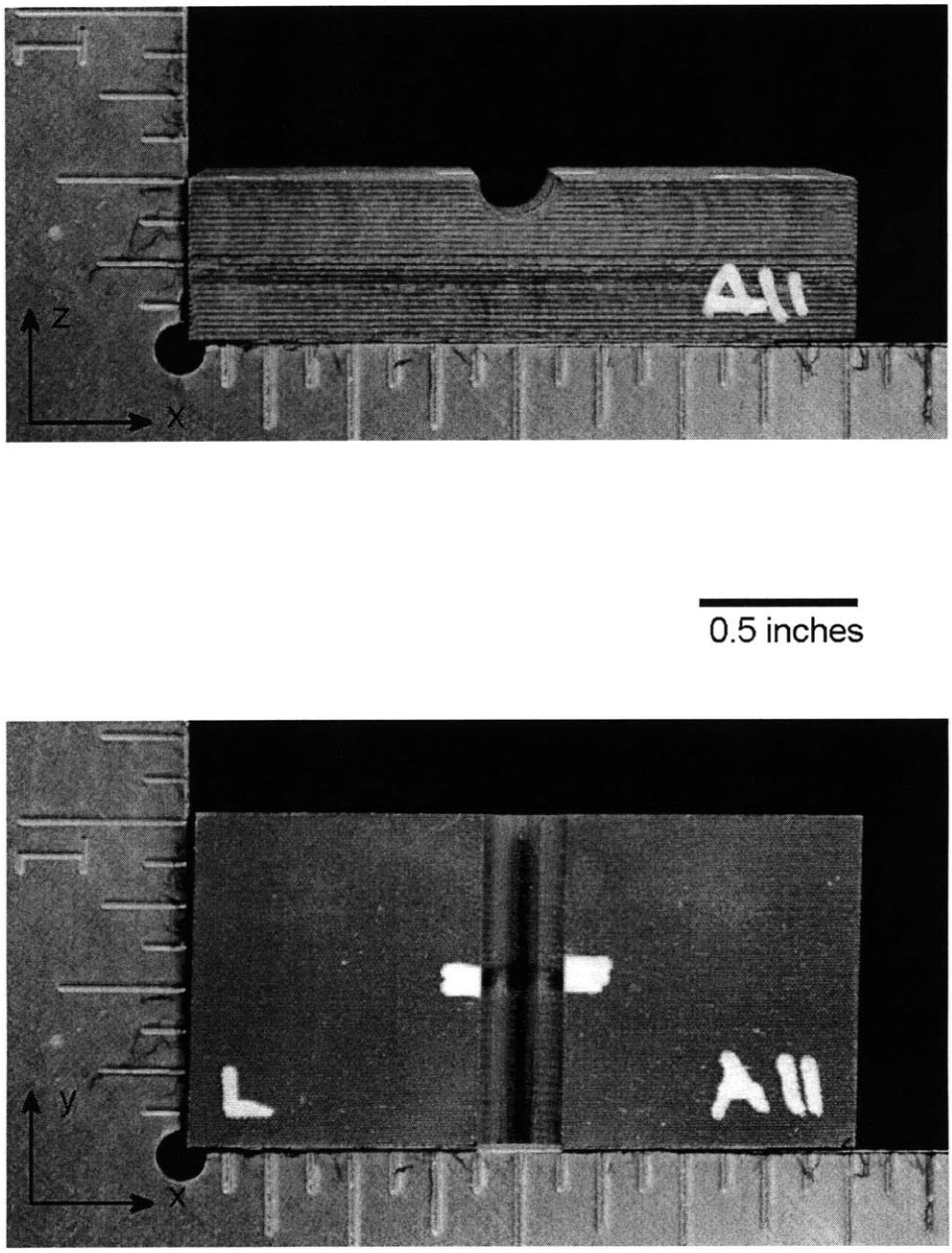

Figure E.12 Photographs of $[\pm 45/0]_{13S}$ specimen, tested to crushing in "three-dimensional loading", shown via (*top*) side view, and (*bottom*) top view.

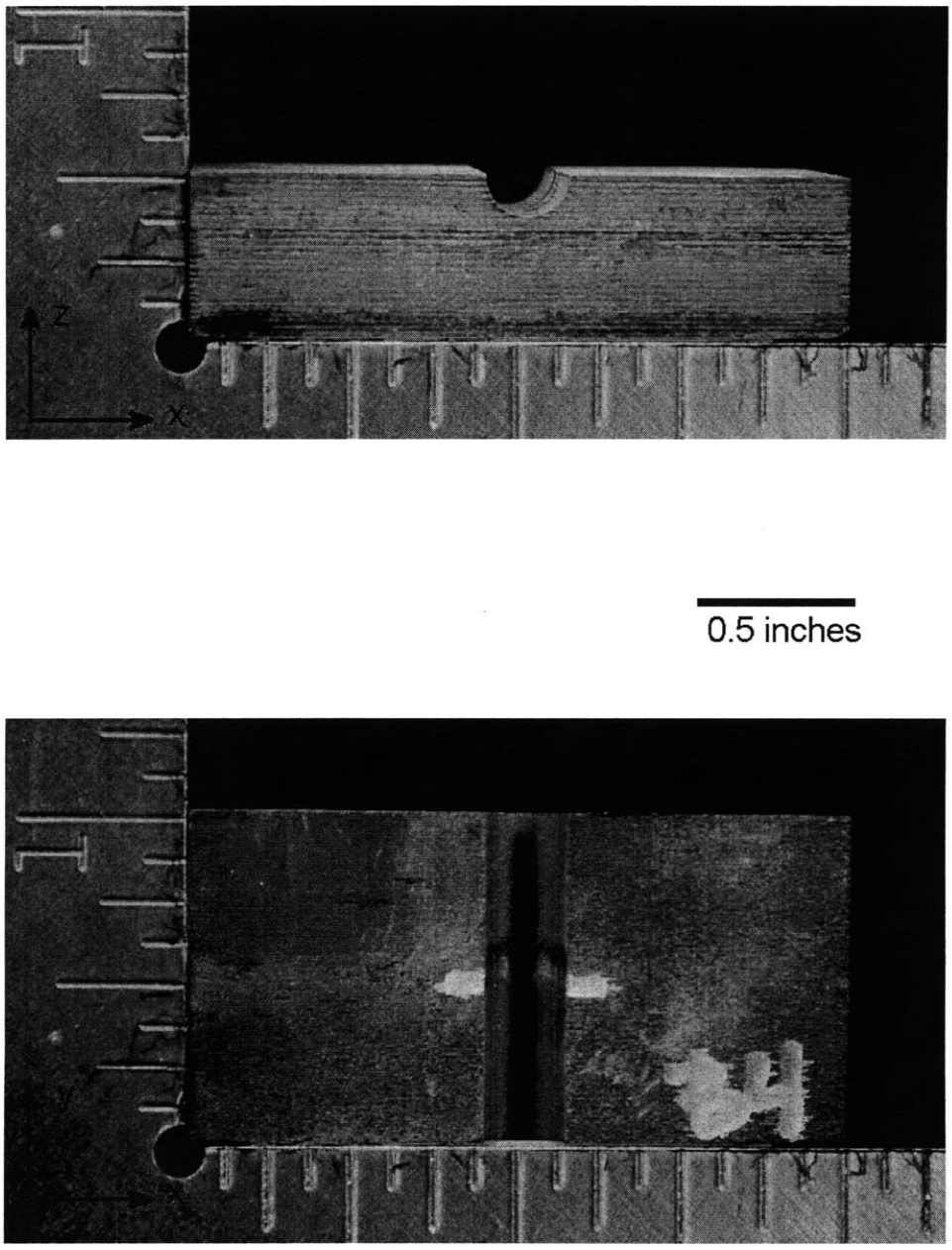

Figure E.13 Photographs of $[\pm 30/0]_{13S}$ specimen, tested to crushing in "three-dimensional loading", shown via (*top*) side view, and (*bottom*) top view.

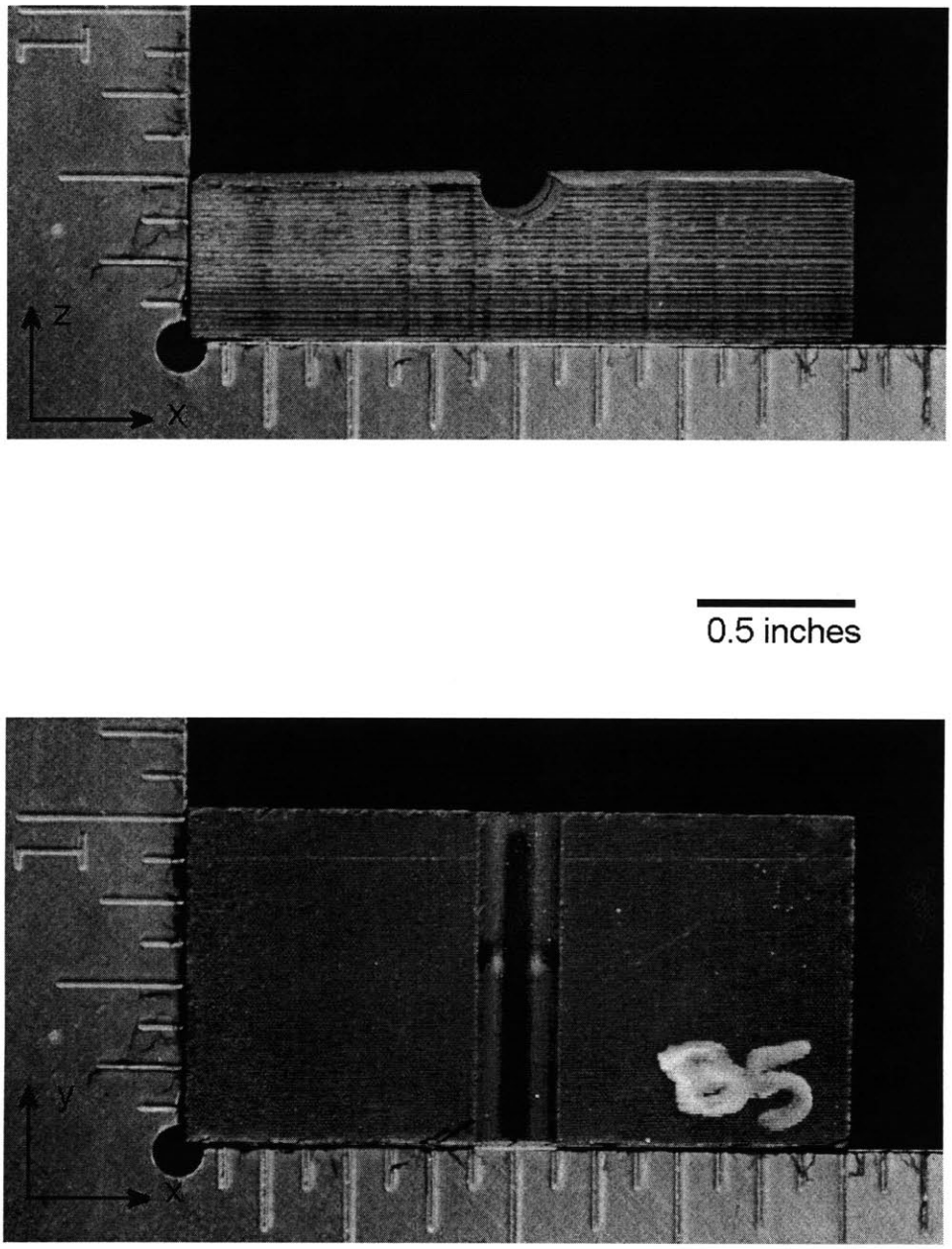

Figure E.14 Photographs of $[\pm 30/0]_{13S}$ specimen, tested to crushing in "three-dimensional loading", shown via (*top*) side view, and (*bottom*) top view.

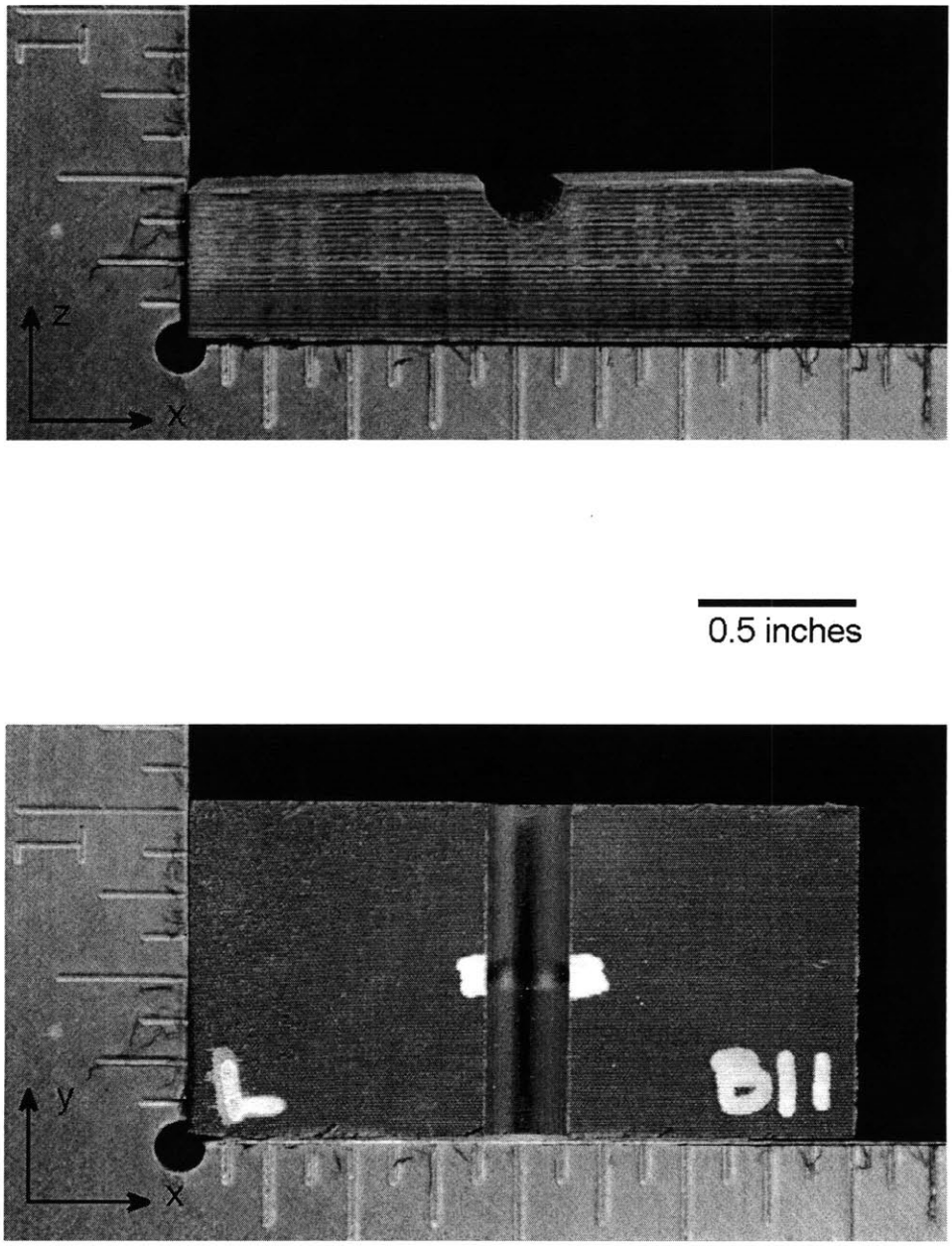

Figure E.15 Photographs of $[\pm 30/0]_{13S}$ specimen, tested to crushing in "three-dimensional loading", shown via (*top*) side view, and (*bottom*) top view.

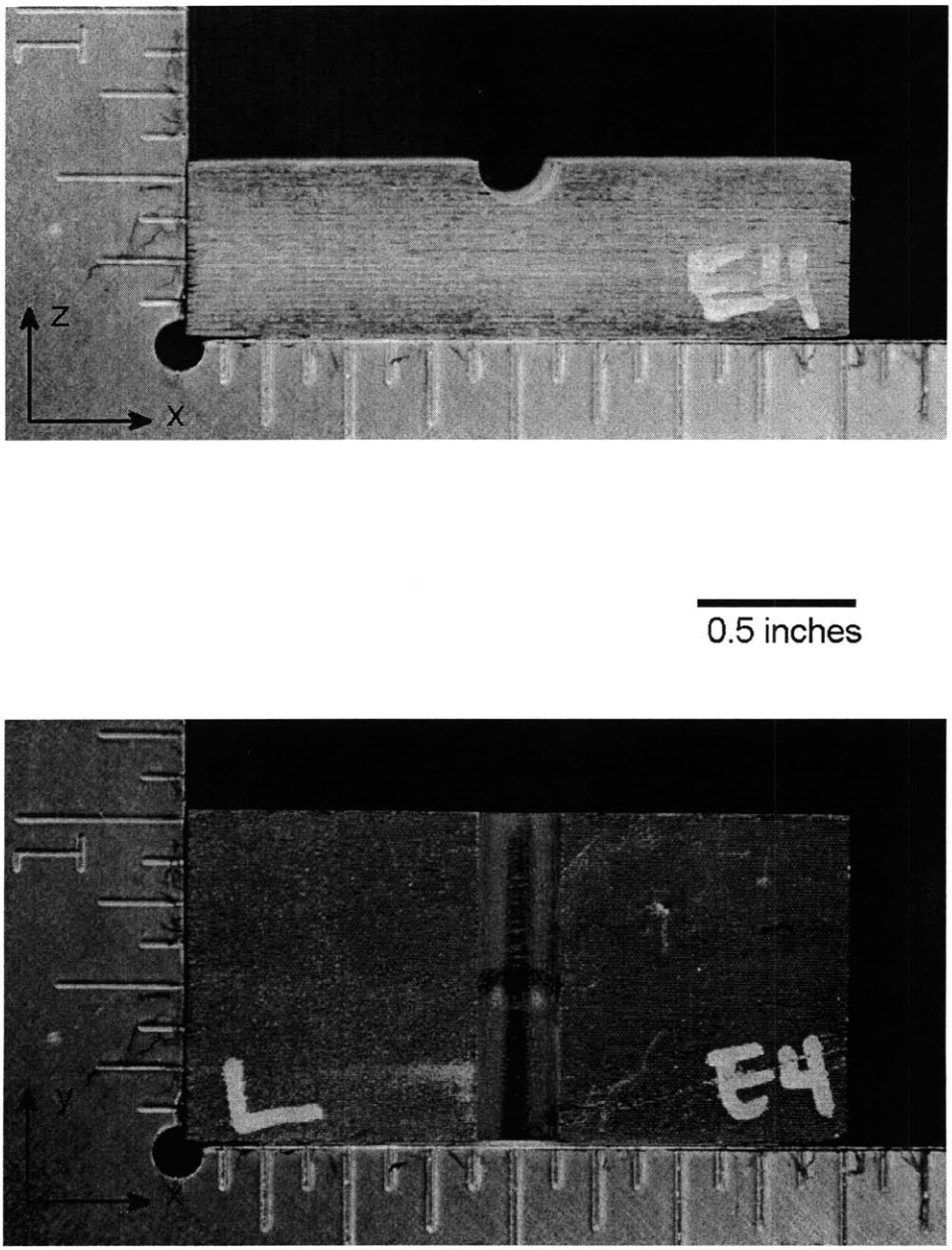

Figure E.16 Photographs of $[\pm 15/0]_{13S}$ specimen, tested to crushing in "three-dimensional loading", shown via (*top*) side view, and (*bottom*) top view.

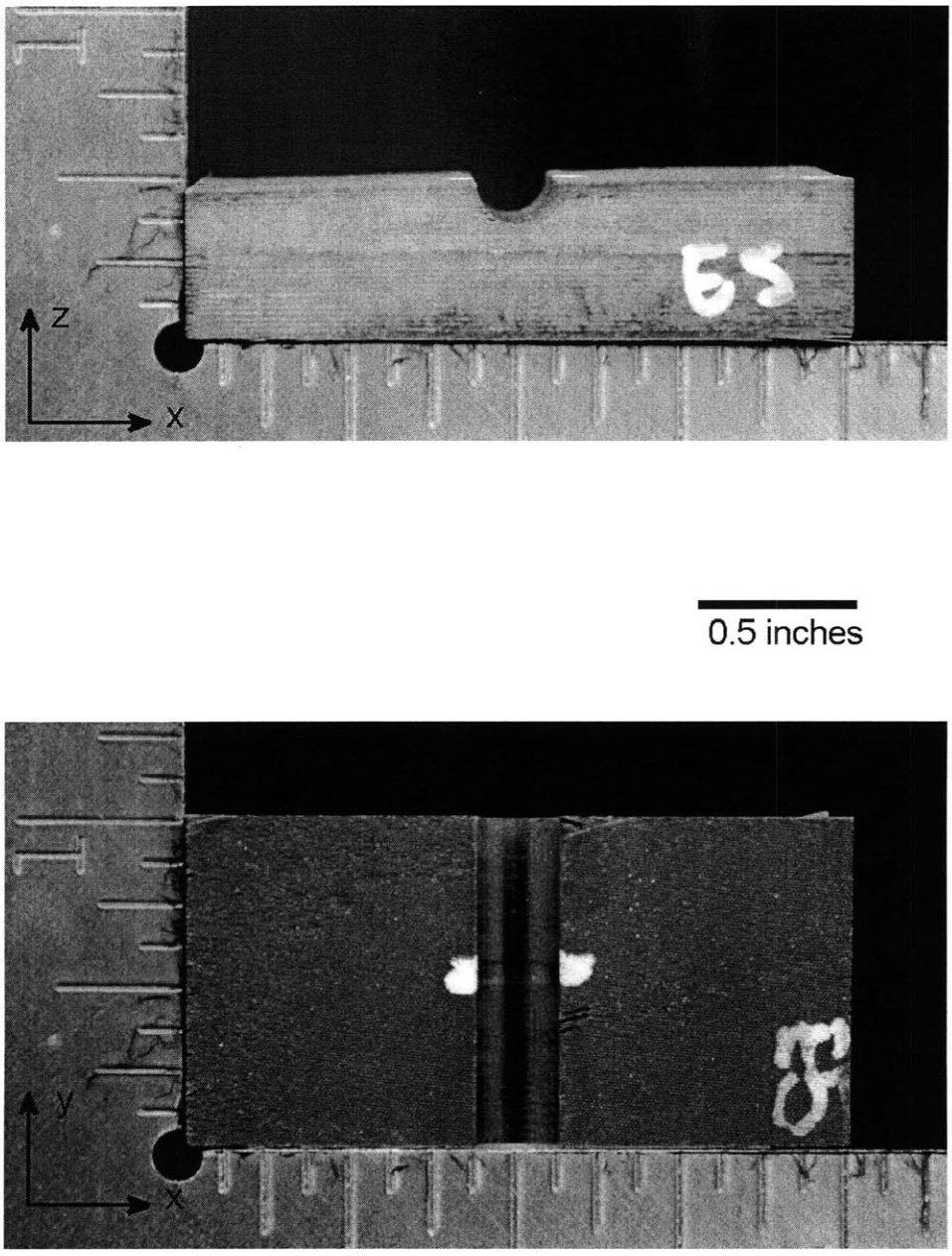

Figure E.17 Photographs of $[\pm 15/0]_{13S}$ specimen, tested to crushing in "three-dimensional loading", shown via (*top*) side view, and (*bottom*) top view.

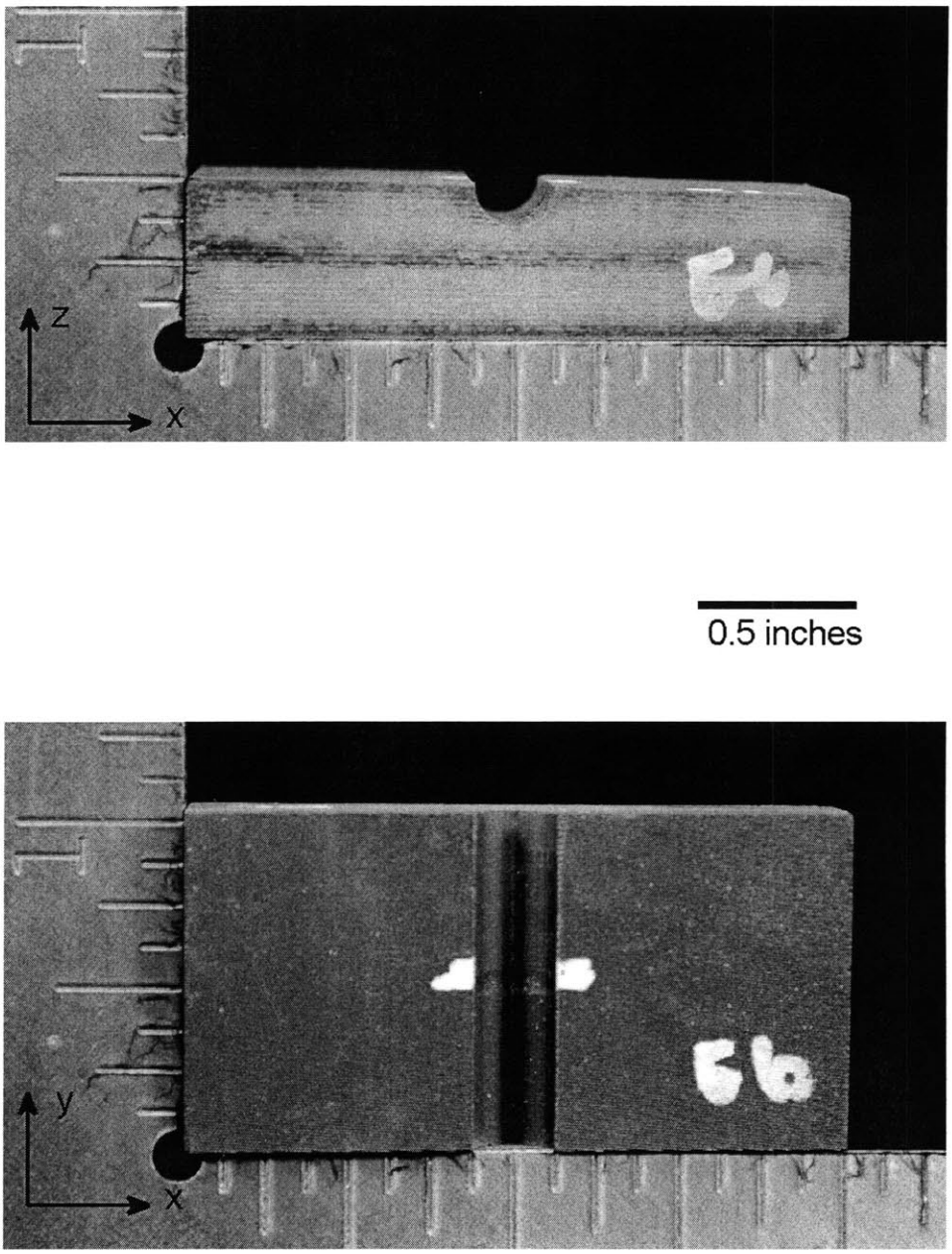

Figure E.18 Photographs of $[\pm 15/0]_{13S}$ specimen, tested to crushing in "three-dimensional loading", shown via (*top*) side view, and (*bottom*) top view.